Pseudospin dynamics in hybrid nanojunctions

DISSERTATION

zur Erlangung des
Doktorgrades der Naturwissenschaften (Dr. rer. nat.)
der Fakultät für Physik der Universität Regensburg

vorgelegt von

Christoph Brückner geb. Rohrmeier

aus Regensburg

im Jahr 2023

Das Promotionsgesuch wurde eingereicht am 07.12.2022.

Die Arbeit wurde angeleitet von apl. Prof. Dr. Andrea Donarini.

Prüfungsausschuss:

Vorsitzender:	PD Dr. Andreas Hüttel
Erstgutachter:	apl. Prof. Dr. Andrea Donarini
Zweitgutachter:	Prof. Dr. Jaroslav Fabian
Weiterer Prüfer:	Prof. Dr. Vladimir Braun

Contents

Introduction

Quantum entanglement is at the very heart of quantum mechanics. It is one of the decisive properties, which separates the classical world from the quantum one. Entanglement, in its essence, describes the phenomenon that different particles may form a combined quantum state in such a way that one particle of this state cannot be represented independently of the other constitute states. As Erwin Schrödinger framed it in 1935 [1]:

> When two systems, of which we know the states by their respective representatives, enter into temporary physical interaction due to known forces between them, and when after a time of mutual influence the systems separate again, then they can no longer be described in the same way as before, [namely] by endowing each of them with a representative of its own. I would not call that one, but rather the characteristic trait of quantum mechanics, the one that enforces its entire departure from classical lines of thought. By the interaction, the two representatives (or Ψ-functions) have become entangled.

An example of entangled particles is a spin-singlet state (total spin $S = 0$) formed by two electrons, which is illustrated in Fig. 1 **a**:

$$|\Psi_-\rangle = \frac{1}{\sqrt{2}} \left(|\uparrow\downarrow\rangle - |\downarrow\uparrow\rangle \right). \tag{0.1}$$

Also referred by Albert Einstein as the *spooky action at a distance*, entanglement of the former state ensures that even if the electrons get separated far from each other, a

measurement of one of the electron's spin would determine the other's instantaneously. A similar thought experiment, where the position and the momenta of two particles are entangled, is known as the Einstein–Podolsky–Rosen (EPR) paradox, named after its proposers [2]. Remarkably, Albert Einstein, considered as one of the founders of quantum mechanics with his theory of quantized light, contested though the non-locality of the entanglement and thus of quantum mechanics in general, which corresponds to actions propagating faster than the speed of light. He proposed as a solution to the thought experiment the so-called local hidden-variable theory. However, as one

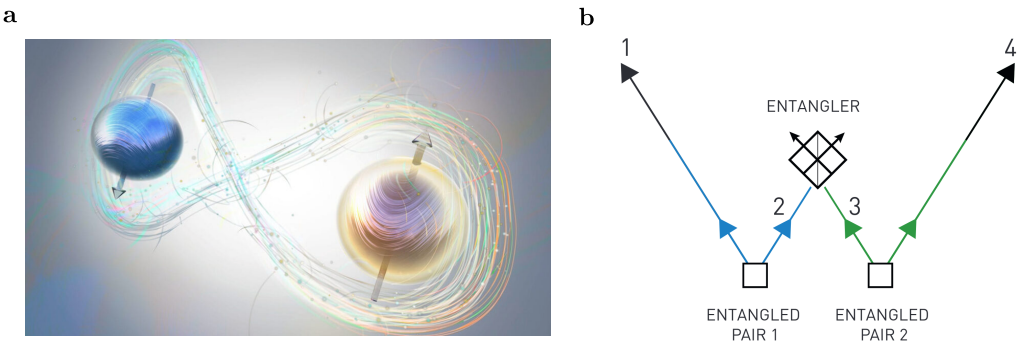

Figure 1: Quantum entanglement of particles: **a** Illustration of an entangled spin up and spin down electron. © 2022 Nicolle R. Fuller/NSF. **b** Two pairs of entangled particles are emitted from different sources. One particle from each pair is brought together in a special way that entangles them. The two other particles (1 and 4 in the diagram) are then also entangled. In this way, two particles that have never been in contact can become entangled. Figure and description taken from [3]. © 2022 Johan Jarnestad/The Royal Swedish Academy of Sciences.

could think after this introduction, the study of entanglement was not only restricted to a dispute between the founding fathers of quantum mechanics in its early days. Its significance as a current research topic was underscored by the Nobel Prize in Physics of 2022. The prize was awarded to Alain Aspect, John Clauser and Anton Zeilinger "for experiments with entangled photons, establishing the violation of Bell inequalities and pioneering quantum information science". In their groundbreaking work, Aspect and Clauser managed to obtain, among other things, a source of singlet states, similar to the one sketched earlier in Eq. (0.1). With the help of these states, they could probe the Bell inequality and show experimentally its violation [4, 5]. This result helped to establish the now-consensus understanding of entanglement, with rejecting firmly the

local hidden-variable theory in quantum mechanics proposed by Einstein.

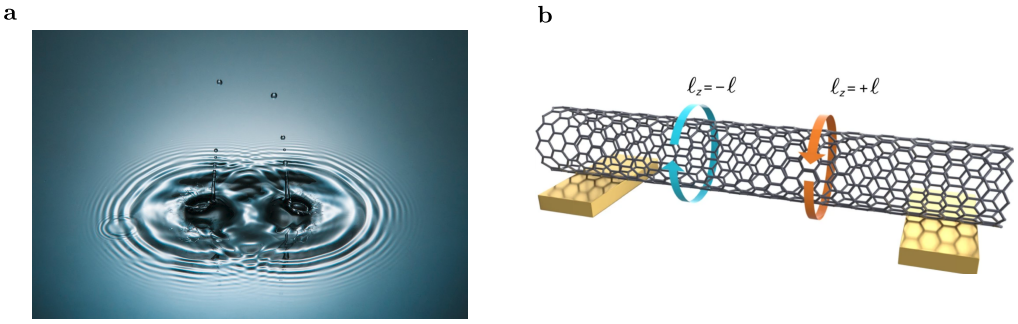

Figure 2: Interference: a Two water drops illustrate an interference pattern. The ripples represent constructive and destructive interference of the two concentric water waves. © 2013 Josh Valcarcel photography. **b** Setup of the interference experiment of [6]. In a CNT, a linear combination of the two prevailing momentum states can lead to the formation of a dark state.

With quantum interference, we have another fundamental concept of quantum physics protruding into our research. It is a direct consequence of the superposition principle, which allows quantum systems to be at the same time in two different states. Note that the superposition principle is not the same phenomenon as entanglement since for the latter you inevitably need two degrees of freedom. Furthermore, all entangled states are (special cases) of superposed states, while the opposite is not true. Generally, quantum interference characterizes two coherent states or wave packets combining each other in a constructive or destructive way, in close analogy to water waves (cf. Fig. 2 **a**). It should be noted that only if there exists some form of quantum coherence in a system, the effect of interference can arise. In order to have perfectly coherent states, these states need to have a constant phase relation. The most prominent experiment in this context is definitely the original double-slit experiment by Young, which measured light interference [7]. Later achievements were the observation of interference patterns with electrons [8, 9] and even with C_{60} molecules [10].
Due to impressive experimental advances, quantum interference, once believed to be too delicate for any attempt to bring it even into the mesoscopic scale, is now studied in a broad range of systems. In order to bring interference effects and thus quantum coherence into realistic experimental scenarios, one must consider the interaction of a system with its environment. The coupling to the leads, however, introduces decoherence with a detrimental effect on interference. Nevertheless, many research groups could

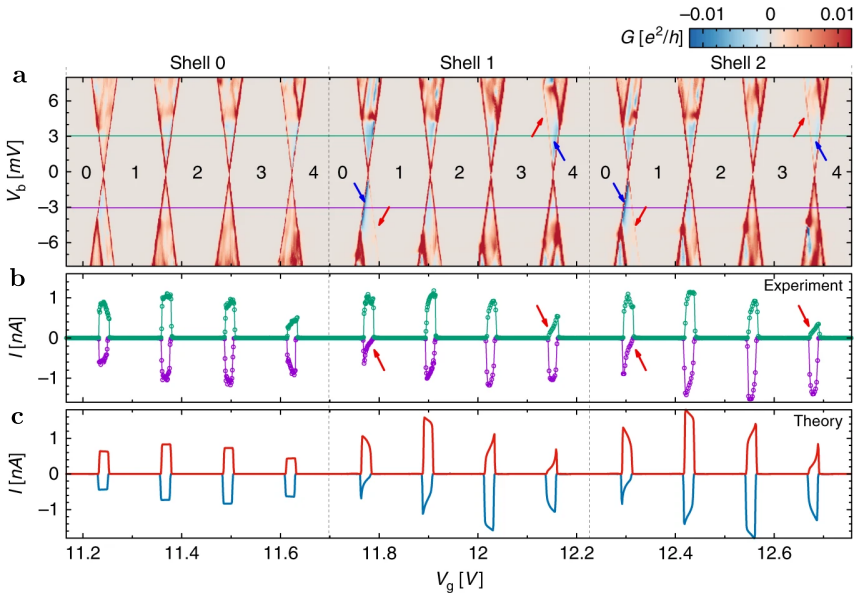

Figure 3: Dark state formation in a CNT: a Stability diagram of the QD reveals missing transition lines, indicated by the red arrows, which can only explained by destructive interference. Blue arrows highlight areas of negative differential conductance. Experimental data of the gate traces of the current (**b**) shows a good agreement with the theoretical results (**c**).

show in recent years striking evidence of interference fingerprints in a variety of setups and regimes, despite the presence of this coupling. In this regard, experiments in the strong [11–13] and weak [14–16] coupling regime could observe different manifestations of interference. All of these implementations share the property that they consist of multiple paths for the traversing particles, which are energetically equivalent. In contrast to the strong coupling regime, where the decoherence rate is negligible, the weak coupling regime is governed by decoherence. There, electrons enter the nanojunction one after the other, in a transport regime dubbed, for this reason, sequential tunneling. The electrons reside then on the system for a relative long time and they potentially can lose their coherence. Nevertheless, the possible coherent pumping from the leads, which is in constant competition to the hindrance of the decoherence, can prevail and lead indeed to interference in these nanojunctions.

Another recent work displays the effect of interfering electrons [6]. The setup is here a carbon nanotube (CNT) suspended on two leads (cf. Fig. 2 **b**), which can be considered as an overall a quantum dot (QD) system. In Fig. 3, we depict their theoretical and experimental findings, where the interference effects are clearly visible through the

disappearance of transition lines. The origin of this effect is found to be in the formation of a so-called dark state, which is decoupled from one of the leads. The resulting suppression of current is not captured within the classical picture, but in the quantum world, it can be seen as the destructive interference of electrons in analogy to a valley in the water wave picture (Fig. 2 **a**). Overall, this particular work is closely related to the presented research of this thesis, where slightly adjusted parameters lead to strikingly new interference features.

Outline This thesis is divided into two main parts. The first one deals with the underlying theory, while the second one is about its applications.

Part 1 - Theory In Cha. 1, we introduce our transport theory based on the density matrix formalism. Transforming the equations into the Liouville space, we obtain here a generalized master equation for an arbitrary system. Special focus is given to the two leading-order approximations with respect to the coupling of the system to the leads. These two approximations, called sequential tunneling and cotunneling, are exclusively used in the later following results. The discussion of a diagrammatic representation of this formalism, its application to the basic example of the single-impurity Anderson model and the role of the coherences complete this chapter.

In Cha. 2, we examine spin and pseudospin valves, with the main focus on valves implemented in QD setups. The pseudospin is considered to be the orbital degree of freedom of a double quantum dot (DQD) in our applications. We dedicate one section to the important role of the exchange fields, which can alter the dynamics in QD valve setups drastically. Sequentially, we give the equations of motion for a QD spin valve, which are the foundation of our studies of more intricate systems in DQDs. Other than that, the concept of spin resonance, central in this thesis, is extensively discussed. Moreover, the concept of concurrence as a measure of entanglement in a bipartite system is introduced.

In Cha. 3, we cover the theoretical basis of the investigation of QD-based Josephson junctions. We achieve this with a particle-conserving ansatz to superconductivity. At first, we introduce the broader context of superconductivity to the reader in terms of its history, the recent developments as well as the deficiencies of the existing underlying theory. The derived generalized master equation, with the proper definitions of the superconducting Kernels, is the foundation of the later work. Additionally, we introduce the Anderson pseudospin in order to describe the proximity-induced superconducting

correlations appearing in the QDs. Using a pseudospin description also for the superconductive nanojunctions helps us to take advantage there from the appropriated methods applied for the analysis of pseudospin dynamics in valve setups.

Part 2 - Applications

In Cha. 4, we discuss the results of our first publication *Pseudospin resonances reveal synthetic spin-orbit interaction*, in which we investigate a DQD pseudospin valve. To start with, we thoroughly introduce a microscopic model of a pseudospin valve setup. Moreover, by manipulating the coupling to the leads, we substantiate our predictions. We realize pseudospin current resonances, which can split due to the addition of ferromagnetic leads. In this particular setup, an intertwinement of the spin and the pseudospin degree of freedom is observed. The discussion is based on a coherent sequential tunneling model, which complements the numerical data obtained by a generalized master equation up to the cotunneling transport regime. In the outlook, experimental results of a possible implementation of pseudospin resonances in a CNT setup are discussed.

In Cha. 5, we present the results of our second publication, titled *Precession of entangled spin and pseudospin resonances in double quantum dots*. Upon the results of the previous chapter, we extend and generalize here the model to allow for arbitrary spin and pseudospin polarizations of the leads. In the particular example of a DQD-based spin valve, we can show intricate current resonances, which stem from the precession dynamics of an entangled spin and pseudospin. Dissecting the interplay of decoherence, pumping and precession in these systems helps us to predict the resonances. Other than that, we identify as the general mechanism behind spin and pseudospin resonances a dephasing process.

In Cha. 6, we investigate proximity-induced superconductivity in a QD-based Josephson junction within a particle-conserving ansatz. We can show that finite superconducting correlations, captured by the Anderson pseudospin, leak into the QD, and that they can assume non-zero values for gate voltages inside the Coulomb blockade region, far away from the previously assumed resonance positions. The finding of non-zero values of the pair amplitude is rationalized by the delicate interplay of quasiparticle processes and the ones involving Cooper pairs. Moreover, we demonstrate a so-called 0-π transition of our system in dependence of temperature or gate voltage. The calculations are performed within the leading-order approximation of the coupling to the leads and encompass also non-equilibrium configurations.

Theory

1

Liouville approach to transport

In this chapter, we introduce the transport theory which represents the foundation of this thesis. We derive a generalized master equation based on the density matrix formalism in the Liouville approach. This method is inherently based on the evolution of states according to the Schrödinger equation. However, due to the enormous number of degrees of freedom of a system connected to large reservoirs, it is impossible to capture the evolution of all states. For that reason, one traces out the reservoir degree of freedoms and focuses instead on the reduced density matrix of the system. The coupling to the leads introduces incoherent processes leading to a loss of information as well as coherent processes building up coherences in our reduced density matrix. Coherences are, in the context of density matrices, phase relations between different states in a given basis. The Liouville approach is now our method of choice to describe transport phenomena, where exactly those coherences are an integral part of the systems, which often cannot be described without them. Going from a Hilbert space description to a Liouville space, it enables us to condense the resulting equations in a more concise manner. Moreover, we prefer the Liouville space representation to the more conventional Hilbert space one. In the Liouville space, the equations of motion for the reduced density matrix are in fact more concise, thus allowing us a better overview of their structure.

1.1 System-bath Hamiltonian

In this thesis, we focus on open quantum systems. This concept is widely used in many fields of physics like quantum optics, statistical mechanics and quantum information. In general, an open quantum system describes a quantum-mechanical system interacting with its environment, called the *bath*. In order to analyze realistic physical setups, these are often the model of choice since many systems cannot be treated as isolated from their surroundings. Moreover, in transport configurations, precisely this interaction of the bath and system is desired and, crucially, characterizes the overall dynamics. By definition, we lack full information of the large baths. Consequently, they introduce dissipation (i.e., irreversible processes) and decoherence to the system. A generic system-bath Hamiltonian describing such a setup reads

$$\hat{H} = \hat{H}_{\mathrm{S}} + \hat{H}_{\mathrm{B}} + \hat{H}_{\mathrm{tun}}, \tag{1.1}$$

where the system Hamiltonian $\hat{H}_{\mathrm{S}}$ is coupled to the bath Hamiltonian $\hat{H}_{\mathrm{B}}$ via the tunneling Hamiltonian $\hat{H}_{\mathrm{tun}}$. Throughout the thesis, we pay special attention to interacting systems. One of the simplest realization of an interacting system is a QD where its small spatial size leads to discrete energy levels for its residing electrons. Usually, one applies a gate voltage V_{g} to the QD, which shifts its energy levels through capacitive coupling, and a bias voltage V_{b} to the leads tuning the current I. The electrons are confined on these islands akin to artificial atoms, and they exhibit strong Coulomb repulsion which fixes the number of particles on a broad gate voltage range, the so-called Coulomb blockade. In Fig. 1.1, a transport setup is shown where the system is chosen to be a QD. With the exception of the superconducting case treated in Cha. 3, the bath Hamiltonian is modeled as two fermionic baths

$$\hat{H}_{\mathrm{B}} = \sum_{l\boldsymbol{k}\sigma_l} \varepsilon_{l\boldsymbol{k}\sigma_l} \hat{c}^{\dagger}_{l\boldsymbol{k}\sigma_l} \hat{c}_{l\boldsymbol{k}\sigma_l}, \tag{1.2}$$

where $l = \mathrm{L}, \mathrm{R}$ comprises the lead index and σ_l labels the spin index of the corresponding lead. The momentum vector $\boldsymbol{k}$ is indicated in boldface.
The distinction of the spin quantization axis of each lead is important when an itinerant ferromagnet is introduced in Sec. 2.2 to describe spin valve setups. The density of states of the leads, a crucial quantity in transport theory, determines the single-particle energies $\varepsilon_{l\boldsymbol{k}\sigma_l}$. We take for simplicity single-band dispersion per spin species and lead, as fermionic transport only involves states close to the Fermi-energy. The annihilation operator $\hat{c}_{l\boldsymbol{k}\sigma_l}$ destroys the lead electron with the corresponding energy $\varepsilon_{l\boldsymbol{k}\sigma_l}$. The

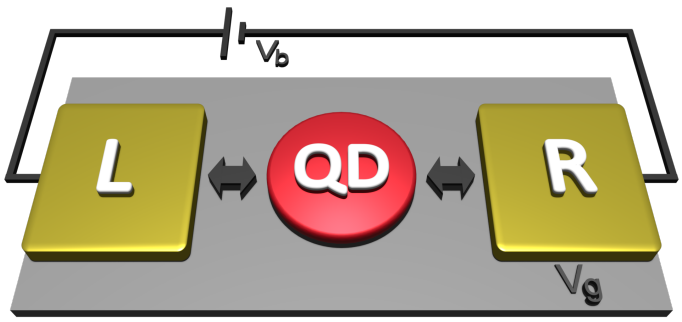

Figure 1.1: Schematic setup of a QD attached to leads: The bath Hamiltonian $\hat{H}_{\mathrm{B}}$ consists of two leads ($l = \mathrm{L}, \mathrm{R}$) in between which a bias voltage V_{b} is applied. A gate voltage V_{g} modifies the energy levels of the system Hamiltonian $\hat{H}_{\mathrm{S}}$ which is here chosen to be a QD. The black arrows indicate the tunneling coupling of the system and the bath via $\hat{H}_{\mathrm{tun}}$.

creation operator is denoted by $\hat{c}^{\dagger}_{l\boldsymbol{k}\sigma_l}$.
Tunneling between the bath and the system is described by the following Hamiltonian,

$$\hat{H}_{\mathrm{tun}} = \sum_{l\boldsymbol{k}\sigma_l i\sigma} t_{l\boldsymbol{k}\sigma_l,i\sigma}\, \hat{c}^{\dagger}_{l\boldsymbol{k}\sigma_l}\, \hat{d}_{i\sigma} + t^{*}_{l\boldsymbol{k}\sigma_l,i\sigma}\, \hat{d}^{\dagger}_{i\sigma}\, \hat{c}_{l\boldsymbol{k}\sigma_l}, \tag{1.3}$$

where the dot annihilation/creation operators $\hat{d}_{i\sigma}/\hat{d}^{\dagger}_{i\sigma}$ are connected with the lead operators via the tunneling amplitudes $t_{l\boldsymbol{k}\sigma_l,i\sigma}$ and its complex counterpart $t^{*}_{l\boldsymbol{k}\sigma_l,i\sigma}$. The tunneling amplitudes describe the interface of the leads with the system. They weight the tunneling from a particular single-particle system state to a certain single-particle lead state, or vice versa. Physically, these amplitudes are a measure of the overlap of the lead and the system wave functions. They are strongly influenced by the geometry of the contacts. The two indices of the dot operators label the transferred electrons with its spin σ and its orbital degree of freedom i.

1.2 Nakajima-Zwanzig equation

This section follows to a great extent the introduction of the transport theory of our publication [17] which is based on [18, 19]. A more detailed derivation of the Nakajima-Zwanzig equation also can be found in [20].
The Nakajima-Zwanzig equation falls into the category of master equations and is expressed in the density matrix formalism. Generally, master equations are used in physics to describe the time evolution of states by differential equations. They are

often applied to open quantum systems, but not exclusively. There are numerous implementations. Here we explicitly derive a general and exact master equation, known in the community as generalized master equation (GME). It is a generalization of the Pauli master equation, as in contrast to the latter, it also incorporates the dynamics of the coherences, i.e., the off-diagonal elements of the density matrix. The important role of the coherences is elaborated in great detail in Sec. 1.7.
The starting point for the derivation of our GME is the Liouville-von Neumann equation, which describes the time evolution of the total density matrix. The Liouville-von Neumann equation is the quantum mechanical analog to the Liouville equation of statistical mechanics and can be directly deduced from the Schrödinger equation. For its formulation, we introduce the concept of a Liouville superoperator $\mathcal{L}$:

$$\dot{\hat{\rho}}_{\mathrm{tot}}(t) = -\frac{i}{\hbar}\big[\hat{H}, \hat{\rho}\big] =: \mathcal{L}\hat{\rho}_{\mathrm{tot}}(t), \tag{1.4}$$

where $\dot{\hat{\rho}}_{\mathrm{tot}}(t)$ is the time derivative of the density matrix for the total system-bath model. The Liouville superoperator is a linear operator acting on the vector space of the Hermitian operators, themselves defined on the Fock space of the system-bath model. It is convenient to split the full Liouvillian $\mathcal{L}$ into the sum of three terms $\mathcal{L} = \mathcal{L}_{\mathrm{S}} + \mathcal{L}_{\mathrm{B}} + \mathcal{L}_{\mathrm{tun}}$, each indicating the commutator with the corresponding component of the Hamiltonian. Since we are primarily interested in the dynamics of the system, we integrate over the bath degrees of freedom and thus obtain an equation of motion for the reduced density matrix $\hat{\rho} = \mathrm{Tr}_{\mathrm{B}}\{\hat{\rho}_{\mathrm{tot}}\}$.
In order to arrive at a GME in an integral form, we deploy the Nakajima-Zwanzig projection operator technique [21, 22]. The main idea behind this approach consists of splitting the total density operator into two parts, namely $\mathcal{P}\hat{\rho}_{\mathrm{tot}}$ and $\mathcal{Q}\hat{\rho}_{\mathrm{tot}}$. The former captures the separated component of $\hat{\rho}_{\mathrm{tot}}$ at a given time. The latter instead takes the entangled part. The projectors extracting these two components are defined as

$$\mathcal{P}\hat{\rho}_{\mathrm{tot}} = \mathrm{Tr}_{\mathrm{B}}\{\hat{\rho}_{\mathrm{tot}}\} \otimes \hat{\rho}_{\mathrm{B}}, \tag{1.5}$$

$$\mathcal{Q}\hat{\rho}_{\mathrm{tot}} = (1 - \mathcal{P})\,\hat{\rho}_{\mathrm{tot}}, \tag{1.6}$$

with $\hat{\rho}_{\mathrm{B}}$ as the reference equilibrium density matrix of the bath.
Subsequently, we solve formally the Liouville equation for $\mathcal{Q}\hat{\rho}_{\mathrm{tot}}$ and inserting the result back into the equation for $\mathcal{P}\hat{\rho}_{\mathrm{tot}}$. The result is called the Nakajima-Zwanzig equation [23]:

$$\mathcal{P}\dot{\hat{\rho}}_{\mathrm{tot}}(t) = \mathcal{L}_{\mathrm{S}}\mathcal{P}\hat{\rho}_{\mathrm{tot}}(t) + \int_0^t \mathrm{d}s\; \mathcal{K}(t-s)\mathcal{P}\hat{\rho}_{\mathrm{tot}}(s). \tag{1.7}$$

One defines the Kernel superoperator as

$$\mathcal{K}(t) = \mathcal{P}\mathcal{L}_{\text{tun}}\bar{\mathcal{G}}_{\mathcal{Q}}(t)\mathcal{L}_{\text{tun}}\mathcal{P}, \tag{1.8}$$

where the propagator for the entangled part $\bar{\mathcal{G}}_{\mathcal{Q}}(t)$ contains all orders in the tunneling Liouvillian $\mathcal{L}_{\text{tun}}$:

$$\bar{\mathcal{G}}_{\mathcal{Q}}(t) = e^{(\mathcal{L}_{\text{S}}+\mathcal{L}_{\text{B}}+\mathcal{Q}\mathcal{L}_{\text{tun}}\mathcal{Q})t}. \tag{1.9}$$

The last step, a formally trivial trace over the leads of Eq. (1.7), yields the desired equation of motion for the reduced density operator.
The so far exact Nakajima-Zwanzig equation depends on the state of the system at all previous times, thus it is non-local in time. However, we restrict ourselves in this thesis to calculate the steady state of the system, which is defined as $\hat{\rho}^{\infty} \coloneqq \text{Tr}_{\text{B}}\{\hat{\rho}_{\text{tot}}(t \to \infty)\}$. By applying a Laplace transformation and with the help of the final value theorem, we get an equation for steady state of the reduced density matrix [19, 24–26]:

$$\text{Tr}_{\text{B}}\left\{\left(\mathcal{L}_{\text{S}} + \tilde{\mathcal{K}}\right)(\hat{\rho}^{\infty} \otimes \hat{\rho}_{\text{B}})\right\} = 0, \tag{1.10}$$

with

$$\tilde{\mathcal{K}} = \mathcal{P}\mathcal{L}_{\text{tun}} \sum_{n=0}^{\infty} \left(\tilde{\mathcal{G}}_0 \mathcal{Q}\mathcal{L}_{\text{tun}}\mathcal{Q}\right)^{2n} \tilde{\mathcal{G}}_0 \mathcal{L}_{\text{tun}}\mathcal{P}, \tag{1.11}$$

where

$$\tilde{\mathcal{G}}_0 = \lim_{\lambda \to 0^+} \frac{1}{\lambda - \mathcal{L}_{\text{S}} - \mathcal{L}_{\text{B}}} \tag{1.12}$$

is the Laplace transform of the free propagator, for the system and the bath, in the absence of tunneling. Since the tunneling Hamiltonian does not conserve the leads' particle number, $\mathcal{P}\mathcal{L}_{\text{tun}}^{2n+1}\mathcal{P} = 0$ for $n \in \mathbb{N}$, only an even number of $\mathcal{L}_{\text{tun}}$ survives the trace over the bath degrees of freedom in Eq. (1.11).
The Laplace transform of the propagation Kernel is used to define the equation of motion within the Markov approximation of the GME:

$$\mathcal{P}\dot{\hat{\rho}}_{\text{tot}}(t) = \left(\mathcal{L}_{\text{S}} + \tilde{\mathcal{K}}\right)\mathcal{P}\hat{\rho}_{\text{tot}}(t). \tag{1.13}$$

Here, one is not restricted to the steady state but assumes that the timescale of the evolution of the reduced density matrix is much longer than the decay time of the propagation Kernel $\mathcal{K}(t-s)$, thus, ultimately, of the bath correlator functions [23]. This condition ensures that memory effects do not play a role so that the equation can be seen as local in time.

1.3 Weak coupling limit

Throughout this thesis, we opt to treat the interaction exactly. We approximate, on the other hand, the coupling to the leads to the two lowest orders to be able to tackle more complex setups. Such a perturbative expansion of the propagation Kernel is a valid approximation if the coupling to the leads ($\Gamma_0 \ll U, k_\mathrm{B}T$) is sufficiently small. The following subsections are dedicated to the lowest order, the often used sequential tunneling limit and the next-to-leading order known shortly as the cotunneling regime. It should be stated that the naming of this regime as *cotunneling* can be ambiguous since this order also encompasses other tunneling phenomena such as, e.g., pair tunneling.

1.3.1 Sequential tunneling

The first term of the sum in Eq. (1.11) reproduces the sequential tunneling regime. The propagation Kernel reads

$$\tilde{\mathcal{K}}^{(2)} = \mathcal{P}\mathcal{L}_\mathrm{tun}\frac{1}{0^+ - \mathcal{L}_\mathrm{S} - \mathcal{L}_\mathrm{B}}\mathcal{L}_\mathrm{tun}\mathcal{P}, \tag{1.14}$$

with the two tunneling Liouvillians $\mathcal{L}_\mathrm{tun}$ setting the definition of the perturbative order used in this thesis. With 0^+, we denote the limit coming from the Laplace transformation, which should be performed at the very end of the calculation. It originates from the limit of the free propagator defined in Eq. (1.12), $\tilde{\mathcal{G}}_0 = \lim_{\lambda\to 0^+}\tilde{\mathcal{G}}_0(\lambda) = \lim_{\lambda\to 0^+}(\lambda - \mathcal{L}_\mathrm{S} - \mathcal{L}_\mathrm{B})^{-1}$.
We introduce a Liouville index α for an arbitrary operator $\hat{X}$ in order to shorten the notation:

$$\hat{X}^+\hat{\rho} := \hat{X}\hat{\rho}, \quad \hat{X}^-\hat{\rho} := \hat{\rho}\hat{X}. \tag{1.15}$$

With this definition, we can reformulate a commutator as $\left[\hat{X},\hat{\rho}\right] = \sum_\alpha \alpha\hat{X}^\alpha\hat{\rho}$. Applying this notation to $\mathcal{L}_\mathrm{tun}$ yields

$$\mathcal{L}_\mathrm{tun}\hat{X} = -\frac{i}{\hbar}\sum_{p=\pm}\sum_{\alpha=\pm}\sum_{l\boldsymbol{k}\sigma_l n} p\, t^{\bar{p}}_{l\boldsymbol{k}\sigma_l,n}\,\hat{c}^{p,\alpha}_{l\boldsymbol{k}\sigma_l}\,\hat{d}^{\bar{p},\alpha}_{n}\hat{X}, \tag{1.16}$$

with $n = \{i\sigma\}$ running over the states of the system. We further introduced in Eq. (1.16), the indices $p = \pm$ and $\bar{p} = -p$ which distinguish creators ($p = +$) from annihilators ($p = -$) and, for the tunneling amplitudes, $t^-_{l\boldsymbol{k}\sigma_l,n} := t_{l\boldsymbol{k}\sigma_l,n}$ from its complex value $t^+_{l\boldsymbol{k}\sigma_l,n} := t^*_{l\boldsymbol{k}\sigma_l,n}$.
The tunneling amplitudes between specific bath and system states can be incorporated in the so-called tunneling rate matrix [27], which is defined on the single-particle space

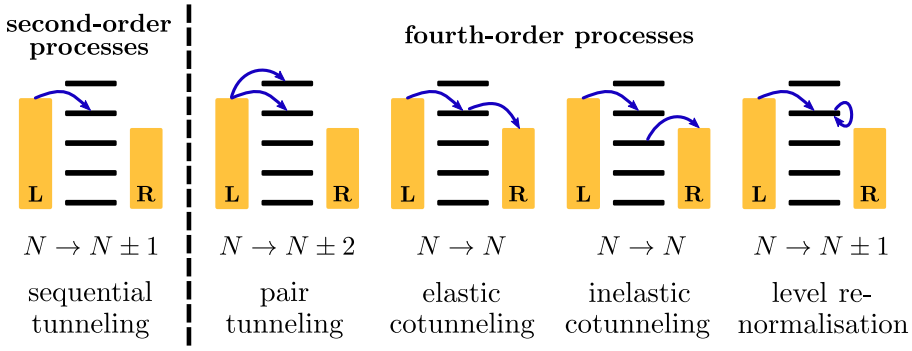

Figure 1.2: Visualization of an one-electron tunneling process and correlated two-electron processes: The leftmost sketch shows an exemplary sequential tunneling process where one electron (blue line) tunnels from the source to one energy level of the system. The other four sketches show instead correlated two-electron processes which extend the transport regime to the cotunneling regime.

of the system as

$$\Gamma^{l}_{n,m}(E) = \frac{2\pi}{\hbar} \sum_{\boldsymbol{k}\sigma_l} t^{*}_{l\boldsymbol{k}\sigma_l,n}\, t_{l\boldsymbol{k}\sigma_l,m}\, \delta(E - \varepsilon_{l\boldsymbol{k}\sigma_l}). \tag{1.17}$$

In Sec. 2.2, we further elaborate on the specific form of the tunneling rate matrices and their important role in the observation of interference effects in spin valve setups. Using now Eqs. (1.16)-(1.17), we can express the second-order Kernel as

$$\tilde{\mathcal{K}}^{(2)} = \frac{-i}{2\pi} \sum_{\substack{nmp \\ l\alpha_1\alpha_2}} \int d\varepsilon\, \Gamma^{l,p}_{n,m} \hat{d}^{\bar{p},\alpha_2}_{n} \frac{\alpha_1\alpha_2 f_l^{(p\alpha_1)}(\varepsilon)}{i0^{+} + p\varepsilon - i\hbar\mathcal{L}_{\mathrm{S}}} \hat{d}^{p,\alpha_1}_{m} \mathcal{P}. \tag{1.18}$$

The Fermi-function is defined as $f_l^{\pm}(\varepsilon) = [e^{\pm(\varepsilon-\mu_l)/(k_{\mathrm{B}}T)}+1]^{-1}$. Hereby is μ_l the chemical potential of the l-lead, k_{B} the Boltzmann constant and T the temperature. Furthermore, we set $\varepsilon := \varepsilon_{l\mathbf{k}\sigma_l}$ in the integral and added an index p also to the tunneling rate matrix, which obeys then $\Gamma^{l}_{n,m} = \Gamma^{l,-}_{n,m} = \Gamma^{l,+}_{m,n}$. Moreover, we drop in this expression the energy dependence of the tunneling rate matrix. The rationale behind it lies in the wide-band limit, which we use for the solution of this energy integral. This approximation assumes that the bands around the Fermi-energy are sufficiently flat so that the detailed structure of the density of states is not important for the description of the transport. It is valid if the bandwidth is large in comparison to the applied bias.
In general, the integral of Eq. (1.18), for a certain set of parameters, can be understood as the weight of a certain tunneling event. The leftmost sketch of Fig. 1.2 shows a

sequential tunneling event, which is characterized by the transfer of exactly one electron from or to the leads indicated by the blue arrow. It may seem at the first glance counterintuitively that one needs for a single charge transfer two $\hat{d}$-system operators in the integral. However, this is inherently tied to the fact the bra- and the ket-vector of the reduced density matrix need to change for sequential tunneling by one considering, e.g., a state with initially N-particles and finally $N \pm 1$-particles: $\hat{\rho}_{\text{initial}} = |N\rangle\langle N| \rightarrow \hat{\rho}_{\text{final}} = |N \pm 1\rangle\langle N \pm 1|$. For the concrete but rather technical solution of the sequential tunneling integral, we direct the interested reader to Appx. A.

1.3.2 Cotunneling

The next-to-leading-order in the expansion of the Kernel of Eq. (1.11) is the cotunneling transport regime:

$$\tilde{\mathcal{K}} = \tilde{\mathcal{K}}^{(2)} + \tilde{\mathcal{K}}^{(4)} + \mathcal{O}\left(H_{\text{tun}}^{6}\right). \tag{1.19}$$

We indicate the cotunneling Kernel as $\tilde{\mathcal{K}}^{(4)}$ since there tunneling events up to the fourth order in $\mathcal{L}_{\text{tun}}$ are kept:

$$\tilde{\mathcal{K}}^{(4)} = \mathcal{P}\mathcal{L}_{\text{tun}}\tilde{\mathcal{G}}_0\mathcal{Q}\mathcal{L}_{\text{tun}}\mathcal{Q}\tilde{\mathcal{G}}_0\mathcal{Q}\mathcal{L}_{\text{tun}}\mathcal{Q}\tilde{\mathcal{G}}_0\mathcal{L}_{\text{tun}}\mathcal{P}. \tag{1.20}$$

Simplifying the expression yields

$$\begin{aligned}\tilde{\mathcal{K}}^{(4)} = &\mathcal{P}\mathcal{L}_{\text{tun}}\tilde{\mathcal{G}}_0\mathcal{L}_{\text{tun}}\tilde{\mathcal{G}}_0\mathcal{L}_{\text{tun}}\tilde{\mathcal{G}}_0\mathcal{L}_{\text{tun}}\mathcal{P} \\ &- \mathcal{P}\mathcal{L}_{\text{tun}}\tilde{\mathcal{G}}_0\mathcal{L}_{\text{tun}}\mathcal{P}\tilde{\mathcal{G}}_0\mathcal{P}\mathcal{L}_{\text{tun}}\tilde{\mathcal{G}}_0\mathcal{L}_{\text{tun}}\mathcal{P}.\end{aligned} \tag{1.21}$$

Since $\tilde{\mathcal{G}}_0$ commutes with $\mathcal{Q}$ respective $\mathcal{P}$ and both projection operators square to themselves, the innermost $\mathcal{Q}$-operators break down to $\mathcal{Q}$. The outermost $\mathcal{Q}$-operators vanish according to $\mathcal{P}\mathcal{L}_{\text{tun}}^{2n+1}\mathcal{P} = 0$. The second term compensates the reducible Wick's contraction still contained in the first term with the effect that only irreducible diagrams (i.e., diagrams which are not separated solely by a free evolution) persist in the cotunneling Kernel [24]. The fourth-order Kernel can be split into the contributions $\tilde{\mathcal{K}}^{(4,D)}$,

$$\begin{aligned}\tilde{\mathcal{K}}^{(4,D)} = &\frac{-i\hbar}{(4\pi)^2}\sum_{\{l\}\{p\}}\sum_{\{m\}\{n\}}\sum_{\{\alpha_i\}}\int d\varepsilon\int d\varepsilon'\,\alpha_1\alpha_4\hat{d}_n^{\bar{p},\alpha_4}\frac{f_{l'}^{(p'\alpha_2)}(\varepsilon')}{i0^+ + p\varepsilon - i\hbar\mathcal{L}_{\text{S}}}\hat{d}_{n'}^{\bar{p}',\alpha_3} \\ &\frac{\Gamma_{n,m}^{l,p}\Gamma_{n',m'}^{l',p'}}{i0^+ + p\varepsilon + p'\varepsilon' - i\hbar\mathcal{L}_{\text{S}}}\hat{d}_{m'}^{p',\alpha_2}\frac{f_l^{(p\alpha_1)}(\varepsilon)}{i0^+ + p\varepsilon - i\hbar\mathcal{L}_{\text{S}}}\hat{d}_m^{p,\alpha_1}\mathcal{P},\end{aligned} \tag{1.22}$$

and $\tilde{\mathcal{K}}^{(4,X)}$,

$$\tilde{\mathcal{K}}^{(4,X)} = \frac{i\hbar}{(4\pi)^2} \sum_{\{l\}\{p\}} \sum_{\{m\}\{n\}} \sum_{\{\alpha_i\}} \int d\varepsilon \int d\varepsilon' \hat{d}^{\bar{p},\alpha_4}_n \frac{f_l^{(p\alpha_2)}(\varepsilon)}{i0^+ + p\varepsilon - i\hbar\mathcal{L}_{\mathrm{S}}} \hat{d}^{\bar{p}',\alpha_3}_{n'} \frac{\alpha_1\alpha_4 \Gamma^{l,p}_{n,m} \Gamma^{l',p'}_{n',m'}}{i0^+ + p\varepsilon + p'\varepsilon' - i\hbar\mathcal{L}_{\mathrm{S}}} \hat{d}^{p,\alpha_2}_m \frac{f_l^{(p'\alpha_1)}(\varepsilon)}{i0^+ + p'\varepsilon' - i\hbar\mathcal{L}_{\mathrm{S}}} \hat{d}^{p',\alpha_1}_{m'} \mathcal{P}. \tag{1.23}$$

Both $\tilde{\mathcal{K}}^{(4,D)}$ and $\tilde{\mathcal{K}}^{(4,X)}$ involve double energy integrals, which can be solved by the residual theorem. In Appx. B, further remarks and the technical solution of the cotunneling integrals are given. The label of D and X of the Kernels stems from its diagrammatic representation, which is introduced in Sec. 1.5. With the help of a treatment of the cotunneling integrals founded on the work of [20, 24–26, 28, 29], we have implemented a transport code which includes all coherences necessary to capture the interference effects in our system. Moreover, the next-to-leading-order expansion allows for a systematic test of robustness of the interference effects beyond the sequential tunneling approximation. In the cotunneling regime, one sums up three processes, namely the cotunneling ones, pair tunneling ones and level renormalization processes (cf. Fig. 1.2 and [26]). They cannot be directly linked to either the X- or the D-functions.

Pair tunneling describes processes where two different electrons both enter or both leave the central system simultaneously, as opposed to cotunneling where one electron enters and one leaves the central system [30]. The number of electrons of the initial state thus differs by two from the final state ($N \to N \pm 2$).

Cotunneling can further be split into elastic and inelastic processes. The former are processes where the in- and the outgoing tunneling event involves only one energy level of the system, letting the system unchanged ($N \to N$). The latter, however, involve two different electrons and alter the electronic occupation of the system. In pair tunneling and cotunneling the individual tunneling processes are linked by an overall conservation of energy at the end of the total process. However, in the intermediate virtual state of the system where only one of the two correlated events has happened, there can be a (short-lived) violation of the energy conservation. Pair and cotunneling both can contribute to a current through the junction.

Level renormalization describes the last type of fourth-order processes, which are amendments to sequential tunneling [26]. They are processes where a charge fluctuation is accompanied by an electron transfer between lead and system ($N \to N \pm 1$). In fact,

it can be shown that these amendments to sequential tunneling are the linear-order contribution in a renormalization of the energy argument of the Fermi-function. Only if one would go to all orders by including all possible charge fluctuations, the full tunneling-induced level renormalization would be achieved [31].

1.4 Current

Starting from the stationary density matrix $\hat{\rho}^{\infty}$, one can obtain any stationary expectation value of a system observable as $O = \mathrm{Tr}_{\mathrm{S}}\{\hat{O}\hat{\rho}^{\infty}\}$. In transport calculations, the stationary current at lead l is of main interest:

$$I_l = \mathrm{Tr}_{\mathrm{S+B}}\left\{\tilde{\mathcal{K}}_{I_l}\hat{\rho}^{\infty} \otimes \hat{\rho}_{\mathrm{B}}\right\}. \tag{1.24}$$

The current Kernel $\tilde{\mathcal{K}}_{I_l}$ can be derived from the propagator Kernel in Eq. (1.11) by changing the leftmost tunneling Liouvillian with the current operator,

$$\hat{I}_l = \frac{i\mathrm{e}}{\hbar}\sum_{\boldsymbol{k}\sigma_l a\sigma} t_{l\boldsymbol{k}\sigma_l,a\sigma}\,\hat{c}^{\dagger}_{l\boldsymbol{k}\sigma_l}\,\hat{d}_{a\sigma} - t^{*}_{l\boldsymbol{k}\sigma_l,a\sigma}\,\hat{d}^{\dagger}_{a\sigma}\,\hat{c}_{l\boldsymbol{k}\sigma_l}, \tag{1.25}$$

where e is the electronic charge. For consistency, we keep the same order in the perturbation expansion of the propagator and of the current Kernel. In the following section, more details can be found regarding the exact modification of the propagation Kernel to deduce the current Kernel.

1.5 Diagrammatics

This section is dedicated to a diagrammatic formulation of the transport Kernel of Eq. (1.11) which helps to visualize certain tunneling events as well as to straightforwardly calculate them. At first, we introduce a diagrammatic representation with two timelines based on the real time diagrammatics framework initially developed by Gerd Schön, Herbert Schoeller and Jürgen König [32, 33]. Major contributions in this context also can be found in [24, 26]. Secondly, we show the connection to a more compact single-timeline Liouville space diagrammatics based on [18, 19]. The diagrammatic rules of this approach are given in Appx. C to allow the interested reader to perform the calculations on its own. To start with, we can write the GME of Eq. (1.10) as a matrix equation. Every final state ($|b\rangle\langle b'|$) is obtained from a sum over all possible tunneling

events contained in the Kernel starting from the initial states ($|a\rangle\langle a'|$):

$$\dot{\rho}_{bb'} = 0^b_{b'} = -\frac{i}{\hbar}\sum_{aa'}\delta_{ab}\delta_{a'b'}E_{aa'}\rho^a_{a'} + \sum_{aa'}K^{b,a}_{b',a'}\rho^a_{a'}$$

$$:= \quad |a\rangle \longleftarrow |a\rangle \quad \rho^a_{a'} + \sum_{a'a}\left(\quad |b\rangle \longleftarrow |a\rangle \quad \rho^a_{a'} \right). \qquad (1.26)$$

$$\langle a'| \longrightarrow \langle a'| \qquad\qquad \langle b'| \longrightarrow \langle a'|$$

with $E_{aa'} = E_a - E_{a'}$. The matrix and Kernel elements are set to

$$\hat{\rho} = \sum_{aa'}\rho^a_{a'}\,|a\rangle\langle a'|\,, \qquad (1.27)$$

$$K^{b,a}_{b',a'} = \langle b|\,\tilde{\mathcal{K}}\left(|a\rangle\langle a'|\right)|b'\rangle\,. \qquad (1.28)$$

The GME can be divided in a free coherent propagation stemming from the system Liouvillian $\mathcal{L}_\mathrm{S}$ and a propagation containing all possible tunneling events to all orders indicated by the gray block. The approximation of the Kernel to sequential tunneling yields the following eight diagrams in the two-timeline formalism. The timelines represent forward and backward propagation on a Keldysh contour for the ket- and the bra-part of the density matrix, respectively:

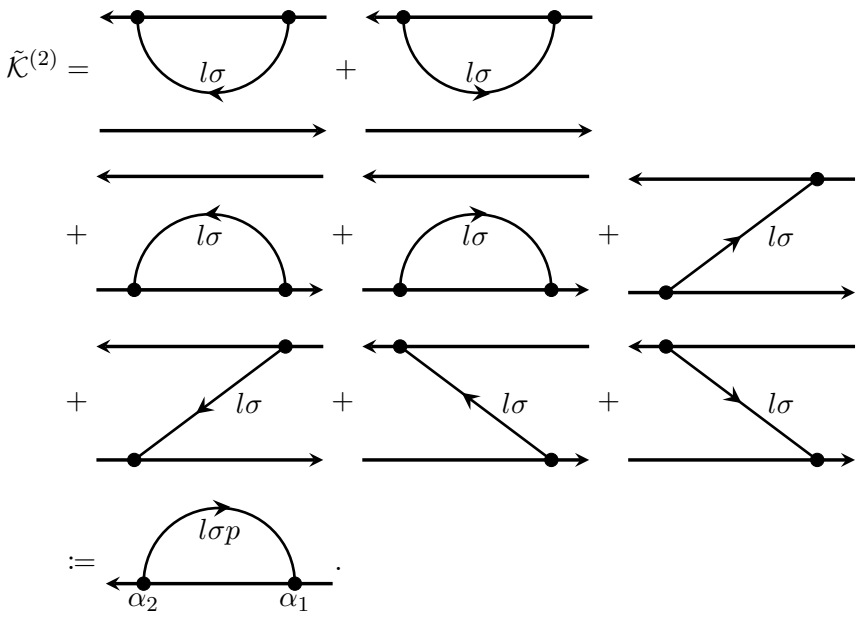

(1.29)

The eight two-timeline diagrams should be interpreted in the following way. The dark circles from right to left represent the time-wise first and second tunneling operator of Eq. (1.18). Every line connecting tunneling events is associated with a fixed p-value

and representing a Fermi-function. The direction of the arrow determines the p-value. If the arrow points to a certain tunneling event, this event is a creation operation in the system space and if the arrow points away, it is an annihilation event. In general, the upper contour represents $\hat{d}$-operators acting from the left on the density matrix with the respective Liouville index ($\alpha = +$), while the lower contours represent accordingly ($\alpha = -$)-operators acting from the right on the density matrix. Other than that, there are the σ- and l-indices which determine the spin and the lead index of the fermion line, while the tunneling matrix elements are not properly accounted for. For example, off-diagonal tunneling matrices in the spin space can lead to a mixing of the spin, with the effect that the diagrams with both spin species have to be considered. It occurs when a spin up electron entering from one lead does not only inject a spin up in the system space. To every diagram, an energy function can be assigned which gives then the weighting of the particular diagram depending on the electronic configuration like gate or bias voltage. From a vertical cut between neighboring tunneling events, the energy denominator for the energy integral can be read out as the difference between the energy from the temporary state on the upper contour minus the energy of the state on the lower contour weighted by the p-index. For the complete set of rules, the interested reader is referred to [26, 28]. In the last step of Eq. (1.29), the more compact single-timeline formalism is introduced, which is respecting the structure of the Liouville superoperators in a more natural way. With its three additional parameters α_1, α_2 and p, the full space of all possible tunneling configurations is recovered. The projection of the fourth-order Kernel into single-timeline diagrammatics yields only two conceptionally different types of diagrams, namely the D- and the X-diagrams:

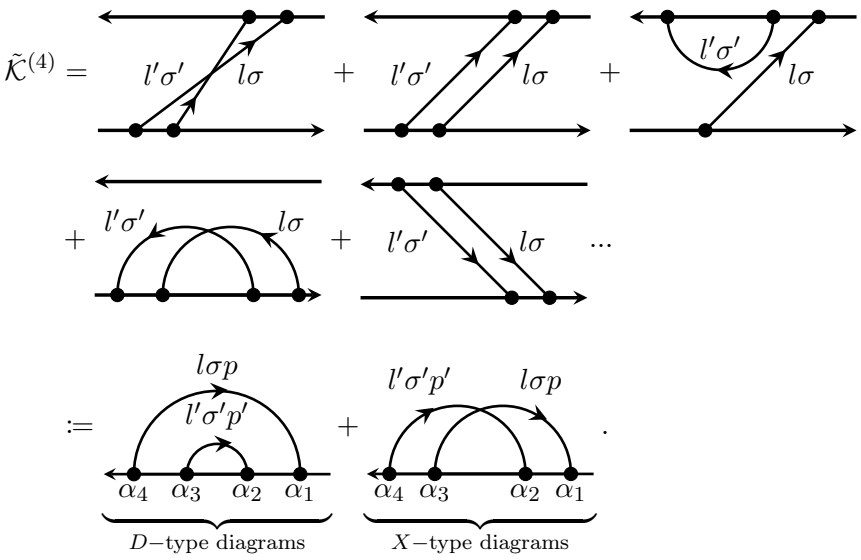

(1.30)

The conciseness of the single-time line diagrammatics becomes now clear since $\tilde{\mathcal{K}}^{(4)}$ consists already of $2^7 = 128$ irreducible diagrams in the former formalism (2^4 for the four Liouville indices, 2^2 for the p/p' indices and 2 for the D/X diagrams).
Two restrictions on the Kernel elements and density matrix elements help to check the consistency of an implementation of these diagrammatics:

$$\sum_a \rho_{aa} = 1, \qquad \sum_b K^{ba}_{ba'} = 0 \quad \forall a, a'. \tag{1.31}$$

The last equation is also known as the *sum-rule*. In [26], this rule leads to the introduction of the so-called gain-loss relations. In their essence, they state that a certain diagram has not a physical meaning on its own since in the physical rates always a set of diagrams are appearing. The gain-loss partner of a diagram is found, if the last vertex is moved on the other contour (change of α). In the sum rule, these gain-loss partners cancel then according to the sum-rule.
At this point, we give an example of a pair tunneling diagram of the D-type in both diagrammatics. We start with the initial density matrix $|0\rangle\langle 0|$ of a single QD with the four available states $\{|0\rangle, |\uparrow\rangle, |\downarrow\rangle, |2\rangle\}$. Two in-tunneling events from the left lead alter the system so that the final state is the double-occupied state $|2\rangle\langle 2|$:

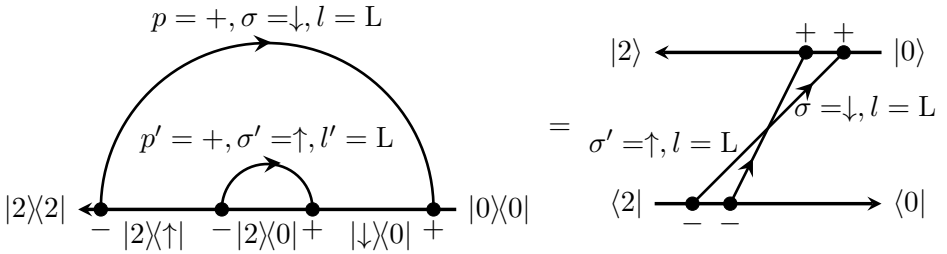

(1.32)

The three virtual intermediate states during the tunneling event and their energies are then the parameters of the respective D-function:

$$\begin{aligned} K^{20}_{20} &= \langle 2|\, \tilde{\mathcal{K}}^{(4,D)}\left(|0\rangle\langle 0|\right)|2\rangle \\ &= \frac{i\hbar}{(4\pi)^2}\sum_{\substack{\{n\}\\\{m\}}} \int d\varepsilon \int d\varepsilon' \hat{d}^{-,-}_n \underbrace{\frac{f^{(+)}_{\mathrm{L}}(\varepsilon')}{i0^+ + \varepsilon - E_{2\uparrow}}}_{\text{3. propagator}} \hat{d}^{-,-}_{n'} \underbrace{\frac{\Gamma^{\mathrm{L},+}_{n,m}\Gamma^{\mathrm{L},+}_{n',m'}}{i0^+ + \varepsilon + \varepsilon' - E_{20}}}_{\text{2. propagator}} \hat{d}^{+,+}_{m'} \underbrace{\frac{f^{(+)}_{\mathrm{L}}(\varepsilon)}{i0^+ + \varepsilon - E_{\downarrow 0}}}_{\text{1. propagator}} \hat{d}^{+,+}_{m} \\ &= \sum_{\substack{\{n\}\\\{m\}}} \frac{-\Gamma^{\mathrm{L},+}_{n,m}\Gamma^{\mathrm{L},+}_{n',m'}}{k_{\mathrm{B}}T} D^{++}(\nu,\xi,\delta)\hat{d}^{-,-}_n \hat{d}^{-,-}_{n'} \hat{d}^{+,+}_{m'} \hat{d}^{+,+}_m \end{aligned} \tag{1.33}$$

with $\nu = (E_{2\uparrow} - \mu_{\mathrm{L}})/(k_{\mathrm{B}}T)$, $\xi = (E_{\downarrow 0} - \mu_{\mathrm{L}})/(k_{\mathrm{B}}T)$ and $\delta = (E_{20} - 2\mu_{\mathrm{L}})/(k_{\mathrm{B}}T)$.

From this concrete example, one can deduce how one can translate a diagram into the mathematical expression and vice versa. The complete set of rules for the single-line diagrammatics can be found in Appx. C and are in the following briefly sketched. The three free propagators are captured by a fraction with the respective energy according to Eq. (1.12) as, e.g., for the first propagator with $1/(i0^+ + p\varepsilon - E_{\downarrow 0})$. The four system operators are denoted by their α-value and if they are creation or annihilation processes ($p = +/-$). Fermi-functions are linked to the rightmost vertex of the fermionic line connecting the two $\hat{d}$-operators, and they adopt the product of (αp) of this $\hat{d}$-operator. The tunneling rate matrices, associated to a Fermi-function, accompany the respective indices of the fermionic line. The prefactors for X-/D-diagrams are $\pm i\hbar\alpha_1\alpha_4/(4\pi)^2$ and for sequential tunneling diagrams $-i\alpha_1\alpha_2/(2\pi)$. Adding the respective summation of the indices and the integrals completes the rules.

Current Kernel: In order to obtain the current Kernel from the propagation Kernel, one has to consider only a subset of all possible diagrams. The following rules apply:

- *Lead index:* There is no summation of l-index of the leftmost vertex. The replacement of a tunneling Liouvillian with the current operator $\hat{I}_l$ fixes the lead index.

- *Position of last vertex:* Only diagrams where the last vertex is a left superoperator have to be considered ($\alpha = +$) since the current operator $\hat{I}_l$ always acts from the left. In the two-timeline diagrammatics this corresponds to diagrams where the leftmost vertex lies on the upper contour.

- *Direction of last fermion line:* The sign of the diagrams where the fermion line points away from the leftmost vertex has to be inverted. This difference stems from a sign change in $\hat{H}_{\mathrm{tun}}$ with respect to $\hat{I}_l$.

1.6 Single-impurity Anderson model

One of the simplest models of a transport setup is the well-studied single-impurity Anderson model (SIAM), named after Anderson, which used this model initially for describing magnetic impurities embedded in metals [35]. The SIAM is describing a single spin-degenerate level, and thus it can be seen as a single QD. The Hamiltonian can be written as

$$\hat{H}_{\mathrm{QD}} = \sum_{\sigma} \left(\varepsilon_\sigma + \mathrm{e}V_{\mathrm{g}}\right) \hat{d}_\sigma^\dagger \hat{d}_\sigma + U \hat{d}_\uparrow^\dagger \hat{d}_\uparrow \hat{d}_\downarrow^\dagger \hat{d}_\downarrow, \tag{1.34}$$

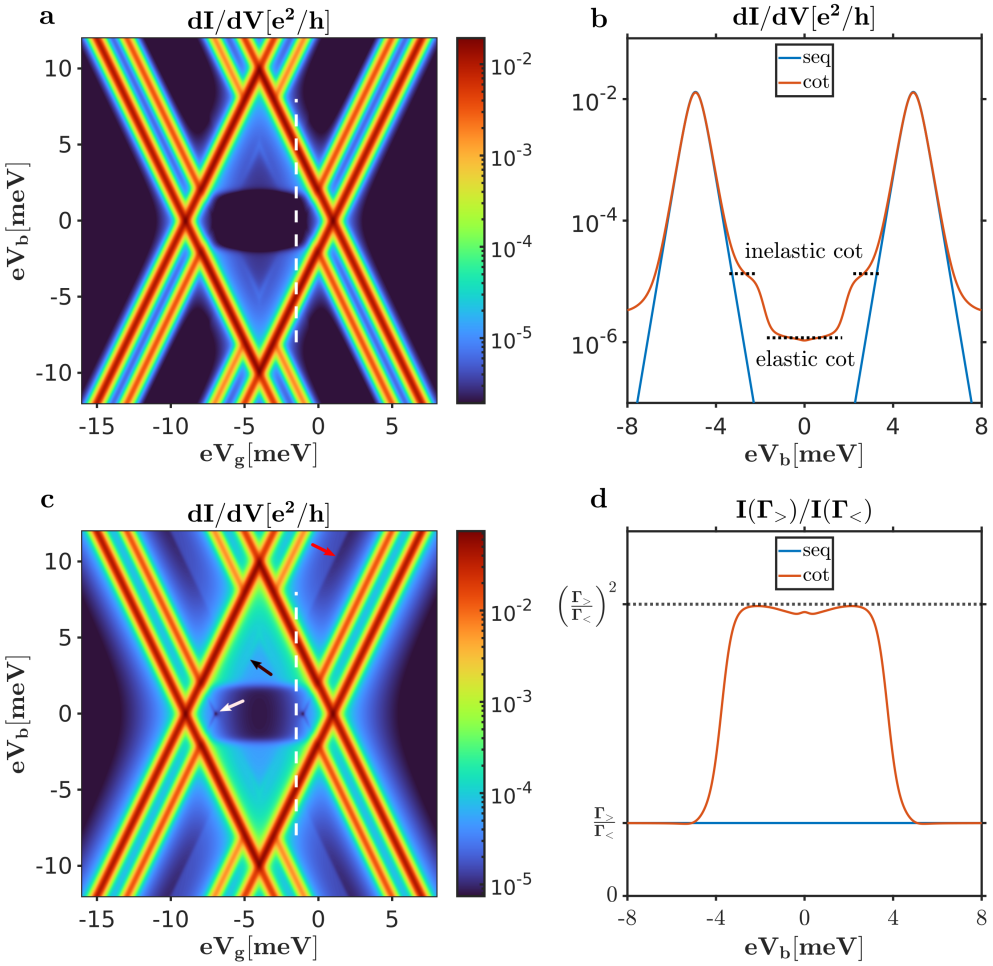

Figure 1.3: Single-impurity Anderson model with exited states due to Zeeman splitting: **a** Differential conductance of a SIAM centered around the Coulomb diamond with particle number $N=1$ where the current is strongly suppressed. The parameters are: $U = 8\,\mathrm{meV}$, $k_\mathrm{B}T = 0.1\,\mathrm{meV}$, $E_\mathrm{z} = 2\,\mathrm{meV}$ and $\Gamma_0^\mathrm{L} = \Gamma_0^\mathrm{R} = 0.005\,\mathrm{meV}$. **b** Bias cut of dI/dV at a gate voltage of $eV_\mathrm{g} = -1.5\,\mathrm{meV}$ up to the sequential tunneling (seq) and the cotunneling (cot) approximation. The inelastic cotunneling threshold can be clearly identified. **c** Differential conductance with same parameters as **a** except a stronger coupling to the leads: $\Gamma_0^\mathrm{L} = \Gamma_0^\mathrm{R} = 0.02\,\mathrm{meV}$. The arrows indicate from top to bottom: a pair-tunneling resonance [34], cotunneling-assisted sequential tunneling (cf. Fig. 1.4) and a reduced differential conductance feature also observed in [26]. **d** Comparison of the bias traces of the current from the low coupling case ($\Gamma_<$: **a**) and the high coupling case ($\Gamma_>$: **c**) shows the non-linear scaling of cotunneling features with the coupling strength.

where U is the on-site Coulomb repulsion, e is the elementary electric charge, V_g is the applied bias voltage and ε_σ the spin-dependent level position. The four dimensional Hilbert space is spanned by the basis $\{|0\rangle, |\uparrow\rangle, |\downarrow\rangle, |2\rangle\}$. In order to enrich the spectrum, one can add a Zeeman splitting E_z due to an external magnetic field, which modifies the level position of the spin states as $\varepsilon_\uparrow = \varepsilon_0 + E_z/2$ and $\varepsilon_\downarrow = \varepsilon_0 - E_z/2$. In Fig. 1.3, the differential conductance $dI/dV := dI/dV_\mathrm{b}$ of a SIAM with Zeeman split states, is plotted. It is a good example to highlight the effects of the different tunneling processes. Panel **a** shows the so-called stability diagram where one can clearly identify the Coulomb blockade region in the center which is confined by the diamond-shaped transition lines. Another feature is the enhanced differential conductance above the inelastic cotunneling threshold $|eV_\mathrm{b}| > E_z$ inside the Coulomb diamond, which also is highlighted in panel **b**. One can extract that the differential conductance inside the Coulomb diamond is predominantly due to cotunneling processes. Panel **c** shows a stability diagram with a bigger coupling strength leading to an enhancement of different fourth-order processes.

The red arrow for example indicates a pair tunneling resonance, which is located exactly in between two transition lines [34]. The explanation for this truly non-equilibrium transport feature is the following: If an electron tunnels from the source to the state $|\sigma\rangle$, there is an excess energy of Δ. In case that this Δ matches exactly the energy needed to assist an excitation to the higher lying state $|2\rangle$, one can observe these two tunneling events happening coherently via a pair tunneling process. This two-electron process preserves energy conservation at its end while violating it for a short time in the transitory virtual state in between.

Other than that, one also can observe cotunneling-assisted sequential tunneling, which leads to enhanced differential conductance in a triangle shaped area inside the Coulomb blockade region (black arrow). This effect is discussed in more details at the end of this section and in Fig. 1.4.

The last feature of Fig. 1.3 **a**, on which we focus, is marked with the white arrow. It is a half diamond shape area where the differential conductance is reduced compared to its surrounding. The explanation of this is given in [26] with Fig. 8. Amendments to sequential tunneling diagrams can lead to a reduction of the sequential tunneling rate $\Gamma^{\sigma\to 0}$ when fluctuations towards the initial state $|\sigma\rangle$ occur. They are then described as 'backward' fluctuations since they diminish the rate to $\Gamma^{\sigma\to 0}$ and can be understood as a fluctuation back to the positively biased lead, counteracting the enhancing character of elastic cotunneling contributions to the current.

As a benchmark for our differential conductance plot, we took the analytical result for a SIAM without a Zeeman splitting. The bias voltage and the gate voltage are set around

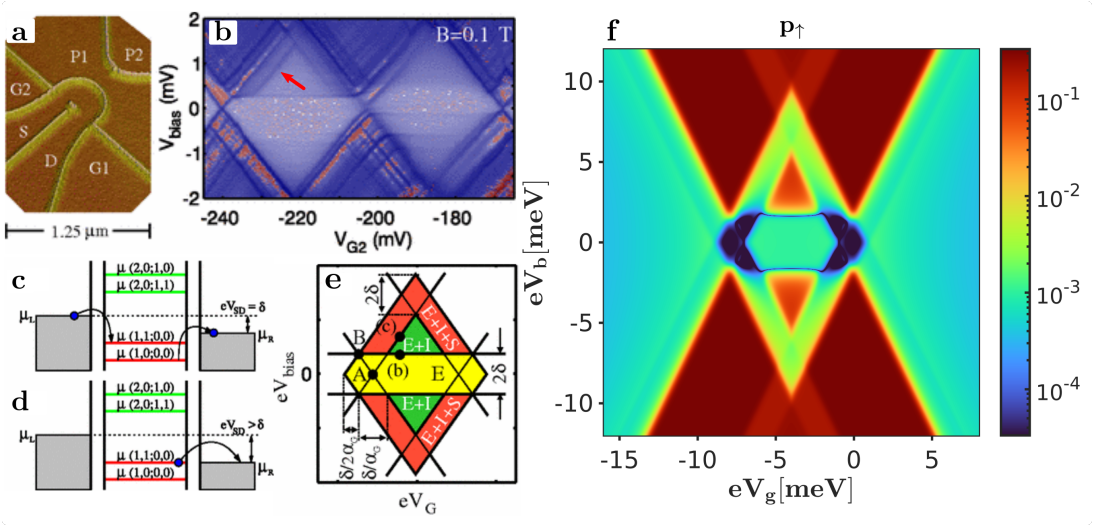

Figure 1.4: Cotunneling-assisted sequential tunneling: **a** A few-electron QD (GaAs/AlGas heterostructure) shows in the differential conductance (**b**) a resonance feature (red arrow). **c** Inelastic cotunneling event. **d** Sequential tunneling event. **e** Sketch of Coulomb diamond with various tunneling regimes including elastic cotunneling (E), inelastic cotunneling (I) and sequential tunneling (S). The excitation energy δ between the involved states determines the size of the areas where cotunneling-assisted sequential tunneling can appear (red). The electronic configuration of the two previous panels are marked with (b) and (c) respectively. **f** Population of the ↑-state plotted in logarithmic scale of a comparable setup. The triangular shaped areas inside the Coulomb diamond show increased probability of energetically unfavored state due to inelastic cotunneling (cf. with green area of **e**). Above the inelastic cotunneling threshold, the ↑-state can be the starting point of a sequential tunneling transition which leads to a lowering of $p_\uparrow$ (cf. red area of **e**). The parameters of **f** are: $U = 8\,\mathrm{meV}$, $k_\mathrm{B}T = 0.1\,\mathrm{meV}$, $E_\mathrm{z} = 2\,\mathrm{meV}$ and $\Gamma_0^\mathrm{L} = \Gamma_0^\mathrm{R} = 0.02\,\mathrm{meV}$. Pictures **a-e** are taken from [36].

the charge degeneracy point $N=0 \leftrightarrow N=1$:

$$\frac{dI}{dV_\mathrm{b}}|_{V_\mathrm{b}=0,V_\mathrm{g}=0} = \frac{\mathrm{e}^2\Gamma_0}{12\hbar k_\mathrm{B}T} \tag{1.35}$$

where $\Gamma_0 = \Gamma_0^\mathrm{L} = \Gamma_0^\mathrm{R}$. Note that we measure throughout this thesis the coupling to the leads of Γ_0 in units of energy, with the effect of adjusting it by the factor of $\hbar$ to recover its rate character. Moreover, for us, Γ_0 is always the sum of the coupling to all the (spin) channels, as in Eq. (2.16).

In Fig. 1.4 **a**, the setup of a cotunneling-assisted sequential tunneling experiment is shown, while in panel **b** its measurement of the differential conductance is displayed [36]. The red arrow indicates the increased differential conductance along a resonance inside the Coulomb diamond. The effect describes the modification of the electronic configuration due to an inelastic cotunneling event (**c**) followed by sequential tunneling process (**d**). The area above the inelastic cotunneling threshold can be divided into an area (green part of **e**) where only elastic and inelastic cotunneling events can occur and an area (red part of **e**) where additionally the transition for sequential tunneling for the excited state back to neighboring particle number ($\Gamma^{N\to N\pm1}$) is open. The result is a depopulation of the excited state via an extra current channel and thus a spike in differential conductance (cf. model calculation of **f** which is comparable to the experimental setup).

1.7 Coherences

In this section, we discuss the important role of coherences in the context of density matrices. In general, we distinguish in a density matrix its diagonal elements, the *populations* which are a measure of the probability of a certain state, and its off-diagonal elements, the *coherences*. As the name of the latter suggests, they are closely linked to the broad quantum mechanical concept of coherence. In optics, for example, it is said that two wave functions are coherent if they have a fixed phase relation during their evolution. Only the superposition of coherent waves enables constructive or destructive interference. Density matrices now generalize the description of quantum mechanical states beyond the more usual description of state vectors and wave functions. Similarly to optics, coherences of density matrices are a necessary prerequisite to observe interference effects.

To better understand the notion of coherences, it is necessary to introduce the concept of pure and mixed states. While the widespread description of quantum mechanical states with state vectors and wave functions are only able to describe pure states, one can also describe statistical mixtures of pure states with density matrices. A pure state can be written as an outer product of a state vector $|\Psi\rangle$ as $|\Psi\rangle\langle\Psi|$. Furthermore, a pure state has to fulfill

$$\mathrm{Tr}\left\{\hat{\rho}\right\} = \mathrm{Tr}\left\{\hat{\rho}^2\right\} = 1. \tag{1.36}$$

Mixed states can arise out of a lack of information about the preparation of the system so that one has to deal with a statistical ensemble of different states. An example for this is the tracing out of the leads in open systems. Theoretically, another observer

could have all knowledge about the system and thus describe it with a pure state. An alternative origin of mixed states is quantum entanglement, which inevitably brings in another statistical component to the description. However, here, it is impossible that another observer can describe an entangled state as a pure state. In other words, entanglement prevents full knowledge about the subsystem.
It is important to state that the concept of coherences is in general basis dependent, i.e., the same system can have off-diagonal elements in one basis and is completely diagonal in another basis. However, the most practicable basis to describe the system is given by the interaction of the system with its leads, which has usually a preferential basis. If the preferential basis of the interaction and the basis of the system do not coincide, then off-diagonal elements get inevitably pumped and do not decay. An example of such a setup is transport through a QD attached to non-collinear ferromagnetic leads, where in general three different quantization axes play a role. In these systems, coherence-induced phenomena can be observed, what is extensively discussed in Sec. 2.4. The distinction between pure and mixed states is however basis independent. In Fig. 1.5, the simplest

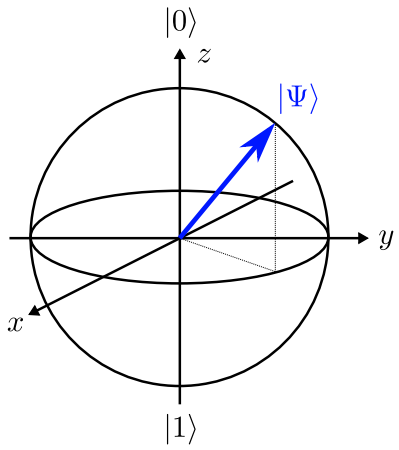

Figure 1.5: Bloch sphere representation: Any state vector $|\Psi\rangle$ of a pure state of a two-level setup is residing on the sphere and can be uniquely specified by its coordinates. The completely mixed state is in the origin of the sphere. As with any other mixed state in the interior of the sphere, it is not possible to assign a state vector.

example of a set of density matrices, the ones of a two-level system, is usually visualized in terms of a Bloch sphere. A vector pointing to the North or the South Pole represents the two pure states $|0\rangle$ and $|1\rangle$ respectively. All other vectors residing on the unit sphere are also pure states since there is a perfect superposition of $|0\rangle$ and $|1\rangle$. Mixed states

however are described by vectors which point somewhere in the interior of the unit sphere. In terms of the Pauli matrices, the qubit state can be written as

$$\hat{\rho}_{\text{qubit}} = \frac{1}{2}\left(\mathbb{1} + \vec{n}\cdot\vec{\sigma}\right), \tag{1.37}$$

with the vector $\vec{n} = (x, y, z)$ pointing somewhere in or at the unit sphere and the vector $\vec{\sigma} = (\sigma^x, \sigma^y, \sigma^z)$ containing the Pauli matrices.

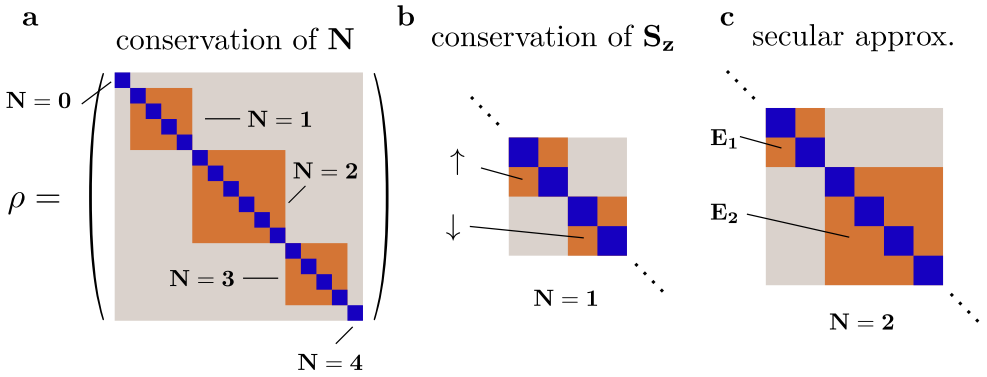

Figure 1.6: Reduction of relevant coherences in an exemplary density matrix: **a** If the total Hamilton conserves particle number N, the reduced density matrix acquires a block diagonal structure. The diagonal elements are the populations, marked in blue, and the non-vanishing off-diagonal coherences are marked in orange. **b** Conservation of the z-component of the spin leads to vanishing coherences between different spin species. **c** The secular approximation, when applicable, can reduce the number of relevant coherences similar to conservation laws.

Since the size of the reduced density matrix grows with its number of available states as n^2_{state}, certain selection rules are of great help to reduce the number of variables with ensuring that many entries of the reduced density matrix can by default be set to zero. In the following, we discuss three prominent examples of such a reduction. If one deals with a total Hamiltonian which conserves particle number, all coherences between states which differ in their particle number vanish. In Fig. 1.6 **a**, the effect of the conservation of particle number on an exemplary reduced density matrix, assumed to host up to four particles, is visualized. In panel **b**, the effect of conservation of the spin component S_z is shown, which is the case when there is no spin mixing allowed, i.e., parallel spin polarized leads. Here, only coherences within a spin species have to be considered, so that the $\uparrow$-sector and the $\downarrow$-sector are completely separated. Panel **c** is depicting an example of the appliance of the secular approximation. The secular

approximation states that all coherences between non-degenerate states are set to zero since they correspond to rapidly oscillating terms. In the shown example, where it is assumed that there is a finite energy difference in the $N = 2$-block between generic states associated with the energies E_1 and E_2, a further division into two subblocks is occurring. A path to extend the validity of secular approximation in a rigorous way into the perturbation expansion in order of $\hbar\Gamma$ is given in Sec. 1.3 of [26]. However, it is still an approximation and crucially depends on the spacing of the energy spectrum in the system.

2

Quantum dot spin and pseudospin valves

2.1 Orbital pseudospin

The concept of pseudospin is occurring in many areas of physics. In general, one uses it to describe a twofold degenerate setup in close analogy to the spin of an electron. A prominent example is the sublattice degree of freedom in graphene with sublattice "A" and "B". It also can be exploited in the realm of valleytronics, when two energy extrema in the band structure exist, the so-called valleys, which represent then an additional degree of freedom for the electrons other than charge or spin. In the first two chapters of the Applications part, we apply the concept of a pseudospin to describe the orbital degree of freedom in a DQD. We label one dot as orbital "1" and the other dot with orbital "2" (cf. Fig. 2.1). Assuming a pseudospin-1/2 system, which represents exactly one electron in the DQD, the pseudospin can then be visualized by the means of the Bloch sphere (cf. Fig. 1.5). If the vector describing the pseudospin points in the center of the unit sphere, one deals with an incoherent superposition of both orbitals, i.e., a full delocalized electron. A mere z-polarization would correspond to an increased occupation of one of the dots depending on the direction. A polarization in the x- or y-direction represents then the degree of coherence in the superposition of a delocalized state. However, we allow for any number of electrons from $N=0$ to $N=4$ since we consider a spinful interacting double-level system as our model setup. Consequently, we have to deal with a more complicated pseudospin space where no simple visualization like with the Bloch sphere exists.

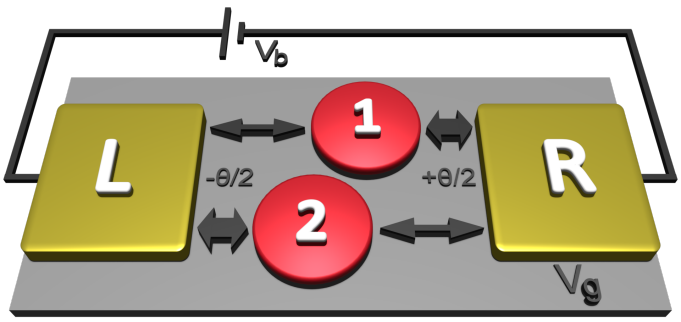

Figure 2.1: Schematic setup of a DQD in a pseudospin valve configuration: The left lead (L) is more strongly coupled to dot "2", the right lead (R) to dot "1". The opening angle $\theta \lesssim \pi$ between the pseudospin polarization of the leads ensures the mixing of the pseudospin states during the tunneling event (cf. Sec. 2.2). The bias voltage (V_b) applied to the leads and the gate voltage (V_g) control together the transport characteristics of the DQD.

The Hamiltonian of the DQD reads

$$\hat{H}_\mathrm{DQD} = \sum_{i=1,2} \left[(\mathrm{e}V_\mathrm{g} + \varepsilon_0)\, \hat{n}_i + U \hat{n}_{i\uparrow} \hat{n}_{i\downarrow} \right] + V \hat{n}_1 \hat{n}_2. \tag{2.1}$$

The operator $\hat{n}_{i\sigma} = \hat{d}^\dagger_{i\sigma} \hat{d}_{i\sigma}$ counts the number of electrons on the ith dot with spin σ, where $\hat{d}_{i\sigma}$ is the corresponding electronic annihilation operator, e the electronic charge, and $\hat{n}_i = \sum_\sigma \hat{n}_{i\sigma}$. Furthermore, the on-site energy is denoted as ε_0 and the gate voltage as V_g. The local (U) and the inter-dot (V) Coulomb interaction are in general not equal. We expect $U > V$ so that it is energetically more favorable to distribute electrons on two separated dots, rather than to confine them on the same one, due to the decay of the Coulomb interaction as a function of the distance between the involved electrons. This choice of our system leads inevitably to an anisotropy in the pseudospin space. As we see in Cha. 4 and in Cha. 5, the anisotropy is of crucial importance in the understanding of the appearing interference effects. Other than that, it represents an important tuning knob to alter the later analyzed interference effects.
This anisotropy reveals itself if $\hat{H}_\mathrm{DQD}$ is expressed in terms of its pseudospin. For this reason, we introduce the three components of the pseudospin operator,

$$\hat{T}_\alpha = \frac{1}{2} \sum_{\tau ij} \hat{d}^\dagger_{i\tau} \sigma^\alpha_{ij} \hat{d}_{j\tau}, \tag{2.2}$$

where $\alpha = x, y, z$ and σ^α are the Pauli matrices. Moreover, the total pseudospin operator

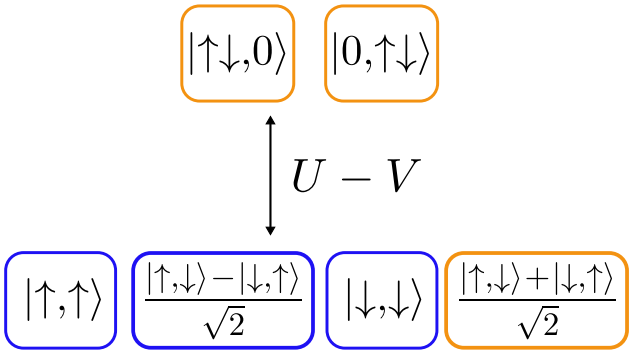

Figure 2.2: Energy splitting of the two-particle states: The spin-triplet, pseudospin-singlet states are depicted in blue ($S_z = 0, \pm 1$ and $T = 0$). The pseudospin anisotropy splits the pseudospin-triplet, spin-singlet states ($T_z = 0, \pm 1$ and $S = 0$) energetically. They are highlighted in orange.

is given by $\hat{T}^2 = \hat{T}_x^2 + \hat{T}_y^2 + \hat{T}_z^2$. The occupation number operators for the both dots are

$$\hat{n}_{1,2} = \frac{\hat{N}}{2} \pm \hat{T}_z, \tag{2.3}$$

where $\hat{N} = \hat{n}_1 + \hat{n}_2$ is the total particle number operator of the system. The reformulated DQD Hamiltonian yields then

$$\hat{H}_{\mathrm{DQD}} = \left(\varepsilon - \frac{U}{2}\right)\hat{N} + \frac{U+V}{4}\hat{N}^2 + (U-V)\,\hat{T}_z^2, \tag{2.4}$$

where $\varepsilon = \mathrm{e}V_\mathrm{g} + \varepsilon_0$. In this representation, the difference between the local and inter-site Coulomb repulsion leads to an easy-plane anisotropy of the pseudospin, due to the last term of Eq. (2.4). The pseudospin vanishes in the zero- and four-particle subspaces which are both pseudospin singlets while it reduces to a constant energy shift when evaluated on the one- and the three-particle subspaces, corresponding both to pseudospin doublets. The richest structure can be found in the two-particle subspace, where we can classify the states according to their spin and pseudospin. The spin-singlet, pseudospin-triplet states

$$\begin{aligned}
|S = 0, T_z = +1\rangle &= \hat{d}_{1\uparrow}^\dagger \hat{d}_{1\downarrow}^\dagger |\emptyset\rangle, \\
|S = 0, T_z = \ \ 0\rangle &= \frac{1}{\sqrt{2}}\left(\hat{d}_{1\uparrow}^\dagger \hat{d}_{2\downarrow}^\dagger - \hat{d}_{1\downarrow}^\dagger \hat{d}_{2\uparrow}^\dagger\right)|\emptyset\rangle, \\
|S = 0, T_z = -1\rangle &= \hat{d}_{2\uparrow}^\dagger \hat{d}_{2\downarrow}^\dagger |\emptyset\rangle,
\end{aligned} \tag{2.5}$$

are complemented by the spin-triplet, pseudospin-singlet ones

$$\begin{aligned}
|S_z = +1, T = 0\rangle &= \hat{d}^\dagger_{1\uparrow}\hat{d}^\dagger_{2\uparrow}|\emptyset\rangle, \\
|S_z = \quad 0, T = 0\rangle &= \frac{1}{\sqrt{2}}\left(\hat{d}^\dagger_{1\uparrow}\hat{d}^\dagger_{2\downarrow} + \hat{d}^\dagger_{1\downarrow}\hat{d}^\dagger_{2\uparrow}\right)|\emptyset\rangle, \\
|S_z = -1, T = 0\rangle &= \hat{d}^\dagger_{1\downarrow}\hat{d}^\dagger_{2\downarrow}|\emptyset\rangle.
\end{aligned} \tag{2.6}$$

It is only on the pseudospin-triplet component of the two-particle subspace, spanned by the vectors in Eq. (2.5), that one appreciates the anisotropy: It is energetically more favorable for the pseudospin vector to be in the x-y-plane rather than to point toward the z-direction as it costs additional energy to localize both electrons on the same dot. The energy landscape of the two-particle sector is depicted in Fig. 2.2.

2.2 Spin and pseudospin valve setup

Spin valves are structures which consist of two or more conducting spin-polarized, thus magnetic, layers with an electrical resistance changed by the relative alignment of the spin polarization of the layers. The two well-known effects of tunneling magnetoresistance (TMR) [37] and giant magnetoresistance (GMR) [38, 39] can be observed in spin valves. In general, spin valves are, under exploitation of these effects, widely used in technology applications, most notably in magnetic sensors and in storage devices like hard disk drives. The former effect is associated to a setup of two magnetic layers with an insulating tunneling barrier in between. The quantum mechanical effect describes in its essence that electrons tunnel more likely from one ferromagnet to the other ferromagnet if their magnetization is parallel (P) rather than antiparallel (AP) aligned, which manifests then into the resistance. The TMR $\coloneqq (R_{\mathrm{AP}} - R_{\mathrm{P}})/R_{\mathrm{P}}$ can be defined by the resistance R in the two different configurations. The largest observed ratio is 604% at 300 K in so-called pseudo spin valves [40].
We want to mention here the often used term in this community of "pseudo spin valves", in order to avoid confusion, even if we use the term of a pseudospin valve differently. This is the reason why we deliberately choose here to write "pseudo spin" instead of our former introduced "pseudospin", the orbital degree of freedom. In the TMR community, a pseudo spin valve describes a magnetic valve configuration which uses two different materials with different magnetic coercivities, the ability to withstand an external magnetic field, instead of an ordinary spin valve with two equal materials. A deviation from TMR is the so-called tunneling anisotropic magnetoresistance (TAMR) which is able to mimic a spin valve effect with the help of spin-orbit coupling [41]. It relies on just one ferromagnetic layer which is coupled with a tunneling barrier to a

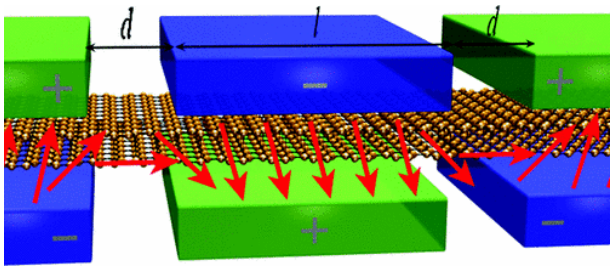

Figure 2.3: Pseudospin valve transistor: Gating bilayer graphene changes the polarization of the pseudospin. It is thus switching the polarity of the central gate with the effect that one can control the flow of electrons through the junction. Figure taken from [52].

non-ferromagnetic material and can be explained by the interplay of spin-orbit coupling at the interfaces [42]. The setup of observing GMR is similar to the TMR setup with the distinction that the layer in between the two ferromagnets is a material which can be polarized itself (for example a metal) instead of the insulating tunneling barrier in case of a TMR configuration. The switching of one ferromagnet (soft layer) to an antiparallel configuration with respect to the other fixed layer (hard layer) is usually done with the application of an external field. The pinning of the fixed layer is obtained often by an adjacent antiferromagnet, which raises the coercivity of that ferromagnet.

In our research, we are interested in QD spin valves where a QD is coupled to ferromagnetic leads. Experimentally, they are realized in different ways, for example, using QDs defined in CNTs [43–45] or nanowires [46], single molecules [47], nanoparticles [48, 49] or semiconductor QDs [50]. A DQD spin valve setup with relative high QD spin polarization of up to 80% was reported in [51]. Throughout the thesis, we also use the concept of a pseudospin valve. We define it as a replica of a spin valve with the distinction that instead of the spin degree of freedom, we are using the orbital degree of freedom to obstruct electron transport. In Fig. 2.1, a possible setup of a pseudospin valve is shown: a DQD is attached to leads which have pseudospin polarization, i.e., they couple differently to the two orbitals, dot "1" and dot "2". If supposedly the left lead is more coupled to dot "2", and the right lead to dot "1", we obtain a suppression of current similarly to a spin valve. A microscopic model which provides this desired parametrization is given in Sec. 4.1.

The concept of a pseudospin valve is used in a plethora of materials and setups. For example in (bilayer) graphene, it also is coined as a valley valve, investigated theoretically

in [53] and experimentally in [54]. In Fig. 2.3, a possible *pseudospintronics* device is sketched where the pseudospin in bilayer graphene is used to realize an all-electronic, pseudospin-based version of a spin valve [52]. Another implementation of a pseudospin valve can be found in topological insulators, where one exploits the emergent orbital pseudospin in the surface states to model a spin valve analogue [55].

Valve parametrization of a DQD: For the explicit modeling of valve configurations, we make use of the tunneling rate matrices since they incorporate the specific geometry of the tunnel barriers and their spin properties. The following derivation mainly follows our publication [17] and it focuses on DQDs since there, one is able to construct a spin and a pseudospin valve. The tunneling rate matrices, recapturing their definition of Eq. (1.17) as

$$\Gamma^{l}_{i\sigma,j\sigma'}(E) = \frac{2\pi}{\hbar} \sum_{\boldsymbol{k}\sigma_l} t^{*}_{l\boldsymbol{k}\sigma_l,i\sigma}\, t_{l\boldsymbol{k}\sigma_l,j\sigma'}\, \delta(E - \varepsilon_{l\boldsymbol{k}\sigma_l}), \tag{2.7}$$

consist of the tunneling amplitudes and the density of states. Firstly, in order to describe spin polarization, we utilize the Stoner model for itinerant ferromagnetism. At the Fermi-energy, the density of states $g_{l\sigma_l}(E_\mathrm{F})$ for the different spin species differ due to a spin-dependent dispersion relation $\varepsilon_{l\boldsymbol{k}\uparrow_l} \neq \varepsilon_{l\boldsymbol{k}\downarrow_l}$. The spin polarization for the lead l yields

$$P^{l}_{S} = \frac{g_{l\uparrow_l}(E_\mathrm{F}) - g_{l\downarrow_l}(E_\mathrm{F})}{g_{l\uparrow_l}(E_\mathrm{F}) + g_{l\downarrow_l}(E_\mathrm{F})}. \tag{2.8}$$

The leads are kept at the same temperature T and their electrochemical potentials μ_l are modulated by the external bias $\mu_{\mathrm{L,R}} = \pm \mathrm{e}V_\mathrm{b}/2$. For systems with negligible intrinsic spin-orbit interaction (SOI) and very localized dot-wave functions, the tunneling amplitudes $t_{l\boldsymbol{k}\sigma_l,i\sigma}$ can be factorized into a spin and an orbital overlap:

$$t_{l\boldsymbol{k}\sigma_l,i\sigma} \approx \varepsilon_0 \left\langle l\boldsymbol{k}\sigma_l | i\sigma \right\rangle = \varepsilon_0 \left\langle l\boldsymbol{k} | i \right\rangle \left\langle \sigma_l | \sigma \right\rangle . \tag{2.9}$$

To proceed further in the analysis of the tunneling rate matrices, we also assume the density of states for both spin species to be rather smooth in the vicinity of the Fermi-level. We thus introduce the approximation

$$\delta(E - \varepsilon_{l\boldsymbol{k}\sigma_l}) \approx \frac{g_{l\sigma_l}(E_\mathrm{F})}{g_{l\uparrow_l}(E_\mathrm{F}) + g_{l\downarrow_l}(E_\mathrm{F})} \sum_{\tau_l} \delta(E - \varepsilon_{l\boldsymbol{k}\tau_l}). \tag{2.10}$$

The sum over the lead spin index τ_l compensates, in the limit $E \to E_\mathrm{F}$, the denominator and Eq. (2.10), integrated on the momenta $\boldsymbol{k}$, becomes exact.

By combining Eqs. (2.9)-(2.10), we obtain a tunneling rate matrix of the form

$$\Gamma^l_{i\sigma,j\sigma'}(E) = \frac{2\pi}{\hbar}\varepsilon_0^2 \sum_{\boldsymbol{k}} \langle i|l\boldsymbol{k}\rangle \langle l\boldsymbol{k}|j\rangle \sum_{\tau_l} \delta(E - \varepsilon_{l\boldsymbol{k}\tau_l}) \sum_{\sigma_l} \frac{g_{l\sigma_l}(E_\mathrm{F})}{g_{l\uparrow_l}(E_\mathrm{F}) + g_{l\downarrow_l}(E_\mathrm{F})} \langle \sigma|\sigma_l\rangle \langle \sigma_l|\sigma'\rangle , \tag{2.11}$$

which can be factorized into a bare tunneling rate, a pseudospin (orbital) and a spin part,

$$\Gamma^l = \Gamma^l_0 A^l \otimes B^l, \tag{2.12}$$

where we omit, for simplicity, the energy dependence. The bare tunneling rate Γ^l_0, and the generic elements of the pseudospin A^l_{ij} and of the spin matrix $B^l_{\sigma\sigma'}$, are defined in terms of the wave function overlaps and the single-particle spectra:

$$\Gamma^l_0 = \frac{2\pi}{\hbar}\varepsilon_0^2 \sum_{i\boldsymbol{k}\sigma_l} |\langle i|l\boldsymbol{k}\rangle|^2 \delta(E - \varepsilon_{l\boldsymbol{k}\sigma_l}), \tag{2.13}$$

$$A^l_{ij} = \frac{\sum_{\boldsymbol{k}\sigma_l} \langle i|l\boldsymbol{k}\rangle \langle l\boldsymbol{k}|j\rangle \delta(E - \varepsilon_{l\boldsymbol{k}\sigma_l})}{\sum_{a\boldsymbol{q}\tau_l} |\langle a|l\boldsymbol{q}\rangle|^2 \delta(E - \varepsilon_{l\boldsymbol{q}\tau_l})}, \tag{2.14}$$

$$B^l_{\sigma\sigma'} = \sum_{\sigma_l} \frac{g_{l\sigma_l}(E_\mathrm{F})}{g_{l\uparrow_l}(E_\mathrm{F}) + g_{l\downarrow_l}(E_\mathrm{F})} \langle \sigma|\sigma_l\rangle \langle \sigma_l|\sigma'\rangle . \tag{2.15}$$

Since both A^l and B^l are Hermitian 2×2 matrices of trace 1, the tunneling rate matrix can be expanded in terms of Pauli matrices as

$$\Gamma^l = \Gamma^l_0 \left(\frac{\mathbb{1}_2}{2} + \frac{P^l_T}{2}\vec{n}^l_T \cdot \vec{\sigma}\right) \otimes \left(\frac{\mathbb{1}_2}{2} + \frac{P^l_S}{2}\vec{n}^l_S \cdot \vec{\sigma}\right), \tag{2.16}$$

where P^l_S is the spin polarization defined in Eq. (2.8), $\vec{n}^l_S$ is the direction of the spin quantization axis for the lead l, and $\vec{\sigma}$ is the vector of the Pauli matrices. Analogously, we define P^l_T and $\vec{n}^l_T$ as the strength and the direction of the pseudospin polarization of the l-lead.

Throughout the thesis, we describe valve configurations with the help of Eq. (2.16). Whenever two leads are now polarized, either in spin or pseudospin, almost antiparallel so that their opening angle is $\theta \approx \pi$, we speak of a valve configuration. A possible pseudospin valve can be parameterized in the following way,

$$\vec{n}^{\mathrm{L,R}}_T = \left(\cos\frac{\theta}{2}, 0, \mp\sin\frac{\theta}{2}\right), \tag{2.17}$$

with the opening angle θ. This parameterization corresponds to the setup shown in

Fig. 2.1 since $\theta \approx \pi$ results in two vectors which point mainly in the $-z$- and the $+z$-direction.
The pseudospin polarization of the lead allows for a simple physical interpretation, in connection to the pseudospin formulation of the system Hamiltonian. Full pseudospin polarization in the z-direction indicates an exclusive coupling to one or the other dot. Components in the x-y-plane describe instead coherent tunneling of one electron to both orbitals.
It is thus understandable how such off-diagonal components of the tunneling rate matrix are necessary for the observation of interference effects. In particular, in complete analogy to the spin valve [56], tunneling is forbidden from a DQD with maximum expectation value of the pseudospin in a given direction (i.e., $1/2$ for the one- and three-particle sector, 1 for the two-particle sector) and a lead fully polarized in the opposite direction. Exemplarily, a state with double occupation of one dot cannot release any electron to a lead which only couples to the other dot. The pseudospin formulation allows us to capture on an equal footing also the other polarization direction, which, on the contrary, is not so easily described within the position representation. A concrete example of pseudospin polarization is given in [6]. The angular momentum states of the CNT provide a two-level system with symmetry-protected degeneracy. The pseudospin polarization of the leads is there related to the extent and position of the contact region between the lead and the CNT. The localized contact provides an almost full polarization. The control of the phase and strength of the tunneling amplitudes can be achieved with the help of a longitudinal magnetic field acting on the CNT, as recently proved in [57].

2.3 Exchange fields

An important consequence of having Coulomb interaction in nanostructures is the appearance of so-called exchange fields. These exchange fields can act similarly as magnetic fields on the spin of a QD system. Thus, they are sometimes called effective magnetic fields. The exchange fields originate from virtual fluctuations between the system and the leads and are generally governed by Coulomb interaction and the indistinguishability of particles. In fact, exchange is a manifestation of the Coulomb interaction *and* the Pauli exclusion principle, as it is pointed out in [58]. A prominent example where exchange fields play a major role in determining the transport and the dynamics is a QD attached to non-collinear polarized ferromagnetic leads. In such systems, Kondo peaks can split up due to an exchange field in the absence of an applied external magnetic field [59] or the spin of a QD can precess, which is then detectable in

the conductance [60]. In the latter publication, the concept of exchange fields in such setups was mentioned the first time and in a follow-up publication, it is elaborated in more detail [56]. The combination of spin-dependent tunneling and Coulomb interaction gives rise to a spin torque, which is then captured in a simple way by the exchange fields.
The inspection of any second-order diagram reveals the origin of the exchange fields to its first order. Every tunneling event incorporates the tunneling rate matrix accounting for possible spin polarization of the leads. Moreover, every diagram accompanies the energy-dependent Y-function [cf. Eq. (A.4)] containing the Coulomb interaction U. The real part of this function turns out to be the Fermi-function and can be associated to real tunneling events. The imaginary part of the Y-function, corresponding to the real part of a digamma-function, represents then also the effect of possible virtual transitions since at an individual tunneling process the energy may not be conserved temporarily. However, quite often this imaginary part of the digamma-function cancels out upon summation of Hermitian conjugate diagrams, as it is the case, for example, for non-ferromagnetic leads. In the case of spin-dependent tunneling in a non-collinear setup, this cancelation is not given. The result is then a spin torque which is best described by an exchange field containing the real part of the digamma-function.

2.4 Equation of motion for QD spin valve

An insightful minimal model to study exchange field-induced dynamics is the one of a QD attached to ferromagnetic leads [56]. This spin valve setup allows for the investigation of the interplay of magnetization with the spin polarization of the leads and the interaction at the level of the central system, which goes beyond the standard influence of exchange interaction in the formation of ferromagnetism. In Fig. 2.4, a schematic setup is displayed. In order to describe the setup in the sequential tunneling limit, one needs 6 parameters, namely the three populations (p_0 for empty, p_1 for single-occupied and p_2 for double-occupied) and the three components of the spin ($\vec{S}$) of the QD. The equations of motion can be written as

$$\dot{p}_0 = -2\gamma_{10}^{+}\, p_0 + \gamma_{10}^{-}\, p_1 + 2\vec{\gamma}_{10}^{-} \cdot \vec{S}, \tag{2.18}$$

$$\dot{p}_1 = 2\gamma_{10}^{+}\, p_0 - \left(\gamma_{10}^{-} + \gamma_{21}^{+}\right) p_1 + 2\gamma_{21}^{-}\, p_2 - 2\left(\vec{\gamma}_{10}^{-} - \vec{\gamma}_{21}^{+}\right) \cdot \vec{S}, \tag{2.19}$$

$$\dot{p}_2 = \gamma_{21}^{+}\, p_1 - 2\gamma_{21}^{-}\, p_2 - 2\vec{\gamma}_{21}^{+} \cdot \vec{S}, \tag{2.20}$$

$$\dot{\vec{S}} = \vec{\gamma}_{10}^{+}\, p_0 + \left(-\tfrac{1}{2}\vec{\gamma}_{10}^{-} + \tfrac{1}{2}\vec{\gamma}_{21}^{+}\right) p_1 - \vec{\gamma}_{21}^{-}\, p_2 - \left(\gamma_{10}^{-} + \gamma_{21}^{+}\right) \vec{S} + \vec{B} \times \vec{S}, \tag{2.21}$$

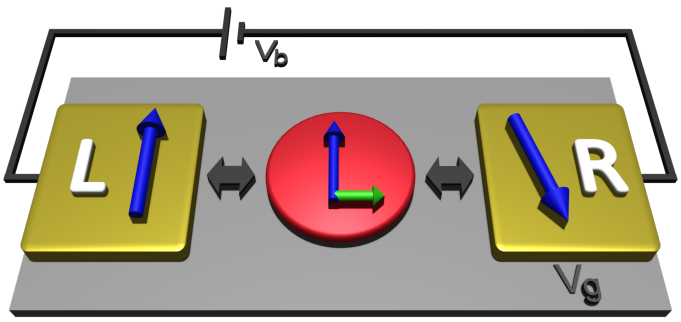

Figure 2.4: QD spin valve: The polarization of the two ferromagnetic leads (blue arrows) have a certain opening angle, which determines the spin accumulation on the dot (blue arrow) via a precession stipulated by an exchange field $\vec{B}$ (green arrow).

with $\gamma^{\pm}_{nm} = \sum_l \gamma^{\pm}_{l,nm}$ and $\gamma^{\pm}_{l,nm} = \Gamma^l_0/2 f^{\pm}_l(\varepsilon - E_{nm})$. For Γ^l_0, we use as the definition Eq. (2.16) without the orbital part, i.e., it is the sum of the coupling of the two spin channels. The subscript of the energy E_{nm} labels the energy difference between the state n and m which can be the zero-particle state (0), the one-particle state (1), and the two-particle state (2). The vectorial form is given by $\vec{\gamma}^{\pm}_{nm} = \sum_l \vec{n}^l_S P^l_S \gamma^{\pm}_{l,nm}$. The two spin polarization vectors of the leads $\vec{n}^l_S$ are defined analogously to Eq. (2.17) and they enclose the opening angle ϕ. Out of an analysis of these equations, we can deduce two things. Firstly, we encounter in the last term of Eq. (2.21) a part which contains an exchange field $\vec{B}$:

$$\vec{B} = \sum_l P^l_S \Gamma^l_0 \left[p_l(E_{10}) - p_l(E_{21})\right] \vec{n}^l_S, \tag{2.22}$$

with

$$p_l(x) = \frac{1}{2\pi} \mathrm{Re}\Psi^{(0)}\left(\frac{1}{2} + i\frac{x-\mu_l}{2\pi k_\mathrm{B} T}\right). \tag{2.23}$$

The effective magnetic field is characterized by the difference of the principal parts p_l of the energy function Y and thus by the real part of the digamma-functions [cf. Eq. (A.4)]. One sees now, that this effective magnetic field vanishes if the Coulomb interaction U becomes zero. It causes precession as well as dephasing of the spin $\vec{S}$ but it also generates a spin splitting of order Γ^l_0 [56]. For a complete analysis of this aspect, we refer the reader to our second publication (Cha. 5).
In Fig. 2.5 **a**, the components of this exchange field induced by the left and the right lead for an exemplary parameter set are depicted in blue and red, respectively. Clearly, the

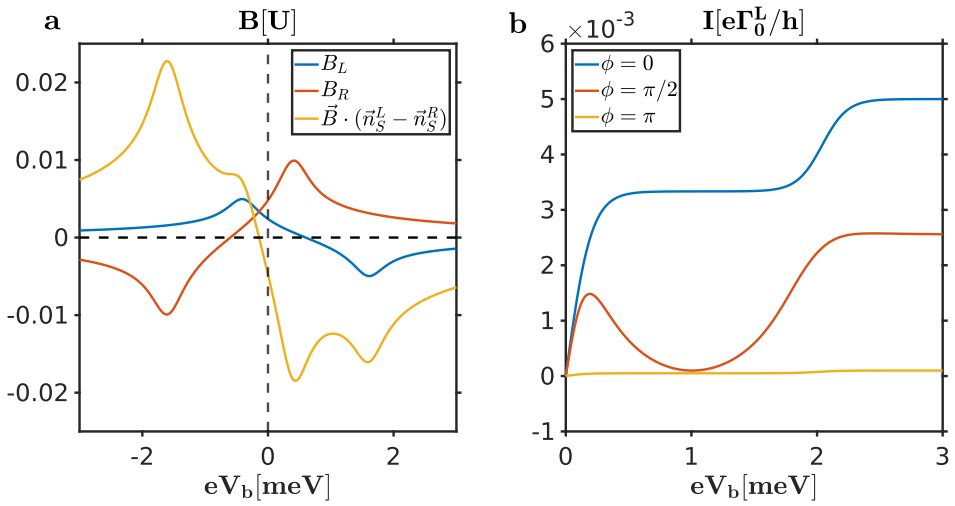

Figure 2.5: Exchange field-induced phenomena in spin valves: a The exchange field components for the left lead B_L and for the right lead B_R are shown. The yellow line represents the condition where a spin resonance is predicted (cf. Sec. 2.2). Parameters: $U = 1\,\mathrm{meV}$, $k_\mathrm{B}T = 0.05\,\mathrm{meV}$, $\phi = 0.99\,\pi$, $P_S^\mathrm{L} = P_S^\mathrm{R} = 0.99$, $\mathrm{e}V_\mathrm{g} = 0.3\,\mathrm{meV}$, and $2\Gamma_0^\mathrm{L} = \Gamma_0^\mathrm{R} = 0.01\,\mathrm{meV}$. **b** Current for different opening angles of a spin valve. Parameters equal to **a** except of $\Gamma_0^\mathrm{L} = \Gamma_0^\mathrm{R} = 0.01\,\mathrm{meV}$ and $\mathrm{e}V_\mathrm{g} = 0.5\,\mathrm{meV}$.

peaks of the principal parts due to the respective energy arguments can be observed. Generally, Eq. (2.21) describes the time evolution of the spin, which is non-trivial for spin polarized leads. The equation can be divided in three different terms: a pumping, a decoherence and a precession term:

$$\frac{d\vec{S}}{dt} = \left(\frac{\vec{S}}{dt}\right)_\text{pumping} + \left(\frac{\vec{S}}{dt}\right)_\text{decoherence} + \left(\frac{\vec{S}}{dt}\right)_\text{precession} \tag{2.24}$$

The pumping term, also referred as source or accumulation term, accounts for tunneling in and out of the QD. It contains all contributions involving the populations $[\widehat{=}\vec{\gamma}_{10}^{+}\,p_0 + \left(-\frac{1}{2}\vec{\gamma}_{10}^{-} + \frac{1}{2}\vec{\gamma}_{21}^{+}\right)p_1 - \vec{\gamma}_{21}^{-}\,p_2]$. The decoherence term is the counterpart to pumping since it reduces the spin of the dot. The decoherence term $\left(-\gamma_{10}^{-} - \gamma_{21}^{+}\right)\vec{S}$ can be identified to be the only one proportional to $\vec{S}$. It is also often coined the relaxation term, where the intrinsic spin relaxation rate τ_c can be deduced from the absolute value of the prefactor as $1/\tau_\mathrm{c} = \gamma_{10}^{-} + \gamma_{21}^{+}$. In our context, we prefer the term decoherence over relaxation since the latter is more applicable when states relax to the ground state rather than the observed reduction of the spin vector towards the center of the Bloch sphere into

a completely incoherent state. The precession term, as already outlined, is a vector product of the exchange field and the spin ($\hat{=}\vec{B}\times\vec{S}$).
For zero bias, equal spin polarization ($P_S\colon = P_S^{\mathrm{L}} = P_S^{\mathrm{R}}$) and symmetric coupling ($\Gamma_0^{\mathrm{L}} = \Gamma_0^{\mathrm{R}}$), there is no spin pumping, thus in equilibrium it holds $\vec{S} = 0$. For small non-zero bias and in the linear response regime, one obtains that the linear conductance, $G^{\mathrm{lin}} = (dI/dV)|_{V_{\mathrm{b}}=0}$, depends crucially on the opening angle ϕ:

$$\frac{G^{\mathrm{lin}}(\phi)}{G^{\mathrm{lin}}(0)} = 1 - P_S^2 \frac{\sin^2(\phi/2)}{1+(B_0\tau_c)^2\cos^2(\phi/2)}, \tag{2.25}$$

where we deduce B_0 from the exchange field $\vec{B} = B_0\cos(\phi/2)\vec{e}_x$. The gate voltage is assumed to be zero in this formula. The interplay between the lifetime τ_{c} of the spin of the dot, which decreases if the gate is favoring an empty or double-occupied QD state, and the opening angle are the determining parameters. The minimum of the conductance is reached for $\phi = \pi$, i.e., an antiparallel alignment of the polarization of the leads, regardless of the polarization strength and the gate voltage. This minimum can be attributed to the spin valve effect, where the dot accumulates with the spin species which shares the spin polarization of the source. The accumulated electron gets trapped since tunneling out of the dot is suppressed by the low density of states for the given spin direction. For longer lifetimes which correspond to gate voltages favoring a single-occupied QD state, the exchange field is able to rotate the QD spin more so that a stronger lifting of the spin valve can occur except in the vicinity of antiparallel alignment.
Another interesting result of this model is the current I_0 in the non-linear response regime ($\mathrm{e}V_{\mathrm{b}} < k_{\mathrm{B}}T$):

$$I_0 = \frac{2\Gamma_0^{\mathrm{L}}\Gamma_0^{\mathrm{R}}}{\Gamma_0^{\mathrm{L}}+\Gamma_0^{\mathrm{R}}}\left\{1-[P_S\sin(\phi/2)]^2\right\}. \tag{2.26}$$

In Fig. 2.5 **b**, the current at the charge degeneracy point $N=0 \leftrightarrow N=1$ for different opening angles is displayed. The red curve for perpendicular alignment of the leads strikingly shows a decrease of the current even for an increase of applied bias, what can only be explained by interference. Areas of negative differential conductance can be caused by so-called blocking or dark states which decouple from the drain, as it is the case in [6]. The exact local minimum occurs whenever the source component of the exchange field vanishes (here B_{L}) so that no precession is possible and the full spin valve effect prevails.

2.5 Spin resonances

The coherent manipulation of spins is at the heart of quantum information technology. In this regard, *electron spin resonance* (ESR) is a compelling tool able to accomplish for this task in a controlled way [61–63]. The basic working principle of ESR requires a constant magnetic field, splitting the spin energy levels, together with a magnetic field oscillating at the resonant frequency. In a system comprising several spin centers, however, it is very challenging to produce localized magnetic fields which address one spin at a time. To overcome this obstacle, it was shown that, by mixing charge and spin degrees of freedom, it is possible to manipulate the electronic spins also by electrical gates [64].

With the same advantage, there exists yet another approach to manipulate the spin in a nanojunction. This effect, appearing in QD spin valves, is called *spin resonances without spin splitting*. The latter are a main point of interest of this thesis. They were first studied by M. Hell et al. in [65] and are still investigated in several groups [66–69]. Interestingly, an onset of these resonances was already observed in Fig. 2 of [70] some years earlier. From now on, we refer to them only by spin resonances if not stated otherwise. They can be distinguished from the more familiar ESR signals by the lack of an external magnetic field.

In the parameter regime of spin resonances, the lifting of the spin valve is resonantly enhanced. It is observed within the Coulomb diamond and for an almost antiparallel alignment of the leads. A complete antiparallel alignment destroys the effect since the resulting exchange field points in the direction of the leads' polarization and thus cannot precess the spin in any other direction, which is crucial for this phenomenon. Spin resonances can be detected by dI/dV-spectroscopy, or possibly in pulsed pump-prope schemes. In Fig. 2.6 **a**, the numerical results of the differential conductance up to the cotunneling regime are shown. Clearly, a resonance feature is cutting through the otherwise flat region of the Coulomb diamond.

In [65], they gave a vectorial argument for the lifting of the spin valve. The resonance occurs when the exchange field is perpendicular to the source polarization of the lead to maximize the lifting of the spin valve for a fixed opening angle $\phi \approx \pi$. Their argument is that a component perpendicular to the source polarization rotates the spin inside the QD from $\vec{n}_S^{\mathrm{L}}$ to $\vec{n}_S^{\mathrm{R}}$. In our second publication, we show that this argument has to be refined since in reality maximal dephasing rather than maximal precession matters [71]. However, the vectorial condition stays unchanged, so we use it nevertheless to predict the resonances and refer the reader for more details about the exact mechanism to our results part (cf. Sec. 5.4). Since the exchange field strength and more importantly its

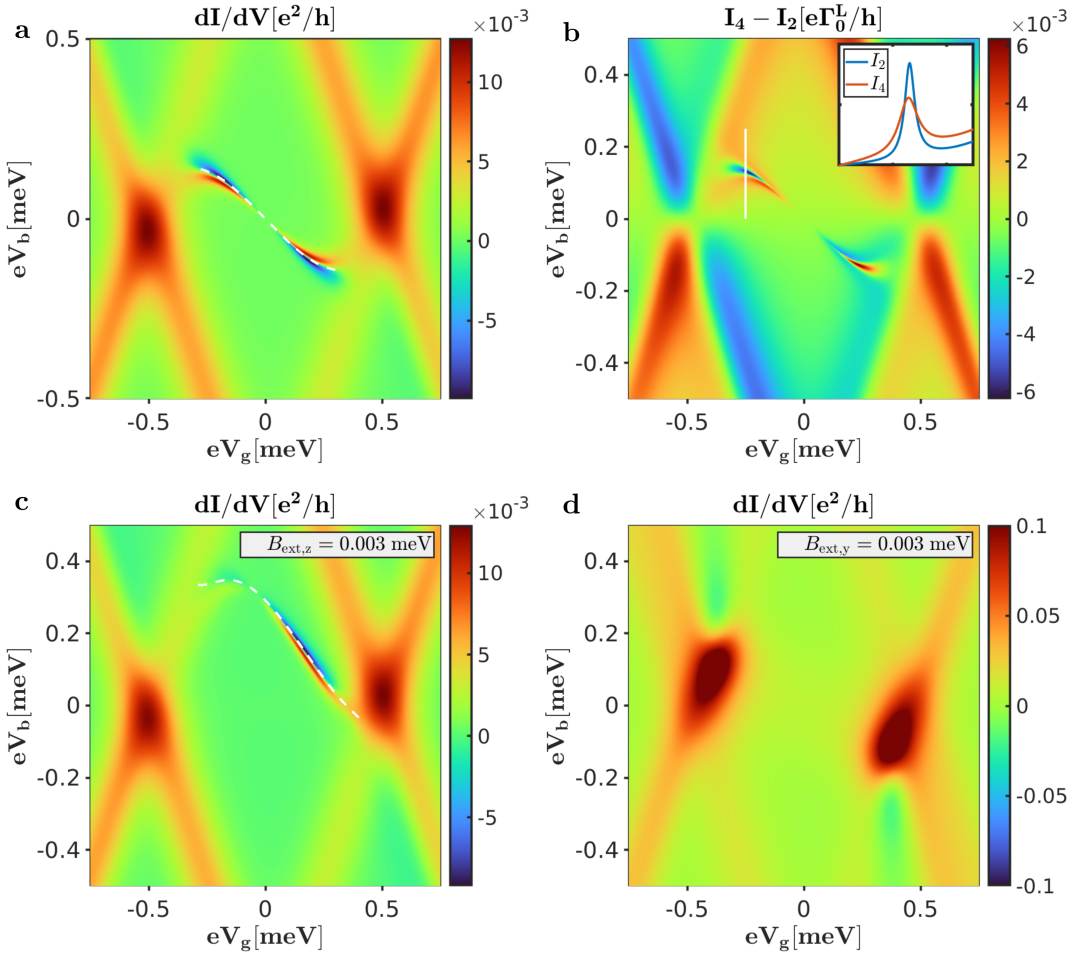

Figure 2.6: QD spin resonance: a Differential conductance obtained by fourth-order calculations. The s-shape of the spin resonance line is centered around the particle-hole symmetric point. With the white dashed line, the predicted resonance position is marked. **b** Difference of fourth-order and second-order current highlights the increased current through cotunneling events inside the Coulomb blockade region. Furthermore, suppression of the resonance line through increased spin decay can be extracted. An external field is added in the z-direction (**c**) and in the y-direction (**d**). Parameters of all plots: $U = 1\,\mathrm{meV}$, $k_\mathrm{B}T = 0.05\,\mathrm{meV}$, $\phi = 0.99\,\pi$, $P_S = 0.99$ and $2\Gamma_0^\mathrm{L} = \Gamma_0^\mathrm{R} = 0.01$.

direction can be tuned by electrical means, one has great control of the resonances and is not dependent on external induced energy splittings. In contrast to the resonance condition formulated in [65], we choose a slightly adopted condition, where the drain and the source equally participate since it matches the numerical resonances on a broader parameter range:

$$\vec{B} \cdot \left(\vec{n}_S^{\mathrm{L}} - \vec{n}_S^{\mathrm{R}}\right) = 0. \tag{2.27}$$

The yellow curve of Fig. 2.5 **a** shows the exemplary graphical determination of resonant bias voltage as the intersection of $\vec{B} \cdot (\vec{n}_S^{\mathrm{L}} - \vec{n}_S^{\mathrm{R}})$ with 0. Panel **b** of Fig. 2.6 displays the difference between the fourth- and second-order current. In its subpanel, a bias cut shows a lowering and a broadening of the resonance with including higher order terms. In Fig. 2.6 **c**, the effect of an external magnetic field in the z-direction is shown. The resonance condition changes according to

$$\left(\vec{B} + \vec{B}_{\mathrm{ext}}\right) \cdot \left(\vec{n}_S^{\mathrm{L}} - \vec{n}_S^{\mathrm{R}}\right) = 0. \tag{2.28}$$

The direction as well as the strength of the external magnetic field is of crucial importance. If the strength of the Zeeman splitting is higher than the resolution of the tunneling which is of order Γ_0, the condition of having a degenerate or quasi degenerate energy spectrum is then not anymore fulfilled, and the virtual fluctuations cannot lift the valve. The direction of the external magnetic field with respect to the valve polarization direction determines if a valve configuration still persists. The valve polarization of the left lead is mainly in $-z$-direction and the right lead is in $+z$-direction, both having a small positive component in the $+x$-direction. The external magnetic field can be compensated by the exchange field, which has due to the polarization of the leads a big component in the z-direction, so that the combined field can indeed point perpendicular to the source polarization. If the same external magnetic field is applied now in the y-direction (perpendicular to the valve polarization plane of x-z), the precession or the dephasing of the spin is facilitated everywhere in the parameter space, thus no distinct resonance and a less pronounced current suppression can be observed in the stability diagram (cf. Fig. 2.6 **d**). Almost the same stability diagram is the result if the external magnetic field points along the x-direction, with the effect that the lifting of the resonance is possible everywhere in the gate and bias landscape (not shown here).

2.6 Concurrence as measure of entanglement

The entanglement of a quantum mechanical system, as sketched in the introduction, is a fundamental quantity which attracted recently a lot of interest since it is one of

the necessary prerequisites for quantum computation. Other than that, it is the central property to show the violation of the Bell's inequality, which proves the non-local character of quantum mechanics and rules out the theory of *local* hidden variables. In our research, we are as well interested in the entanglement in DQDs as a manifestation of synthetic SOI. Generally, entanglement can be measured with the help of the concurrence, which is closely related to the *entanglement of formation*. Both measures are able to quantify the degree of quantum entanglement of a system [72]. Explicitly, for a bipartite system, the entanglement of formation can be calculated as

$$\mathcal{E}(C) = h\left(\frac{1+\sqrt{1-C^2}}{2}\right), \tag{2.29}$$

with $h(x) = -x\log_2 x - (1-x)\log_2(1-x)$ as the Shannon entropy function [73] and C as the concurrence. The entanglement of formation $\mathcal{E}$ is a monotonically increasing function of the concurrence and ranges from 0 to 1. The concurrence C also ranges from 0 to 1 so that it itself can be considered as a standalone measurement of entanglement. To obtain the value for the concurrence, two different, but compatible formulas can be used. For a pure state $|\Psi\rangle$, C can be expressed, with the help of the spin-flip operation in both degrees and captured in $|\tilde{\Psi}\rangle = \sigma^y \otimes \sigma^y |\Psi^*\rangle$, as

$$C(\Psi) = |\langle\Psi|\tilde{\Psi}\rangle|. \tag{2.30}$$

The * in the vector $|\Psi^*\rangle$ denotes complex conjugation. For the one-particle sector of our DQD, we can adopt this combined spin-flip operation to our problem with using the spin and pseudospin operators: $|\tilde{\Psi}\rangle = 4\hat{S}_y\hat{T}_y|\Psi^*\rangle$. It is important to notice, that we opt in our research to measure the concurrence between the spin and the pseudospin rather than the more standard approach to capture the concurrence between two spins. An example of a maximal entangled state in our definition is then $(|\uparrow,0\rangle - |0,\downarrow\rangle)/\sqrt{2}$, where we differentiate in the state vector with a comma between the occupation of the two different dots. This state is associated with concurrence 1 because a simultaneous pseudospin and spin flip, up to a sign, does not change the state. In contrast, $(|\uparrow,0\rangle - |0,\uparrow\rangle)/\sqrt{2}$ yields concurrence of 0 since the simultaneous flip of spin and pseudospin results in a state orthogonal to the initial one. Another way of seeing it is that the spin and pseudospin degree can be factorized in the latter example but not in the former one.
The second approach to calculate the concurrence is better suited for our purpose since it is tailored for a *generic* state of our bipartite spin-pseudospin DQD and not only for pure states. However, we are with the following formula again restricted to the one-particle subblock of the reduced density matrix, namely $\hat{\rho}_1$, since we want to retain

the pseudospin-1/2 structure. Following [72], we calculate the concurrence C as

$$C\left(\hat{\rho}_1\right) = \max(0, \lambda_1 - \lambda_2 - \lambda_3 - \lambda_4), \tag{2.31}$$

where the λ_i's are the square roots of the eigenvalues, in decreasing order, of the non-Hermitian matrix $\hat{\rho}_1\tilde{\rho}_1$. Analogously to $|\tilde{\Psi}\rangle$, we define the pseudospin- and spin-flipped state as $\tilde{\rho}_1 = (\sigma^y \otimes \sigma^y)\hat{\rho}_1^*(\sigma^y \otimes \sigma^y)$.

3

Quantum dot-based Josephson junctions

3.1 Introduction to superconductivity

In 1911, Heike Kamerlingh Onnes discovered superconductivity while measuring the resistivity of metals close to zero Kelvin. He was the first observing the abrupt vanishing of the resistivity of mercury at its critical temperature T_c, one of the main characteristics of superconductors (cf. Fig. 3.1). In 1933, Robert Ochsenfeld and Walther Meissner were then first to describe another important property of superconductors, the expulsion of magnetic fields, which is now known as the Meissner-Ochsenfeld effect [75]. The London equations, named after their developers Fritz and Heinz London, put another piece into the puzzle of understanding superconductivity with relating the superconducting current with the magnetic field from which one can deduce the penetration depth of the magnetic field into the superconductors [76]. The next major step in explaining superconductivity was the phenomenological Ginzburg–Landau theory of superconductivity from 1950, where macroscopic properties were deduced from a Schrödinger-like wave equation describing a phase transition from a normal to a superconducting state [77].
However, it took up until 1957 to come up with the first microscopic theory for superconductivity, namely the Bardeen–Cooper–Schrieffer (BCS) theory [78]. They established that superconductivity can be explained as a collective phenomenon in which a macroscopic fraction of electrons builds time-reversal related Cooper pairs. The pairing of normally repelling electrons is considered to stem from an attractive potential due to lattice phonons. This mechanism is in accordance with the isotope effect, discovered by Maxwell [79] and Reynolds [80]. The BCS-theory with its mean-field ansatz can predict many properties correctly: the excitation spectrum, the critical temperature as well as

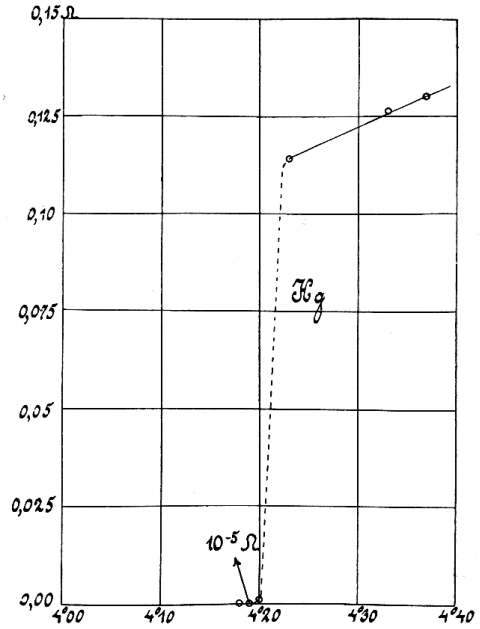

Figure 3.1: First measurement of a superconducting phase transition [74]: The resistivity of a capillary of mercury as a function of temperature.

the temperature dependence of the superconducting gap and the supercurrent. Up to now, it is still the theory of choice to explain the latest experimental findings. However, there are also many examples of unconventional superconductors where the BCS theory fails, like in the case of cuprates or heavy fermion superconductors. It is assumed that in these systems the electron interaction plays a major role so that the mean-field approach breaks down. Also, the exact pairing process in many high-temperature superconductors is not yet known [81]. The full understanding of high-temperature superconductors is thus considered to be one of the major unsolved problems of theoretical physics. However, this lack of understanding does not hinder the wide technological adaption of superconductors, quite often the less understood high-temperatures ones. The use of superconductors is manifold, spanning from magnetic resonance imaging (MRI) in medicine to quantum computers, where one of the best performing architecture is based on superconducting circuits [82, 83]. Another interesting application of superconductors is in the area of electricity generation and transmission. In Denmark, a MW-scale wind turbine for example is producing energy with a superconducting rotor, which has, among others, the advantage of a huge weight reduction [84]. In Essen, and soon also in Munich, superconducting power cables are integrated in the local electricity grid [85, 86] in order to reduce the power loss of transmission.

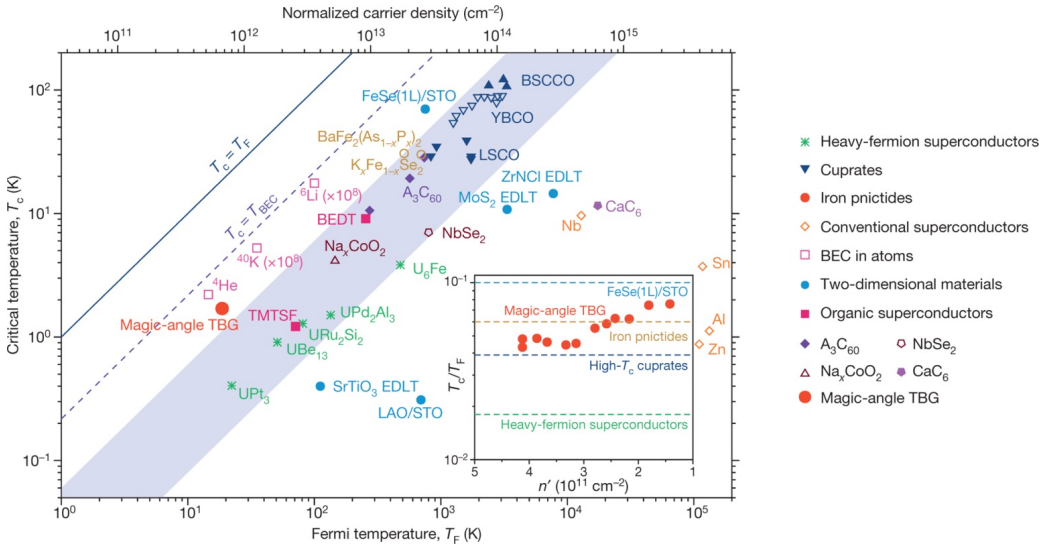

Figure 3.2: Superconductivity in the strong coupling limit: Materials which are located at the top of this plot have a high critical temperature. From left to right, the materials are ordered in terms of their normalized carrier density. Magic-angle graphene is in this respect special because only few electrons participate in the Cooper-pair formation and thus, it can be argued, is still a high-temperature superconductor. The blue shaded region is the approximate region in which almost all known unconventional superconductors lie. One is very much interested in a superconducting material which is very much in the upper left corner of the plot, what corresponds to high critical temperatures and to a material which cannot be easily disturbed. Such a material could have vast applications in technology. The inset shows the variation in T_c/T_F as a function of doping n' for magic-angle twisted bilayer graphene (red filled circles). The horizontal dashed lines are the approximate T_c/T_F values of the corresponding material. Picture and part of description taken from [87].

Recently, there is a convincing hint that unconventional superconductivity like high-temperature superconductors indeed arise if one has to deal with strongly interacting and thus also strongly correlated systems. In 2018, it was discovered that in bilayer graphene, where the angle between the layers allows for a certain tunability of such correlations, unconventional superconductivity can arise for certain configurations, called magic angles [87]. This discovery where two layers of graphene are stacked on top of each other and twisted by a magic angle attracted a lot of attention in the physics

community. On the one side, many groups around the world have a lot of experience with graphene, both experimentally and theoretically, because it is seen since a long time as an interesting material with particular electronic and mechanical properties. On the other side, it is despite its low absolute critical temperature claimed to be one of the best high-temperature superconductors (cf. Fig. 3.2) since there is an insulating state close to the superconducting one, which is often also the case with cuprates. The hope is now that with the help of magic-angle graphene, one can get a step closer to explain unconventional superconductivity. In magic-angle graphene superlattices, the electrons are densely packed, interactions play an important role, so that one needs to find a new theory which goes beyond a mean-field approach. It is clear that we have to abandon the single-particle description and instead introduce a full many-body description of our system. This is exactly what we explore and use in this part of the thesis: A many-body description of a QD-based Josephson junction.

3.2 Particle-conserving theory of superconductivity

In 1962, B.D. Josephson proposed a fundamental superconducting effect, for which he was later rewarded the Nobel Prize in Physics [88]. The Josephson effect describes in essence that a supercurrent can flow without applying any voltage when two superconductors are brought into close proximity. In his work, he employed for the first time a particle-conserving ansatz to describe superconductivity. While nowadays the mean-field BCS approach is more well-known, the particle-conserving ansatz provides however a clearer picture of superconductivity and at the same time it retains the related U(1)-symmetry. For a dedicated introduction to the concept, see, for instance, the book by Nobel laureate A. Leggett [81]. Apart from removing the non-physical violation of particle conservation, this ansatz solves many of the interpretation issues that appear in the BCS theory. Moreover, this approach could provide a way to capture long-range interactions which are considered important as an additional pairing mechanism, but cannot be properly accounted for by mean-field Hamiltonians. It is now very interesting to search for new features which can be predicted by this framework but not with the conventional BCS theory. Eventually, it could give a hint how superconductivity arises in the presence of strong correlations, like in QD systems. Knowing about the origin of high-temperature superconductivity could help to find more stable superconductors which also prevail at room temperature. Right now, researchers are still dependent on their intuition which materials should be brought together to create a high-temperature superconductor. Not only a refinement of superconductivity itself, but also interference effects in superconducting setups are in the scope of this topic of the thesis. A better

understanding of how Cooper pairs interfere with the electrons and their all-important Coulomb interaction is desirable. When a superconductor is connected to a normal conductor, superconducting correlations can leak into it, giving rise to pair correlations and to an induced superconducting gap, a phenomenon known as the proximity effect. The results presented here are based on the PhD thesis of Jordi Picó-Cortés [89] and a joint publication of Julian Siegl and Jordi Picó-Cortés [90]. We extend their work to an analysis of the interplay of Cooper pair and quasiparticle tunneling and investigate the superconducting coherences via the concept of Anderson pseudospin (cf. Sec. 3.5). The results are based on a generalized master equation calculated in the leading-order approximation.

We model a QD system connected to two superconductors, a S-QD-S junction, with the following Hamiltonian:

$$\hat{H} = \hat{H}_{\mathrm{QD}} + \sum_{l} \hat{H}_{l} + \hat{H}_{\mathrm{tun}}. \tag{3.1}$$

For our QD system, we take the Hamiltonian of a SIAM [cf. Eq. (1.34)]. The Hamiltonian of the l-lead takes the general form of

$$\hat{H}_{l} = \sum_{\sigma \boldsymbol{k}} \left(\xi_{l\boldsymbol{k}} + \mu_{l}\right) \hat{c}^{\dagger}_{l\boldsymbol{k}\sigma} \hat{c}_{l\boldsymbol{k}\sigma} \tag{3.2}$$

$$+ \sum_{\sigma\sigma' \boldsymbol{k}\boldsymbol{k}' \boldsymbol{q}} V_{l}(\boldsymbol{q}) \hat{c}^{\dagger}_{l\boldsymbol{k}+\boldsymbol{q}\sigma} \hat{c}^{\dagger}_{l\boldsymbol{k}'-\boldsymbol{q}\sigma'} \hat{c}_{l\boldsymbol{k}'\sigma'} \hat{c}_{l\boldsymbol{k}\sigma}. \tag{3.3}$$

Here, the spin-independent lead energies $\xi_{l\boldsymbol{k}}$ are associated to the lead creation/annihilation operators $\hat{c}^{\dagger}_{l\boldsymbol{k}\sigma}/\hat{c}_{l\boldsymbol{k}\sigma}$, where the momentum vector of the respective electrons is denoted as $\boldsymbol{k}$ and the spin as σ. We write the chemical potential of the l-lead as μ_{l} and for the electron-electron interaction $V_{l}(\boldsymbol{q})$, we use a form which is general in its momentum dependence.

Superconductivity can arise now with the formation of a Cooper pair condensate if the interaction becomes attractive [91]. The ground state within the particle-conserving ansatz can be written as $|M_{l}\rangle$, where the number of the Cooper pairs M_{l} in the l-lead are sufficient to describe the state [81]. The Cooper pairs are protected from breaking up due to, e.g., thermal fluctuations by twice the superconducting gap. Hence, the superconducting gap is considered to be the energy needed for one electron to leave the superconducting state. The characteristic energy spectrum of a superconductor is, for that reason, gapped. Now, we use a mean-field description for the interaction in order to describe the excited energy spectrum. However, we define crucially the average of all states $\langle\rangle$ in the definition of the superconducting gap $\Delta_{l\boldsymbol{k}}$ in a particle-conserving

fashion:

$$\Delta_{l\boldsymbol{k}} = \sum_{\boldsymbol{k}'} V_l(\boldsymbol{k}-\boldsymbol{k}')\langle \hat{S}_l^\dagger \hat{c}_{l\boldsymbol{k}\uparrow}\hat{c}_{l\bar{\boldsymbol{k}}\downarrow}\rangle. \tag{3.4}$$

The addition of the Cooper pair creation and annihilation operators, which are defined as

$$\hat{S}_l^\dagger \left|M_l\right\rangle = \left|M_l+1\right\rangle, \qquad \hat{S}_l \left|M_l\right\rangle = \left|M_l-1\right\rangle, \tag{3.5}$$

is the main difference with the standard BCS-approach. The Cooper pair operators preserve the particle number in the above-mentioned average. Other than that, $\hat{S}_l^\dagger \hat{S}_l = 1-\hat{P}_{l,0}$ holds with $\hat{P}_{l,0}$ projecting to the state with zero Cooper pairs. In the following, we use the assumption that the state with zero Cooper pairs is negligible (i.e., macroscopic leads), so that the two Cooper pair operators commute [89]. Applying the mean-field approach to the interaction, the Hamiltonian yields

$$\hat{H}_l^{\mathrm{MF}} = \sum_{\sigma\boldsymbol{k}} \left(\xi_{lk}+\mu_l\right)\hat{c}_{l\boldsymbol{k}\sigma}^\dagger \hat{c}_{l\boldsymbol{k}\sigma} - \sum_{\boldsymbol{k}} \left(\Delta_{l\boldsymbol{k}}\hat{S}_l\hat{c}_{l\boldsymbol{k}\uparrow}^\dagger \hat{c}_{l\bar{\boldsymbol{k}}\downarrow}^\dagger + \text{h. c.}\right). \tag{3.6}$$

In the following, we consider a momentum-independent gap, $\Delta_{l,\boldsymbol{k}} = \Delta_l$, which corresponds to s-type superconductivity. Furthermore, we can divide the complex superconducting gap into its amplitude $|\Delta_l|$ and its phase part $e^{i\phi_l} = e^{i\arg(\Delta_l)}$, which is essential to explain the supercurrent. The diagonalization of $\hat{H}_l^{\mathrm{MF}}$ can be achieved through the particle-conserving Bogoliubov-Valatin transformations outlined, e.g., in [88]. The electron creation operator transforms then according to

$$\hat{c}_{l\boldsymbol{k}\sigma}^\dagger = u_{lk}\hat{\gamma}_{l\boldsymbol{k}\sigma}^\dagger + \mathrm{sgn}(\sigma)v_{lk}^*\hat{S}_l^\dagger\hat{\gamma}_{l\bar{\boldsymbol{k}}\bar{\sigma}} + \mathcal{O}\left(\hat{P}_{l,0}\right), \tag{3.7}$$

where

$$u_{lk} = \sqrt{\tfrac{1}{2}\left(1+\tfrac{\xi_{lk}}{E_{lk}}\right)}, \tag{3.8}$$

$$v_{lk} = \mathrm{e}^{i\phi_l}\sqrt{\tfrac{1}{2}\left(1-\tfrac{\xi_{lk}}{E_{lk}}\right)}. \tag{3.9}$$

To this end, we employ the Bogoliubov quasiparticle operators $\hat{\gamma}_{l\boldsymbol{k}\sigma}/\hat{\gamma}_{l\boldsymbol{k}\sigma}^\dagger$, which are able to describe fermionic excitations of the systems and the quasiparticle excitation energy $E_{lk} = \sqrt{\xi_{lk}+|\Delta_l|^2}$. Under the assumption of macroscopic leads, the anti-commutation relations of fermions apply $\{\hat{\gamma}_{l\boldsymbol{k}\sigma}, \hat{\gamma}_{l\boldsymbol{k}\sigma}^\dagger\} = \delta_{ll'}[\delta_{\boldsymbol{k}\boldsymbol{k}'}\delta_{\sigma\sigma'} + \mathcal{O}(\hat{P}_{l,0})]$. Furthermore, it holds that $\hat{\gamma}_{l\boldsymbol{k}\sigma}\left|M_l\right\rangle = 0$ for all values of $\{l, \boldsymbol{k}, \sigma\}$, hence, we can conclude that the vacuum of quasiparticle excitations is the ground state for the superconductor. Applying the Cooper pair and quasiparticle operators, which commute mutually up to factors of $\hat{P}_{l,0}$,

to the ground state leads to an eigenstate with N_l particles. These excited energy states can be written as $|M, l, \{\nu_{l\boldsymbol{k}\sigma}\}\rangle$, where the occupation of a quasiparticle mode with momentum $\boldsymbol{k}$ and spin σ is denoted by $\nu_{l\boldsymbol{k}\sigma}$.
Now, we split the Hamiltonian describing the leads [Eq. (3.6)] into two parts

$$\hat{H}_l = \hat{H}_{\mathrm{QP},l} + \hat{H}_{\mathrm{CP},l}, \tag{3.10}$$

with one part describing the quasiparticles $\hat{H}_{\mathrm{QP},l}$ and one part describing the Cooper pairs $\hat{H}_{\mathrm{CP},l}$. The definitions of quasiparticle and the Cooper pair Hamiltonian are given by

$$\hat{H}_{\mathrm{QP},l} = \sum_{\boldsymbol{k}\sigma} \left(E_{lk} + \mu_l\right) \hat{\gamma}^\dagger_{l\boldsymbol{k}\sigma} \hat{\gamma}_{l\boldsymbol{k}\sigma}, \tag{3.11}$$

$$\hat{H}_{\mathrm{CP},l} = \mu_l \sum_{\boldsymbol{k}\sigma} \left(\hat{c}^\dagger_{l\bar{\boldsymbol{k}}\bar{\sigma}} \hat{c}_{l\boldsymbol{k}\sigma} - \hat{\gamma}^\dagger_{l\boldsymbol{k}\sigma} \hat{\gamma}_{l\boldsymbol{k}\sigma} \right). \tag{3.12}$$

The Cooper pair Hamiltonian can be seen in this definition as everything what is left if one subtracts the rather standard fermionic quasiparticle Hamiltonian contribution from the total lead Hamiltonian.
Eventually, the tunneling Hamiltonian can be rewritten with the Bogoliubov-Valatin transformations as

$$\begin{aligned} \hat{H}_{\mathrm{tun}} &= \sum_{l\boldsymbol{k}\sigma} t_l \hat{c}_{l\boldsymbol{k}\sigma} \hat{d}_\sigma + \text{h. c.} \\ &= \sum_{l\boldsymbol{k}\sigma p} p t_l^p \left[u^{\bar{p}}_{lk} \hat{\gamma}^p_{l\boldsymbol{k}\sigma} + \mathrm{sgn}(\sigma) v^p_{lk} \hat{S}^p_l \hat{\gamma}^{\bar{p}}_{l\bar{\boldsymbol{k}}\bar{\sigma}} \right] \hat{d}^{\bar{p}}_\sigma. \end{aligned} \tag{3.13}$$

The last step in the equation is obtained by introducing the Fock index $p = \pm$ analogous to Eq. (1.16). This formulation of the tunneling Hamiltonian leaves us with one part involving only quasiparticles and one involving also Cooper pairs.

3.3 Generalized master equation for superconducting leads

In order to derive a GME for our superconducting setup, we will make use of the Nakajima-Zwanzig formalism outlined in Cha. 1. The main task is hereby finding the solution for the steady state of our reduced density matrix, $\hat{\rho}$, with the help of the propagation Kernel defined in Eq. (1.11):

$$\left[\mathcal{L}_{\mathrm{S}} - \lambda + \tilde{\mathcal{K}}(\lambda) \right] \hat{\rho} = 0, \tag{3.14}$$

with $\lambda \to 0^+$ due to the Laplace transform. We explicitly opt here to write the dependence of the Kernel on λ, which should be considered as a frequency. It should be noted that in general, one could write the reduced density matrix in a time-dependent form, as in [90]. However, since we will derive only analytical equations on the dc-component of the current, we refrain from using the most general description, which would unnecessarily enlarge the already intricate formalism. Subsequently, the current through the system is given by Eq. (1.24):

$$I = \mathrm{Tr}_\mathrm{S}\left\{\tilde{K}_I \hat{\rho}\right\}, \tag{3.15}$$

where $\tilde{K}_I$ is the current Kernel for the symmetrized current operator $\hat{I} = (\hat{I}_\mathrm{L} - \hat{I}_\mathrm{R})/2$ as in Eq. (1.25). The advantage of using the Nakajima-Zwanzig projector technique for our transport calculation is that we are flexible in the exact distinction of what is the bath and what is the system part. As the most convenient distinction, we define the system part as the QD Hamiltonian and the Cooper pair one:

$$\hat{H}_\mathrm{S} = \hat{H}_\mathrm{QD} + \hat{H}_\mathrm{CP}, \qquad \hat{H}_\mathrm{B} = \hat{H}_\mathrm{QP}. \tag{3.16}$$

Since $\hat{H}_\mathrm{CP}$ commutes with the $\hat{H}_\mathrm{tun}$, we observe that the quasiparticle and the Cooper pair degrees of freedom are uncoupled. The quasiparticle degrees of freedom are the only dissipative part so that the Cooper pair time evolution can be considered as fully coherent. However, this is just the result of our model assumptions, where we do not consider charging effects which can couple the Cooper pairs with the quasiparticles. The timescale of these effects is nonetheless usually large so that the assumption, that the Cooper pair dynamics are decoupled from the quasiparticle dynamics, is indeed reasonable. Eventually, this observation of the coherent evolution of Cooper pairs will lead to the famous ac-Josephson effect. With this distinction between $\hat{H}_\mathrm{S}$ and $\hat{H}_\mathrm{B}$ at hand, we can write the reduced density matrix as

$$\hat{\rho} = \sum_{\boldsymbol{M}\Delta\boldsymbol{M}} \sum_{\chi\chi'} \rho_{\chi\chi'}(\Delta\boldsymbol{M}, \boldsymbol{M}) \left|\chi, \boldsymbol{M} + \Delta\boldsymbol{M}\right\rangle\!\left\langle\chi', \boldsymbol{M}\right|, \tag{3.17}$$

where $\chi \in \{0, \uparrow, \downarrow, 2\}$ describes the electronic population of the QD and the vector $\boldsymbol{M} = (M_\mathrm{L}, M_\mathrm{R})$ accounts for the Cooper pairs in the left and right lead, respectively. Coherences in the Cooper pair space can be described by a vector accounting for the Cooper pair imbalances in the leads with $\Delta\boldsymbol{M} = (\Delta M_\mathrm{L}, \Delta M_\mathrm{R}) \in \mathbb{Z}^2$. Overall, $\hat{\rho}$ can be considered as a system operator only. The action of the Cooper pair Liouvillian on the

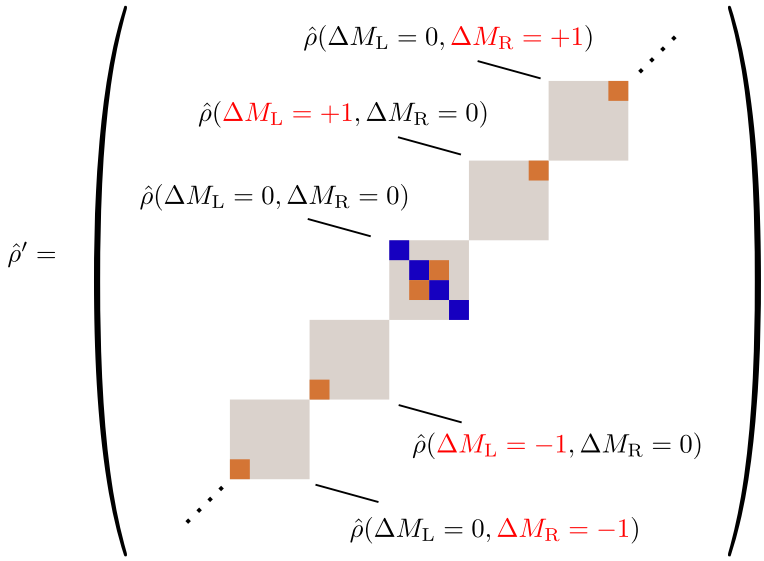

Figure 3.3: Sketch of the effective density matrix: The density matrix consists of blocks (gray), which differ in the imbalance of Cooper pairs $\Delta \boldsymbol{M}$. The blue entries, considered as the populations, correspond to the sum over all states with absolute Cooper pair number $\boldsymbol{M}$ and no Cooper pair imbalance, which can be formalized by $\rho_{\chi\chi}(\Delta \boldsymbol{M} = \boldsymbol{0})$. These four entries sum to 1 due to population conservation. In principle, also spin coherences (orange) are part of this block, however we can neglect them in our setup. The non-vanishing elements in the blocks, which are off-diagonal in the "Cooper pair imbalance"-space, are depicted in orange. These elements are associated with coherences between the empty and double-occupied electronic state ($|2\rangle\langle 0|$ for $\Delta M_l = -1$ and $|0\rangle\langle 2|$ for $\Delta M_l = +1$). In general, $\hat{\rho}'$ is infinite in its size.

density matrix is

$$i\hbar \mathcal{L}_\mathrm{CP} \left|\chi, \boldsymbol{M} + \Delta \boldsymbol{M}\right\rangle\!\left\langle \chi', \boldsymbol{M}\right| = 2\Delta \boldsymbol{M} \cdot \boldsymbol{\mu} \left|\chi, \boldsymbol{M} + \Delta \boldsymbol{M}\right\rangle\!\left\langle \chi', \boldsymbol{M}\right|, \tag{3.18}$$

where $\boldsymbol{\mu} = (\mu_\mathrm{L}, \mu_\mathrm{R})$ is the vector of the chemical potentials of the leads. We can deduce here that the absolute number of Cooper pairs is not relevant in the calculation of the Kernels, where $\mathcal{L}_\mathrm{CP}$ is appearing, but rather the imbalance of Cooper pairs $\Delta \boldsymbol{M}$. A generalization of the partial traces helps us to write the GME in a form, which is independent of the absolute number of Cooper pairs $\boldsymbol{M}$. We define the generalized traces by

$$\hat{O}(\Delta \boldsymbol{M}) = \sum_{\boldsymbol{M} \in \mathbb{Z}^2} \hat{O}(\Delta \boldsymbol{M}, \boldsymbol{M}). \tag{3.19}$$

As an example, the trace $\hat{\rho}(\boldsymbol{0})$ corresponds to the partial trace over the Cooper pair and quasiparticle sector, which is equivalent to the reduced density matrix of the QD

space only. A sketch of the effective density matrix $\hat{\rho}' = \sum_{\boldsymbol{M}\in\mathbb{Z}^2} \hat{\rho}$, under consideration in the following, is depicted in Fig. 3.3. The effective GME, connecting elements which differ in $\Delta\boldsymbol{M}$, can be thus written as

$$\begin{aligned} 0 = &\left(\mathcal{L}_{\mathrm{QD}} - 2i\Delta\boldsymbol{M}\cdot\boldsymbol{\mu}/\hbar - \lambda\right)\hat{\rho}(\Delta\boldsymbol{M}) \\ &+ \sum_{\Delta\boldsymbol{M}'} \tilde{\mathcal{K}}_{\mathrm{red}}(\Delta\boldsymbol{M} - \Delta\boldsymbol{M}', \lambda + 2i\Delta\boldsymbol{M}'\cdot\boldsymbol{\mu}/\hbar)\hat{\rho}(\Delta\boldsymbol{M}). \end{aligned} \tag{3.20}$$

Here, the Kernel $\tilde{\mathcal{K}}_{\mathrm{red}}(\Delta\boldsymbol{M}, \lambda)$ is obtained by collecting all the elements of $\tilde{\mathcal{K}}(\lambda)$ which change the Cooper pair imbalance by $\Delta\boldsymbol{M}$ after accounting for the Cooper pair operators appearing in the Kernel. We compensate the vanishing Cooper pair Liouvillians by the shift $\lambda \to \lambda + 2i\Delta\boldsymbol{M}'\cdot\boldsymbol{\mu}/\hbar$. Note that $\tilde{\mathcal{K}}_{\mathrm{red}}(\Delta\boldsymbol{M}, \lambda)$ is acting now only on a reduced density matrix, namely the one of $\hat{\rho}(\Delta\boldsymbol{M})$. The exact derivation of Eq. (3.20) is given in [89, 90].

In Fig. 3.3, we already anticipate that the only relevant entries of our considered density matrix have to fulfil the particle number selection rule [92] of

$$N_{\chi'} - N_{\chi} + 2\sum \Delta M_l = 0. \tag{3.21}$$

Since our SIAM model can host only up to 2 electrons, we deal with the following restriction on ΔM_l,

$$-1 \leq \Delta M_{\mathrm{L}} + \Delta M_{\mathrm{R}} \leq 1, \tag{3.22}$$

for ΔM_{L}, $\Delta M_{\mathrm{R}} \in \mathbb{Z}$. Hence, in the blocks where $\Delta M_{\mathrm{L}} + \Delta M_{\mathrm{R}} = \pm 1$, the only non-vanishing elements in the QD space are $|2\rangle\langle 0|$ and $|0\rangle\langle 2|$, depending on the sign of ΔM_l (cf. Fig. 3.3). These elements can be considered as the superconducting correlations, and the investigation of them recently attracted a lot of interest [90, 93–96]. The superconducting correlations, often also dubbed *pair-amplitude*, are induced by the proximity effect, through which superconductivity from the adjacent leads leaks into the dot.

As already mentioned, we focus in our analysis on the leading-order contribution of the Kernel to the steady state and to the current. The perturbation in the coupling to the leads is applied in terms of the tunneling coupling,

$$\Gamma_l = 2\pi g_{l,0}|t_l|^2, \tag{3.23}$$

where $g_{l,0}$ denotes the density of states of the l-lead in the normal state and t_l is the tunneling amplitude of the corresponding lead. With this definition, we are consistent with the convenient unit of energy of Γ_l. The original rate character of it is obtained by

a division of $\hbar$ as in Eq. (1.17). Starting from the definition of the sequential tunneling Kernel [cf. Eq. (1.14)],

$$\tilde{\mathcal{K}}^{(2)}(\lambda) = \mathcal{P}\mathcal{L}_{\mathrm{tun}} \frac{1}{\lambda - \mathcal{L}_{\mathrm{S}} - \mathcal{L}_{\mathrm{B}}} \mathcal{L}_{\mathrm{tun}} \mathcal{P}, \tag{3.24}$$

we can insert the exact form of the tunneling Hamiltonian with its two parts, namely the one $\propto u_{lk}^{\bar{p}} \hat{\gamma}_{l\boldsymbol{k}\sigma}^{p}$ and the other $\propto \mathrm{sgn}(\sigma) v_{lk}^{p} \hat{S}_{l}^{p} \hat{\gamma}_{l\bar{\boldsymbol{k}}\bar{\sigma}}^{\bar{p}}$ into the Liouvillians $\mathcal{L}_{\mathrm{tun}}$. We collect now all terms where no Cooper pair operators $\hat{S}_{l}^{p}$ are left after tracing out the bath degree of freedom (quasiparticle degree of freedom) and call it the *normal* terms. The normal terms are characterized therefore by no change in the Cooper pair number, and they can be associated to two electron-like or two hole-like excitations of opposite Hermicity. The other main contribution of the Kernel, coined *anomalous* terms, are obtained by collecting all the remaining terms with Cooper pair operators. They correspond then to an electron- and hole-like excitation of the same Hermicity together with a transport event of a Cooper pair. The next step is to apply the aforementioned generalized trace so that we correctly transform into the space where different $\hat{\rho}(\Delta \boldsymbol{M})$ are connected. In the following two sections, we derive now the Kernel $\tilde{\mathcal{K}}^{(2)}_{\mathrm{red}}(\mathbf{0}, \lambda)$, describing the normal terms, and the Kernels $\tilde{\mathcal{K}}^{(2)}_{\mathrm{red}}[(\pm 1, 0), \lambda]$ and $\tilde{\mathcal{K}}^{(2)}_{\mathrm{red}}[(0, \pm 1), \lambda]$, describing the anomalous terms.

3.3.1 Normal terms

The normal (reduced) Kernel yields

$$\tilde{\mathcal{K}}^{(2)}_{\mathrm{red}}(\mathbf{0}, \lambda) = -\frac{i}{\hbar} \sum_{\substack{l\sigma p \\ \alpha_1 \alpha_2}} |t_l|^2 \alpha_1 \alpha_2 \int_{-\infty}^{\infty} \mathrm{d}\varepsilon \hat{d}_{\sigma}^{\bar{p}\alpha_2} \frac{g_l(\varepsilon) f^{\alpha_1}(\varepsilon)}{\varepsilon - i\hbar\mathcal{L}_{\mathrm{QD}} + p\mu_l + i\hbar\lambda} \hat{d}_{\sigma}^{p\alpha_1}. \tag{3.25}$$

The only relevant difference of this Kernel to the one of non-superconducting leads introduced previously [cf. Eq. (1.18)] is, besides a slight adoption of the Fermi-function to $f^{q}(\varepsilon) = [e^{q\varepsilon/(k_{\mathrm{B}}T)} + 1]^{-1}$, which is more convenient in this chapter, the exchange of the density of states with the one characteristic for superconductivity:

$$g_l(\varepsilon) = g_{l,0} \mathrm{Re}\left\{ \sqrt{\frac{(\varepsilon - i\gamma)^2}{(\varepsilon - i\gamma)^2 - |\Delta_l|^2}} \right\}. \tag{3.26}$$

The shape of this function is governed by the superconducting gap $|\Delta_l|$ where for energies below it, the integral will vanish. However, due to a more realistic finite broadening of the superconducting density of states which would have otherwise divergent peaks at $\varepsilon = \pm|\Delta_l|$, we introduce the Dynes parameter γ [97, 98]. The solution of the energy

integral is given in [89, 90] by

$$\mathcal{I}_l^q(\nu) = -i\pi f^{\bar{q}}(\nu)h_l(\nu) - q\left[\mathcal{S}_l^{(2)}(\nu) - \lim_{W\to\infty}\mathcal{C}_l^{(2)}(W)\right], \tag{3.27}$$

which obeys $\mathcal{I}_l^q(\nu) = -\left(\mathcal{I}_l^{\bar{q}}(-\nu)\right)^*$ and where

$$\mathcal{S}_l^{(2)}(\nu) = 2\pi k_\mathrm{B}T\sum_{k=0}^{\infty}\frac{\omega_k h_l(i\omega_k)}{\omega_k^2+\nu^2}, \tag{3.28}$$

$$\mathcal{C}_l^{(2)}(W) = \pi k_\mathrm{B}T\sum_{k=0}^{\infty}\frac{h_l(i\omega_k)+h_l(iW)}{\omega_k+W} + \pi k_\mathrm{B}T\sum_{k=0}^{\infty}\frac{h_l(i\omega_k)-h_l(iW)}{\omega_k-W}, \tag{3.29}$$

with $\omega_k = 2\pi k_\mathrm{B}T(k+1/2)$ and the bandwidth W. The solution is obtained by using the residuum theorem. As a result, the function appearing in Eq. (3.27) is not $g_l(\varepsilon)$ but

$$h_l(z) = g_{l,0}\sqrt{\frac{z^2}{z^2-|\Delta_l|^2}}. \tag{3.30}$$

This can be understood as the result of the Kramers-Kronig relations. The action of the final form of the normal Kernel on $\hat{\rho}(\Delta\boldsymbol{M})$ can be written with the help of the above definitions as

$$\tilde{\mathcal{K}}_\mathrm{red}^{(2)}\left(\mathbf{0},\lambda+\frac{2i\Delta\boldsymbol{M}\cdot\boldsymbol{\mu}}{\hbar}\right)\hat{\rho}(\Delta\boldsymbol{M}) = -\frac{i}{\hbar}\sum_{\substack{l\sigma p\\ \alpha_1\alpha_2}}|t_l|^2\alpha_1\alpha_2 \hat{d}_\sigma^{\bar{p}\alpha_2}\mathcal{I}_l^{\alpha_1}(p\mu_l - i\hbar\mathcal{L}_\mathrm{QD})\hat{d}_\sigma^{p\alpha_1}\hat{\rho}(\Delta\boldsymbol{M}). \tag{3.31}$$

3.3.2 Anomalous terms

The anomalous (reduced) Kernel reads

$$\tilde{\mathcal{K}}_\mathrm{red}^{(2)}(p\boldsymbol{u}_l,\lambda) = -\frac{i}{\hbar}\sum_{l\sigma}\sum_{p\alpha_1\alpha_2}e^{ip\phi_l}|t_l|^2\alpha_1\alpha_2\int_{-\infty}^{\infty}\mathrm{d}\varepsilon\hat{d}_\sigma^{\bar{p}\alpha_2}\frac{\mathrm{sgn}(\sigma)p\tilde{g}_l(\varepsilon)f^{\alpha_1}(\varepsilon)}{\varepsilon - i\hbar\mathcal{L}_\mathrm{QD} - p\mu_l + i\hbar\lambda}\hat{d}_{\bar{\sigma}}^{\bar{p}\alpha_1}, \tag{3.32}$$

with $\boldsymbol{u}_\mathrm{L} = (1,0)$ and $\boldsymbol{u}_\mathrm{R} = (0,1)$. The former introduced phase of the superconductor ϕ_l enters this Kernel as well as the anomalous density of states

$$\tilde{g}_l(\varepsilon) = g_{l,0}\mathrm{Re}\left\{\sqrt{\frac{|\Delta_l|^2}{(\varepsilon-i\gamma)^2-|\Delta_l|^2}}\right\}\mathrm{sgn}(\varepsilon). \tag{3.33}$$

Employing again the residuum theory, we solve the anomalous energy integral with

$$\tilde{\mathcal{I}}_l^q(\nu) = i\pi f^{\bar{q}}(\nu)\tilde{g}_l(\nu) + q\tilde{\mathcal{S}}_l^{(2)}(\nu), \tag{3.34}$$

where the following functions are used

$$\tilde{\mathcal{S}}_l^{(2)}(\nu) = 2\pi k_{\mathrm{B}}T\sum_{k=0}^{\infty}\frac{i\nu\tilde{h}_l(i\omega_k)}{\omega_k^2+\nu^2}, \tag{3.35}$$

$$\tilde{h}_l(z) = g_{l,0}\sqrt{\frac{|\Delta_l|^2}{z^2-|\Delta_l|^2}}\mathrm{sgn}\left(\mathrm{Re}\{z\}+0^+\right). \tag{3.36}$$

Here, the property $\tilde{\mathcal{I}}_l^q(\nu) = [\tilde{\mathcal{I}}_l^{\bar{q}}(-\nu)]^*$ is satisfied. Eventually, we can express the anomalous Kernel in its final form:

$$\tilde{\mathcal{K}}_{\mathrm{red}}^{(2)}\left(p\boldsymbol{u}_l, \lambda + \frac{2i\Delta\boldsymbol{M}\cdot\boldsymbol{\mu}}{\hbar}\right)\hat{\rho}(\Delta\boldsymbol{M}) = -\frac{i}{\hbar}\sum_{l\sigma}\sum_{p\alpha_1\alpha_2}|t_l|^2 p\alpha_1\alpha_2\mathrm{sgn}(\sigma)e^{-ip\phi_l}$$
$$\hat{d}_\sigma^{\bar{p}\alpha_2}\tilde{\mathcal{I}}_l^{\alpha_1}(p\mu_l - i\hbar\mathcal{L}_{\mathrm{QD}})\hat{d}_{\bar{\sigma}}^{\bar{p}\alpha_1}\hat{\rho}(\Delta\boldsymbol{M}). \tag{3.37}$$

For more insights about the technicalities of the solution of the integrals, we refer the interested reader to [89, 90].

3.4 Current

According to [89, 90], it can be shown that the current Kernel can be equally cast into a form which is consistent with the block structure of $\hat{\rho}(\Delta\boldsymbol{M})$. Hereby, we explicitly follow the same approach outlined in the general Theory part (Sec. 1.4), where one replaces the leftmost tunneling Liouvillian with the current operator. In general, the obtained current is time-dependent, even in its steady state limit, which can explain the famous ac-Josephson effect. The steady state current can be expressed as

$$I(t) \coloneqq I_l^{\infty}(t) = \sum_{\Delta M} I^{(\Delta\boldsymbol{M})}e^{2i\Delta\boldsymbol{M}\cdot\boldsymbol{\mu}t/\hbar}, \tag{3.38}$$

where the current harmonics are given by

$$I^{(\Delta\boldsymbol{M})} = \mathrm{Tr}_{\mathrm{QD}}\left\{c_{\Delta\boldsymbol{M}}\sum_{\Delta M'}\tilde{\mathcal{K}}_{I,\mathrm{red}}^{(2)}(\Delta M - \Delta M', 2i\Delta\boldsymbol{M}'\cdot\boldsymbol{\mu}t/\hbar)\rho(\Delta\boldsymbol{M}')\right\}, \tag{3.39}$$

with the coefficients of the initial state defined as

$$c_{\Delta \boldsymbol{M}} = \mathrm{Tr}_{\mathrm{QD}} \left\{ \hat{\rho}(-\Delta \boldsymbol{M})(t=0) \right\}. \tag{3.40}$$

The reason that the current harmonics are dependent on the initial preparation of the density matrix is explained in full detail in [90]. In essence, this is due to the absence of a mechanism which couples the Cooper pairs to the dissipative degrees of freedom (namely the quasiparticles). It can be rationalized by the commutation of the Cooper pair operators with the tunneling Hamiltonian. However, since we focus on the first harmonic of the current, namely $I^{(\mathbf{0})}$, we can use $c_{\mathbf{0}} = 1$ due the conservation of probabilities.

3.5 Anderson pseudospin

In 1958, Phil Anderson introduced a pseudospin concept to explain the excitation spectrum of a bulk superconductor [99]. He showed that the superconductor can be described by a set of interacting pseudospins, where one pseudospin represents a pair of electronic states. When both states of such a pair are unoccupied, this is represented by the pseudospin pointing in the positive z-direction. Otherwise, if both states are occupied, the pseudospin is pointing in the negative z-direction. Similar to the Bloch sphere of Fig. 1.5, any other direction of the pseudospin vector can be seen as a superposition of the former states.
A review article by Josephson summarizes nicely the main ideas and the origin of the Anderson pseudospin concept in superconductivity [100], and here we briefly sketch it. The effective Hamiltonian of the bulk superconductor can be written according to Anderson as

$$H_{\mathrm{eff}} = -2 \sum_{k} \left(\epsilon_k - \mu \right) I_{k,z} - \sum_{k \neq k'} V_{kk'} \left(I_{k,x} I_{k',x} + I_{k,y} I_{k',y} \right). \tag{3.41}$$

Here, the first term describes the kinetic energy, while the second one stems from the interaction. The single-particle kinetic energy is denoted as ϵ_k, the chemical potential as μ, the matrix element for the scattering of a pair of electrons of equal momentum and opposite spin as $V_{kk'}$, while the three components of the kth pseudospin are $I_{k,x}$, $I_{k,y}$ and $I_{k,z}$.
One can formulate an effective field for the kth pseudospin:

$$\vec{H}_k = 2 \left(\epsilon_k - \mu \right) \vec{e}_z + 2 \sum_{k \neq k'} V_{kk'} \vec{I}_{k',\perp}, \tag{3.42}$$

where $\vec{e}_z$ is the unit vector in the z-direction and $\vec{I}_{k',\perp}$ indicates the component of the pseudospin in the x-y plane. In Fig. 3.4 **a**, a possible configuration of the pseudospins

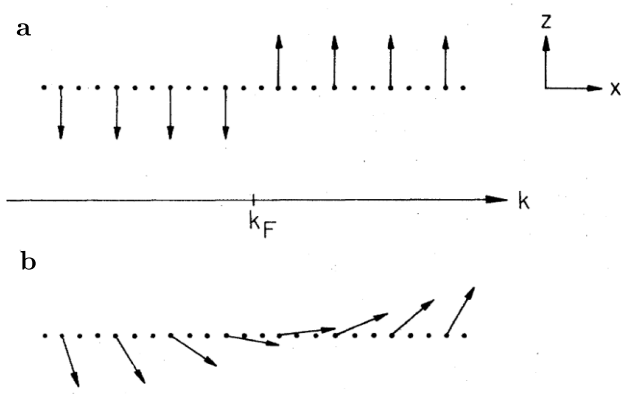

Figure 3.4: Anderson pseudospin configurations: a In a normal metal, the pseudospin changes abruptly its direction at the Fermi-momentum k_F, whereas in **b**, the pseudospins in a superconductor perform a vectorial rotation similar as in domain walls in magnetic textures. Figure taken from [100].

associated to a normal metal is depicted. In analogy to the semiclassical theory of magnetism, the spins align as a first approximation with applied effect field so that at the Fermi-surface, the signs of the pseudospins reverse due to the sign change in $\epsilon_k - \mu$ in $\vec{H}_k$. However, if there is an attractive interaction (corresponding to negative $V_{kk'}$), another configuration exists with lower total energy. In **b**, we display such lower energy configuration where the pseudospins are rotated inside the x-z plane in the vicinity of the Fermi-surface. Interestingly, the ground state of the superconductor breaks now the symmetry of the pseudospin Hamiltonian (H_eff) with respect to the rotation around the z-axis, which one can link to the particle conservation in the initial Hamiltonian. Furthermore, there is a degeneracy in the ground states of the superconductor, where the pseudospins can indeed lie in any plane through the z-axis. Another interesting fact is that the angle between this degenerate set and the plane of x-z can be related to the phase of the superconductor ϕ_l.

After setting the historic background of the Anderson pseudospin, we adopt it to our model where we deal only with one pair of electronic states, namely the spin states of

our SIAM, and thus with only one pseudospin. We define its three components as

$$I_x = \mathrm{Re}\{C_{20}\}, \tag{3.43}$$

$$I_y = \mathrm{Im}\{C_{20}\}, \tag{3.44}$$

$$I_z = \frac{p_0 - p_2}{2}, \tag{3.45}$$

where the real and the imaginary part of the superconducting correlations are the x- and y-component of the pseudospin and the difference of the populations of the empty (p_0) and double-occupied state (p_2) of the QD define the z-component. The superconducting correlations C_{20} are building up in the QD due to the proximity effect of the neighboring superconductors. Expressing the correlations with the help of the density matrix formalism, we write them as $C_{20} = |2\rangle\langle 0|$, where we have in mind a density matrix as

$$\hat{\varrho} = \begin{pmatrix} p_0 & 0 & 0 & C_{02} \\ 0 & p_\uparrow & 0 & 0 \\ 0 & 0 & p_\downarrow & 0 \\ C_{20} & 0 & 0 & p_2 \end{pmatrix}. \tag{3.46}$$

The off-diagonal elements of this density matrix, $|2\rangle\langle 0|$ and its complex conjugate partner $|0\rangle\langle 2|$, can be seen as a measure of the superconducting correlations. In the application part in Cha. 6, we will address the issue how to transform the a priori infinite matrix $\hat{\rho}'$ to the simple one of $\hat{\varrho}$ in order to have a firm footing of our defined pseudospin.

II Applications

4

Pseudospin resonances reveal synthetic spin-orbit interaction

In this chapter, we investigate pseudospin current resonances, which we predict in DQDs. Therefore, we employ a pseudospin valve in the spirit of a spin valve by manipulating the orbital coupling of the leads to the DQD. With adding also the spin degree of freedom through ferromagnetic leads, we show the interesting intertwinement between the orbital and the spin degree of freedom in such systems. The realized pseudospin resonances are a manifestation of many-body interference influenced by interaction and facilitated by the virtual electronic fluctuations between the leads and the system. We present a rich variety of these current resonances which can split, turn into dips, and even acquire a Fano shape. We accompany the numerical results obtained by a generalized master equation with an analytical minimal rate model. The analytic findings help us to understand the mechanism behind the pseudospin resonances and give insight into the underlying synthetic SOI. In the outlook of this chapter, we present some experimental data of a CNT which could indeed show remanences of pseudospin resonances. The following sections are based to a large extent on our publication *Physical Review B 103, 205420 (2021)* with the same title as this chapter [17].

4.1 Microscopic model of a pseudospin valve

As our setup, we take a spinful DQD and attach it to two leads in a pseudospin valve configuration as outlined in Sec. 2.2. The Hamiltonian of the DQD is defined by Eq. (2.4) and is characterized by the on-site and inter-site Coulomb interaction U and V, which results in a pseudospin anisotropy. At this stage, we present an extension of the used Hamiltonian in order to analyze the robustness of its degenerate spectrum. In a real DQD setup, one can encounter inter-dot tunneling t and asymmetry in the on-site energies of the DQD, which we could include in our pseudospin framework as

$$\hat{H}_{\mathrm{DQD}} = \left(\bar{\varepsilon} - \frac{U}{2}\right)\hat{N} + \frac{U+V}{4}\hat{N}^2 + (U-V)\,\hat{T}_z^2 + \vec{B}_t \cdot \hat{\vec{T}}. \tag{4.1}$$

We adjust the on-site energies to its average $\bar{\varepsilon} = (\varepsilon_1 + \varepsilon_2)/2 + \mathrm{e}V_\mathrm{g}$ and define a magnetic field $\vec{B}_t$ acting on the orbital degree as $B_{t,x} = 2\,\mathrm{Re}\,t$, $B_{t,y} = 2\,\mathrm{Im}\,t$, and $B_{t,z} = \Delta\varepsilon = \varepsilon_1 - \varepsilon_2$. The tunneling and the orbital asymmetry would lift the orbital degeneracy of our system and thus destroy our interference effect of pseudospin resonances if the magnitude of such Zeeman-like splitting is big enough. We argue that a small hopping and asymmetry $|t|, \Delta\varepsilon < \hbar\Gamma^0$ are not detrimental, as the coupling to the leads Γ^0 cannot resolve the lifted degeneracies. Therefore, one still expects interference effects to appear and the pseudo-magnetic field $\vec{B}_t$ would simply add to the exchange field in the spirit of Fig. 2.6 **c**. From now on, we restrict ourselves to the simpler case of $t = 0$ and $\varepsilon_1 = \varepsilon_2$.

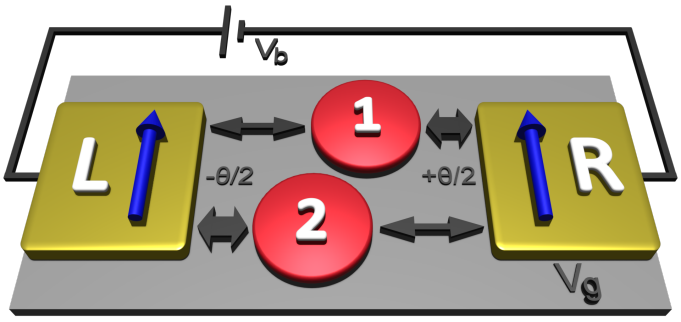

Figure 4.1: Schematic setup of a DQD in a pseudospin valve configuration with ferromagnetic leads: The blue arrows indicate parallel spin polarization of the leads. A pseudospin valve is obtained by coupling the dots differently to the leads highlighted by the black arrows. The total opening angle of the pseudospin polarization θ is applied equally to the left lead (L) and the right lead (R) as $\pm\theta/2$ and ensures coherent tunneling for $\theta \neq \pi, 0$.

On top of the pseudospin valve, we are adding spin polarization to the leads. In Fig. 4.1, such a setup is displayed. We opt for parallel spin and almost antiparallel pseudospin directions with an opening angle $\theta = 0.95\pi$ based on Eq. (2.17). Furthermore, we always use equal spin and orbital polarization for both leads in our calculations ($P_S = P_S^{\mathrm{L}} = P_S^{\mathrm{R}}$ and $P_T = P_T^{\mathrm{L}} = P_T^{\mathrm{R}}$). Moreover, we set the pseudospin polarization to the high value of $P_T = 0.99$ in order to increase the visibility of the effects and obtain an essentially closed pseudospin valve. This prerequisite of high pseudospin polarization is however within experimental reach, as shown in [6]. In this experiment, the angular momentum states of a CNT provide a two-level system with symmetry-protected degeneracy. The pseudospin polarization of the leads is there related to the extent and position of the contact region between the lead and the CNT. The localized contact provides then an almost full polarization. Furthermore, in [57] it was recently shown that the control of the phase and strength of the tunneling amplitudes can be achieved with the help of a longitudinal magnetic field acting on a CNT.

In this chapter, we however outline an alternative model based on the DQD geometry, which differs from the CNT implementation but results in a comparable pseudospin valve setup. The big advantage of our microscopic model is to be able to control the decisive parameters of the polarization strength and vectors by the relative distance of the dots to the leads and by the relative distance between the dots. The main goal of this section is to show that a realistic implementation of a pseudospin valve is indeed possible. We explicitly relate the position of the dots to the parametrization of the tunneling rate matrix components A^l and B^l and thus reproduce the desired pseudospin valve parameters Γ_0^l, P_T, and θ (cf. Sec. 2.2). The specific setup chosen here corresponds then to a situation where the left (right) lead is primarily coupled to dot "2" ("1") dot. Additionally, the opening angle $\theta \lesssim \pi$ accounts for a small component of coherent, simultaneous tunneling through both dots.

To start with, we define the wave functions of the leads and of the dots in real space as

$$\Psi_{l\boldsymbol{k}}(\boldsymbol{r})\delta_{\tau\sigma_l} = \langle \boldsymbol{r}\tau | l\boldsymbol{k}\sigma_l\rangle \quad \text{and} \quad \phi_i(\boldsymbol{r})\delta_{\tau\sigma} = \langle \boldsymbol{r}\tau | i\sigma\rangle\,. \tag{4.2}$$

To simplify the notation, we assume from now on that the axis of the lead spin σ_l and the one of the system σ coincide so that we switch to σ as the overall spin index. Furthermore, we denote in this section vectors in boldface to facilitate the readability.

The tunneling amplitude reads, accordingly,

$$t_{l\boldsymbol{k}\sigma,i\sigma'} = \int d\boldsymbol{r}\Psi^*_{l\boldsymbol{k}}(\boldsymbol{r})\Big[-\frac{\hbar^2\nabla^2}{2m_{\rm el}} + v_{\rm DQD}(\boldsymbol{r}) + v_{\rm leads}(\boldsymbol{r})\Big]\phi_i(\boldsymbol{r})\delta_{\sigma\sigma'} \approx \varepsilon_i \int d\boldsymbol{r}\Psi^*_{l\boldsymbol{k}}(\boldsymbol{r})\phi_i(\boldsymbol{r})\delta_{\sigma\sigma'}, \tag{4.3}$$

where, due to the strong localization of the system wave function, we neglect, in the approximation, the contribution of the leads' potential $v_{\rm leads}$. The energy of the localized dot state is denoted by ε_i.

The lead wave function is parametrized, in the tunneling barrier separating the leads from the dots, in terms of k_y and k_z, the components of the momentum parallel to the lead surface, and κ, the inverse penetration length inside the tunneling barrier:

$$\Psi_{l\boldsymbol{k}}(\boldsymbol{r}) = \Psi^{\perp}_{l\kappa}(x)\Psi^{\parallel}_{lk_yk_z}(y,z) = \frac{e^{-\kappa x + i(k_y y + k_z z)}}{\sqrt{SL_x}}, \tag{4.4}$$

where L_x and S are, respectively, the width of the well and the area of the lead surface perpendicular to the transport direction. Along the x-direction, the wave function decays exponentially. It is useful, for the following, to express the inverse penetration length κ in terms of the electron energy $E_{\rm el}$ and the parallel momenta k_y and k_z:

$$\kappa = \sqrt{k_y^2 + k_z^2 - \frac{2m_{\rm el}}{\hbar^2}E_{\rm el}}, \tag{4.5}$$

where $m_{\rm el}$ is the (effective) electronic mass.

The potential landscape for one lead and one QD is sketched in Fig. 4.2. The potential landscape confines the electrons only along the x-direction. The bottom energy of the rectangular potential well $E^{\sigma}_{\rm b}$ is spin-dependent, and the Fermi-energy $E_{\rm F}$ is separated from the vacuum energy ($E = 0$) by the work function of the metal ϕ_0 [1]. With this ansatz, made in the spirit of the Stoner model for itinerant ferromagnets, we assure a different density of states at the Fermi-energy for the different spin species, and obtain the desired spin polarization.

The two QD's are at distances x^l_1 and x^l_2 from the surface of the lead l and they feature localized bound states which we model as δ peaks centered at the position $\boldsymbol{R}_i$ of the

[1] In a more realistic setup, the vacuum level would be replaced by the top of the valence band of the insulator separating the metallic lead from the dot. The essence of the model remains, though, unchanged.

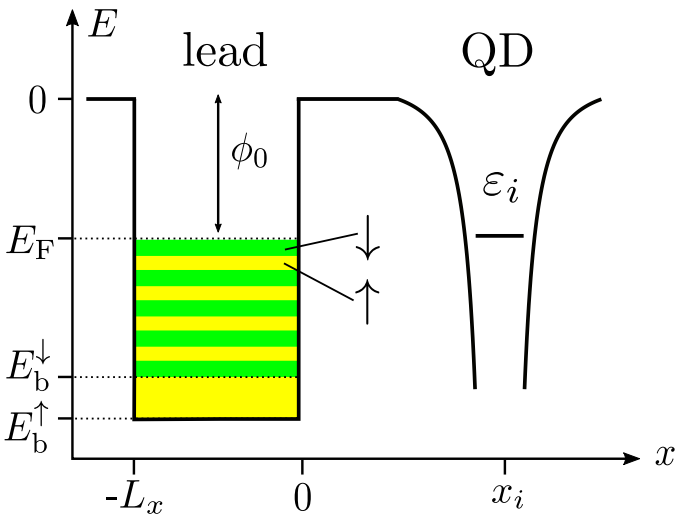

Figure 4.2: Potential landscape of a lead coupled to a QD: The lead is modeled as a (large) rectangular potential well of width L_x and is separated by a distance x_i from the QD. The work function of the lead is denoted by ϕ_0 and the Fermi-energy by E_F. The color coding emphasizes that the bottom energy E_b^σ is bigger in its absolute value for $\uparrow$-electrons than for $\downarrow$-electrons.

dot. The tunneling amplitude gets thus further simplified to

$$\begin{aligned} t_{l\boldsymbol{k}\sigma,i\sigma'} =& \varepsilon_i \langle l\boldsymbol{k}|i\rangle \approx \varepsilon_i \int d\boldsymbol{r} \Psi^*_{l\boldsymbol{k}}(\boldsymbol{r}) a^{3/2} \delta(\boldsymbol{r}-\boldsymbol{R}_i) \\ =& \varepsilon_i a^{3/2} \Psi^*_{l\boldsymbol{k}}(\boldsymbol{R}_i) = \varepsilon_i \frac{a^{3/2}}{\sqrt{SL_x}} e^{-\kappa x_i^l - i\boldsymbol{k}_\parallel \boldsymbol{R}_i}, \end{aligned} \tag{4.6}$$

where a is a normalization factor in units of length and where we have introduced the parallel component of the momentum $\boldsymbol{k}_\parallel = (0, k_y, k_z)$.
In the following, we calculate the parameters Γ_0^l, P_T, and θ starting from the definition of the tunneling rate matrix of Eq. (1.17). We follow two different approaches. At first, we employ the so-called surface Γ-point approximation (SGPA) [101]. Subsequently, we generalize our result by taking into account the full dispersion relation of the ferromagnetic leads.

4.1.1 Surface Gamma-point approximation

In a first approximation, we assume that only the state at the surface Γ-point, i.e., with $k_y = k_z = 0$, participates in the transport. From Eq. (4.5), we know that such a

state minimizes the inverse penetration length for a fixed electronic energy and thus is expected to give the largest contribution to the tunneling. Moreover, we calculate the tunneling density matrix at the Fermi-energy $E_F = -\phi_0$. Under those two conditions, the penetration length for the leads wave function reads $\lambda = \sqrt{\hbar^2/(2m_{\mathrm{el}}\phi_0)}$. Eventually, by inserting Eq. (4.6) into the definition of the bare tunneling rate Γ_0^l of Eq. (2.13), we obtain

$$\tilde{\Gamma}_0^l(E_F) = \frac{2\pi}{\hbar}\varepsilon_0^2 a^3 \sum_\sigma g_\sigma\left(E_{\mathrm{F}}\right) \sum_i e^{-\frac{2x_i^l}{\lambda}}, \tag{4.7}$$

where the tilde indicates the SGPA. In order to restore the correct units, the density of states are defined inverse proportional to the volume SL_x. The bare tunneling rate is proportional to the total density of states of the lead at the Fermi-energy which scales as the volume in the thermodynamic limit, and it is thus compensated by the factor SL_x at the denominator. Moreover, $\tilde{\Gamma}_0^l$ decreases exponentially upon increasing the distance between the dots and the lead. For a typical work function $\phi_0 = 5\,\mathrm{eV}$, the penetration length is approximately $\lambda = 0.9\,\text{Å}$ and the bare tunneling rate is reduced roughly by an order of magnitude if one increases the distance between the dots and the leads by 1 Å.

For the pseudospin component of the tunneling rate matrix, one obtains

$$\tilde{A}_{ij}^l = \frac{\exp\left(-\frac{x_i^l + x_j^l}{\lambda}\right)}{\exp\left(-\frac{2x_1^l}{\lambda}\right) + \exp\left(-\frac{2x_2^l}{\lambda}\right)}. \tag{4.8}$$

From $\tilde{A}^l$, we can deduce the polarization angle, calculated within the same approximation:

$$\tilde{\theta}_l = \arctan\left[\sinh\left(\frac{x_2^l - x_1^l}{\lambda}\right)\right]. \tag{4.9}$$

In our setup, we define the angle $\theta = \theta_{\mathrm{R}} - \theta_{\mathrm{L}}$ as the opening angle between the two polarization vectors. Moreover, we distribute the tilting symmetrically: $\theta_{\mathrm{L,R}} = \mp\theta/2$. Thus, an angle $\theta = 0$ corresponds to a DQD connected in parallel, with the state $|i=1\rangle - |i=2\rangle$ completely decoupled from both leads. Conversely, for $\theta = \pi$ the left (right) lead only couples to dot "2" ("1"), i.e., a completely closed pseudospin valve configuration.

From Eq. (4.9), it is clear that the calibration of the pseudospin polarization angle requires the control of the dot position on the scale of the penetration length λ. Alternatively, one should control with local gating the barrier height and thus have access to penetration length itself. Starting from Eq. (4.8), it is straightforward to prove that, within the SGPA, the strength of the pseudospin polarization is always maximal,

i.e., $\tilde{P}_T^l = 1$. This fact is not so surprising if one considers that only the tunneling amplitude to the state at the surface Γ-point is considered in the calculation of the $\tilde{A}^l$ matrix. All the other states at the Fermi-energy are simply accounted for in the density of states. A more careful evaluation of the tunneling amplitudes softens the condition of full polarization. Such an evaluation offers more insight into the dependence of the pseudospin polarization strength and direction on the geometry of the junction.

4.1.2 Three-dimensional Stoner model

Relaxing the SGPA requires us to calculate the $\boldsymbol{k}$-space integrals in the definition of tunneling rate matrices of Eqs. (2.13)-(2.14). The fundamental integral reads:

$$\begin{aligned} I_{ij}^l =& \sum_{\boldsymbol{k}\sigma} \langle i|l\boldsymbol{k}\rangle \langle l\boldsymbol{k}|j\rangle \, \delta\left(E_\mathrm{F} - \varepsilon_{l\boldsymbol{k}\sigma}\right) \\ =& \frac{a^3 m_\mathrm{el}}{2\pi^2\hbar^2} \sum_\sigma \int_0^{k_\mathrm{F}^\sigma} dk_\parallel k_\parallel \frac{J_0\left[k_\parallel(y_i - y_j)\right] e^{-(x_i^l + x_j^l)\sqrt{\lambda^{-2} + k_\parallel^2}}}{\sqrt{\frac{2m_\mathrm{el}}{\hbar^2}(E_\mathrm{F} - E_\mathrm{b}^\sigma) - k_\parallel^2}}, \end{aligned} \tag{4.10}$$

where J_0 is the Bessel-function of the first kind, $k_\parallel = \sqrt{k_y^2 + k_z^2}$, and the upper integration limit

$$k_\mathrm{F}^\sigma = \sqrt{\frac{2m_\mathrm{el}}{\hbar^2}(E_\mathrm{F} - E_\mathrm{b}^\sigma)}, \tag{4.11}$$

is the Fermi-momentum for the electrons of spin σ. Without any loss of generality, we chose the coordinate system such that $z_1 = z_2 = 0$. Moreover, we denote with y_i the l-independent distance of the i-dot in the y-direction.

On the one side, we evaluated numerically the integral in Eq. (4.10), and extracted the tunneling rate parameters plotted in Fig. 4.3. On the other side, further insight is gained from analytical calculations carried out under specific conditions. As we are interested in a DQD in weak tunneling coupling, we assume $x_i^l + x_j^l > 3\lambda$. Furthermore, we concentrate on the two limiting cases of an almost vanishing and almost full spin polarization. In the first case, we have, for a typical metallic electron density, $k_\mathrm{F}^\sigma \gtrsim \lambda^{-1}$, for both spin species. Hence, the numerator in Eq. (4.10) is exponentially suppressed at the upper integration limit since the absolute value of the argument of the exponential function is at least bigger than $|3\sqrt{2}|$, and the integration limit can be shifted at no price to ∞. We further neglect the $k_\parallel$ dependence in the denominator and Taylor-expand the exponent up to the second order. Under these simplifications the integral can thus be solved, to give

$$I_{ij}^{l,0} = \mathcal{C} \exp\left[-\frac{x_i^l + x_j^l}{\lambda} - \frac{(y_i - y_j)^2}{2\lambda(x_i^l + x_j^l)}\right] \frac{1}{x_i^l + x_j^l}, \tag{4.12}$$

with

$$\mathcal{C} = \frac{2a^3 m_{\mathrm{el}}}{h^2} \sum_{\sigma} \left(\frac{E_{\mathrm{b}}^{\sigma}}{E_{\mathrm{F}}} - 1 \right)^{-\frac{1}{2}}. \tag{4.13}$$

In the limit of almost full polarization, instead, $E_{\mathrm{b}}^{\downarrow} \approx -\phi_0$. We can thus apply the SGPA for the minority spin and obtain

$$I_{ij}^{l,\mathrm{fm}} = g_{\uparrow}(E_{\mathrm{F}}) e^{-\frac{x_i^l + x_j^l}{\lambda}} \frac{\phi_0}{E_{\mathrm{F}} - E_{\mathrm{b}}^{\uparrow}} \frac{\lambda}{x_i^l + x_j^l} e^{-\frac{(y_i - y_j)^2}{2\lambda(x_i^l + x_j^l)}} + g_{\downarrow}(E_{\mathrm{F}}) e^{-\frac{x_i^l - x_j^l}{\lambda}}, \tag{4.14}$$

where

$$g_{\sigma}(E_{\mathrm{F}}) = \frac{1}{4\pi^2} \left(\frac{2m_{\mathrm{el}}}{\hbar^2} \right)^{3/2} \sqrt{E_{\mathrm{F}} - E_{\mathrm{b}}^{\sigma}}. \tag{4.15}$$

With the help of Eq. (4.12) or Eq. (4.14), we calculate the bare tunneling coupling Γ_0^l at the Fermi-energy and compare it to the one obtained in the SGPA. One obtains in both cases a reduction of the bare tunneling rate, with the ratio being proportional to $(2\lambda)/(x_1^l + x_2^l) < 1$ in the range of validity of our analysis. The SGPA yields an upper limit for the bare tunneling strength, as the tunneling amplitude is smaller for states with finite $k_{\parallel}$ in comparison to the one at the Γ-point.
Finally, the generic element of the pseudospin matrix reads, independently of the spin polarization,

$$A_{ij}^l(E_{\mathrm{F}}) = \frac{\exp\left[-\frac{x_i^l + x_j^l}{\lambda} - \frac{(y_i - y_j)^2}{2\lambda(x_i^l + x_j^l)} \right] (x_i^l + x_j^l)^{-1}}{\exp\left(-\frac{2x_1^l}{\lambda} \right) (2x_1^l)^{-1} + \exp\left(-2\frac{x_2^l}{\lambda} \right) (2x_2^l)^{-1}}. \tag{4.16}$$

In the limit of small spin polarization, this result is obtained as the constant $\mathcal{C}$ in Eq. (4.13) factorizes both in the numerator and in the denominator of the A-matrix. In the limit of high spin polarization, the same simplification is obtained by neglecting the minority spin contribution to the integral $I_{ij}^{l,\mathrm{fm}}$. The orbital polarization strength and orientation angle follow as

$$P_T^l = \sqrt{X^2 + Z^2}, \tag{4.17}$$

$$\theta_l = \arctan\left(\frac{Z}{X} \right), \tag{4.18}$$

where

$$X = \frac{\left[1 - \left(\frac{\Delta x}{2\bar{x}^l} \right)^2 \right] \exp\left(-\frac{\Delta y^2}{4\lambda \bar{x}^l} \right)}{2\cosh\left(\frac{\Delta x}{\lambda} \right) + \frac{\Delta x}{\bar{x}^l} \sinh\left(\frac{\Delta x}{\lambda} \right)}, \tag{4.19}$$

and

$$Z = -\frac{\sinh\left(\frac{\Delta x}{\lambda}\right) + \frac{\Delta x}{2\bar{x}^l}\cosh\left(\frac{\Delta x}{\lambda}\right)}{2\cosh\left(\frac{\Delta x}{\lambda}\right) + \frac{\Delta x}{\bar{x}^l}\sinh\left(\frac{\Delta x}{\lambda}\right)}, \tag{4.20}$$

are the components of A^l multiplying, respectively, the σ^x- and σ^z-Pauli matrices, while

$$\bar{x}^l = \frac{x_1^l + x_2^l}{2},\ \Delta x = x_1^{\mathrm{L}} - x_2^{\mathrm{L}} \ \text{ and } \ \Delta y = y_1 - y_2. \tag{4.21}$$

In Fig. 4.3, we represent the pseudospin tunneling matrix parameters θ_{L} and P_T^{L},

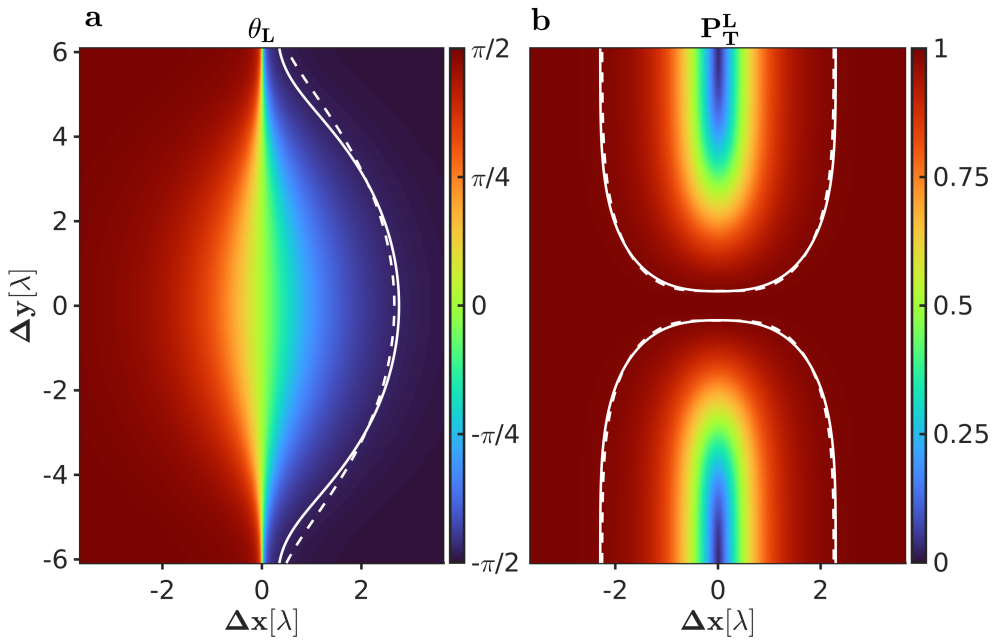

Figure 4.3: Pseudospin valve parameters in variation of the relative separation of the dots exemplarily shown for the left lead: a The polarization angle θ_{L} and **b** the polarization strength P_T^{L} depend on the Δx- and Δy-separation of the dots. The values are obtained by a numerical integration of Eq. (4.10). The parameters of the solid white lines are $P_T^{\mathrm{L}} = 0.99$ and $\theta_{\mathrm{L}} = -0.95\pi/2$. The dashed white lines, which coincide mostly with the solid ones, indicate the contour lines obtained by using the analytical Eqs. (4.17) and (4.18). The other parameters are: $x_1^{\mathrm{L}} + x_2^{\mathrm{L}} = 5\,\text{Å}$, $E_{\mathrm{b}}^{\uparrow} = -16.4\,\mathrm{eV}$, $E_{\mathrm{b}}^{\downarrow} = -5.0003\,\mathrm{eV}$, and $\phi_0 = 5\,\mathrm{eV}$ which correspond to a spin polarization of $P_S = 0.99$.

as obtained from the numerical evaluation of I_{ij}^l combined with the definition of the pseudospin matrix in Eqs. (2.14), (2.16), and (2.17), plotted as a function of the relative position between the two dots measured in unit of the penetration length λ. In accordance with the general trend already observed in the SGPA, the polarization angle

tends to $\pm\pi/2$ for a negative (positive) large Δx (cf. panel **a** in Fig. 4.3). The switch between the extreme orientation directions becomes though smoother in the vicinity of $\Delta y = 0$, once the contributions of finite $k_\parallel$ are taken into account.
At the same time, we also notice that the strength of the pseudospin polarization does assume values in the full range between 0 and 1. In particular, well separated dots ($\Delta y \approx 4\lambda$), kept though at similar distances from the leads, yield an almost vanishing polarization strength (i.e., an incoherent tunneling). Moving toward any other geometrical configuration, the polarization strength rapidly increases toward the maximum value of $P_T = 1$.
In Fig. 4.3, we also indicate the contour lines corresponding to the polarization strength and orientation angle assumed later in the results section. The full lines refer to the numerical calculation of the parameters. The dashed lines correspond, instead, to the analytical functions given in Eqs. (4.17)-(4.20). The crossing points between the full contour line for $\theta_{\rm L}$ and the full contour line for $P_T^{\rm L}$ fix both parameters to the desired values for one concrete $\Delta x/\Delta y$-configuration.

4.2 Coherent sequential tunneling model

Now that we gave a concrete example of pseudospin valve realization, we have established and substantiated in depth our setup of a DQD in an orbital valve configuration. In the following section, we want to introduce an analytical model which we use in order to describe and analyze the electronic dynamics on such a DQD. This model, which is in the regime of *coherent sequential tunneling* (CST) [102], helps us to gain a clearer physical understanding of the numerical results presented later on. The numerical findings are based on our developed transport theory (cf. Cha. 1) and also cover the cotunneling regime, with the caveat that there are more opaque in their interpretation.
The starting point of the analytic model is the generalized master equation in the steady state limit of Eq. (1.13), retaining only the CST-Kernel $\tilde{\mathcal{K}}^{(2)}$ given in Eq. (1.11). The equation of motion for the reduced density operator can be cast into the simple form:

$$\dot{\hat{\rho}} = (\mathcal{L}_{\rm DQD} + \tilde{\mathcal{K}}^{(2)})\hat{\rho} = -\frac{i}{\hbar}[\hat{H}_{\rm DQD} + \hat{H}_{\rm LS}, \hat{\rho}] + \mathcal{L}_{\rm T}\hat{\rho}, \tag{4.22}$$

where $\mathcal{L}_{\rm T}$ describes the tunneling events among many-body states with consecutive particle numbers and $\hat{H}_{\rm LS}$ is the Lamb shift Hamiltonian, which renormalizes the coherent DQD dynamics and is due to virtual charge fluctuations [103]. This splitting into $\mathcal{L}_{\rm T}$ and $\mathcal{L}_{\rm LS}$ is achieved by dividing all Kernel contributions into Fermi-function components and principal part components. However, in order to do this, we have

to restrict ourselves to a certain parameter space. This is necessary since in general, Eq. (4.22) would yield, for the system at hand, a set of 256 coupled equations for the different matrix elements of $\hat{\rho}$. A first reduction of the parameter space is obtained when we apply the conservation of charge, leading to a block diagonal matrix with only $1\times1+4\times4+6\times6+4\times4+1\times1=70$ elements calculated in an arbitrary many-body basis (cf. Sec. 1.7). To further limit the number of observables, we focus our interest on gate and bias voltages corresponding to at most one particle in the DQD, leading to coupled dynamics of the populations p_0 and p_σ (empty and single-occupied DQD with spin σ) complemented each by one of the spin-resolved pseudospin vectors $\vec{T}_\sigma$. Due to the solely S_z-polarization of the leads, we can describe the one-particle sector instead of the general 16 variables with only 8 variables. These observables are obtained as the expectation values of system operators:

$$p_0=\langle\hat{P}_0\rangle,\quad p_\sigma=\langle\hat{P}_\sigma\rangle,\quad T_{\sigma,\alpha}=\langle\hat{P}_\sigma\hat{T}_\alpha\hat{P}_\sigma\rangle, \tag{4.23}$$

where $\langle\bullet\rangle=\mathrm{Tr}_{\mathrm{DQD}}\{\bullet\hat{\rho}\}$, $\hat{P}_0=|\emptyset\rangle\langle\emptyset|$ is the projector on the empty state, $\hat{P}_\sigma=\sum_i\hat{d}_{i\sigma}^\dagger\hat{P}_0\hat{d}_{i\sigma}$, and $\hat{T}_\alpha$ is the $\alpha=x,y,z$ component of the pseudospin operator defined in Eq. (2.2). With this chosen division of the one-particle subspace, we look at the pseudospin of each spin channel individually, for example, if a spin up electron is more located on one dot or the other (z-polarization of the pseudospin); or if it is localized on both dots equally (x/y-polarization of the pseudospin).
Due to the conservation of particle number and z-component of the spin for parallel polarized leads, in the range of bias and gate voltages relevant for our considerations, the reduced density matrix is block diagonal and can be approximated with the expression

$$\rho\approx p_0\oplus\left(\frac{p_\uparrow}{2}\mathbb{1}_2+\vec{T}_\uparrow\cdot\vec{\sigma}\right)\oplus\left(\frac{p_\downarrow}{2}\mathbb{1}_2+\vec{T}_\downarrow\cdot\vec{\sigma}\right), \tag{4.24}$$

where $\oplus$ denotes a direct sum. With these definitions at hand, we outline in the following subsection the exact derivation of the Lamb shift Hamiltonian in order to originate the all important exchange fields acting on the pseudospin vectors $\vec{T}_\uparrow$ respectively $\vec{T}_\downarrow$.

4.2.1 Lamb shift Hamiltonian

In this subsection, we derive the Lamb shift Hamiltonian, which enables us to read out the spin-resolved pseudo-exchange field $\vec{B}_\sigma$. We start from the definition of the Lamb

shift Hamiltonian for the one-particle subspace:

$$\hat{H}_{\mathrm{LS},1} = \sum_{li\sigma j\sigma'} \hbar\Gamma^l_{i\sigma,j\sigma'} \hat{P}_1 \left[\hat{d}^\dagger_{i\sigma} p_l \left(E_1 - H_{\mathrm{DQD}} \right) \hat{d}_{j\sigma'} + \hat{d}_{j\sigma'} p_l \left(\hat{H}_{\mathrm{DQD}} - E_1 \right) \hat{d}^\dagger_{i\sigma} \right] \hat{P}_1. \tag{4.25}$$

Its commutator with the reduced density matrix captures the contributions of $\tilde{K}^{(2)}$ proportional to the principal parts [Eq. (2.23)] which stem from the imaginary part of the Y^n-function. Moreover, the projector on the one-particle space in Eq. (4.25) reads $\hat{P}_1 = \sum_{i\sigma} \hat{d}^\dagger_{i\sigma} |\emptyset\rangle\langle\emptyset| \hat{d}_{i\sigma}$, being $|\emptyset\rangle$ the vacuum state vector.
To proceed further, we insert the DQD Hamiltonian written in the pseudospin formulation, as given in Eq. (2.4), into Eq. (4.25) and perform a complete Taylor expansion with respect to the anisotropy component proportional to the operator $\hat{T}_z^2$. The two-particle subspace consists of a singlet and a triplet pseudospin sector; thus the relation $\hat{P}_2 \hat{T}_z^2 \hat{P}_2 = \left(\hat{P}_2 \hat{T}_z^2 \hat{P}_2 \right)^n$ for $n \geq 1$ holds, where $\hat{P}_2$ is the projector operator on the two-particle subspace. We can thus simplify the Taylor expansion:

$$\begin{aligned}
\hat{P}_2 p_l \left[\varepsilon + V + (U-V)\hat{T}_z^2 \right] \hat{P}_2 &= \hat{P}_2 p_l \left(\varepsilon + V \right) + \hat{P}_2 \hat{T}_z^2 \hat{P}_2 \sum_{n=1}^{\infty} \frac{(U-V)^n}{n!} p_l^{(n)} \left(\varepsilon + V \right) \\
&= \hat{P}_2 \left\{ p_l \left(\varepsilon + V \right) + \hat{T}_z^2 [p_l \left(\varepsilon + U \right) - p_l \left(\varepsilon + V \right)] \right\} \hat{P}_2 \\
&= \hat{P}_2 \left\{ [p_l \left(E_{2\mathrm{g}1} \right) + \hat{T}_z^2 [p_l \left(E_{2\mathrm{e}1} \right) - p_l \left(E_{2\mathrm{g}1} \right)] \right\} \hat{P}_2. \quad (4.26)
\end{aligned}$$

We distinguish in the energy differences the two-particle ground state (2g) and excited state energy (2e) to account for the U-V anisotropy (cf. Fig. 2.2). At this stage, the following operator identity is useful:

$$\hat{P}_1 \hat{d}_{j\sigma'} \hat{T}_z^2 \hat{d}^\dagger_{i\sigma} \hat{P}_1 = \frac{1}{2} \hat{P}_1 \hat{d}_{j\sigma'} \hat{d}^\dagger_{i\sigma} \hat{P}_1 + \sum_k \sigma^z_{ki} \hat{P}_1 \hat{d}_{j\sigma'} \hat{d}^\dagger_{k\sigma} \hat{T}_z \hat{P}_1. \tag{4.27}$$

Some algebra leads, eventually, to the formulation of the Lamb shift Hamiltonian, obtained under the additional assumption of parallel spin polarization of the leads:

$$\begin{aligned}
\hat{H}_{\mathrm{LS},1} = &\sum_l \hbar\Gamma^l_0 \left[p_l \left(E_{10} \right) + 2 p_l \left(E_{2\mathrm{g}1} \right) + p_l \left(E_{2\mathrm{e}1} \right) \right] \hat{P}_1 \\
&+ \sum_l \hbar\Gamma^l_0 (D_\uparrow - D_\downarrow) \left[p_l \left(E_{10} \right) - p_l \left(E_{2\mathrm{e}1} \right) \right] \vec{n}^l_S \cdot \hat{P}_1 \hat{\vec{S}} \hat{P}_1 \\
&+ \sum_{l\sigma} 2\hbar\Gamma^l_0 D_\sigma \left[p_l \left(E_{10} \right) - p_l \left(E_{2\mathrm{g}1} \right) \right] P_T \vec{n}^l_T \cdot \hat{P}_\sigma \hat{\vec{T}} \hat{P}_\sigma \\
&+ \sum_{l\sigma} 2\hbar\Gamma^l_0 D_{\bar{\sigma}} \left[p_l \left(E_{2\mathrm{e}1} \right) - p_l \left(E_{2\mathrm{g}1} \right) \right] P_T \left(\vec{n}^l_T \cdot \vec{e}_z \right) \hat{P}_\sigma \hat{T}_z \hat{P}_\sigma, \quad (4.28)
\end{aligned}$$

where the spin operator $\hat{\vec{S}}$, similarly to the pseudospin one defined in Eq. (2.2), reads, in components,

$$\hat{S}_\alpha = \frac{1}{2}\sum_{i\tau\tau'} \hat{d}^\dagger_{i\tau}\sigma^\alpha_{\tau\tau'}\hat{d}_{i\tau'}. \tag{4.29}$$

Furthermore, we define $D_{\uparrow,\downarrow} = 1 \pm P_S$. The first and the second term in Eq. (4.28) do not contribute to the time evolution of the reduced density matrix, which is block diagonal in spin, as the parallel spin polarization of the leads defines a common quantization axis for the entire DQD junction. Thus, the Lamb shift Hamiltonian reduces, effectively, to a pseudospin Zeeman term:

$$\hat{\tilde{H}}_{\mathrm{LS},1} = \sum_\sigma \hbar\vec{B}_\sigma \cdot \hat{\vec{T}}_\sigma, \tag{4.30}$$

where we have introduced the spin-resolved pseudo-exchange field

$$\begin{aligned}\vec{B}_\sigma = \sum_l 2P_T\Gamma^l_0 \Big\{ & D_\sigma \left[p_l(E_{10}) - p_l(E_{2\mathrm{g}1})\right]\vec{n}^l_T \\ & + D_{\bar{\sigma}} \left[p_l(E_{2\mathrm{e}1}) - p_l(E_{2\mathrm{g}1})\right]\left(\vec{n}^l_T \cdot \vec{e}_z\right)\vec{e}_z \Big\}.\end{aligned} \tag{4.31}$$

The pseudospin operator is defined as

$$\hat{\vec{T}}_\sigma = \hat{P}_\sigma \hat{\vec{T}} \hat{P}_\sigma. \tag{4.32}$$

The exchange field arises due to virtual fluctuations of the system to the neighboring empty *and* double-occupied DQD states. It is crucial to include in the exchange field the two-particle states, even though we do not account explicitly for the dynamics of their populations. Also, energy levels far from the CST-resonance do influence the exchange field due to the logarithmic tails of the digamma-functions (cf. Fig. 2.5). It is now straightforward to demonstrate that the commutator with the Lamb shift Hamiltonian results in a precession dynamics:

$$-\frac{i}{\hbar}\left[\hat{H}_{\mathrm{LS},1}, \hat{\rho}_1\right] \Longleftrightarrow \vec{B}_\sigma \times \vec{T}_\sigma. \tag{4.33}$$

The pseudo-exchange fields associated with the majority and the minority spins differ from each other both in strength and orientation, thus giving rise to a SOI, which, due to the complete absence of intrinsic SOI in the system, we call synthetic. As shown in Sec. 4.3, such synthetic SOI determines the rich variety of phenomena decorating the $N = 1$-Coulomb diamond.

It is the first line in Eq. (4.31) which gives the most relevant contribution to $\vec{B}_\uparrow$. The second line dominates, instead, $\vec{B}_\downarrow$. Especially for leads with a very high spin

polarization, we can conclude that the pseudo-exchange field of minority spins always points approximately toward the z-direction, which represents the hard axis of the pseudospin anisotropy. Instead, the majority spin field $\vec{B}_\uparrow$ oscillates, as a function of the bias and gate voltage, between the two directions $\vec{n}_T^{\mathrm{L}}$ and $\vec{n}_T^{\mathrm{R}}$. Interestingly, for an isotropic system ($U = V$) the two fields would be collinear, with the difference in strength stemming merely from the different spin-resolved density of states in the leads. For normal metallic leads, the two fields even coincide.

4.2.2 Equations of motion

By inserting the approximate block diagonal reduced density matrix of Eq. (4.24) into the generalized master equation of Eq. (1.13) with the Kernel evaluated in the CST-limit, we compute the time derivatives of the expectation values of our observables according to Eq. (4.23). In analogy to the spin valve case discussed in Sec. 2.4, the following set of coupled Bloch-like equations can be obtained:

$$\dot{p}_0 = -4\gamma^+ p_0 + \sum_\sigma D_\sigma \left(\gamma^- p_\sigma + 2\vec{\gamma}^- \cdot \vec{T}_\sigma\right), \tag{4.34}$$

$$\dot{p}_\sigma = D_\sigma \left(2\gamma^+ p_0 - \gamma^- p_\sigma - 2\vec{\gamma}^- \cdot \vec{T}_\sigma\right), \tag{4.35}$$

$$\dot{\vec{T}}_\sigma = D_\sigma \left(-\gamma^- \vec{T}_\sigma + p_0 \vec{\gamma}^+ - \frac{p_\sigma}{2}\vec{\gamma}^-\right) + \vec{B}_\sigma \times \vec{T}_\sigma, \tag{4.36}$$

where we have introduced scalar and vector rates, respectively $\gamma^\pm = \sum_l \Gamma_0^l f_l^\pm(\varepsilon)$ and $\vec{\gamma}^\pm = \sum_l P_T \Gamma_0^l f_l^\pm(\varepsilon)\vec{n}_T^l$. For the Fermi-functions, we adopt again the notation $f_l^\pm(\varepsilon) = [e^{\pm(\varepsilon-\mu_l)/(k_\mathrm{B}T)} + 1]^{-1}$. The conservation of probability imposes that $\dot{p}_0 + \dot{p}_\uparrow + \dot{p}_\downarrow = 0$. This relation is clearly satisfied by the differential equations (4.34) and (4.35). Besides the gain-loss relations between the populations p_0 and p_σ, they contain the terms $\pm 2D_\sigma \vec{\gamma}^- \cdot \vec{T}_\sigma$ which ensure the coupling of the populations to the dynamics of the spin-resolved pseudospin vectors $\vec{T}_\sigma$.

4.3 Results

The stability diagram, i.e., the differential conductance displayed as a function of bias and gate voltage, of a DQD in the cotunneling regime is shown in Fig. 4.4 for several spin polarizations of the leads. Our analysis is focused on the one-particle Coulomb diamond, highlighted in panel **a** by the dotted white lines. Here, we would normally expect a featureless exponentially suppressed differential conductance, as the consequence of an essentially fixed particle number and, due to Coulomb repulsion, a smooth, exponentially suppressed current.

Contrary to the expectations, we can clearly see in this panel a distinctive resonance, highlighted by the dashed black line, cutting through the Coulomb diamond. Increasing the spin polarization P_S [Fig. 4.4 **b-d**] leads to a splitting of this resonance, marked by the dashed lines. In the upper right corner of Fig. 4.4 **d**, a resonance can be observed even outside the diamond. Although introduced as current resonances, the aforementioned transport features are more visible in the differential conductance. The latter enhances, in fact, sharp current modulations within the generally suppressed Coulomb diamond background. We rationalize those transport effects in terms of pseudospin resonances,

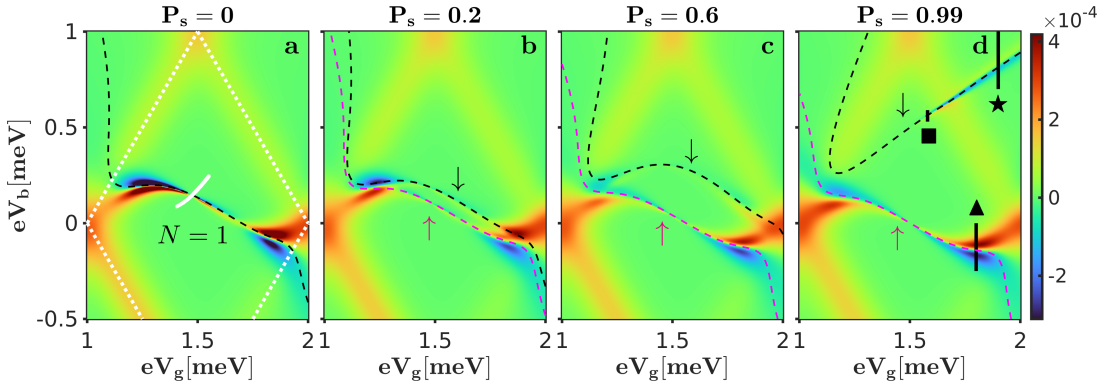

Figure 4.4: Differential conductance of a DQD shows pseudospin resonances tuned by spin polarization P_S: a The one-particle diamond is highlighted by the dotted white lines. **b-d** Increasing the spin polarization leads to a splitting of the resonances. The three vertical black lines (★, ■, ▲) indicate the bias traces of Fig. 4.5. The dashed magenta (black) line is the resonance condition of the ↑-(↓-)electrons [cf. Eq. (4.37)]. The solid white line indicates the minimum of $B_{\sigma,\perp}$ which matches perfectly a local minimum within the pseudospin resonance. The parameters are the following: $U = 2\,\mathrm{meV}$, $k_\mathrm{B}T = 0.05\,\mathrm{meV}$, $P_T = 0.99$, $\theta = 0.95\pi$, $\Gamma_0^\mathrm{R} = 2.5 \times 10^{-3}\,\mathrm{meV} = 2\Gamma_0^\mathrm{L}$, and $\varepsilon_0 = -2\,\mathrm{meV}$.

in analogy to the spin resonances reported firstly in [65]. The valve configuration blocks the current since an electron occupying the dot strongly coupled to the source is only weakly coupled to the drain. Due to a lack of a direct hopping term to the other dot and the Coulomb repulsion, the electron can reside for a long time on the dot in terms of the internal time scales, leading to a suppression of current. The pseudo-exchange fields are now able to lift the pseudospin valve configuration since they offer the possibility, at a certain resonance condition, to transfer population of this blocked electrons to the other open dot by the virtue of virtual fluctuations. It is important to point out that this transfer of populations is facilitated by tunneling to a coherent superposition of two different orbitals. It can only arise for σ^x- or, equivalently, σ^y-orbital polarized leads.

Experimental evidence of such coherent superpositions for QDs in the weak tunneling regime has been reported in [6, 104]. A valve of only σ^z-polarization of the leads is not sufficient for this effect to arise so that non-collinear Γ^l-matrices are a necessary prerequisite. Other than that, we require an asymmetry in the bare coupling strength ($\Gamma_0^{\mathrm{L}} \neq \Gamma_0^{\mathrm{R}}$) of the right and the left lead which shifts the resonance away from the zero bias line exactly as in the case of spin resonances.
We can formulate, in the framework of Eqs. (4.34)-(4.36), vectorial pseudospin resonance conditions similarly to the ansatz in [65, 102]:

$$\vec{B}_\sigma \cdot \left(\vec{n}_T^{\mathrm{L}} - \vec{n}_T^{\mathrm{R}}\right) = 0. \tag{4.37}$$

The spin-dependent exchange field generates two distinct conditions, each determining the position of the corresponding resonance in the V_{g}-V_{b} plane: the magenta (black) dashed line in Fig. 4.4 for the ↑-(↓)-electrons. The accuracy of Eq. (4.37) in determining the resonance positions reduces as the angle θ is chosen farther away from antiparallel alignment. In contrast to the resonance conditions formulated in [65] and in [102], we choose Eq. (4.37), where the drain and the source equally participate since it matches the numerical resonances on a broader parameter range. The main idea behind all these conditions is that an exchange field perpendicular to the injected (pseudo)spin can cause precession of the equilibrium (pseudo)spin. In a large parameter space, the effective pseudo-magnetic field is pointing mainly parallel to the injected pseudospin, resulting in no or limited precession dynamics. Only at specific values of gate and bias, a compensation of left and right lead components in $\vec{B}_\sigma$ parallel to the injected pseudospin leads to drastic direction change of the exchange field. The result is a drastically different pseudospin equilibrium vector and population situation, where a channel of transport is open despite the valve configuration of the leads.
Despite the subtle differences, though, all three conditions mentioned above can only predict the *position* of the resonances, but not their *character*. The same resonance condition corresponds to a dip in the current (★ in Fig. 4.4), or to a peak (▲) and even to a Fano-like asymmetric peak-dip (■). Finally, the current peak is strongly modulated along the same resonance line and it can even disappear, as exemplarily highlighted in panel **a** of Fig. 4.4 with the solid white line. The discovery and explanation of such *qualitative* differences in the pseudospin resonances, which originate from the intertwining of spin and pseudospin, represent the main result presented in this chapter.
As a first step in the analytical understanding of the rich variety of transport phenomena illustrated in Fig. 4.4, we calculate the stationary current in the CST-limit. The current through the DQD can be expressed as the charge variation due to the coupling to a

specific lead. From Eq. (4.35), we readily obtain

$$I_{\mathrm{L}} = 4\gamma_{\mathrm{L}}^{+} p_0 - \sum_{\sigma} D_\sigma \left(\gamma_{\mathrm{L}}^{-} p_\sigma + 2\vec{\gamma}_{\mathrm{L}}^{-} \cdot \vec{T}_\sigma \right), \tag{4.38}$$

where the vector and scalar rates for the left lead read, respectively, $\vec{\gamma}_{\mathrm{L}}^{-} = \Gamma_0^{\mathrm{L}} P_T f_{\mathrm{L}}^{-}(\varepsilon) \vec{n}_T^{\mathrm{L}}$ and $\gamma_{\mathrm{L}}^{\pm} = \Gamma_0^{\mathrm{L}} f_{\mathrm{L}}^{\pm}(\varepsilon)$. The stationary current is obtained by inserting in Eq. (4.38) the populations p_0^∞, p_σ^∞, and $\vec{T}_\sigma^\infty$, i.e., the stationary solutions of Eqs. (4.34)-(4.36).
Panels **a**, **c**, and **e** of Fig. 4.5 show a direct comparison between the absolute value of the current as obtained from the full numerical calculation (orange) and the analytical approach (blue) of Eq. (4.38). In all three cases, the analytical result well reproduces the qualitative behavior of the current and the position of its extrema.
For a deeper understanding of the resonances of Fig. 4.4 and Fig. 4.5, we further elaborate on the equations of motion (Eqs. (4.34)-(4.36)). To this end, we solve Eq. (4.36) in the stationary limit, and obtain, for the accumulated pseudospin,

$$\vec{T}_\sigma^\infty = \vec{F}_\sigma(\vec{b}_\sigma), \tag{4.39}$$

where we introduced the auxiliary function

$$\vec{F}_\sigma(\vec{x}) = \frac{a_\sigma}{a_\sigma^2 + |\vec{B}_\sigma|^2} \left(\vec{x} + \frac{\vec{B}_\sigma \cdot \vec{x}}{a_\sigma^2} \vec{B}_\sigma + \frac{\vec{B}_\sigma \times \vec{x}}{a_\sigma} \right), \tag{4.40}$$

with $a_\sigma = D_\sigma \gamma^{-}$, together with the vector $\vec{b}_\sigma = D_\sigma \left(p_0 \vec{\gamma}^{+} - p_\sigma \vec{\gamma}^{-}/2 \right)$.
By substituting $\vec{T}_\sigma^\infty$ into Eqs. (4.34)-(4.35), we obtain a set of effective rate equations for the populations p_0 and p_σ:

$$\begin{pmatrix} \dot{p}_0 \\ \dot{p}_\uparrow \\ \dot{p}_\downarrow \end{pmatrix} = \begin{pmatrix} -R_{00} & R_{0\uparrow} & R_{0\downarrow} \\ R_{\uparrow 0} & -R_{\uparrow\uparrow} & 0 \\ R_{\downarrow 0} & 0 & -R_{\downarrow\downarrow} \end{pmatrix} \begin{pmatrix} p_0 \\ p_\uparrow \\ p_\downarrow \end{pmatrix}. \tag{4.41}$$

The transition rates are indicated in Fig. 4.6 and defined as

$$R_{0\uparrow} = D_\uparrow \gamma^{-} - D_\uparrow^2 \vec{\gamma}^{-} \cdot \vec{F}_\uparrow(\vec{\gamma}^{-}), \tag{4.42}$$

$$R_{0\downarrow} = D_\downarrow \gamma^{-} - D_\downarrow^2 \vec{\gamma}^{-} \cdot \vec{F}_\downarrow(\vec{\gamma}^{-}), \tag{4.43}$$

$$R_{\uparrow 0} = 2D_\uparrow \gamma^{+} - 2D_\uparrow^2 \vec{\gamma}^{-} \cdot \vec{F}_\uparrow(\vec{\gamma}^{+}), \tag{4.44}$$

$$R_{\downarrow 0} = 2D_\downarrow \gamma^{+} - 2D_\downarrow^2 \vec{\gamma}^{-} \cdot \vec{F}_\downarrow(\vec{\gamma}^{+}). \tag{4.45}$$

Furthermore, the conservation of probability requires for the depopulation rates R_{ii}

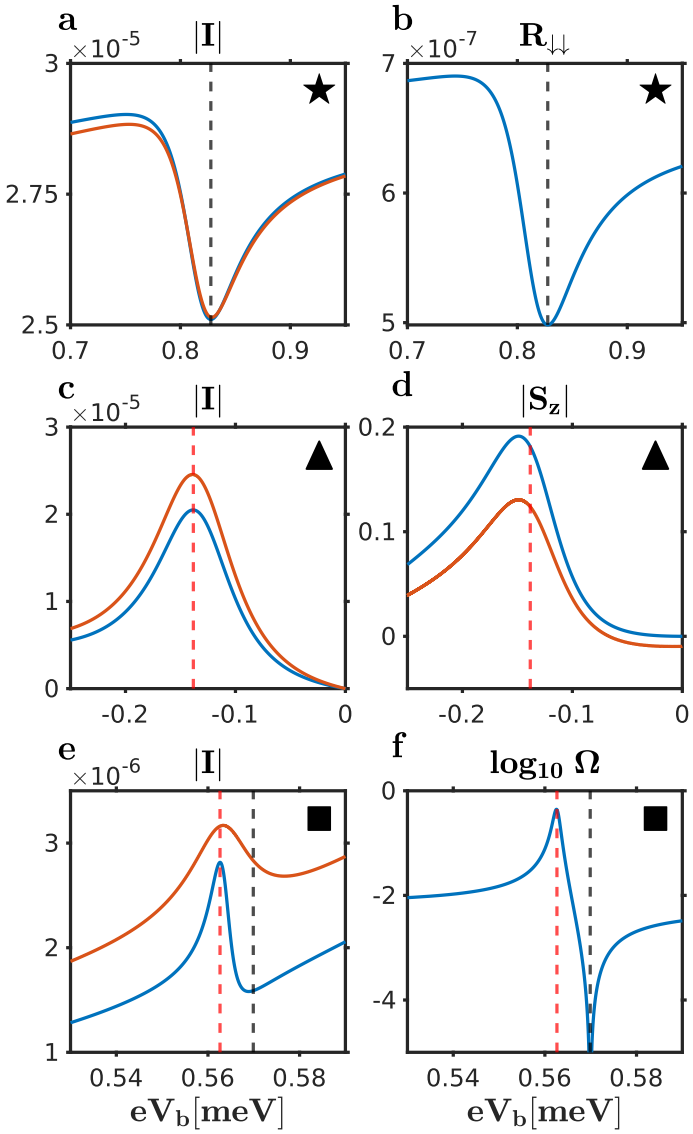

Figure 4.5: Character of pseudospin resonances: The absolute value of the current dips in **a** at $eV_g = 1.9\,\mathrm{meV}$, peaks in **c** at $eV_g = 1.8\,\mathrm{meV}$, and acquires in **e** a Fano-like shape at $eV_g = 1.58\,\mathrm{meV}$. The analytic solution of the CST-model is depicted in blue, whereas the orange line shows the full cotunneling calculations. The black (red) dashed lines indicate the position of the minimum of $B_{\sigma,\perp}$ ($B_{\sigma,\parallel}$) and correspond to a minimum (maximum) of $|I|$. The rate $R_{\downarrow\downarrow}$ (**b**) and $|S_z|$ (**d**) correlate to the current. **f** The logarithm of the ratio $\Omega = B_{\downarrow,\perp}^2/(a_\downarrow^2 + B_{\downarrow,\parallel}^2)$ highlights the two extrema of Ω that result in a peak and a dip in $|I|$. The bias traces are indicated in Fig. 4.4 **d**.

with $i = 0, \uparrow, \downarrow$:

$$R_{00} = R_{\uparrow 0} + R_{\downarrow 0}, \quad R_{\sigma\sigma} = R_{0\sigma}. \tag{4.46}$$

In a simple physical picture, we expect a peak in the current whenever the pseudospin precession caused by the exchange field releases the blockade induced by the pseudospin valve. A dip arises, instead, whenever this mechanism is locally suppressed. Both phenomena happen in close vicinity to the aforementioned resonance condition of Eq. (4.37). Only the analysis of the effective rates represented in Fig. 4.6 allows us, though, to distinguish them.

In the gate and bias voltages corresponding to the one-particle Coulomb diamond, the rates $R_{\sigma 0}$ are much larger than the depopulation rates $R_{\sigma\sigma}$. In particular, $R_{\downarrow\downarrow}$ is the smallest rate, due to the additional small density of states of the minority spins. The current is obtained by the incoherent superposition of the minority and majority spin channels. Its modulation is thus determined, within the one-particle Coulomb diamond, by the depopulation rates $R_{\uparrow\uparrow}$ and $R_{\downarrow\downarrow}$. As confirmed by the resemblance between panels **a** and **b** in Fig. 4.5, the shape of a $\downarrow$-resonance is essentially given by the *bottleneck* rate

$$R_{\downarrow\downarrow} = D_{\downarrow}\gamma^{-}\left[1 - \frac{|\vec{\gamma}^{-}|^2}{(\gamma^{-})^2}\frac{1}{1 + \frac{B^2_{\downarrow,\perp}}{a^2_{\downarrow} + B^2_{\downarrow,\parallel}}}\right] \tag{4.47}$$

with $B^2_{\downarrow,\parallel} = (\vec{\gamma}^{-} \cdot \vec{B}_{\downarrow})^2/|\vec{\gamma}^{-}|^2$ and $B^2_{\downarrow,\perp} = |\vec{B}_{\downarrow}|^2 - B^2_{\downarrow,\parallel}$ the exchange field components parallel and perpendicular to $\vec{\gamma}^{-}$. The injected pseudospin is proportional to $\vec{\gamma}^{-}$ in the applicable regions, as can be read out from the equations of motion. In itself, $R_{\downarrow\downarrow}$ is strongly influenced by the ratio $\Omega = B^2_{\downarrow,\perp}/(a^2_{\downarrow} + B^2_{\downarrow,\parallel})$ in which the proposed physical explanation based on the precession dynamics is encoded.

In absence of a perpendicular pseudo-magnetic field component, no precession occurs and the bare pseudospin valve factor $|\vec{\gamma}^{-}|^2/(\gamma^{-})^2$ reduces the rate. The other extreme is reached when the ratio Ω peaks, therefore suppressing the pseudospin valve factor. Such phenomenon only occurs if the parallel component $B_{\downarrow,\parallel}$ is minimized since the dephasing rate $a_{\downarrow}$ is proportional to a Fermi-function, which varies only smoothly within the Coulomb diamond.

The dashed lines in Fig. 4.5 substantiate the accuracy of the precession argument in determining the position of the current extrema. The rate $R_{\uparrow\uparrow}$, obtained by replacing $\downarrow$ with $\uparrow$ in all the elements of Eq. (4.47), is used for panels **c** and **d** of Fig. 4.5. In Fig. 4.5 **e**, both the suppression and the enhancing of the current appear in close vicinity and form a Fano-like line shape. In order to emphasize the rather weak dip, we depicted in Fig. 4.5 **f** the logarithm of base 10 of the ratio Ω. The ratio Ω has two extrema

which stem from minima of the corresponding exchange field components $B_{\downarrow,\perp}$ and $B_{\downarrow,\parallel}$. Despite its superficial resemblance to a Fano resonance, the origin of this peak-dip current resonance cannot be ascribed to the interference processes typical of a Fano resonance, also seen in QD setups [105–109]. Interestingly, the ratio Ω can explain features within a resonance line, as indicated by the solid white line of Fig. 4.4 **a**. The local minimum at the current resonance can be ascribed to the line of a minimum of $B_{\downarrow,\perp}$ which leads to a less pronounced current resonance at this point. Moreover,

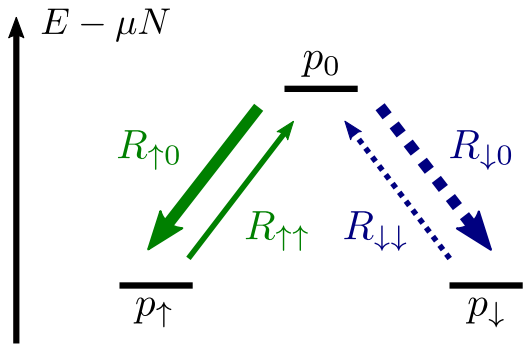

Figure 4.6: Rate scheme of the three populations $\mathbf{p_0}$, $\mathbf{p_\uparrow}$, and $\mathbf{p_\downarrow}$: The four arrows indicate the rates between the populations while their size specifies the strength of them. The dashed rates for the minority spin are further lowered by the majority spin polarization of the leads.

the relevance of Ω decreases if $a_\sigma \gg |\vec{B}_\sigma|$, i.e., when the dephasing rate exceeds the precession frequency and the direction of the exchange field becomes irrelevant for the transport. Thus, no resonances appear on the left upper corner in correspondence to the black and magenta dashed lines of panels **a-d** of Fig. 4.4 even if they would be predicted by the resonance condition Eq. (4.37).

In order to highlight the effect of the synthetic SOI, one can look at the case of constant interaction ($U = V$). In Fig. 4.7, we can observe that then only one resonance arises in the stability diagram, which is a result of the coincidence of the energy differences E_{2e1} and E_{2g1}. This fact implies that the second term of the exchange field pointing in the anisotropy direction $\vec{e}_z$ vanishes (cf. 4.31) so that the spin-resolved exchange fields become collinear. Furthermore, the resulting single resonance becomes independent of the spin polarization. Overall, the figure clearly indicates that the pseudospin anisotropy is a necessary condition for the emergence of the synthetic SOI.

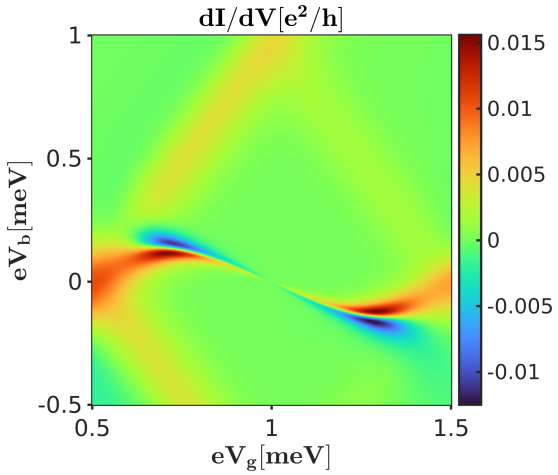

Figure 4.7: Differential conductance for $P_S = 0.99$ and constant interaction ($U = V$): The stability diagram of a DQD shows only one pseudospin resonance in comparison with Fig. 4.4 **d** where two resonances for the different spin species appear. Changing the spin polarization at constant interaction does not alter the differential conductance, in agreement with Eq. (2.22). The parameters are the following: $U = 1\,\mathrm{meV}$, $k_\mathrm{B}T = 0.05\,\mathrm{meV}$, $P_T = 0.99$, $\theta = 0.95\pi$, $\Gamma_0^\mathrm{R} = 2.5 \times 10^{-3}\,\mathrm{meV} = 2\Gamma_0^\mathrm{L}$, and $\varepsilon_0 = -1.5\,\mathrm{meV}$.

4.4 Summary

A DQD weakly coupled to ferromagnetic leads in a pseudospin valve configuration is characterized by a rich variety of pseudospin current resonances. They decorate the Coulomb diamonds with novel features which range from a peak to a dip to a Fano shape in the current. These transport characteristics reveal the synthetic SOI induced on the system by the interplay of the spin polarization of the leads and the pseudospin anisotropy on the DQD. Those current resonances mainly occur within the Coulomb diamonds. Despite their small amplitude, they are rather sharp. Differential conductance measurements thus represent a preferential tool to highlight them. We derive the tunneling rate matrices for a microscopic model capable of reproducing the desired pseudospin polarization. To this end, we also gain physical insight into the role played by the DQD geometry in the realization of a pseudospin valve. The cotunneling calculations ensure the robustness of the discussed effects also beyond the coherent-sequential-tunneling regime. Moreover, with the help of a minimal model, we give an accurate physical picture of the resonances and relate their position and character to a precession dynamics which modulates the pseudospin valve effect. The analysis of the pseudospin resonances also reveals the fundamental role played by the synthetic SOI in the understanding of the transport characteristics of our system. The

different orientations of the spin-resolved exchange fields explain the splitting of the resonances. Their qualitatively different behavior as a function of the bias is rationalized instead by the depopulation rates and, ultimately, again by the different orientation and strength of the pseudo-exchange fields.

4.5 Outlook

To our knowledge, the spin or pseudospin resonances discussed here have not yet been realized experimentally. However, we are convinced that, though very challenging, these experiments are feasible. The quest is to combine the two main prerequisites which are already individually achieved in experiments: On the one side, a valve configuration [51] and on the other side off-diagonal tunneling rate matrices, i.e., coherent tunneling [6, 110]. In our opinion, pseudospin resonances bear some advantages for a concrete realization over spin resonances. First of all, a huge variety of systems exhibit the necessary twofold degeneracy in their valley/orbital degree of freedom so that our used model is applicable. Furthermore, an easier tunability of the system parameters characterizes, in general, the pseudospin degree of freedom. The polarization of the leads, for example, is for the pseudospin a property of the interface, and as such tunable in strength and direction, together with the tunneling amplitudes. The spin polarization, however, relies on material properties, hardly tunable and, above all, difficult to integrate, for example, in semiconductor heterostructures. The necessary high pseudospin polarizations of the leads are already and rather easily accessible, as shown in an interference experiment of a suspended CNT-QD [6]. The high polarization is achieved there through local tunneling from the leads to the orbitals of the CNT. It bears the decisive advantage, that in comparison with the high spin polarization case with ferromagnetic materials, a rather good contact region is maintained which enables a clean transport measurement. In the aforementioned interference experiment [6], precursors of pseudospin precession have been demonstrated with a tunneling coupling similar to the one proposed here. Besides the high pseudospin polarization, the necessary coherent tunneling also was achieved there, with the only difference being that the opening angle of the pseudospin polarization vectors of the leads was intermediate and not almost antiparallel as we would need it for the pseudospin resonances. In general, suitable candidates for detection of these resonances are QDs realized in semiconductors [51], in CNTs [6, 43], or in molecules within a STM setup [111].

In the following, we focus on another experiment which shows resonance features which strikingly resemble the pseudospin resonances proposed here. In this experiment [112], curved resonances are cutting through the Coulomb diamonds of a sample of an ultra-

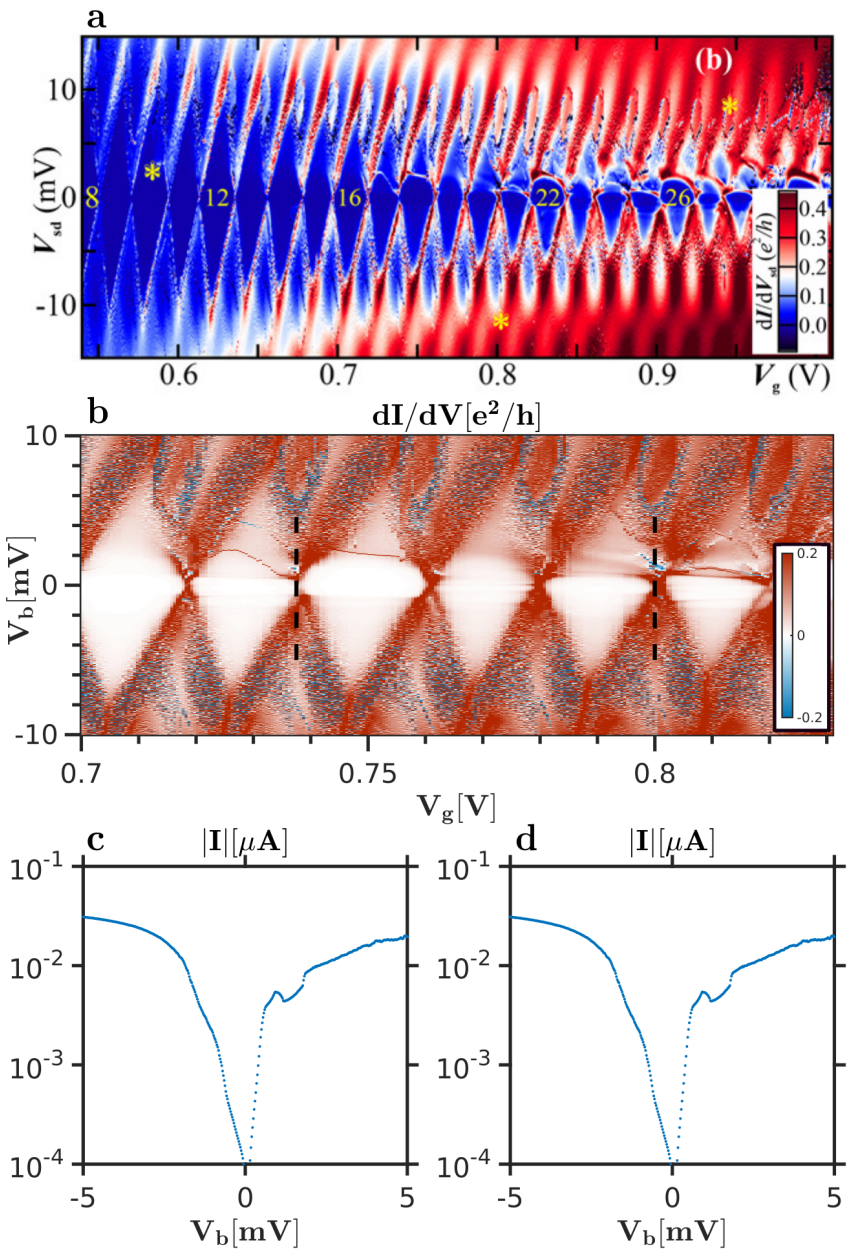

Figure 4.8: Experimental transport data of a suspended CNT shows reminiscences of pseudospin resonances: a Differential conductance map taken from [112]. **b** Zoom into the stability diagram with the leftmost Coulomb diamond corresponding to $N = 16$. **c-d** Bias cuts, indicated in the previous panel, at gate voltages of $V_g = 0.7375\,V$ and $V_g = 0.8\,V$ show dips in the current for positive bias.

clean suspended CNT. We want to thank explicitly Andreas Hüttel, an author of this publication, for a fruitful discussion and the possibility to access their raw data. In Fig. 4.8 **a**, we display their experimental data of the differential conductance of the Coulomb diamonds with the electron number ranging from $N=8$ to $N=30$. Below particle number $N=16$, they rationalize a twofold shell filling which turns to fourfold shell filling for particle numbers greater than $N=16$, according to an analysis of the charging energies extrapolated from the size of the Coulomb diamonds. However, they state that this analysis needs further verification, and they claim that the origin of this observation is due to electron-electron interaction.
Interestingly, starting from the supposed change of the filling factor to fourfold, the resonances inside the Coulomb diamonds appear. They give as possible explanations for these artifacts inelastic cotunneling and the non-equilibrium Kondo effect. However, it is remarkable that the observed features are in some cases rather tilted, which is not usually the case with inelastic cotunneling lines. There is the possibility to obtain split Kondo peaks away from the zero bias line as in [113], though this is achieved by ferromagnetic leads or an external magnetic field, which both are not present here. The fourfold pattern of the charging energies also is repeated in the resonances, with similar resonances in the $N=18$-, $N=22$- and $N=26$-diamond. Possible split resonances are observed in the $N=17$-, $N=20$- and $N=21$-diamond. In panel **b** of Fig. 4.8, we depict a zoom into the raw data of the resonances $16 \leq N \leq 21$. A current resonance would result in negative differential conductance. For a conclusive judgement, the resolution is not sufficient to clearly identify the negative differential conductance which is consistent with our theory (e.g., in the $N=17$-diamond). However, in the bias cuts of panel **c** and **d**, one can indeed see a reduction in the current for increasing the bias. As a conclusion, the presented experiment is a very promising host for the first detection of pseudospin resonances. It is clear that further verification is needed.
The realization of pseudospin resonances would put the spotlight on the internal dynamics of this widespread degree of freedom. The possibility of altering the direction of the pseudospin drastically by solely electrical means is a promising research platform. To this end, we also envisage, driven pump-probe protocols, which would unravel the dynamics induced by the synthetic SOI directly in the time domain.

5

Precession of entangled spin and pseudospin in double quantum dots

In general, QD spin valves are characterized by exchange fields which induce spin precession and generate current spin resonances even in absence of spin splitting. In the previous chapter, we showed analogous phenomena in DQDs, in which the orbital degree of freedom, the pseudospin, replaces the spin in the valve configuration. We generalize, now, this setup to allow for arbitrary spin and orbital polarization of the leads, thus obtaining an even richer variety of current resonances, stemming from the precession dynamics of the entangled spin and pseudospin. We observe for both vectors a delicate interplay of decoherence, pumping and precession which can only be understood by also considering the dynamics of the spin-pseudospin correlators. This analysis sheds light on the mechanism of spin or pseudospin resonances in general and relates its origin to a dephasing effect rather than to a precession one. The numerical results are again obtained in the framework of a generalized master equation within the cotunneling approximation and are complemented by the analytics of a coherent sequential tunneling model. The following sections are based to a large extent on our publication *Physical Review B 105, 205418 (2022)* with the same title as this chapter [71].

5.1 Setup

We consider for our setup a spinful DQD with the same Hamiltonian as in the previous chapter [cf. Eq. (2.1)]:

$$\hat{H}_{\mathrm{DQD}} = \left(\varepsilon - \frac{U}{2}\right)\hat{N} + \frac{U+V}{4}\hat{N}^2 + (U-V)\,\hat{T}_z^2. \tag{5.1}$$

The Hamiltonian is characterized by U, the local and V, the inter-dot Coulomb interaction, with the general condition $U > V$ favoring electron delocalization over the full DQD. An important property of this system is its pseudospin anisotropy, which exactly stems from this difference in the Coulomb interactions and is contained in the last term of the Hamiltonian. The coupling to the leads is captured by the tunneling rate matrix

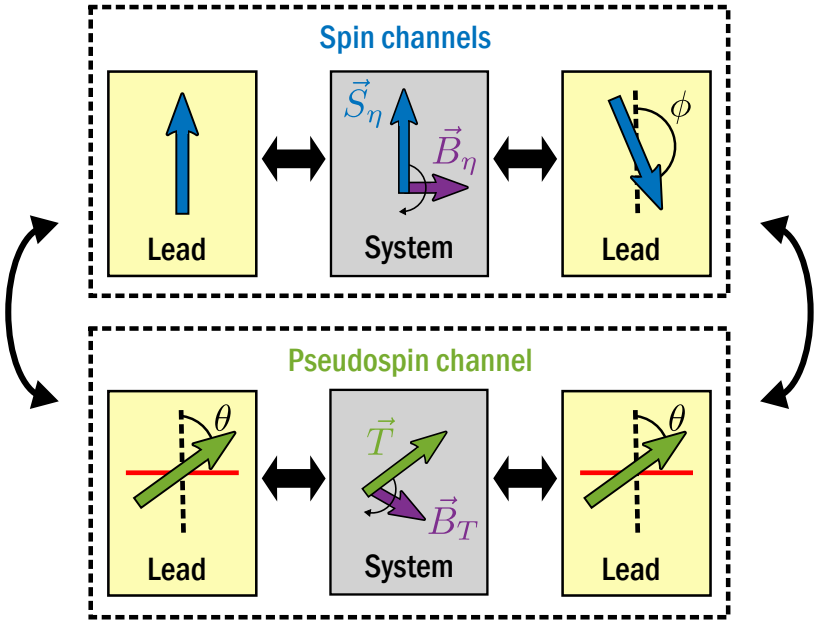

Figure 5.1: Interplay of spin and pseudospin channels determines the transport through the system: In the spin space, the polarization vectors of the leads are almost antiparallel ($\phi \approx \pi$) which translates into a spin valve configuration. Through pseudo exchange fields (purple), one can rotate the spin of the system, thus lift the current suppression of the spin valve. In the pseudospin space, we consider parallel polarization of the leads. Since there is a preferential plane in the pseudospin, indicated by the red lines, one defines the polarization direction of the leads in respect with this plane (θ). The pseudospin of the system can precess under the influence of the pseudo exchange field $\vec{B}_T$.

[cf. Eq. (2.16)] as

$$\Gamma^l = \Gamma_0^l \left(\frac{\mathbb{1}_2}{2} + \frac{P_T^l}{2} \vec{n}_T^l \cdot \vec{\sigma} \right) \otimes \left(\frac{\mathbb{1}_2}{2} + \frac{P_S^l}{2} \vec{n}_S^l \cdot \vec{\sigma} \right), \tag{5.2}$$

with the bare tunneling rate Γ_0^l, the spin/pseudospin polarization strength $P_{S/T}^l$ and direction $\vec{n}_{S/T}^l$.
In contrast to the previous chapter, we couple this time the DQD to ferromagnetic leads to obtain a spin valve configuration rather than a pseudospin valve, and on top of that, we add parallel pseudospin polarization. In essence, we mirror the configuration of the previous publication, where we have an almost antiparallel pseudospin but parallel spin polarization. One could now expect that, with the exact exchange of the role of spin and pseudospin, that one replicates the results of the previous publication. However, this is not the case since the spin degree of freedom is isotropic on the DQD while the pseudospin degree is not. As we substantiate later, this fact, alters the results drastically.
In Fig. 5.1, one of the tunneling configurations considered in this chapter is visualized. We distinguish for clarity between spin and pseudospin channels, even if, except of some limiting cases, the full system dynamics results from their interplay, as suggested by the curved arrows. The pseudospin polarization vectors of the leads are, instead, parallel to each other, though they do not coincide, in general, with the pseudospin hard axis of the DQD (indicated by dashed black line) nor do they belong to the easy plane (indicated schematically by the solid red lines). The angle θ measures the angle away from the hard pseudospin axis and is the crucial parameter, eventually tuning the entanglement between spin and pseudospin on the DQD.
Due to the spin isotropy of the DQD and its rotational invariance around its pseudospin hard axis, we can parametrize the polarization vectors with just two angles:

$$\vec{n}_S^{\mathrm{L}} = (0, 0, 1)\,, \vec{n}_S^{\mathrm{R}} = (\sin\phi, 0, \cos\phi)\,, \tag{5.3}$$

$$\vec{n}_T^{\mathrm{L/R}} = (\sin\theta, 0, \cos\theta) = \vec{n}_T. \tag{5.4}$$

Moreover, throughout this chapter we use equal spin and orbital polarization for the leads ($P_S = P_S^{\mathrm{L/R}}$; $P_T = P_T^{\mathrm{L/R}}$).

5.2 Numerical results

In Fig. 5.2, we show the current through the DQD calculated within the cotunneling limit. In particular, we set parallel pseudospin polarization with $P_T = 0.6$ and pseudospin

polarization angle with respect to the hard z-axis of $\theta = 1.5 \approx \pi/2$, as well as $P_S = 0.99$ with a relative spin polarization angle $\phi = 0.95\pi$. The current, given in logarithmic

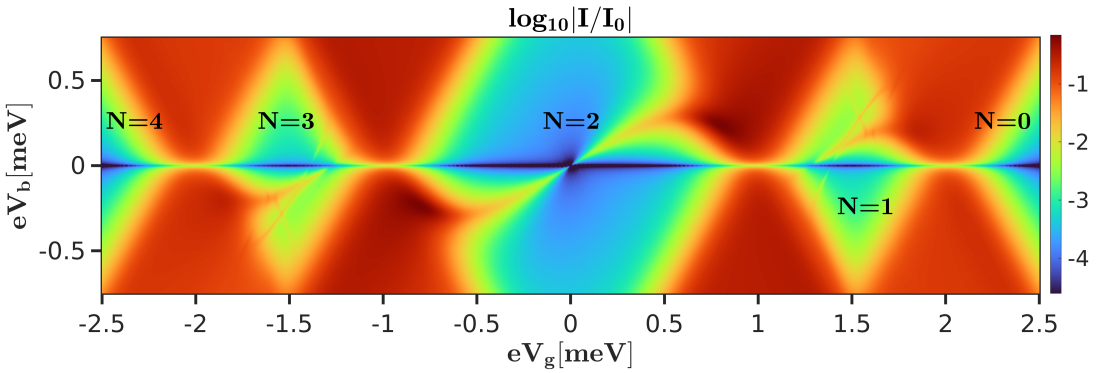

Figure 5.2: Current plot of a DQD in a V_g-V_b map shows an intricate set of current resonances: The $N = 1, 2, 3$-Coulomb diamonds are decorated with resonances which cut deep into the Coulomb blockade regions. In the central $N = 2$-diamond, a simple ground-state-to-ground-state-transition is appearing. The parameters are the following: $U = 2\,\text{meV}$, $V = 1\,\text{meV}$, $k_\text{B}T = 0.05\,\text{meV}$, $P_T = 0.6$, $P_S = 0.99$, $\theta = 1.5$, $\phi = 0.95\pi$, $\Gamma_0^\text{L} = 1 \times 10^{-2}\,\text{meV} = 2\Gamma_0^\text{R}$ and $\varepsilon_0 = -2\,\text{meV}$.

scale, is normalized to a reference value I_0 [cf. Eq. (2.26)]. The latter is the one expected for a QD spin valve in the non-linear response regime, but without pseudospin polarization [56]. Such a current normalization highlights the effects of the pseudospin on the transport characteristics since I_0 gives the scale of the underlying spin valve suppression.

The stability diagram is characterized, on the large scale, by five Coulomb diamonds where the Coulomb interaction suppresses the current, thus stabilizing a constant charge on the system. The quantized occupation of the DQD increases from 0 to 4 electrons by lowering the single-particle level, as indicated in the figure. The size U and V for, respectively, the two- and one- or three-particle Coulomb diamonds is determined by the corresponding addition energies. Besides of the electron-electron interaction, the current in the Coulomb diamonds is further suppressed, at biases larger than the temperature, by the spin valve configuration, which promotes spin accumulation on the system with an orientation antiparallel to the one of the drain lead.

A distinctive current resonance protrudes into the Coulomb blockade area of the central diamond. It is a spin resonance which lifts the additional current suppression due to the spin valve configuration. We rationalize such a resonance, in the same spirit of [17,

65], by introducing the exchange field:

$$\vec{B}_{2S} = \sum_{l} 2P_S\Gamma_0^l \left[p_l(E_{32g}) - p_l(E_{2g1})\right] \vec{n}_S^l, \tag{5.5}$$

with the principal part $p_l(x)$ defined in Eq. (2.23). The energy differences are derived from the two-particle ground-state (2g) and its neighboring states, the one-particle (1), respectively three-particle state (3). In contrast to exchange fields involving the excited energies and due to symmetry reasons, the resulting resonance is centered point symmetrically around the middle of the Coulomb diamond.
The electronic fluctuations from and to the leads, in combination with the Coulomb interaction on the system, are at the origin of this exchange field, which generates spin dephasing and spin precession on the degenerate triplet sector of the two-particle ground state (cf. Fig. 5.1). In previous works, spin precession is attributed to counteract the spin accumulation and to lift the spin valve suppression by promoting precession towards the spin states more aligned to the drain polarization. The position of the resonance can thus be predicted by the vector condition $\vec{B}_{2S} \cdot \left(\vec{n}_S^{\mathrm{L}} - \vec{n}_S^{\mathrm{R}}\right) = 0$ [analogous to Eq. (4.37)]. However, as we will detail in Sec. 5.4, in fact, the underlying mechanism is explained by spin dephasing rather than spin precession. Nevertheless, the resonance conditions are broadly unchanged by this refined explanation.

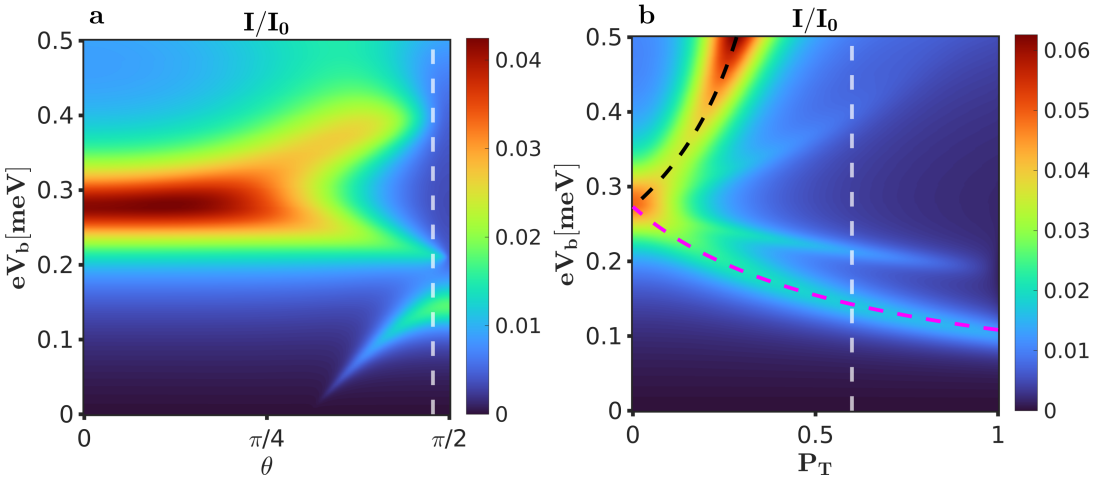

Figure 5.3: Current resonances modulated by the pseudospin polarization angle $\boldsymbol{\theta}$ and strength $\mathbf{P_T}$: **a** θ-V_b map and **b** P_T-V_b map, both at $V_\mathrm{g} = 1.5\,\mathrm{meV}$, exhibit a strong dependence on the respective parameters. The white dashed lines indicate the parameter set of Fig. 5.2. The black and magenta dashed lines are the resonance conditions for the $\vec{S}_-$ and $\vec{S}_+$ channel, which are explicitly discussed in Sec. 5.4.

Also, the one- and three-particle diamonds are decorated by current resonances. Their pattern is, though, more intricate than the one of the central Coulomb diamond and it cannot be explained solely in terms of exchange field induced spin precession. The explanation requires a more detailed analysis involving the interplay with the pseudospin degree of freedom. Due to the particle-hole symmetry of the Hamiltonian, we restrict ourselves to the one-particle diamond. Results for negative energies can be deduced by a simultaneous reflection of both the bias and the gate voltage.
The intimate relation between the current resonances of the one-particle diamond and the pseudospin degree of freedom is presented in Fig. 5.3. The current resonances are plotted here as a function of the pseudospin polarization P_T and the pseudospin polarization angle θ. Not only the position and the strength of the resonances, but even their number, depends on the control parameters. For example, the angle dependence shows a single peak for $\theta = 0$ which splits into two and even acquire a third resonance for larger angles. The mere z-polarization of the leads for $\theta = 0$ allows us to identify parallel transport channels for each of the dots and is rationalized by a spin exchange field similar to Eq. (5.5). The same procedure, though, fails to capture all the resonances for intermediate angles $0 < \theta < \pi/2$ and intermediate polarization strengths $0 < P_T < 1$. For a more complete understanding of the entire parameter range, we introduce, in the next section, a reduced model and study the dynamics of the system within the lowest order in the tunneling coupling.

5.3 Coherent sequential tunneling model

In this section, we introduce a CST-model which is capable to capture the main features of the full cotunneling numerical results. First, we present the equations of motion for our minimal model, then we investigate, starting from a current formula, the pseudospin and the spin dynamics of our system.

5.3.1 Equations of motion

We deduce the equations for the minimal model by considering only the sequential tunneling contributions to the full generalized master equation, in the same spirit as in the previous chapter [cf. Eq. (4.22)], where, though, a completely different parameter regime has been analyzed. The richest pattern of anomalous current resonances is found in the one-particle Coulomb diamond (cf. Fig. 5.2). Thus, we further restrict ourselves only to the elements of the density matrix describing the empty and the single-occupied DQD. The system exhibits a fourfold degenerate one-particle spectrum and single-particle tunneling rate matrices which cannot be diagonalized simultaneously. Thus,

in general, all the one-particle coherences should be retained for a correct description of interference effects [103]. Their dynamics is, in fact, coupled to the one of the corresponding populations, independently of the representation basis.
In summary, the non-equilibrium dynamics of the DQD weakly coupled to the source and drain leads reduces to a set of 17 coupled linear differential equations, involving the empty-state population and each of the 16 elements of the one-particle density matrix. An alternative description involves the expectation values of a complete set of operators: $p_0 = \langle \hat{P}_0 \rangle$ and $p_1 = \langle \hat{P}_1 \rangle$ are the populations of the empty and the single-occupied state, respectively, with $\hat{P}_0 = |\emptyset\rangle\langle\emptyset|$ and $\hat{P}_1 = \sum_{i\sigma} \hat{d}^\dagger_{i\sigma} \hat{P}_0 \hat{d}_{i\sigma}$ the corresponding projectors; $T_\alpha = \langle \hat{T}_\alpha \rangle$ and $S_\alpha = \langle \hat{S}_\alpha \rangle$ are the pseudospin and the spin vectors, respectively, with $\hat{T}_\alpha$ as the $\alpha = x, y, z$ component of the pseudospin operator defined in Eq. (2.2) and, analogously, $\hat{S}_\alpha = 1/2 \sum_{i\tau\tau'} \hat{d}^\dagger_{i\tau} \sigma^\alpha_{\tau\tau'} \hat{d}_{i\tau'}$. The spin-pseudospin correlator,

$$\Lambda_{\alpha\beta} = \langle \hat{T}_\alpha \hat{S}_\beta \rangle, \tag{5.6}$$

completes the set and is of decisive importance. In our considered setup, this correlator is in general not proportional to the product of the spin and pseudospin due to their intertwined dynamics: $p_1 \langle \hat{T}_\alpha \hat{S}_\beta \rangle \neq \langle \hat{T}_\alpha \rangle \langle \hat{S}_\beta \rangle$. The correlator captures therefore the mutual influence on each other of the spin and pseudospin variables. Within these 17 linearly independent variables, we replace $\vec{S}$ and Λ by the four vectors:

$$\vec{S}_\pm = \frac{\vec{S}}{2} \pm \vec{e}_T \cdot \Lambda, \quad \vec{\Lambda}_\perp = \vec{e}_\perp \cdot \Lambda, \quad \vec{\Lambda}_y = \vec{e}_y \cdot \Lambda, \tag{5.7}$$

which involve the orthogonal basis $\vec{e}_y = (0, 1, 0)$, $\vec{e}_T = \vec{n}_T$ and $\vec{e}_\perp = (\vec{e}_y \times \vec{e}_T)$. This basis adapts to the orientation of the (parallel) pseudospin polarization of the leads, and analogously it occurs to the set of variables in Eq. (5.7) chosen to describe the

system. The equation of motion for such observables read:

$$\dot{p_0} = +\gamma^- \left(p_1 + 2P_T \vec{e}_T \cdot \vec{T}\right) - 4\gamma^+ p_0 + 2D_+ \vec{\gamma}^- \cdot \vec{S}_+ + 2D_- \vec{\gamma}^- \cdot \vec{S}_-, \tag{5.8}$$

$$\dot{p_1} = -\gamma^- \left(p_1 + 2P_T \vec{e}_T \cdot \vec{T}\right) + 4\gamma^+ p_0 - 2D_+ \vec{\gamma}^- \cdot \vec{S}_+ - 2D_- \vec{\gamma}^- \cdot \vec{S}_-, \tag{5.9}$$

$$\begin{aligned}\dot{\vec{T}} = &-\gamma^- \vec{T} + 2\vec{\omega}_T \times \vec{T} - \left[4\vec{\omega}_- \cdot \vec{\Lambda}_y + 2\vec{\gamma}^- \cdot \vec{\Lambda}_\perp\right] \vec{e}_\perp \\ &- \left[\gamma^- \tfrac{P_T}{2} p_1 - 2\gamma^+ P_T p_0 + D_+ \vec{\gamma}^- \cdot \vec{S}_+ - D_- \vec{\gamma}^- \cdot \vec{S}_- - 4\vec{\omega}_S^{\,\mathrm{a}} \cdot \vec{\Lambda}_y\right] \vec{e}_T \\ &+ \left[4\vec{\omega}_- \cdot \vec{\Lambda}_\perp - 2\vec{\omega}_S^{\,\mathrm{a}} \cdot (\vec{S}_+ - \vec{S}_-) - 2\vec{\gamma}^- \cdot \vec{\Lambda}_y\right] \vec{e}_y,\end{aligned} \tag{5.10}$$

$$\begin{aligned}\dot{\vec{S}}_\pm = &-\gamma^- D_\pm \vec{S}_\pm + 2\left(\vec{\omega}_S \pm \vec{\omega}_-\right) \times \vec{S}_\pm + D_\pm \left[\vec{\gamma}^+ p_0 - \tfrac{\vec{\gamma}^-}{4}(p_1 \pm 2\vec{e}_T \cdot \vec{T})\right] \\ &+ 2\vec{\omega}_S^{\,\mathrm{a}} \times \vec{\Lambda}_\perp \mp 2\omega_T^{\mathrm{a}} \vec{\Lambda}_y \pm \vec{\omega}_S^{\,\mathrm{a}} (\vec{e}_y \cdot \vec{T}),\end{aligned} \tag{5.11}$$

$$\begin{aligned}\dot{\vec{\Lambda}}_\perp = &-\gamma^- \vec{\Lambda}_\perp + 2\vec{\omega}_S \times \vec{\Lambda}_\perp - 2\omega_+ \vec{\Lambda}_y - P_T \vec{\gamma}^- \times \vec{\Lambda}_y - \vec{\omega}_-(\vec{e}_y \cdot \vec{T}) \\ &- \tfrac{\vec{\gamma}^-}{2} \vec{e}_\perp \cdot \vec{T} + \vec{\omega}_S^{\,\mathrm{a}} \times (\vec{S}_+ + \vec{S}_-),\end{aligned} \tag{5.12}$$

$$\begin{aligned}\dot{\vec{\Lambda}}_y = &-\gamma^- \vec{\Lambda}_y + 2\vec{\omega}_S \times \vec{\Lambda}_y + 2\omega_+ \vec{\Lambda}_\perp + P_T \vec{\gamma}^- \times \vec{\Lambda}_\perp + \vec{\omega}_-(\vec{e}_\perp \cdot \vec{T}) \\ &- \tfrac{\vec{\gamma}^-}{2} \vec{e}_y \cdot \vec{T} - \vec{\omega}_S^{\,\mathrm{a}} (\vec{e}_T \cdot \vec{T}) + \omega_T^{\mathrm{a}} (\vec{S}_+ - \vec{S}_-),\end{aligned} \tag{5.13}$$

where several functions have been defined to express the tunneling, as well as the Lamb shift contribution of the Liouvillian. On one hand, we have introduced scalar and vector rates, respectively,

$$\gamma^\pm = \sum_l \gamma_l^\pm \quad \text{with} \quad \gamma_l^\pm = \frac{\Gamma_0^l}{4} f_l^\pm(\varepsilon), \tag{5.14}$$

and

$$\vec{\gamma}^\pm = \sum_l \vec{\gamma}_l^\pm \quad \text{with} \quad \vec{\gamma}_l^\pm = P_S \vec{n}_S^l \gamma_l^\pm, \tag{5.15}$$

in which we denote the Fermi-functions with $f_l^\pm(\varepsilon)$. Furthermore, we set $D_\pm = 1 \pm P_T$ to quantify the coupling strength to the different pseudospin sectors.
The Lamb shift contribution to the generalized master equation yields several exchange fields, which are responsible for precession dynamics for the vectorial components in Eqs. (5.8)-(5.13). To this end, we introduce the frequencies $\omega^l_{xx',yy'} = \Gamma_0^l[p_l(E_{xx'}) - p_l(E_{yy'})]/4$, which involve the difference of two digamma-functions, and fluctuations towards both the zero- and the two-particle neighboring states. In terms of those

frequencies, we define the exchange fields:

$$\vec{\omega}_T = P_T \sum_l (\omega^l_{10,2g1}\vec{n}_T + \omega^l_{2e1,2g1}\cos\theta\,\vec{e}_z), \tag{5.16}$$

$$\vec{\omega}_S = P_S \sum_l \omega^l_{10,2e1}\vec{n}^l_S, \tag{5.17}$$

$$\vec{\omega}_- = P_T P_S \sum_l (\omega^l_{10,2g1} - \omega^l_{2e1,2g1}\cos^2\theta)\vec{n}^l_S, \tag{5.18}$$

$$\vec{\omega}^{\rm a}_S = P_T P_S \sin\theta\cos\theta \sum_l \omega^l_{2e1,2g1}\vec{n}^l_S. \tag{5.19}$$

The list of auxiliary functions appearing in the model equations Eqs. (5.8)-(5.13) is complemented by the scalars

$$\omega^{\rm a}_T = P_T \sin\theta\cos\theta \sum_l \omega^l_{2e1,2g1}, \tag{5.20}$$

$$\omega_+ = P_T \sum_l (\omega^l_{10,2g1} + \omega^l_{2e1,2g1}\cos^2\theta). \tag{5.21}$$

Despite their complexity, the equations of motion display simple recurring patterns, which can guide us in the understanding of their physical implications.

The first two equations [Eqs. (5.8)-(5.9)] express the rate of change in the zero- and one-particle populations. It holds, in particular, $\dot{p}_0 = -\dot{p}_1$ as follows from the probability conservation and the neglect of populations with particle number larger than one. This assumption strongly reduces the number of equations needed to describe the DQD, but it also restricts their validity to the region of the one-particle diamond closer to the $N=0 \leftrightarrow N=1$ charge degeneracy point.

The rate of change of p_0 (and p_1) not only depends on populations, but also on the spin and pseudospin vectors, respectively $\vec{S}_\pm$ and $\vec{T}$. The latter appear within scalar products with, respectively, the spin and the pseudospin polarization vectors in the leads. Indeed, like for a spin valve, electron tunneling is favored by the alignment of the spin or the pseudospin degree of freedom of the DQD with the corresponding lead polarization.

We now turn to the equation of motion for the vectorial components [Eqs. (5.10)-(5.13)], which all share the same structure and encompass three main effects: decoherence, precession and pumping. The first two effects are described by the terms involving the very same vector whose time derivative appears on the left-hand side of the equation. We collect instead under the concept of pumping all the other terms, involving populations as well as the other vectors describing the DQD.

The rate of decoherence is always proportional to γ^- as tunneling events towards the zero-particle state reduce both the spin as well as the pseudospin on the DQD. Such processes, though, are strongly suppressed within the one-particle diamond, due to Coulomb interaction. We thus expect weak decoherence. Even the correlator vectors $\vec{\Lambda}_y$ and $\vec{\Lambda}_\perp$ are subject to the same decoherence rate. Notice, moreover, the $D_\pm$-weight is modulating the rate of the spin variables $\vec{S}_\pm$, which implies a further reduction of decoherence for the spin variable $\vec{S}_-$ in presence of large pseudospin polarization.
The exchange fields characterizing the precession terms strongly vary, among the different vectorial components, both in direction and intensity. The pseudospin exchange field always points into the direction $\vec{e}_T$, i.e., the one of the parallel pseudospin polarizations of the leads. The spin exchange field results instead from a delicate balance between the almost antiparallel source and drain contributions. Thus, both the strength and the intensity of the fields $\vec{\omega}_S \pm \vec{\omega}_-$ are strongly modulated within the one-particle Coulomb diamond.
The pumping component of the (pseudo)spin dynamics is the one responsible for the (pseudo)spin accumulation on the DQD observed in the stationary limit. Naturally, such a phenomenon characterizes the spin channels, due to the spin valve configuration of the leads' polarization. The spin pumped from the source lead accumulates, in absence of spin precession, on the DQD, and it has hardly any chance to escape towards the almost antiparallel polarized drain. The terms encompassing this dynamics are the ones proportional to the populations p_0 and p_1. The pumping component contains, moreover, also terms which intertwine the spin dynamics to the one of the pseudospin and that of the correlator vectors $\vec{\Lambda}_y$ and $\vec{\Lambda}_\perp$. Analogously, thanks to the coupling to the other vectorial variables, also the pseudospin can be pumped along a generic direction, despite the parallel polarization of the leads along $\vec{e}_T$.
The effects of such an intricate system dynamics on the transport characteristics and, in particular, the crucial role played by the spin and the pseudospin degree of freedom is illustrated by the current formula:

$$\begin{aligned} I_{\text{model}} =& 4\left(\gamma_L^+ - b\gamma^+\right) - 2P_T\left(\gamma_L^- - b\gamma^-\right)\vec{n}_T \cdot \vec{T}^\infty \\ & - 2\left(\vec{\gamma}_L^- - b\vec{\gamma}^-\right)\cdot\left(D_+\vec{S}_+^\infty + D_-\vec{S}_-^\infty\right), \end{aligned} \tag{5.22}$$

in which $b = (\gamma_L^- + 4\gamma_L^+)/(\gamma^- + 4\gamma^+)$ and the superscript "∞" indicates observables calculated in the steady state limit. A comparison between the current in the one-particle Coulomb-diamond obtained in the cotunneling approximation with the one stemming from this CST-model is depicted in Fig. 5.4. Despite the strong simplifications in the model calculation, the two currents show a good qualitative agreement. In particular,

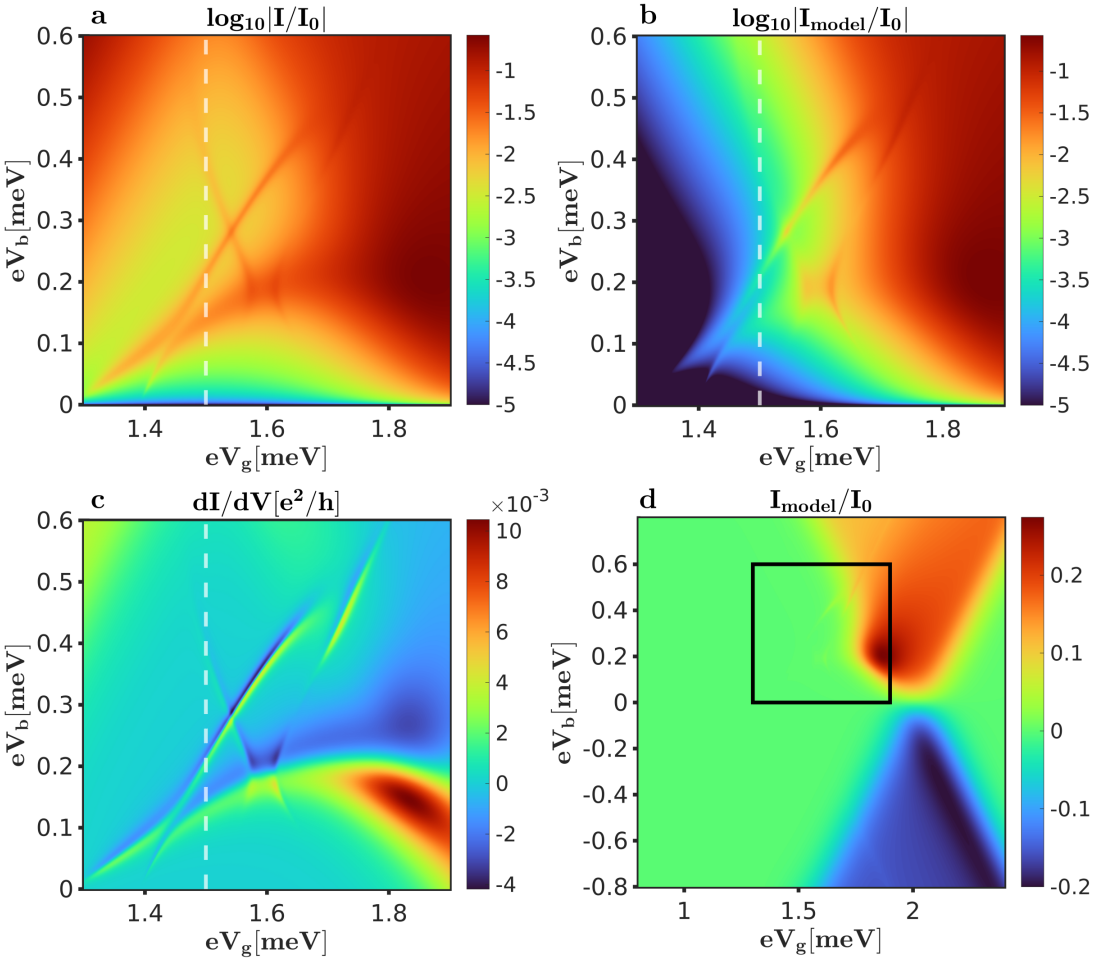

Figure 5.4: Current in the one-particle Coulomb diamond calculated with two different approaches: In panel **a** the full cotunneling calculation is presented. Panel **b** shows the corresponding result for the CST-model. Both currents are renormalized by the current I_0 expected for a spin valve in the high bias limit. The white dashed line helps for a comparison with Fig. 5.3. **c** Resonances are highlighted in differential conductance. **d** CST-model is only capable to reproduce the current around the first charge degeneracy point. The black box indicates voltage map of **b**.

the main resonance which is bending towards the point ($V_g \approx 1.3, V_b = 0$) as well as its anti-crossing near the point ($V_g \approx 1.4, V_b \approx 0.1$) are captured in the model description. Of the distinctive cross-shaped feature of the cotunneling calculation, though, only one arm is well visible in the model calculation. The other arm is buried inside the fermionic tail of the current inside a Coulomb diamond and therefore it is barely discernible. Moreover, a poorer match is expected for the side of the Coulomb diamond closer to the $N=1 \leftrightarrow N=2$ charge degeneracy point. As we neglect, for simplicity, direct tunneling

to the two-particle states, the current of the model decreases exponentially for decreasing gate voltages. This restricted area of validity of the CST-model is visualized in panel **d** of the same figure. The differential conductance of the cotunneling calculations of Fig. 5.4 **c** accentuates the resonances, as for example the one in the upper right corner cutting through the $0-1$ transition resonance of the Coulomb diamond.
The first component in Eq. (5.22) yields the current expected for $P_S = P_T = 0$. As it only contains Fermi-functions centered around the $0-1$ transition resonance, this contribution to the current is smooth within the one-particle Coulomb diamond. Consequently, the sharp current resonances observed in Fig. 5.4 **b** can only be ascribed to the sharp modulations of the stationary pseudospin and spin vectors appearing respectively in the second and third term of Eq. (5.22).

5.3.2 Pseudospin dynamics

In Fig. 5.5, the components of $\vec{T}$ in the basis of $\vec{e}_y$, $\vec{e}_T$, $\vec{e}_\perp$, and its absolute value are displayed.
Distinct features in the pseudospin components are clearly correlated to the current resonances in Fig. 5.4. For most of the bias and gate voltages, $\vec{T}^\infty$ points along the $\vec{e}_T$ direction and in the areas of (anti-)alignment of $\vec{T}$ with respect to $\vec{e}_T$, the current is (lowered) raised. There are, though, also areas in which the other components of $\vec{T}$ prevail and the pseudospin contribution to the current vanishes, as can be derived from Eq. (5.22). Altogether, it is thus clear how the vectorial character of $\vec{T}$ must be considered for a thorough description of the transport phenomena. In particular, it is the intertwining of the spin and pseudospin degrees of freedom which foster the drastic deviation of the pseudospin direction of the DQD from the polarization direction of the leads, as highlighted later by analyzing limiting cases of the pseudospin polarization angle θ. In Fig. 5.5 **d**, we indicate with the black dashed line a resonance condition which is established in the same spirit as in the first publication (cf. Cha. 4) or the original publication of spin resonances [65]. However, the way to obtain this resonance is rather lengthy and not sufficiently accurate. Hence, we intentionally refrained to include it into publication [71]. However, we are convinced that they help to understand better the whole mechanism of spin or pseudospin resonances, especially when knowing about their limitations. For this reason, we include it here in Sec. 5.5. Furthermore, it highlights the distinction of these intriguing and intertwined resonances to the standard ones.

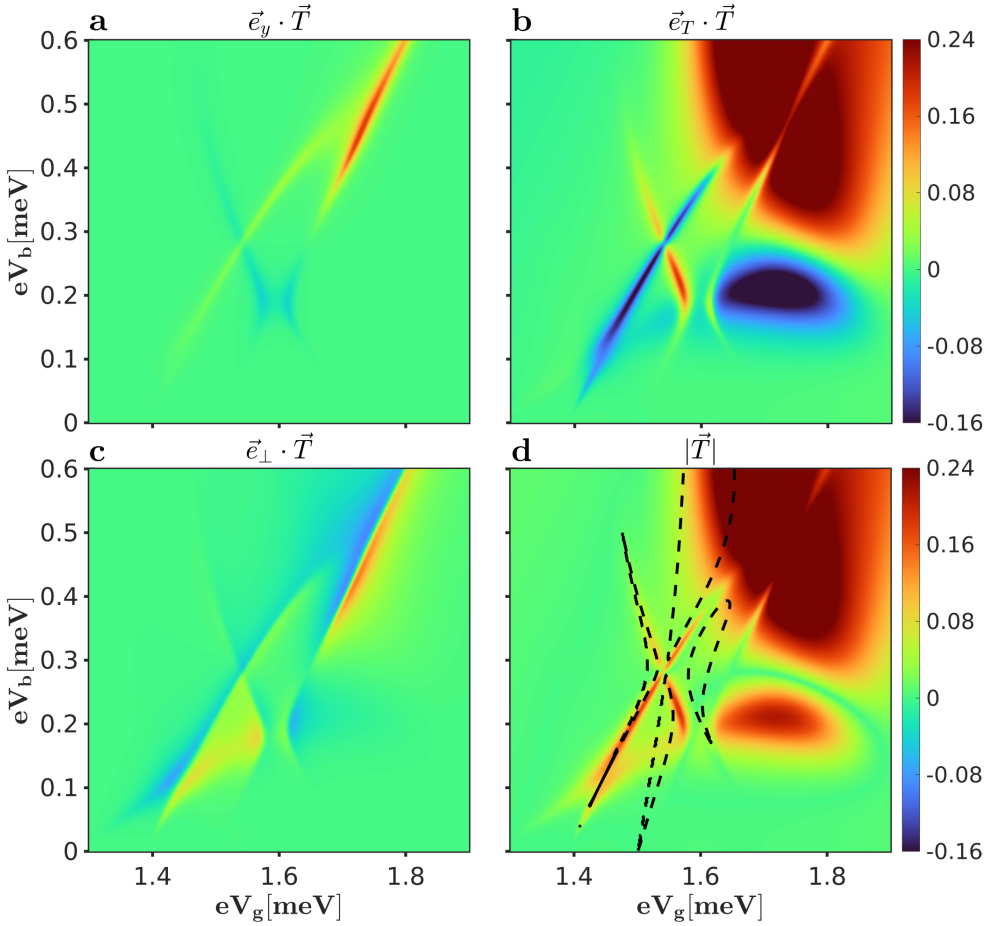

Figure 5.5: Pseudospin depends strongly on gate and bias voltages: The components **a** $\vec{e}_y$, **b** $\vec{e}_T$, **c** $\vec{e}_\perp$ of $\vec{T}$ underline the vector character of the pseudospin. The (anti-)alignment of the pseudospin (decreases) increases the current flow through the DQD. Focusing on the upper right corner, one observes a clear rotation of $\vec{T}$ in the y-direction. **d** Absolute value of $\vec{T}$ with the resonance condition for black dashed line predicting the resonances only partially. Same parameters as in Fig. 5.2.

5.3.3 Spin dynamics

We now turn to the spin contribution of the current. The first qualitative understanding is obtained in the framework of the phenomenology of a QD spin valve. The last term of Eq. (5.22) substantially decreases the current due to the almost antiparallel alignment of the source and drain and the corresponding spin accumulation along the source spin polarization direction.

More specifically, we refer in Eq. (5.22) to the combinations of the spin vector $\vec{S}$ and the spin-pseudospin correlator Λ proposed in Eq. (5.7). The latter define spin observables

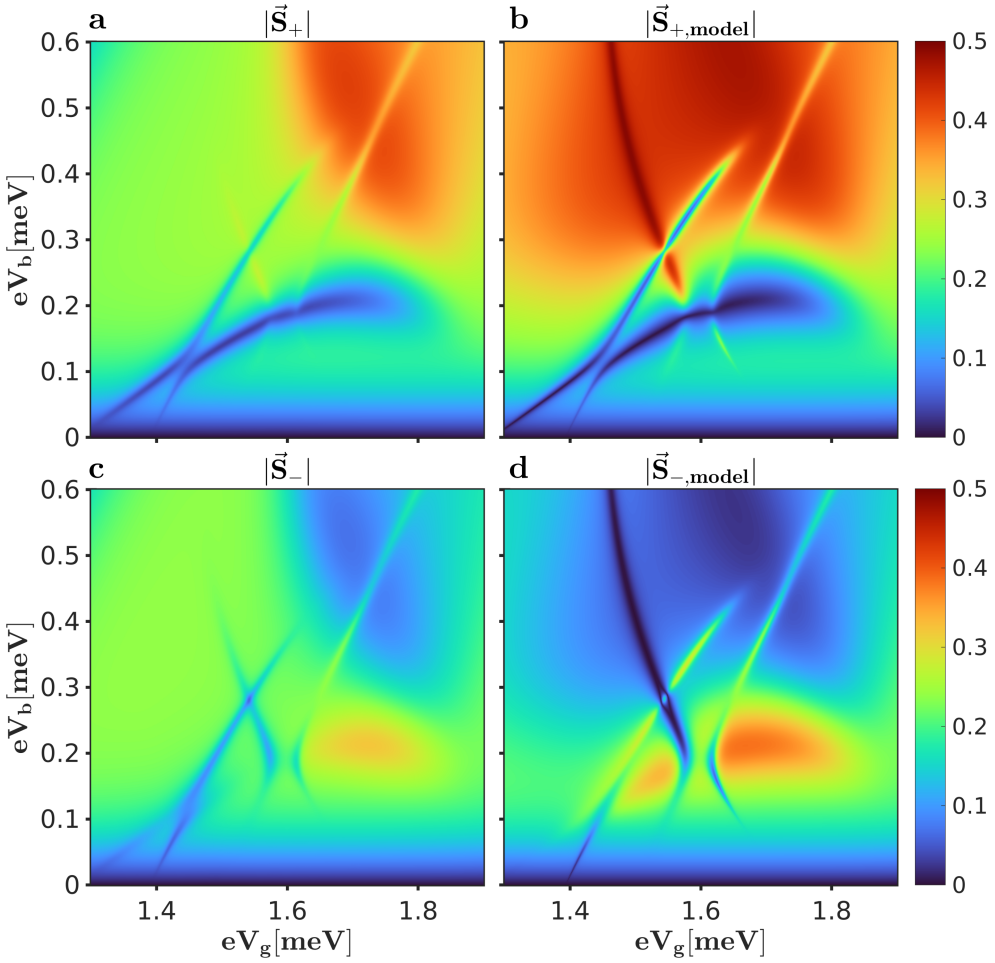

Figure 5.6: Comparison of stationary spin variables $\vec{S}_\pm$: Panel **a** and **c** are obtained from the full cotunneling calculation, while **b** and **d** refer to the reduced sequential tunneling model. Same parameters as in Fig. 5.2.

which, for specific limiting cases, identify independent spin channels. The full separation is only obtained when $\vec{n}_T$ coincides with the hard axis ($\theta = 0$) or it belongs to the easy plane ($\theta = \pi/2$) for the pseudospin of the DQD. These cases are discussed in detail in Sec. 5.4. However, insight into the spin dynamics also can be gained for the case at hand ($\theta = 1.5$) as it is demonstrated by the predicting character of the magenta and black dashes lines in Fig. 5.3 **b**.

In Fig. 5.6, we compare the modulus of the two spin variables $\vec{S}_+$ and $\vec{S}_-$ as calculated from the full cotunneling and from the CST-model. The model captures the rich texture of the stationary spins even better as compared to the current presented in Fig. 5.4. Particularly, the cross-shaped feature appears more distinctively, although for $|\vec{S}_-|$ the model predicts the wrong sign for the positive slope signal. Most interestingly, we

observe how the spin channels can be blocked or unblocked individually, as the separate regions of high, respectively, low modulus indicate. Qualitatively, we can rationalize this phenomenon as a transfer of probability between the "+" and the "−" channel occurring when one of them is unblocked due to a fast precession dynamics.
A more quantitative description is obtained, analyzing the equation of motion for $\vec{S}_\pm$. The latter can be divided into a decoherence, a pumping and a precession component:

$$\dot{\vec{S}}_\pm = \underbrace{-a_\pm \vec{S}_\pm}_{\text{decoherence}} + \underbrace{\vec{x}_\pm(p_1, \vec{T}, \vec{\Lambda}_y, \vec{\Lambda}_\perp)}_{\text{pumping}} + \underbrace{\vec{B}_\pm \times \vec{S}_\pm}_{\text{precession}}. \tag{5.23}$$

The steady state solution of this equation is given by $\vec{S}_\pm^\infty = \vec{F}(a_\pm, \vec{x}_\pm, \vec{B}_\pm)$ with

$$\vec{F}(a, \vec{x}, \vec{B}) = \frac{a}{a^2 + |\vec{B}|^2}\left(\vec{x} + \frac{\vec{B}\cdot\vec{x}}{a^2}\vec{B} + \frac{\vec{B}\times\vec{x}}{a}\right). \tag{5.24}$$

We define the input parameters as $a_\pm = D_\pm \gamma^-$ and $\vec{B}_\pm = 2\,(\vec{\omega}_S \pm \vec{\omega}_-)$. Furthermore, we use for the pumping the steady state solution of the other variables:

$$\begin{aligned}\vec{x}_\pm =& D_\pm\left[\vec{\gamma}^+(1-p_1^\infty) - \frac{\vec{\gamma}^-}{4}(p_1^\infty \pm 2\vec{e}_T\cdot\vec{T}^\infty)\right] \\ &+ 2\vec{\omega}_S^{\,a}\times\vec{\Lambda}_\perp^\infty \mp 2\omega_T^a\vec{\Lambda}_y^\infty \pm \vec{\omega}_S^{\,a}(\vec{e}_y\cdot\vec{T}^\infty).\end{aligned} \tag{5.25}$$

We do not have a closed form solution of the intricate equations of motion [Eqs. (5.8)-(5.13)]. The analysis of the semi-analytical Eq. (5.24) gives, though, relevant insights on the accumulation dynamics of the spin variables.
We distinguish among three different regimes, depending on the ratio of $|\vec{B}_\pm|/a_\pm$ which are visualized in Fig. 5.7 **a-f**. If the decoherence rate is much larger than the precession frequency ($|\vec{B}_\pm|/a_\pm \ll 1$) the respective stationary spin is given by $\vec{S}_\pm \approx \vec{x}_\pm/a_\pm$, at most, corrected by the small precession contribution $\vec{B}_\pm \times \vec{x}_\pm/a_\pm^2$. Essentially, the pumping defines the accumulation direction.
The opposite regime is obtained whenever ($|\vec{B}_\pm|/a_\pm \gg 1$). In this case, the second term of Eq. (5.24) dominates and results in dephasing, with all components suppressed except for the ones pointing in the direction of the exchange fields. In the intermediate regime ($|\vec{B}_\pm|/a_\pm \approx 1$), also the last term, which represents a coherent precession of the pumped spin, plays an important role. Inside the one-particle Coulomb diamond, it holds $|\vec{B}_\pm|/a_\pm \gg 1$ so that the spin is mainly determined by the absolute value of the pumping $|\vec{x}_\pm|$ and the angle $\angle(\vec{x}_\pm, \vec{B}_\pm)$ between pumping direction and exchange field (as can be seen by the dominant contributions of the middle column of Fig. 5.7).

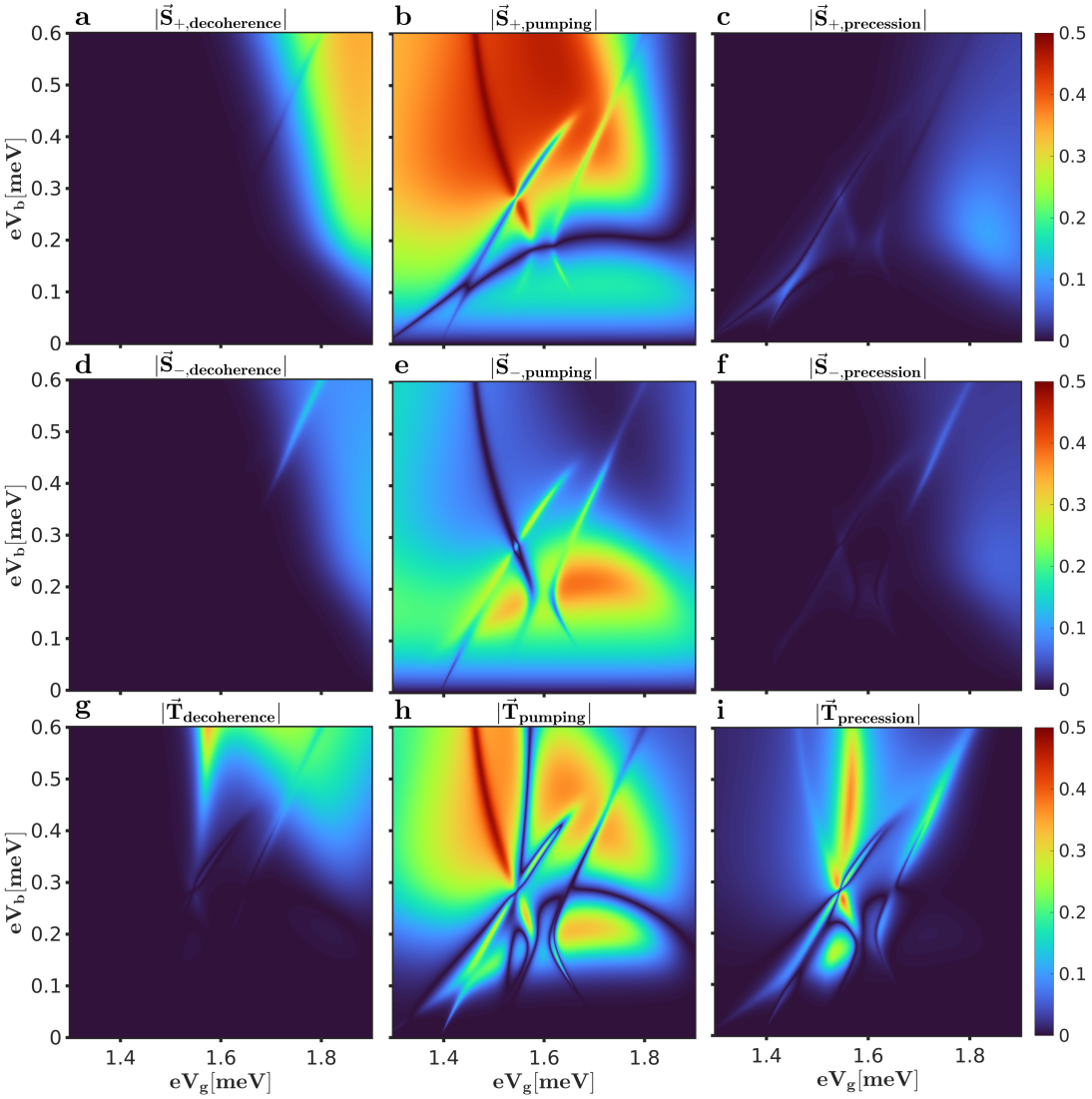

Figure 5.7: Overview of spin and pseudospin dynamics: The steady state components obtained by the auxiliary function $\vec{F}(a_\tau, \vec{x}_\tau, \vec{B}_\tau)$ [Eq. (5.24)] of the respective quantities ($\tau = \pm$ for the spins and $\tau = T$ for the pseudospin) are displayed based on the CST-equations of motion. The first column shows a relevant contribution when $|\vec{B}_\tau|/a_\tau \ll 1$, i.e., the steady state is governed predominantly by the decoherence rate. The second column is prevailing in the regime of $|\vec{B}_\tau|/a_\tau \gg 1$ where the absolute value of the pumping $|\vec{x}_\tau|$ and the angle to the corresponding exchange field $\angle(\vec{x}_\tau, \vec{B}_\tau)$ set the steady state. The last column, tied to precession, is appearing for $|\vec{B}_\tau|/a_\tau \approx 1$, which is an important contribution for the pseudospin analysis but not for the spin channels. Same parameters as in Fig. 5.2.

If the pumping occurs for a given spin variable in a direction perpendicular to the exchange field, the corresponding spin is strongly dephased and, for that channel, the spin blockade is strongly lifted. Since the same condition cannot occur simultaneously for both spin channels, the other one absorbs probability. This probability transfer corresponds to an increase of the pseudospin component along $\vec{e}_T$. However, the latter is also precessing (see Fig. 5.5) and it gives feedback on the spin pumping direction.
While the population transfer between the "+" and the "−" spin channels rationalizes the complementary behavior of the spin plots in Fig. 5.6, the interplay between the spin and the pseudospin is at the origin of the correlation between Figs. 5.5 and 5.6.
All together, the two-spin-channel description represents a good starting point for unraveling the dynamics of the DQD spin valve under consideration. A fully vectorial approach to the pseudospin, going beyond the population difference of the spin channels (the latter being represented by the $\vec{e}_T \cdot \vec{T}$ component) is though necessary for a generic orientation of the pseudospin polarization as it is shown in Fig. 5.5. The notable contribution to the pseudospin of Fig. 5.7 **i**, related to precession, highlights the vectorial character of the pseudospin. Overall, we also can conclude from Fig. 5.7 that the dynamics of the spin are predominantly governed by dephasing rather than precession due to the relative large absolute values of the exchange fields on the relevant gate and bias voltages.

5.4 Limiting cases

We consider, in this section, two limiting cases of pseudospin polarization direction: firstly, we assume with $\theta = 0$ that $\vec{e}_T$ coincides with the hard pseudospin axis; afterwards, we take $\vec{e}_T$ in the easy plane, i.e., $\theta = \pi/2$. The symmetry of the system Hamiltonian with respect to any rotation around the hard pseudospin axis ensures the equivalence of all pseudospin polarizations belonging to the easy plane. The fundamental simplification obtained for $\theta = 0$ or $\theta = \pi/2$ is the vanishing of the exchange field $\vec{\omega}_S^a$ as well as of the scalar ω_T^a. Both functions derive from the Lamb shift contribution of the Liouvillian and, in particular, they originate from the pseudospin anisotropy of the DQD. Interestingly, for both limiting angles the variables $\vec{\Lambda}_\perp$, $\vec{\Lambda}_y$, are only coupled to themselves and to the components $\vec{e}_y \cdot \vec{T}$, $\vec{e}_\perp \cdot \vec{T}$ of the pseudospin, but they are independent of p_0, p_1, $\vec{S}_+$, $\vec{S}_-$ and $\vec{e}_T \cdot \vec{T}$. If the system of Eqs. (5.8)-(5.13) admits a unique stationary solution, the latter corresponds to the trivial choice for the set of coupled variables which do not include the populations. It is in fact the probability conservation to fix the normalization of the Kernel for the Liouvillian. The relevant part of the equations of motion can be

cast with the help of $p_\pm = \frac{p_1}{2} \pm \vec{n}_T \cdot \vec{T}$ into the following equations

$$\dot{p}_\pm = 2D_\pm \left[\gamma^+ p_0 - \gamma^- p_\pm - \vec{\gamma}^- \cdot \vec{S}_\pm\right], \tag{5.26}$$

$$\dot{\vec{S}}_\pm = D_\pm \left[p_0 \vec{\gamma}^+ - \gamma^- \vec{S}_\pm - \tfrac{p_\pm}{2} \vec{\gamma}^-\right] + 2\vec{B}_\pm \times \vec{S}_\pm, \tag{5.27}$$

complemented by $\dot{p}_0 = -\dot{p}_+ - \dot{p}_-$ due to probability conservation. Further simplifications apply if $\theta = 0$, as the exchange field $\vec{B}_\pm$ reduces to $D_\pm \vec{\omega}_S$. Thus, in this limit, $D_\pm$ factorizes in the equations of the spin variables. We are left with a single spin resonance with the condition given by $\vec{\omega}_S \cdot \left(\vec{n}_S^{\mathrm{L}} - \vec{n}_S^{\mathrm{R}}\right) = 0$. Interestingly, the prefactors $D_\pm$ drop completely from the stationary solutions. They can simply be interpreted as scaling factors for the time evolution of the different channels. As such, they cannot influence the stationary state, achieved in the infinite time limit.

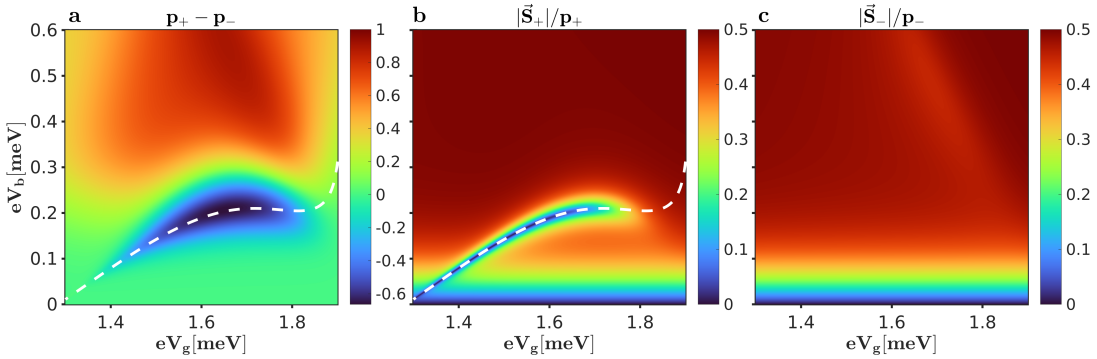

Figure 5.8: Spin dephasing as the main mechanism behind spin resonances: a The limiting case $\theta = \pi/2$ shows a splitting into the $\pm$ channels. The default situation is that the electrons occupy p_+ (red area) since the pumping is polarized in that direction. p_- is prevailing on the resonance condition for the "+" channel (white dashed line) since there the "+" electrons can leave the spin valve blockade and thus only "−" electrons remain. **b** On the resonance, the spin coherence decreases faster than the respective population. **c** Clear resonance condition for the "−" channel is outside of this V_g-V_b window, thus the coherence of this channel is maintained and yields a blockade. Parameters of Fig. 5.2 except of $\theta = \pi/2$.

In the case $\theta = \pi/2$, instead, the two spin variables are characterized by two independent resonant conditions $\vec{B}_\pm \cdot \left(\vec{n}_S^{\mathrm{L}} - \vec{n}_S^{\mathrm{R}}\right) = 0$. The splitting of the resonances as a function of the angle and pseudospin polarization strength is highlighted in Fig. 5.3.

In Fig. 5.8, we further analyze the spin dynamics underlying such resonances. The observable $p_+ - p_- := 2\vec{T} \cdot \vec{e}_T$ shows a very strong transfer of probability from the "+" towards the "−" channel in the vicinity of the $\vec{S}_+$ spin resonance (highlighted by the

white dashed line). A comparison with Fig. 5.8 **b** indicates, moreover, how the spin dephasing is at the origin of the population transfer. The fast precession opens the "+" spin channel, and the *average* spin amplitude (perpendicular to the exchange field) drops even faster than the corresponding population. Spin accumulation for the slow precessing "−" channel completes the picture. This observation contrasts, though, with the picture of coherent rotation as unblocking mechanism, as the latter would conserve the rotating spin length, or at least, the ratio between the spin and the corresponding population.
The understanding of the limiting cases allows us to infer a similar dynamics for $\theta = 1.5 \approx \pi/2$. Fig. 5.3 **b** shows how the resonances predicted for $\theta = \pi/2$ closely follow two of the actual resonances. The other two resonances of this plot can be rationalized, instead, by the semi-analytical ansatz of Eq. (5.24) as a delicate interplay of the pumping vector and the involved magnetic fields. The elements $\vec{e}_y \cdot \vec{T}$ and $\vec{e}_\perp \cdot \vec{T}$ feed into the spin channels and cause, there, an accumulation of spin components which are eventually not blocked.
Remarkably, in the areas where both unblocking conditions are simultaneously satisfied, i.e., in Fig. 5.4 around the anti-crossing of $V_g \approx 1.6$ and $V_b \approx 0.2$, a near-to-perfect lifting of the spin blockade is reached. The current closely approaches the one that would be obtained for normal leads, in the complete absence of spin valve.

5.5 Correlator-induced exchange fields

Now, we want to establish resonance conditions for the spin and pseudospin which also capture the more intriguing resonances like, e.g., the cross-shaped feature of Fig. 5.5. The derived extended exchange fields go beyond the ones which can be directly read out from the vectorial Eqs. (5.10)-(5.11). The ansatz of the resonance conditions is to solve the equations for the correlator vectors $\vec{\Lambda}_y$ and $\vec{\Lambda}_\perp$ in the stationary limit and plug the results into the equations for $\vec{T}$, $\vec{S}_+$ and $\vec{S}_-$. Here, we implicitly assume that the correlator dynamics are faster in the sense that they reside to their steady state limit at first. The last step is then to identify the effective magnetic or pseudo-magnetic fields which are able to induce precession phenomena.
The two correlator equations read initially:

$$\gamma^- \vec{\Lambda}_\perp - 2\vec{\omega}_S \times \vec{\Lambda}_\perp + 2\omega_+ \vec{\Lambda}_y + P_T \vec{\gamma}^- \times \vec{\Lambda}_y = \vec{b}_\perp, \tag{5.28}$$

$$\gamma^- \vec{\Lambda}_y - 2\vec{\omega}_S \times \vec{\Lambda}_y - 2\omega_+ \vec{\Lambda}_\perp - P_T \vec{\gamma}^- \times \vec{\Lambda}_\perp = \vec{b}_y, \tag{5.29}$$

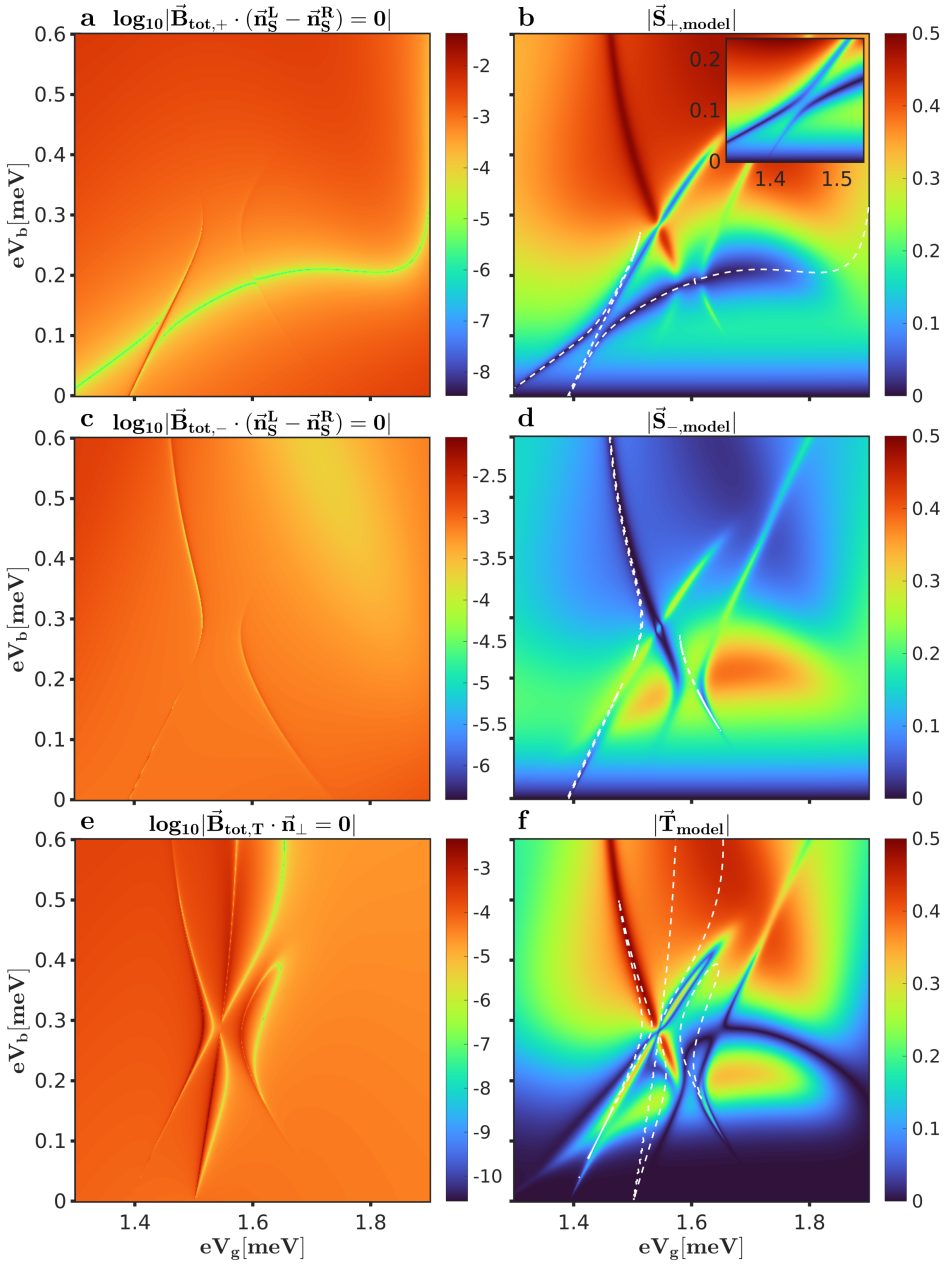

Figure 5.9: Resonance conditions for the three different channels: The left column depicts the functions of the resonance conditions where one expects resonances at their local minima. Local maxima indicate areas where resonances are locally suppressed. In the right column, we display the spin channels and the pseudospin calculated with the CST-model, where the dashed lines show the resonance conditions from the left panels. In panel **b**, the anti-crossing from the bottom left corner is highlighted. Parameters of Fig. 5.2.

where

$$\vec{b}_\perp = -\vec{\omega}_-(\vec{e}_y \cdot \vec{T}) - \tfrac{\vec{\gamma}^-}{2}\vec{e}_\perp \cdot \vec{T} + \vec{\omega}_S^{\mathrm{a}} \times (\vec{S}_+ + \vec{S}_-), \tag{5.30}$$

$$\vec{b}_y = +\vec{\omega}_-(\vec{e}_\perp \cdot \vec{T}) - \tfrac{\vec{\gamma}^-}{2}\vec{e}_y \cdot \vec{T} - \vec{\omega}_S^{\mathrm{a}}(\vec{e}_T \cdot \vec{T}) + \omega_T^{\mathrm{a}}(\vec{S}_+ - \vec{S}_-), \tag{5.31}$$

We can cast the two equations into the following matrix form:

$$\underbrace{\begin{pmatrix} \Gamma_1 & \Gamma_2 \\ -\Gamma_2 & \Gamma_1 \end{pmatrix}}_{:=\Gamma} \begin{pmatrix} \vec{\Lambda}_\perp \\ \vec{\Lambda}_y \end{pmatrix} = \begin{pmatrix} \vec{b}_\perp \\ \vec{b}_y \end{pmatrix}, \tag{5.32}$$

where

$$\Gamma_1(\vec{x}) = \gamma^- \vec{x} - 2\vec{\omega}_S \times \vec{x}, \tag{5.33}$$

$$\Gamma_2(\vec{x}) = 2\omega_+ \vec{x} + P_T \vec{\gamma}^- \times \vec{x}. \tag{5.34}$$

In the region of interest, except for a specific vertical line, where the current shows no specific feature, $\omega_+ \gg |\vec{\gamma}^-|$ holds. For this reason, we neglect the second contribution to Γ_2 which makes the further calculations much easier. The effective Γ is thus inverted by:

$$\Gamma^{-1} \approx \left(4\omega_+^2 + \Gamma_1^2\right)^{-1} \begin{pmatrix} \Gamma_1 & -2\omega_+ \\ 2\omega_+ & \Gamma_1 \end{pmatrix}. \tag{5.35}$$

Now, the task is to find an expression for $(4\omega_+^2 + \Gamma_1^2)^{-1}$. In order to achieve this, we can write equations of the structure of $4\omega_+^2 + \Gamma_1^2$ as

$$\vec{b} = A\vec{y} - B\vec{v} \times \vec{y} + (\vec{v} \cdot \vec{y})\,\vec{v}, \tag{5.36}$$

where we set for our specific equation $A = 4\omega_+^2 + (\gamma^-)^2 - 4(\vec{\omega}_S)^2$, $B = 2\gamma^-$ and $\vec{v} = 2\vec{\omega}_S$. The following equation is able to invert Eq. 5.36,

$$\vec{y} = \frac{1}{A^2 + B^2 v^2}\left[A\vec{b} + \frac{B^2 - A}{A + v^2}\left(\vec{v} \cdot \vec{b}\right)\vec{v} + B\vec{v} \times \vec{b}\right], \tag{5.37}$$

enabling us to write the final solutions for the correlators as

$$\begin{aligned}\vec{\Lambda}_\perp =& \frac{\gamma^-}{A^2+B^2v^2}\left[A\vec{b}_\perp + \frac{B^2-A}{A+v^2}\left(\vec{v}\cdot\vec{b}_\perp\right)\vec{v} + B\vec{v}\times\vec{b}_\perp\right] \\ & -\frac{1}{A^2+B^2v^2}\left[A\left(\vec{v}\times\vec{b}_\perp\right) + B\left(\vec{v}\cdot\vec{b}_\perp\right)\vec{v} - Bv^2\vec{b}_\perp\right] \\ & -\frac{2\omega_+}{A^2+B^2v^2}\left[A\vec{b}_y + \frac{B^2-A}{A+v^2}\left(\vec{v}\cdot\vec{b}_y\right)\vec{v} + B\vec{v}\times\vec{b}_y\right], \end{aligned} \tag{5.38}$$

and

$$\begin{aligned}\vec{\Lambda}_y =& \frac{\gamma^-}{A^2+B^2v^2}\left[A\vec{b}_y + \frac{B^2-A}{A+v^2}\left(\vec{v}\cdot\vec{b}_y\right)\vec{v} + B\vec{v}\times\vec{b}_y\right] \\ & -\frac{1}{A^2+B^2v^2}\left[A\left(\vec{v}\times\vec{b}_y\right) + B\left(\vec{v}\cdot\vec{b}_y\right)\vec{v} - Bv^2\vec{b}_y\right] \\ & +\frac{2\omega_+}{A^2+B^2v^2}\left[A\vec{b}_\perp + \frac{B^2-A}{A+v^2}\left(\vec{v}\cdot\vec{b}_\perp\right)\vec{v} + B\vec{v}\times\vec{b}_\perp\right]. \end{aligned} \tag{5.39}$$

Subsequently, we insert the expressions for $\vec{\Lambda}_\perp$ and $\vec{\Lambda}_y$ into the equations for $\vec{S}_+$ and $\vec{S}_-$ in order to collect all precession terms, which we define then as $\delta\vec{B}_\pm$. The total magnetic field for the $\vec{S}_\pm$-channels, denoted by $\vec{B}_{\mathrm{tot},\pm}$, consist then of two parts, the one stemming directly from Eq. (5.11) [$\vec{B}_\pm = 2\left(\vec{\omega}_S \pm \vec{\omega}_-\right)$] and one from terms in $\vec{\Lambda}_\perp$ which are proportional to $\propto \vec{S}_\pm$ as well as by terms in $\vec{\Lambda}_y$ which are proportional to $\propto \vec{X}\times\vec{S}_\pm$. The total magnetic field for the spin channels yields

$$\vec{B}_{\mathrm{tot},\pm} = \vec{B}_\pm + \delta\vec{B}_\pm, \tag{5.40}$$

with

$$\delta\vec{B}_\pm = \mp\frac{4}{A^2+B^2v^2}\left\{2A\omega_+\omega_T^{\mathrm{a}}\vec{\omega}_S^{\mathrm{a}} \pm \left(\gamma^- B - A\right)\left[\left(\vec{\omega}_S\cdot\vec{\omega}_S^{\mathrm{a}}\right)\vec{\omega}_S^{\mathrm{a}} + \left(\omega_T^{\mathrm{a}}\right)^2\vec{\omega}_S\right]\right\}. \tag{5.41}$$

For the pseudospin, we can repeat the procedure and obtain

$$\vec{B}_{\mathrm{tot},T} = \vec{B}_T + \delta\vec{B}_T, \tag{5.42}$$

with $\delta\vec{B}_T = \Omega_y\vec{e}_y + \Omega_T\vec{e}_T + \Omega_\perp\vec{e}_\perp$

$$\Omega_y = 0, \tag{5.43}$$

$$\Omega_T = \frac{-4}{A^2+B^2v^2}\left\{\vec{\gamma}^- \cdot \vec{\omega}_- \left(A\gamma^- + Bv^2\right) + \left(\vec{v}\cdot\vec{\gamma}^-\right)\left(\vec{v}\cdot\vec{\omega}_-\right)\left(\frac{B^2-A}{A+v^2}\gamma^- - B\right)\right.$$
$$\left. +2\omega_+ A\left(|\vec{\omega}_-|^2 - \frac{1}{4}|\vec{\gamma}^-|^2\right) + 2\omega_+\frac{B^2-A}{A+v^2}\left[\left(\vec{v}\cdot\vec{\omega}_-\right)^2 - \frac{1}{4}\left(\vec{v}\cdot\vec{\gamma}^-\right)^2\right]\right\}, \tag{5.44}$$

$$\Omega_\perp = \frac{2}{A^2+B^2v^2}\vec{\omega}_{TS}\cdot\left[-\left(A\gamma^- + Bv^2\right)\vec{\gamma}^- - 4\omega_+ A\vec{\omega}_-\right.$$
$$\left. -\left(\vec{v}\cdot\vec{\gamma}^-\right)\vec{v}\left(\frac{B^2-A}{A+v^2}\gamma^- - B\right) - 4\left(\vec{v}\cdot\vec{\omega}_-\right)\vec{v}\omega_+\frac{B^2-A}{A+v^2}\right]. \tag{5.45}$$

Analyzing the current formula [Eq. (5.22)], we can formulate the resonance conditions for the spin channels as

$$\vec{B}_{\mathrm{tot},\pm}\cdot\left(\vec{n}_S^{\mathrm{L}} - \vec{n}_S^{\mathrm{R}}\right) = 0, \tag{5.46}$$

and for the pseudospin as

$$\vec{B}_{\mathrm{tot},T}\cdot\vec{n}_\perp = 0. \tag{5.47}$$

In the case of the spin channels, for increased current it is beneficial to lift the spin valve by maximal dephasing which is achieved if the pumping [$\propto (\vec{n}_S^{\mathrm{L}} - \vec{n}_S^{\mathrm{R}})$] is perpendicular to the exchange field. However, for the pseudospin, which gets pumped mostly along the polarization directions of the leads ($\propto \vec{n}_T$), one expects more current for alignment of pseudospin and the parallel pseudospin polarization of the leads. For this reason, the vectorial conditions are opposite in the sense that the exchange fields should be either perpendicular (spin) or parallel (pseudospin) to the pumping. We get further insight with the analysis of these resonance conditions depicted in Fig. 5.9. In panel **a**, the condition of the main resonance of the "+" channel (cf. Fig. 5.8) gets distorted so that an anti-crossing forms, which is highlighted in the inset of panel **b**. One can rationalize the anti-crossing with the fact that locally the resonance gets suppressed where the function of **a** has a local maxima. Moreover, we can deduce that only using the resonance condition can be misleading since many local maxima have a narrow minimum in its peaks, as it is the case with the white dashed line along the anti-crossing of **b**. The condition for the "−" channel, depicted in **c** can predict two arms of cross-shaped feature. This cross-shaped feature also can be found in the condition for the pseudospin (**e**). Quite strikingly, the center of the resonance and the onset of all four arms are captured. Moreover, the prediction character of the white dashed lines of panel **f** gets refined if one excludes the local maxima, which are located around the cross since they correspond in their essence to maxima. The vertical line cutting the cross-shaped

feature is not relevant since there our model assumptions from the derivation of the exchange fields $\omega_+ \gg |\vec{\gamma}^-|$ do not hold.
Combining the insights on the resonances, we can conclude that the main knob for the current is the lifting of the spin valve setup. If one hits one resonance condition, an imbalance of two different spin channels develops, which inevitably pumps the pseudospin component in the $\vec{e}_T$-direction. If now the exchange field for the pseudospin is not aligned with the pseudospin pumping direction, the amplitude of $\vec{T}$ can diminish and eventually will have then a back action to the spin channels. The resonance, which is located in the upper right corner, is not captured by any of the conditions. If one compares with Fig. 5.5 and especially with Fig. 5.7 **i**, this coincides with a strong precession of the pseudospin and relative less pronounced dephasing term, i.e., a relative weak exchange field strength. Another hint, that this resonance is more intricate, is given in the next chapter.

5.6 Entanglement of spin and pseudospin

The interaction between the spin and the pseudospin, discussed in the previous sections and triggered by an intermediate pseudospin polarization angle, yields not only correlation but also entanglement between the two degrees of freedom. As a measure of the phenomenon, we choose the *concurrence* as a degree of quantum entanglement of a system. The definition of this quantity is outlined extensively in Sec. 5.6.
In Fig. 5.10 **a**, the concurrence of our system is displayed in dependence of bias and gate voltages. One appreciates how quantum mechanical entanglement of spin and pseudospin is only present on the resonances, which are not captured by the limiting case of the independent "+" and "−" spin channels. Consequently, the finite values of the concurrence closely correlate to the $\vec{e}_y$ and $\vec{e}_\perp$ components of $\vec{T}$ shown in Fig. 5.5 **a** and **c**. The mediator of the entanglement between the spin and pseudospin in the DQD is the synthetic SOI induced by the electronic fluctuations. In the regions with entanglement, the ansatz with the resonance condition breaks down and one has to resort into an analysis of the alignment of the pseudospin and spin vectors to make an assessment of the strength of the current.
With the concurrence, we can quantify and compare the degree of entanglement with respect to other systems or polarization configurations. In graphene, for example, entanglement between spin and sublattice pseudospin leads to the formation of states which violate the Bell inequality [114]. The latter should be detectable via Cooper pair splitting experiments. The time-varying concurrence, generated in graphene by the intrinsic SOI, ranges in their calculation between 0.5 and 0.6. Beyond its relevance for

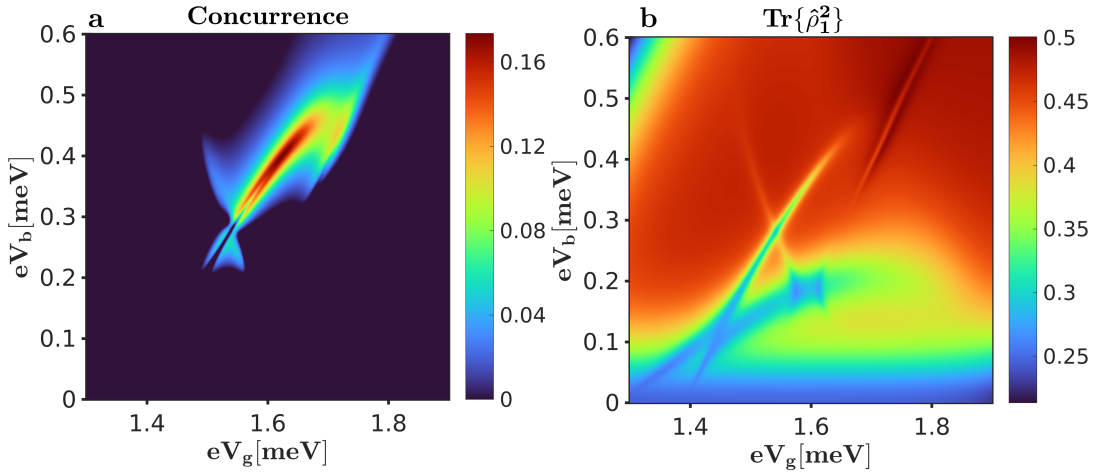

Figure 5.10: Properties of the density matrix reveal entanglement: **a** Concurrence C in dependence of gate and bias voltage. Remarkably, only in a limited area, entanglement between spin and pseudospin can be observed. These features are determined by the correlator vectors $\vec{\Lambda}_y$ and $\vec{\Lambda}_\perp$. **b** Trace over the squared one-particle density matrix highlights the areas of incoherent transport via the two spin channels. Same parameters as in Fig. 5.2.

fundamental physics, the study of entanglement [115] is crucial for the development of current quantum technologies. In this spirit, the discussed electrical manipulation of quantum entanglement represents a new interesting path for the implementation of qubit operations in DQD.

In Fig. 5.10 **b**, we highlight the "mixedness" of the density matrix in the one-particle subsector $\hat{\rho}_1$. For a pure state, one expects $\mathrm{Tr}\{\hat{\rho}_1\} = \mathrm{Tr}\{\hat{\rho}_1^2\} = 1$. In agreement to our description, we can rationalize that an incoherent superposition is the mechanism at the main resonances for the "+" and "−" channel, leading to mixed states rather than pure states. Interestingly, there seems to be only one region where there is enhanced "pureness", which coincides with the resonance of maximum pseudospin rotation.

5.7 Summary and outlook

The transport characteristics of interacting systems with a degenerate many-body spectrum are prone to exhibit interference effects [14, 56, 110, 116] already in the sequential tunneling regime. Interference appears whenever the single-particle tunneling matrices of the leads cannot be diagonalized simultaneously. In other terms, whenever it is not possible to identify parallel transport channels running between the source and the drain lead.

In this chapter, we analyzed an interacting DQD weakly coupled to ferromagnetic leads in almost antiparallel spin valve configuration. This set up naturally ensures interference between the *spin* transport channels. Moreover, we choose a tunneling coupling with parallel pseudospin polarization, which, naively, should correspond to independent pseudospin channels.
On the other hand, the tendency of the electrons to avoid each other due to the Coulomb interaction induces pseudospin anisotropy on the DQD, thus defining a pseudospin hard axis. It is the angle θ between this axis and the polarization direction of the leads to control the mixing of the pseudospin channels.
For $\theta = 0$, the stationary pseudospin is completely quenched, and the dynamics reduces to the one of a QD spin valve [65]. In the case of $\theta = \pi/2$, instead, we can identify two different spin variables, $\vec{S}_+$ and $\vec{S}_-$ associated with opposite pseudospin directions and showing independent dynamics. Thus, the pseudospin reduces itself to a single component, the one parallel to the lead polarization, which measures the imbalance $p_+ - p_-$ between the populations of the two spin channels. Finally, for any other intermediate angle, the spin and the pseudospin are correlated, with the stationary pseudospin changing strength and direction as a function of the bias and gate voltage applied to the system.
We focused on the angle $\theta = 1.5 \approx \pi/2$. Here, the signatures of the intertwined spin and pseudospin dynamics are current resonances emerging inside the one-particle Coulomb diamond. Besides the spin resonances closely related to the ones of the limiting case with $\theta = \pi/2$, we identify a cross-shaped feature which can only be understood in terms of spin-pseudospin correlations.
In general, all the observed current resonances result from the lifting of the spin blockade induced by the spin valve configuration. The exchange fields induce a fast precession of the spin variables, which results in spin dephasing. Therefore, the electrons can again tunnel towards the drain, despite its high spin polarization. In particular, the direction of the exchange fields controls the efficiency of the dephasing and thus the position of the spin resonances within the Coulomb diamond. The cross-shaped resonance, instead, stems from the interplay of spin and pseudospin and their mutual influence in their pumping dynamics, where also the correlation vectors $\vec{\Lambda}_y$ and $\vec{\Lambda}_\perp$ are involved. Ultimately, we could show that, in the vicinity of the cross-shaped resonance, spin and pseudospin are not only correlated, but also entangled. To this end, the calculation of the concurrence gives a figure of merit for the effect. A fundamental issue addressed in this study is the emergence of spin-pseudospin correlation and entanglement, despite the factorized form of the tunneling matrices. Moreover, the different nature of the current resonances observed in the one-particle Coulomb diamond shows how to address

different transport channels and stir the dynamics of different degrees of freedom of an interacting system solely by electrical means, i.e., the bias or the gate voltages across the nanojunction.

Systems with larger ($N>2$) level degeneracy exhibit a coherent dynamics involving a rapidly increasing number of degrees of freedom. Together with their fast-increasing complexity, though, they also offer more control knobs. Modulating the tunneling amplitudes between a multilevel system and the leads induces variations of the exchange fields arising from electronic fluctuation. Ultimately, the results presented here indicate, in principle, how to achieve in a single device, an all-electronic control of the precession dynamics for several entangled degrees of freedom, a very desirable feature for the current quest of scalable quantum information technology.

6

Anderson pseudospin dynamics in a quantum dot

This chapter is dedicated to the investigation of the Anderson pseudospin, a measure for superconducting correlations, of a QD which is attached to superconducting leads. Our analysis is based on a particle-conserving formalism of superconductivity, and we focus on the leading-order in the coupling to the leads while keeping a finite temperature and finite superconducting gap as well as treating the interaction exactly. In this parameter regime at zero bias, we deduce the equations of motions for the populations and the pseudospin for finite gate voltages with the help of the density matrix formalism. Other than that, we show a non-vanishing pseudospin inside the Coulomb diamond through quasiparticle processes. Furthermore, we demonstrate that our QD system is undergoing a so-called 0-π transition depending on the gate voltage or the temperature. Numerical finite bias calculations of the proximity-induced dot-pair amplitude are complementing the analysis, which shed further light on the interplay of Cooper pair processes and the ones involving quasiparticles.

6.1 Equations of motion for finite gate voltages

In Cha. 3, we introduced our model of a S-QD-S junction, where we separate the Hamiltonian into a system and a bath part,

$$\hat{H}_{\mathrm{S}} = \hat{H}_{\mathrm{QD}} + \hat{H}_{\mathrm{CP}} = \sum_{\sigma} \mathrm{e}V_{\mathrm{g}}\hat{N}_{\sigma} + U\hat{N}_{\uparrow}\hat{N}_{\downarrow} + \sum_{l\boldsymbol{k}\sigma} \mu_l \hat{N}_{\mathrm{CP},l\boldsymbol{k}\sigma}, \tag{6.1}$$

$$\hat{H}_{\mathrm{B}} = \hat{H}_{\mathrm{QP}} = \sum_{l\boldsymbol{k}\sigma} \left(E_{l\boldsymbol{k}} + \mu_l\right) \hat{N}_{\mathrm{QP},l\boldsymbol{k}\sigma}. \tag{6.2}$$

In this summarized form, the number operators for dot electrons of spin σ, for the Cooper pairs in lead l and for the quasiparticles are given by $\hat{N}_{\sigma}$, $\hat{N}_{\mathrm{CP},l\boldsymbol{k}\sigma}$ and $\hat{N}_{\mathrm{QP},l\boldsymbol{k}\sigma}$, respectively. The relevant parameters are the energy associated to the gate voltage ($\mathrm{e}V_{\mathrm{g}}$), the interaction energy (U), the quasiparticle excitation energy ($E_{l\boldsymbol{k}}$) as well as the chemical potential for the leads (μ_l) depending on the applied bias voltage (V_{b}).

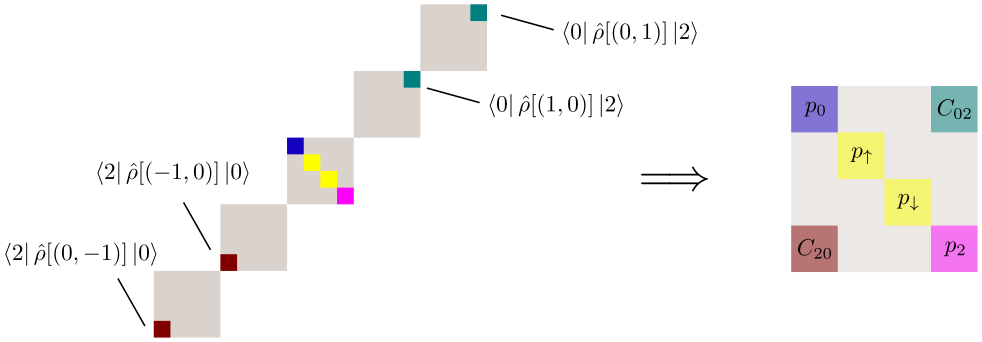

Figure 6.1: Reduction of $\hat{\rho}'$ to $\hat{\varrho}$: In a first assumption, we restrict the a priori infinite-sized $\hat{\rho}'$ to the blocks containing the four nearest neighbors of $\hat{\rho}(\mathbf{0})$ which differ by ± 1 Cooper pair imbalance. The second assumption is to condense the coherences, which are proportional to $|2\rangle\langle 0|$ and $|0\rangle\langle 2|$ in the QD space, into the off-diagonal elements of $\hat{\varrho}$ of C_{20} and C_{02}, respectively.

As the first step, we identified the imbalance of Cooper pairs in the respective leads, expressed by $\Delta\boldsymbol{M} = (\Delta M_{\mathrm{L}}, \Delta M_{\mathrm{R}})$, as the relevant quantity and not its absolute number $\boldsymbol{M} = (M_{\mathrm{L}}, M_{\mathrm{R}})$. For this reason, an effective and explicitly particle-conserving GME [Eq. (3.20)], traced out of $\boldsymbol{M}$, is well suited to describe our setup. In this set of equations, which are capable of treating non-equilibrium configurations, we focus on the leading-order Kernels. The Kernels connect blocks of different Cooper pair imbalances $\Delta\boldsymbol{M}$ to themselves and to each other. We start with restricting ourselves to the equilibrium situation ($V_{\mathrm{b}} = 0$) while addressing finite bias voltages at a later stage (cf. Sec. 6.5). At zero bias, the Cooper pair condensates of the two leads are indistinguishable since there is no energy scale which separates them, especially if we choose $\mu_l = 0$. For

this reason, as also discussed in [93], we can simplify the picture considerably with the result that the obtained supercurrent is time-independent (dc-Josephson effect). We truncate the theoretically infinitely-sized density matrix consisting of all possible Cooper pair imbalances (cf. Fig. 3.3) to only five blocks, namely the four blocks $\hat{\rho}(p\boldsymbol{u}_l)$, which have a Cooper pair imbalance of exactly $p = \pm 1$ in the l-lead, and the block $\hat{\rho}(\mathbf{0})$, which contains the populations. We will show later with a comparison to a numerical evaluation of a truncation with a larger amount of blocks that the assumption we are doing is indeed reasonable. The set of equations is thus written as

$$0 = \left[\mathcal{L}_{\mathrm{QD}} + \tilde{\mathcal{K}}_{\mathrm{red}}(\mathbf{0}, 0^+)\right] \hat{\rho}(\mathbf{0}) + \sum_{pl} \tilde{\mathcal{K}}_{\mathrm{red}}(\bar{p}\boldsymbol{u}_l, 0^+)\hat{\rho}(p\boldsymbol{u}_l), \tag{6.3}$$

$$0 = \left[\mathcal{L}_{\mathrm{QD}} + \tilde{\mathcal{K}}_{\mathrm{red}}(\mathbf{0}, 0^+)\right] \hat{\rho}(p\boldsymbol{u}_l) + \tilde{\mathcal{K}}_{\mathrm{red}}(p\boldsymbol{u}_l, 0^+)\hat{\rho}(\mathbf{0}), \tag{6.4}$$

where the λ-argument of the Kernels [Eq. (3.31) and Eq. (3.37)] simplifies due to the setting of $\mu_l = 0$.

In Fig. 6.1 on the left side, we highlight the only relevant elements of the used density matrix, which can be divided into populations and coherences. The former consist of the four diagonal elements of $\hat{\rho}(\mathbf{0})$, which are the populations of the empty state p_0, of the single-occupied state $p_{\uparrow/\downarrow}$ and the double-occupied state p_2. Due to the selection rule of conserving particle number of Eq. (3.21), $N_{\chi'} - N_\chi + 2\sum \Delta M_l = 0$ for the QD states $\chi \epsilon \{0, \uparrow, \downarrow, 2\}$, only one element does not vanish in each $\hat{\rho}(p\boldsymbol{u}_l)$-block.

In order to define the pseudospin in our system, we opt for the simplification, which is visualized on the right side of Fig. 6.1. In essence, we condense the correlations in the left superconducting lead with the ones of the right superconducting lead with $C_{20} = \langle 2| \hat{\rho}[(0,-1)] |0\rangle + \langle 2| \hat{\rho}[(-1,0)] |0\rangle$ and $C_{02} = \langle 0| \hat{\rho}[(0,1)] |2\rangle + \langle 0| \hat{\rho}[(1,0)] |2\rangle$. We argue that since in the case of zero bias the distinction between the left and right superconductor is anyway arbitrary, we are allowed to do so [93]. In essence, we keep only track if we destroy or create a Cooper pair. Since the spin symmetry is not broken by any process, we can divide the populations into an odd and an even part, and define the Anderson pseudospin:

$$\vec{P} = \begin{pmatrix} p_o \\ p_e \end{pmatrix} = \begin{pmatrix} p_0 + p_2 \\ p_\uparrow + p_\downarrow \end{pmatrix}, \qquad \vec{I} = \begin{pmatrix} I_x \\ I_y \\ I_z \end{pmatrix} = \begin{pmatrix} \mathrm{Re}C_{20} \\ \mathrm{Im}C_{20} \\ \frac{p_0 - p_2}{2} \end{pmatrix}. \tag{6.5}$$

The equations of motion for the populations yield

$$\frac{d\vec{P}}{dt} = \sum_l \Gamma_l \left[\begin{pmatrix} -G_+^- & G_+^+ \\ G_+^- & -G_+^+ \end{pmatrix} \vec{P} + \begin{pmatrix} 2 \\ -2 \end{pmatrix} \vec{I} \cdot \left(\tilde{G}_+^- \vec{n}_l - \tilde{B}_-^- \vec{n}_{\perp,l} - G_-^- \vec{e}_z \right) \right], \tag{6.6}$$

where two types of functions are involved:

$$G_\pm^\pm = -\frac{1}{\pi\hbar} \left[\mathrm{Im} \left\{ \mathcal{I}_Y^+(\pm\omega_{10}) \right\} \pm \mathrm{Im} \left\{ \mathcal{I}_Y^+(\pm\omega_{12}) \right\} \right], \tag{6.7}$$

$$B_\pm^\pm = -\frac{1}{\pi\hbar} \left[\mathrm{Re} \left\{ \mathcal{I}_Y^+(\pm\omega_{10}) \right\} \pm \mathrm{Re} \left\{ \mathcal{I}_Y^+(\pm\omega_{12}) \right\} \right]. \tag{6.8}$$

The upper index of the two auxiliary functions sets the sign in front of the energy differences ω_{xy} while the lower index represents the sum or the difference of the involved integrals. In the use of $\tilde{G}_\pm^\pm$ and $\tilde{B}_\pm^\pm$ the normal integrals [Eq. (3.27)] are replaced by the anomalous ones [Eq. (3.34)]. For simplicity, we drop the l-index from the integrals. The vectors appearing in the equations read

$$\vec{n}_l = (\cos\phi_l, \sin\phi_l, 0), \tag{6.9}$$

$$\vec{n}_{\perp,l} = (\sin\phi_l, -\cos\phi_l, 0), \tag{6.10}$$

$$\vec{e}_z = (0, 0, 1), \tag{6.11}$$

where the superconducting phases of the leads ϕ_l are the crucial parameters. As a first observation, we can conclude that the anomalous functions $\tilde{G}_\pm^\pm$ and $\tilde{B}_\pm^\pm$ are always tied to the vectors $\vec{n}_l$ and $\vec{n}_{\perp,l}$, which contain the superconducting phases. This is indeed reasonable since a transfer of a Cooper pair is always phase-dependent. Indicated already by the choice of notation, we can see $\vec{n}_l$ as the pseudospin polarization of the lead in the same spirit as in the previous two chapters, with however different physics at the origin.

The equation of the Anderson pseudospin can be cast into a form which resembles the ones studied in the previous chapters, of a (pseudo)spin governed by pumping, decoherence and precession:

$$\frac{d\vec{I}}{dt} = \vec{x}(p_e, p_o) - a\vec{I} + \vec{B} \times \vec{I} + \bar{Q}\vec{I} \tag{6.12}$$

with the pumping vector defined as

$$\vec{x}(p_e, p_o) = \sum_l \frac{\Gamma_l}{2} \left(\tilde{G}_+^- \vec{n}_l + \tilde{B}_-^- \vec{n}_{\perp,l} - G_-^- \vec{e}_z \right) p_e + \sum_l \frac{\Gamma_l}{2} \left(\tilde{G}_+^+ \vec{n}_l - \tilde{B}_-^+ \vec{n}_{\perp,l} + G_-^+ \vec{e}_z \right) p_o. \tag{6.13}$$

We observe that the I_x- and I_y-component of the pseudospin are pumped by anomalous terms, while a sole quasiparticle contribution is accumulating the I_z-component. The magnetic-field-like exchange field for the precession term reads

$$\vec{B} = \sum_l \Gamma_l \tilde{B}_+^- \vec{n}_l + - \left(\frac{2\mathrm{e}V_\mathrm{g} + U}{\hbar} + \sum_l \Gamma_l B_-^- \right) \vec{e}_z, \tag{6.14}$$

where three qualitative different processes play a role. The first is feedback of Cooper pair processes and the second one scales with $\mathrm{e}V_\mathrm{g}$ due to the energy splitting of the empty and the double-occupied state. The third part is the only one in the equations which stems from the principal part of the normal energy integral. Only around $\Gamma_l \approx |U/2 + \mathrm{e}V_\mathrm{g}|$ the exchange field changes its direction. Otherwise, the second contribution is the dominating one, with the effect that $\vec{B}$ is primarily pointing in the z-direction. However, we will show that interesting dynamics are unfolding, in contrast as anticipated in [95], also far away from the conditions where the energy difference of $|0\rangle$ and $|2\rangle$ are zero. The decoherence rate is captured by $a = \sum_l \Gamma_l G_+^-$.
In comparison to the previously discussed similar equations [cf. Eq. (4.39) and Eq. (5.23)], we also have an anisotropic damping term, expressed by the matrix $\bar{Q}$:

$$\bar{Q} = \sum_l \Gamma_l \tilde{G}_-^- \begin{pmatrix} 0 & 0 & \cos\phi_l \\ 0 & 0 & \sin\phi_l \\ \cos\phi_l & \sin\phi_l & 0 \end{pmatrix}. \tag{6.15}$$

Such an anisotropy is studied for the spin case in [70, 116]. Overall, the derived equations of motions of the Anderson pseudospin and the populations are an extension of the ones presented in [95], where the focus is on the particle-hole-symmetric point. In this limit ($\mathrm{e}V_\mathrm{g} \to -U/2$), we restore their results. In the calculations of the integrals we have, though, a slight deviation since we also include terms which are proportional to the imaginary part of $\tilde{h}_l(z)$ of Eq. (3.36) in the anomalous integrals. In our calculations, these terms contribute, however, only negligibly to the relevant quantities. The stationary

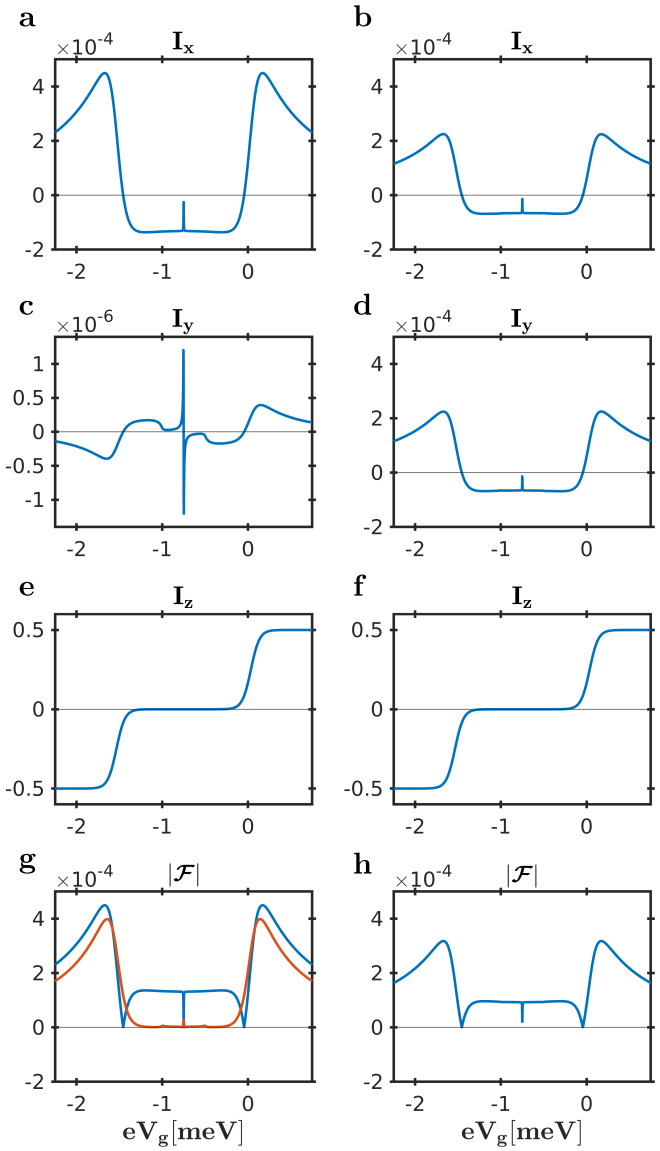

Figure 6.2: Anderson pseudospin components and dot-pair amplitudes: The columns differ by the phase of the right lead: $\phi_\mathrm{R} = 0$ and $\phi_\mathrm{R} = \pi/2$. The common parameters are $\phi_\mathrm{L} = 0$, $|\Delta_l| = 1\,\mathrm{meV}$, $\Gamma = 0.001\,\mathrm{meV}$, $k_\mathrm{B}T = 0.05\,\mathrm{meV}$, $U = 1.5\,\mathrm{meV}$, $\gamma = 0.01\,\mathrm{meV}$. The red curve is the pair amplitude without the $(-a\vec{B} \times \vec{x})$-term of Eq. (6.16).

solution of the Anderson pseudospin is given by

$$\vec{I}^{\infty} = \frac{-1}{\Lambda}\left[(\bar{Q}_{13}^2 + \bar{Q}_{23}^2 - a^2 - \bar{Q}\bar{Q} - a\bar{Q})\,\vec{x} - \left(\vec{x}\cdot\vec{B}\right)\vec{B} + \left(-a\vec{B} + \bar{Q}\vec{B}\right)\times\vec{x}\right], \quad (6.16)$$

with $\Lambda = a^3 + a\vec{B}\cdot\vec{B} - a(\bar{Q}_{13}^2 + \bar{Q}_{23}^2) - (\bar{Q}\vec{B})\cdot\vec{B}$. For the solution, we extended the auxiliary $\vec{F}$-function of Eq. (5.24) to include also the anisotropy term $\bar{Q}$.
In Fig. 6.2, we display the results of the stationary solution for two different values of the superconducting phase of the right superconductor while fixing the phase to $\phi_{\mathrm{L}} = 0$ for the left lead. We find here the steady state numerically, and consequently, as a consistency check, we plugged the populations into Eq. (6.16) to compare to the purely numerically obtained values. The first observation is that I_x and I_y are in general at least lowered by the factor of Γ with the respect to the I_z. We set Γ throughout this chapter to be equal for both leads $\Gamma \coloneqq \Gamma_{\mathrm{L}} = \Gamma_{\mathrm{R}}$ according to the definition of Eq. (3.23). The reduction results from the effect that the superconducting correlations need to be pumped by tunneling events of Cooper pairs and would die out otherwise. For the evaluation of the physical meaning of the I_x- and I_y-components, we resort to the analysis of the dot-pair amplitude and eventually to its connection with the supercurrent.

6.2 Proximity-induced dot-pair amplitude

An important quantity of the dot is the so-called pair amplitude, which we can deduce from the proximity-induced superconducting order parameter of the QD as

$$\mathcal{F} \coloneqq C_{20} = I_x + iI_y = |\mathcal{F}|e^{i\Psi}. \quad (6.17)$$

The pair amplitude is defined as $|\mathcal{F}| = \sqrt{I_x^2 + I_y^2}$ and the superconducting phase is given by $\Psi = \tan^{-1}(I_y/I_x)$. In our case, we can derive the pair amplitude from the following expression:

$$\begin{aligned}
\mathcal{F}_{\mathrm{L}} &= \langle \hat{S}_{\mathrm{L}}^{\dagger}\hat{d}_{\downarrow}\hat{d}_{\uparrow}\rangle = \mathrm{Tr}_{\mathrm{S}}\left\{\hat{S}_{\mathrm{L}}^{\dagger}\hat{d}_{\downarrow}\hat{d}_{\uparrow}\hat{\rho}\right\} \\
&= \sum_{\boldsymbol{M}\Delta\boldsymbol{M}\chi\chi'} \mathrm{Tr}_{\mathrm{S}}\left\{\hat{S}_{\mathrm{L}}^{\dagger}\hat{d}_{\downarrow}\hat{d}_{\uparrow}\rho_{\chi,\chi'}(\boldsymbol{M},\Delta\boldsymbol{M})\,|\chi,\boldsymbol{M}+\Delta\boldsymbol{M}\rangle\langle\chi',\boldsymbol{M}|\right\} \\
&= \sum_{\boldsymbol{M}\Delta\boldsymbol{M}\chi\chi'} \mathrm{Tr}_{\mathrm{S}}\left\{\rho_{\chi,\chi'}(\boldsymbol{M},\Delta\boldsymbol{M})\,|\chi-2,\boldsymbol{M}+(1,0)+\Delta\boldsymbol{M}\rangle\langle\chi',\boldsymbol{M}|\right\} \\
&= \sum_{\boldsymbol{M}} \langle 2|\,\hat{\rho}\,[(\boldsymbol{M},(-1,0)]\,|0\rangle \coloneqq \langle 2|\,\hat{\rho}\,[(-1,0)]\,|0\rangle\,. \quad (6.18)
\end{aligned}$$

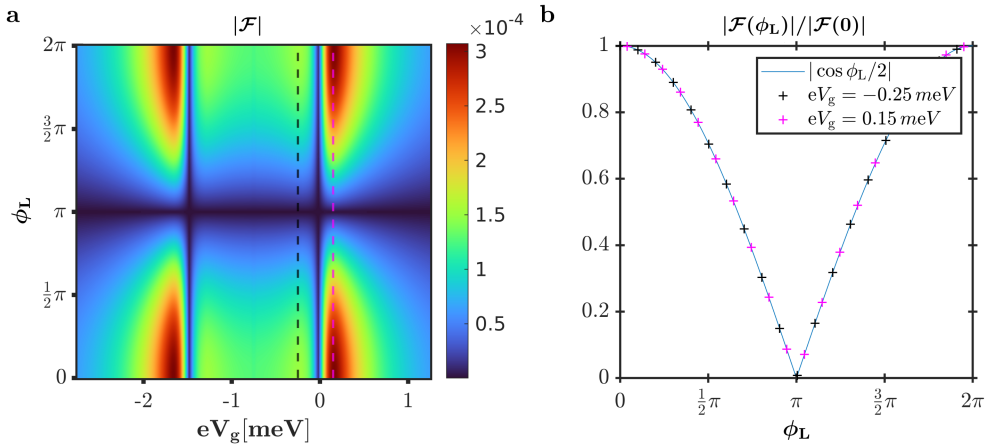

Figure 6.3: Phase dependence of the pair amplitude: a eV_g-ϕ_L map shows periodicity of $|\mathcal{F}|$. The two phase traces of **b** are indicated by the dashed black and magenta lines. The common parameters are: $U = 1.5\,\text{meV}$, $|\Delta_l| = 0.2\,\text{meV}$, $\gamma = 1\text{e-}5\,\text{meV}$, $\Gamma = 0.001\,\text{meV}$, $k_B T = 0.05\,\text{meV}$ and $\phi_R = 0$.

We use in the second line the definition of our general density matrix $\hat{\rho}$ of Eq. (3.17) and the generalized trace of Eq. (3.19) is applied in the last line. Due to our convention to combine the coherences tied to the left lead and to the right lead, we do the same for the derived expression $\mathcal{F}_L$ to obtain $\mathcal{F} = \mathcal{F}_L + \mathcal{F}_R$.

In Fig. 6.2 **g-h**, we depict the pair amplitude for two different phase configurations of the leads in dependence of the gate voltage. We can conclude that their overall shape is similar, while they differ in the absolute values. Indeed, as shown in Fig. 6.3, there is a perfect phase dependence of $|\mathcal{F}| \propto |\cos[(\phi_L - \phi_R)/2]|$. Changing the phases of the leads results in a shift of I_x towards I_y and vice versa, while letting the overall shape of the pair amplitude unchanged. Effectively, one is changing with it the phase of the order parameter of the dot. The dependence of $|\mathcal{F}|$ on the order parameter of the lead superconductor $|\Delta_l|$ is visualized in Fig. 6.4. In the limit of an infinite superconducting gap $|\Delta_l| \to \infty$, the value of the pair amplitude is vanishing inside the Coulomb diamond, as observed in Fig. 4 of [93]. It resembles then the density of states of the superconductors. However, the two quantities are different since the width of the gap in the density of states is given by $2|\Delta_l|$ and for the pair amplitude the "gap" is U (in the infinite limit of $|\Delta_l| \to \infty$). Nevertheless, the two quantities are related so that the effect of raising $|\Delta_l|$ is to push the quasiparticle excitations out of the spectrum. We can therefore deduce that the non-vanishing contribution of $|\mathcal{F}|$ inside the Coulomb diamond is influenced by quasiparticle excitations. Analyzing the steady state solution of Eq. (6.16) in depth sheds even more light on the origin of that

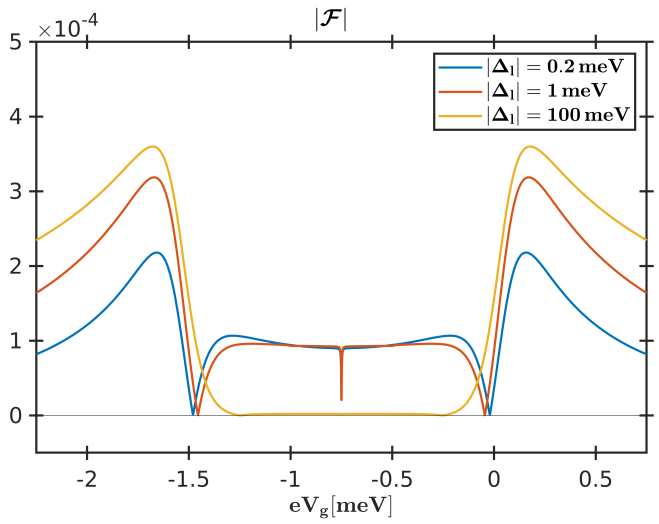

Figure 6.4: Gap dependence of the pair amplitude: Higher superconducting gaps $|\Delta_l|$ lead to a reduction of the pair amplitude inside the Coulomb diamond. The common parameters are: $U = 1.5\,\mathrm{meV}$, $\gamma = 0.01\,\mathrm{meV}$, $\Gamma = 0.001\,\mathrm{meV}$, $k_\mathrm{B}T = 0.05\,\mathrm{meV}$, $\phi_\mathrm{L} = -\pi/4$ and $\phi_\mathrm{R} = +\pi/4$.

non-vanishing contribution inside the Coulomb diamond. For $\phi_\mathrm{L} = \phi_\mathrm{R} = 0$, we find that the main contribution to I_x, and therefore eventually to $|\mathcal{F}|$, is the term $-a\vec{B} \times \vec{x}$. The effect of removing it is depicted in Fig. 6.2 **g** with the red line, where clearly the pair amplitude drops inside the Coulomb diamond. Dissecting the term $-a\vec{B} \times \vec{x}$ further, we can conclude that I_x stems from the x_y-component, due to the almost exclusive polarization of the effective magnetic field $\vec{B}$ into the z-direction. The x_y-component reads

$$\begin{aligned} x_y &\overset{\phi_L=\phi_R=0}{=} \sum_l \Gamma_l p_e \frac{-1}{2\pi\hbar}\left[\mathrm{Re}\left\{\tilde{\mathcal{I}}_Y^+(\omega_{01})\right\} - \mathrm{Re}\left\{\tilde{\mathcal{I}}_Y^-(\omega_{12})\right\}\right] \\ &\quad + \sum_l \Gamma_l p_o \frac{-1}{2\pi\hbar}\left[\mathrm{Re}\left\{\tilde{\mathcal{I}}_Y^+(\omega_{12})\right\} - \mathrm{Re}\left\{\tilde{\mathcal{I}}_Y^-(\omega_{01})\right\}\right] \\ &\overset{P_e\approx 0}{\propto} \sum_l \Gamma_l \frac{-1}{2\pi\hbar}\left[\tilde{\mathcal{S}}_l^{(2)}(\omega_{12}) - \tilde{\mathcal{S}}_l^{(2)}(\omega_{10})\right] \\ &= \sum_l \frac{\Gamma_l k_\mathrm{B}T}{\hbar} \sum_l g_{l,0} \sum_{k=0}^{\infty} \sqrt{\frac{|\Delta_l|^2}{|\Delta_l|^2+\omega_k^2}} \left(\frac{\omega_{12}}{\omega_k^2+\omega_{12}^2} - \frac{\omega_{10}}{\omega_k^2+\omega_{10}^2}\right) \end{aligned} \tag{6.19}$$

with $\omega_k = 2\pi k_\mathrm{B}T(k+1/2)$. The second term with the differences of energies changes it sign after some elements of k and vanishes for big k. The first term with the square

root is determining now how many of the k-elements of the sum have to be considered as relevant. For this reason, higher values of $|\Delta_l|$ lead to a compensation of the first relative big elements with many small elements of opposite sign, thus to a vanishing of x_y. Another interesting observation is that the x_y-component is zero exactly in the center of the Coulomb diamond, due to $\omega_{12} = \omega_{10}$, which results in a substantially lower but non-zero value of I_x (cf. Fig. 6.2).
The dependence of the pair amplitude of the dot inside the Coulomb diamond on the interaction energy U is inverse proportional. It can be rationalized insofar that a higher energy difference between the empty and double-occupied state is reducing superconducting correlations.

6.3 dc-Josephson effect

In general, one expects a supercurrent to have the form of

$$I(t) = I_0 + I_c \sin\left(\phi_0 + \Omega t\right), \tag{6.20}$$

where for non-equilibrium situations, the second term gives the time-dependent ac-Josephson effect. The time-independent current I_0 is in case of finite applied bias a normal current, while the supercurrent has the periodicity of $\Omega = 2\mathrm{e}V_\mathrm{b}/\hbar$ and is shifted by the value of ϕ_0. The term I_c denotes the critical current of the Josephson junction.
Focusing now on the case of zero applied bias, the time-independent I_0 becomes a supercurrent. This is better known as the dc-Josephson effect and has its origin in a phase difference of the two superconductors which form the Josephson junction. In order to derive the formula for the supercurrent at zero bias voltage, we employ Eq. (3.39), which is consistent with our approach of connected blocks of $\hat{\rho}(\Delta \boldsymbol{M})$. The only relevant term for our calculation is now the term $I^{(\mathbf{0})}$, which helps us to write the current for zero bias as

$$\begin{aligned} I =& \mathrm{e}\Bigg\{ \left(p_e G_-^- - p_o G_-^+\right) \frac{\Gamma_\mathrm{L} - \Gamma_\mathrm{R}}{2} \\ &+ \vec{I} \cdot \Big[-\tilde{G}_-^- \left(\Gamma_\mathrm{L} \vec{n}_\mathrm{L} - \Gamma_\mathrm{R} \vec{n}_\mathrm{R}\right) + \tilde{B}_+^- \left(\Gamma_\mathrm{L} \vec{n}_{\perp,\mathrm{L}} - \Gamma_\mathrm{R} \vec{n}_{\perp,\mathrm{R}}\right) + G_+^- \left(\Gamma_\mathrm{L} - \Gamma_\mathrm{R}\right) \vec{e}_z \Big] \Bigg\} \\ &\overset{\Gamma_\mathrm{L}=\Gamma_\mathrm{R}}{=} \mathrm{e}\Gamma_\mathrm{L} \vec{I} \cdot \Big[-\tilde{G}_-^- \left(\vec{n}_\mathrm{L} - \vec{n}_\mathrm{R}\right) + \tilde{B}_+^- \left(\vec{n}_{\perp,\mathrm{L}} - \vec{n}_{\perp,\mathrm{R}}\right) \Big]. \end{aligned} \tag{6.21}$$

At first, we have to clarify how we deduce a supercurrent while using only leading-order energy integrals. Our derived supercurrent is proportional to Γ^2 since in essence two processes, both scaling with Γ, have to happen after each other. The build-up of

superconducting correlations leads to an Anderson pseudospin component. Starting another anomalous tunneling event from such a coherence leads then to a supercurrent. For this reason, we can indeed restore the correct order of the supercurrent with however the caveat that we are *not* capturing all terms which are of Γ^2. A more rigorous inclusion of Γ^2-terms is addressed in [89]. Note that the first term of Eq. (6.21) seems to be at a first glance due to only quasiparticle energy integrals, but its supercurrent character is included by the populations which are influenced by anomalous energy integrals.
In Fig. 6.5, we depict the result of the supercurrent calculated by our formula. There is a good agreement to a non-equilibrium transport code developed by Jordi Picó-Cortés, where we take the limit of $eV_b \to 0$. The reason for comparing it with these non-equilibrium calculations is twofold. Firstly, since the latter calculations, based on the same theoretical background, also include the blocks $\hat{\rho}[(\pm 1, \mp 1)]$, $\hat{\rho}[(\pm 2, \mp 1)]$ and $\hat{\rho}[(\mp 1, \pm 2)]$, our assumption seems to be reasonable to focus only on the neighboring blocks of $\hat{\rho}(\mathbf{0})$. Secondly, our other assumption to combine coherences of the left and the right lead to formulate our Anderson pseudospin also seems plausible since the such-constructed pseudospin $\vec{I}$ leads to the main contribution of the current. The pronounced dips of negative current in Fig. 6.5 are located exactly at the energy of $|\Delta_l|$ away from the charge-degeneracy points. The depth of the minima and their "sharpness" depend on the Dynes parameter γ. We observe that a more peaked density of states, corresponding to a smaller γ, leads, at first, to a sharper feature in the current picture at these points, while it saturates then for very low γ to zero (not shown here). Importantly, for all values of γ, the sign change of the current is at a fixed point. Within our approach, we expect that at the border of the Coulomb diamonds and for small coupling, the leading-order of the supercurrent is captured.
An interesting observation is now the relation of the supercurrent to the pair amplitude of the dot. In [117], they gave for the limit $|\Delta_l| \to \infty$ the following form of the supercurrent for the lead l:

$$I_{\mathrm{sc},l} = \frac{2\mathrm{e}}{\hbar}\Gamma_l |\langle \hat{d}_\downarrow \hat{d}_\uparrow \rangle| \sin(\Psi - \phi_l). \tag{6.22}$$

For them, the term $|\langle \hat{d}_\downarrow \hat{d}_\uparrow \rangle|$ is the pair amplitude. Interestingly, it is scaling directly with the supercurrent. In the derivation of this formula based on the Meir-Wingreen formula [118], however, they do not account explicitly for Cooper pair operators as in our particle-conserving approach. For this reason, we want to study this apparent connection further.

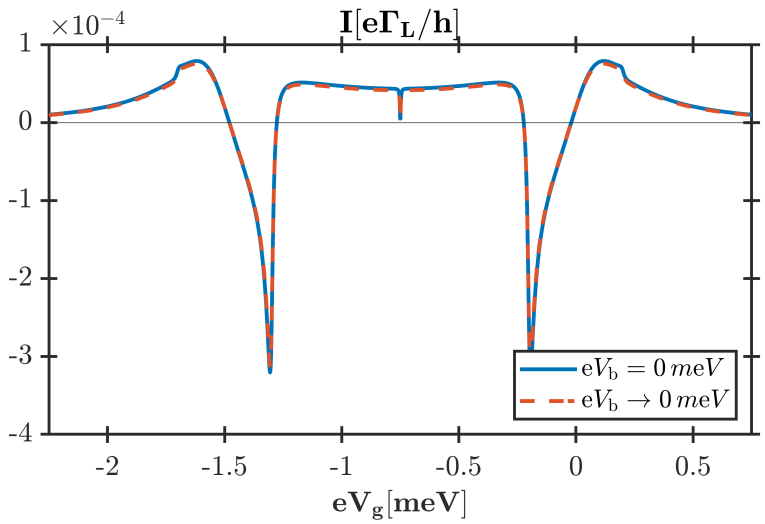

Figure 6.5: Supercurrent for zero bias: Finite bias calculations, not based on our pseudospin formulation, including a larger set of $\hat{\rho}(\Delta \boldsymbol{M})$ and in the limit to zero bias, agree with the current formula of Eq. (6.21). The used parameters are $U = 1.5\,\text{meV}$, $|\Delta_l| = 0.2\,\text{meV}$, $\gamma = 0.01\,\text{meV}$, $\Gamma = 0.001\,\text{meV}$, $k_\text{B}T = 0.05\,\text{meV}$, $\phi_\text{L} = -\pi/4$ and $\phi_\text{R} = +\pi/4$.

6.4 Gate- and temperature-dependent zero-pi transition

It is known that a superconductor can undergo a so-called 0-π transition of its ground state [119, 120]. Such a transition is usually attributed to a change in the sign of the critical current in its dependence on the superconducting phase. It corresponds in our anticipated form of the supercurrent of Eq. (6.20) to the phase shift of $\phi_0 = 0$ for the 0-state and to $\phi_0 = \pi$ for the π-state (cf. Fig. 6.6 **b**). The change of the parity in the ground states at a 0-π transition can be rationalized by a change from a screened spin regime (singlet) to a free spin regime (doublet). Generally, a 0-π transition can be realized, apart from single-occupied quantum dots [121] and ferromagnetic interlayers [122, 123], also in a SIAM setup [124]. In the later configuration, the screening of the spin of the impurity is achieved by the formation of a Yu-Shiba-Rusinov state, a hybridized singlet-state of the superconductors and the impurity. Another possibility to reach the screened spin regime is via a Kondo singlet-state [125]. Overall, the formation of a 0-π transition is governed by a delicate interplay of the relevant quantities in these systems: the tunneling coupling Γ, the Kondo temperature T_K, the interaction U and the superconducting gap $|\Delta_l|$ [126–128].

In [129], experimental evidence of such a critical current 0-π transition in Josephson QD-junctions is reported. The experimental setup of a single-wall CNT in between two

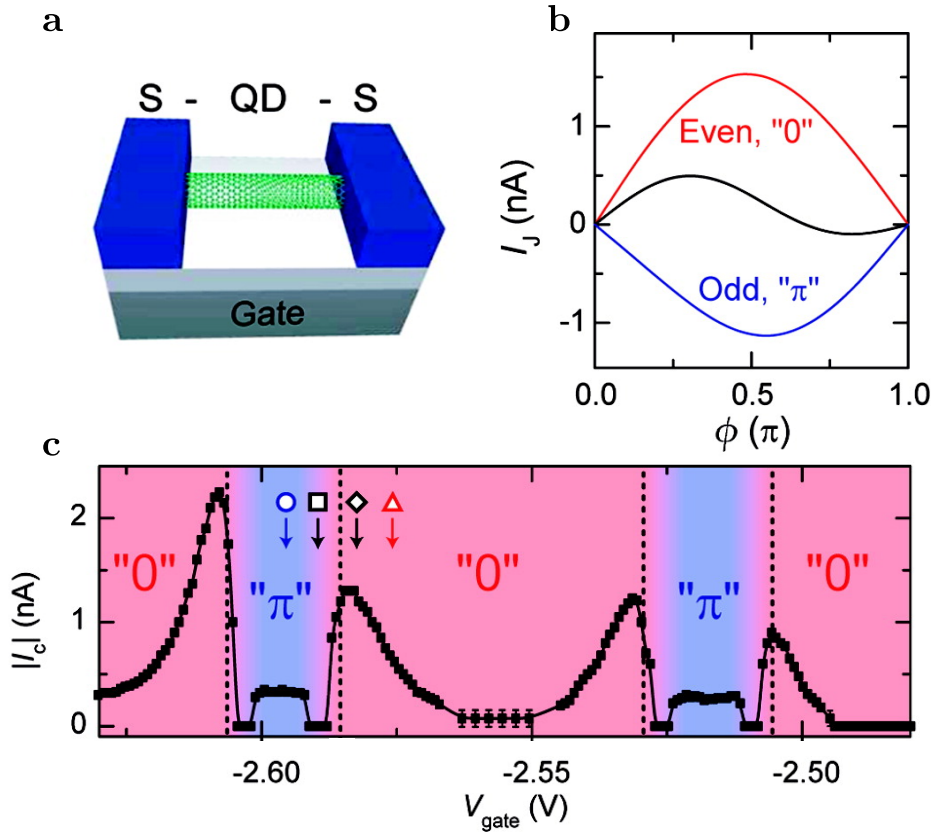

Figure 6.6: Experimental data of a 0-π transition in a CNT: **a** Sketch of the experimental setup. **b** Different sign in the Josephson current in its phase dependence for the 0-ground state (red) and the π-ground state (blue). The black curve depicts the phase dependence of a state directly at the transition marked by the empty black squares in the next panel. **c** Absolute value of the critical current shows strong modulation in dependence of the applied gate voltage. A formation of the π-state coincides with odd population of the QD. Figures taken from [129].

superconductors ($T_c = 0.75\,\mathrm{K}$ and $|\Delta_l| = 0.1\,\mathrm{meV}$) is depicted in Fig. 6.6 **a**. In panel **c**, we can observe that in this device, the critical current is strongly modulated by the applied gate voltage. The red areas are ascribed to the 0-state, while the blue ones to the π-state. The measurements are performed at a temperature of $T = 0.75$ mK and the extracted values of the device are $U = 3\,\mathrm{meV}$ as well as $\Gamma = 1.1\,\mathrm{meV}$. Due to this relatively strong coupling ($k_\mathrm{B}T = 1.93\,\mathrm{meV}$), their parameter regime is not directly comparable to our leading-order expansion. However, it is remarkable that the critical current of Fig. 6.6 **c** resembles very much our plots of the pair amplitude. In our opinion,

this is a strong hint that the pair amplitude $|\mathcal{F}|$ is indeed to a large extent proportional to the supercurrent as predicted by Eq. (6.22). Hence, the measurement of the supercurrent can be seen as a way to probe the Anderson pseudospin. Also, we can conclude that the physical relevant quantity is not the individual I_x- nor the I_y-component, changeable by the individual phases of the superconductors, but rather the pair amplitude which only depends on the relative phase of the two superconductors.
In Fig. 6.7, we depict an observed 0-π transition in dependence of the gate voltage. As a consistency check of the exact ground state, we obtained the same phase dependence as in Fig. 6.6 **b** for gate voltages above and below the transition point (not shown here). Comparable to the experimental results, the 0-π transition is occurring close to the border of the Coulomb diamonds, with a slight shift to the odd-occupied region.

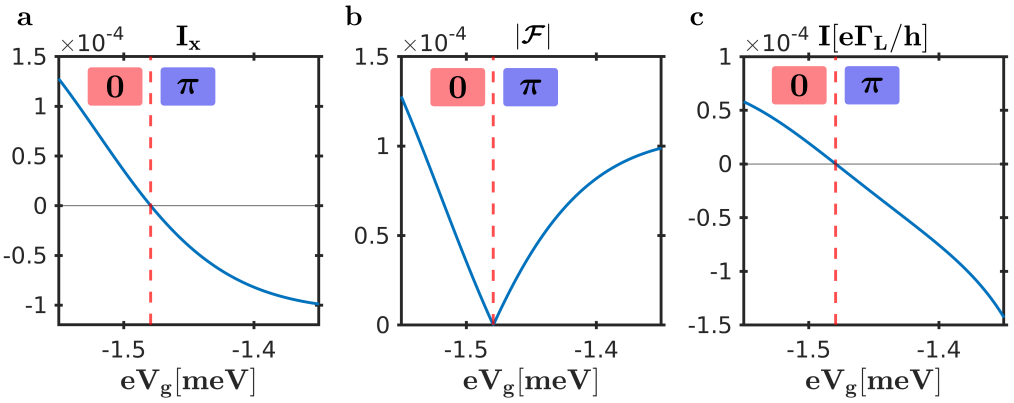

Figure 6.7: 0-π-transition observed in dependence of the gate voltage: Close to the borders of the Coulomb diamond (for reference here at $eV_g = -1.5\,\text{meV}$) the signs of the I_x-component (**a**) and of the current (**c**) reverse simultaneously. The vanishing pair amplitude (**b**) exactly at this transition completes the picture. The red dashed lines indicate the gate voltage of $eV_g = -1.48\,\text{meV}$ in all three plots. The parameters are $U = 1.5\,\text{meV}$, $\gamma = 0.01\,\text{meV}$, $|\Delta_l| = 1\,\text{meV}$, $\Gamma = 0.001\,\text{meV}$, $k_\text{B}T = 0.05\,\text{meV}$, $\phi_\text{L} = -\pi/4$ and $\phi_\text{R} = +\pi/4$.

Another 0-π transition, this time in dependence of the temperature, is depicted in Fig. 6.8. The gate voltage of $eV_g = -0.45\,\text{meV}$ is associated to a configuration inside the Coulomb diamond. Increasing the temperature towards the critical temperature leads to a breakdown of the π-state. The temperature dependence of the superconducting gap is calculated by $|\Delta_l|(T) = |\Delta_l|(0)\tanh\left(1.74\sqrt{T_\text{c}/T - 1}\right)$, where the critical temperature is connected to the gap at zero temperature as $|\Delta_l|(0) = 1.764 k_\text{B}T_\text{c}$ to a good approximation.

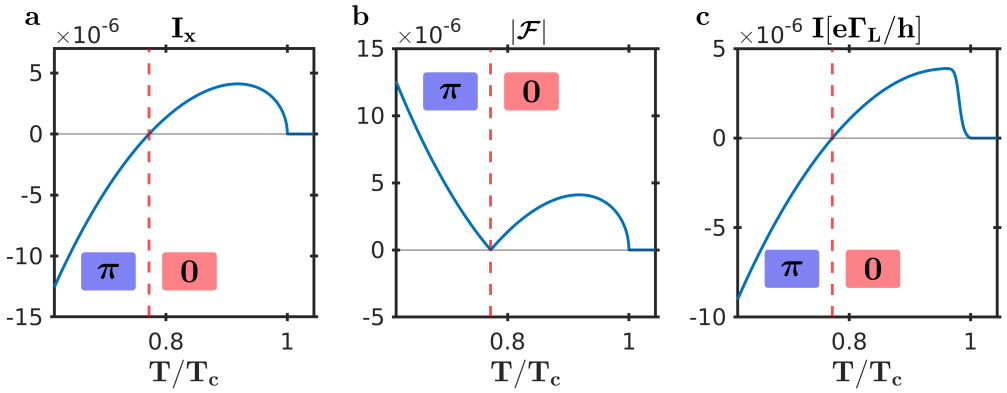

Figure 6.8: 0-π-transition observed in dependence of the temperature: The temperature is expressed as the ratio to the critical temperature T_c. There is a simultaneous sign change in the I_x-component (**a**) and in the current (**c**) accompanied by a vanishing of the pair amplitude (**b**). The red dashed lines indicate the temperature of $T/T_\mathrm{c} = 0.77$ in all three plots. The parameters are $U = 1.5\,\mathrm{meV}$, $\gamma = 0.01\,\mathrm{meV}$, $|\Delta_l| = 1\,\mathrm{meV}$ at zero temperature, $\Gamma = 0.001\,\mathrm{meV}$, $\mathrm{e}V_\mathrm{g} = -0.45\,\mathrm{meV}$, $\phi_\mathrm{L} = -\pi/4$ and $\phi_\mathrm{R} = +\pi/4$.

6.5 Non-equilibrium results

In our particle-conserving framework, we are able to treat non-equilibrium transport setups. We resort for our calculations to the transport code developed by Jordi Picó-Cortés, where, besides the central blocks of Cooper pair imbalances outlined in Fig. 6.1, also additional blocks can be included. For the definition of the pseudospin, we sum up all components proportional to $|2\rangle\langle 0|$ in the QD-space to C_{20} and proceed analogously with C_{02}. Except for zero bias, the code is most accurate for high bias voltages since there, only relatively few blocks have to be considered. More information about the limitations of the transport code for non-equilibrium calculations can be found in [89].

In Fig. 6.9 **a** and **b**, we display the time-independent component of the current $I^{(\mathbf{0})}$ [cf. Eq. (3.39)] for different values of the superconducting gaps. Note that this current component is not associated to a supercurrent, but rather to a normal current (except for the case of zero bias). The gap opening can be clearly seen in panel **a**, while in **b** the gap is comparable to the Coulomb energy U so that the Coulomb diamond is buried inside the superconducting gap. In the latter panel, exactly where the $|2\rangle$- and $|0\rangle$-state are in resonance, which is at

$$2\mathrm{e}V_\mathrm{g} + U \pm \mathrm{e}V_\mathrm{b} = 0, \tag{6.23}$$

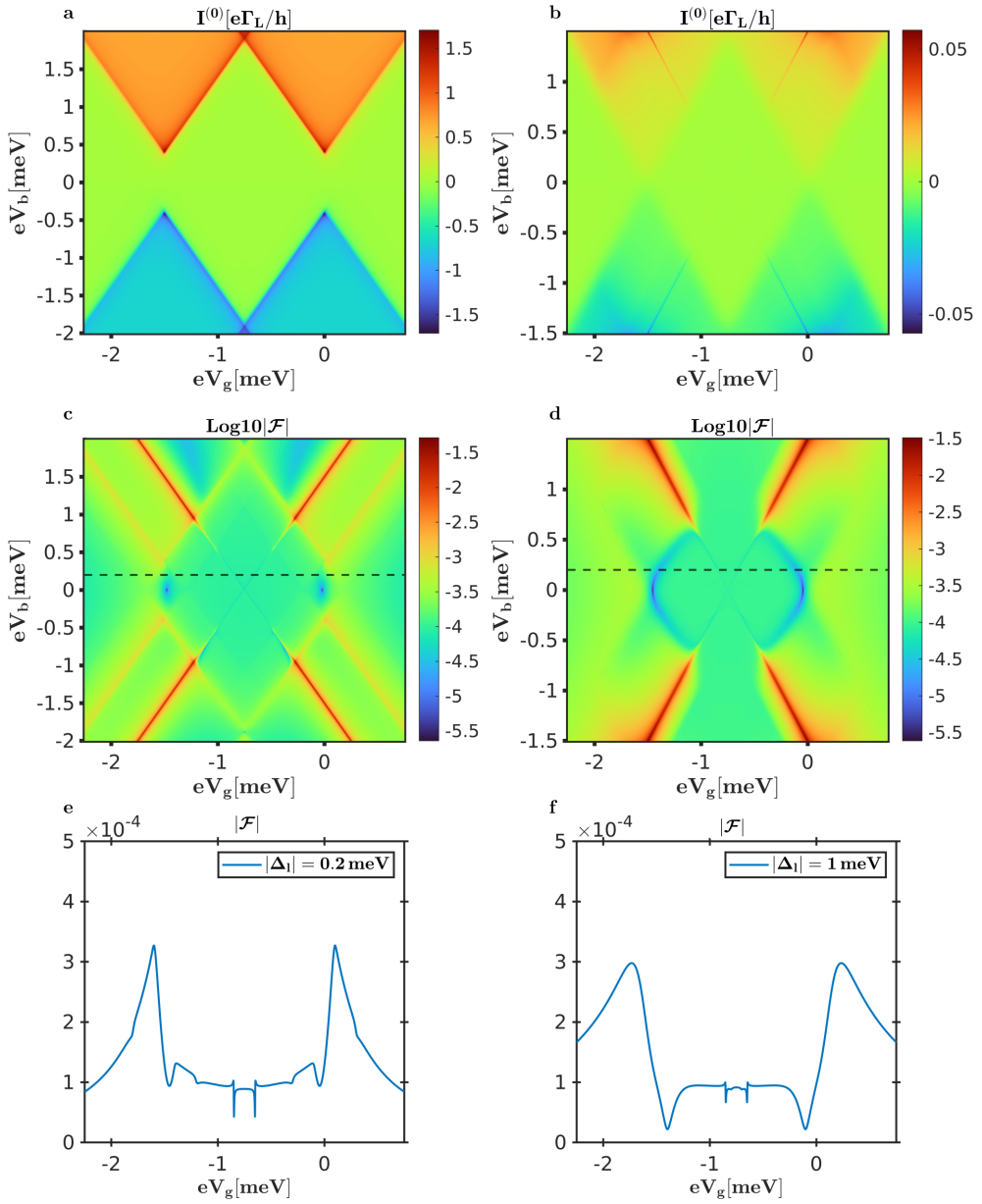

Figure 6.9: Non-equilibrium calculations: The left (right) column shows the results for $|\Delta_l| = 0.2\,\mathrm{meV}$ (1 meV). In **a**, one can clearly observe the opening of the Coulomb diamonds by $2|\Delta_l|$. For the parameter set of **b**, the current has features along the resonance lines of the superconducting coherences outside the Coulomb diamond. With the logarithm of the pair amplitudes, we highlight these resonances further. The two gate traces at $eV_b = 0.2\,\mathrm{meV}$ indicate the plots of **e-f**. The parameters are $\phi_L = -\pi/4$, $\phi_R = +\pi/4$, $\gamma = 0.01\,\mathrm{meV}$, $\Gamma = 0.001\,\mathrm{meV}$, $U = 1.5\,\mathrm{meV}$ and $k_BT = 0.05\,\mathrm{meV}$. The central five blocks of $\hat{\rho}(\Delta \boldsymbol{M})$ are used.

there are features in the current picture, but only outside of Coulomb diamond region. In this parameter regime, where U and $|\Delta_l|$ are comparable, we predict that the superconducting correlations will alter the dc-component of the current, and therefore, they would be indirectly measurable. These features are even more prominent in panel **c** and **d**, where the pair amplitude is depicted. The reasoning why the dot-pair amplitude on the resonance is suppressed inside and outside the Coulomb diamond is given extensively in [90]. At a first glance, one would focus only on regions of the resonance condition in the search for high pair amplitudes, be it in or outside the Coulomb diamonds, due to the favorable alignment of the energies of the $|2\rangle$- and $|0\rangle$-state.

However, due to our findings, we want to reiterate two points. The first one is that inside the Coulomb diamond region, it is actually better to focus on the regions which are not on the resonance, as one can observe in Fig. 6.9 **e** and **f**, with dips exactly at the resonance condition given by Eq. (6.23). The second major point we want to communicate, is that the pair amplitude inside the Coulomb diamond is *not* predominantly induced by the even population, as suggested by [117]. This fact would lead to an exponential suppression of $|\mathcal{F}|$ due to the exponentially reduced p_e facilitated by the interaction strength U.

We want to base our argumentation on the panels of Fig. 6.2 **g** and **h**, where we see a clear dip of the pair amplitude exactly in the center of the Coulomb diamond. This point is fulfilling the resonance condition of Eq. (6.23) and according to it, we also can extend this analysis to finite bias. In Eq. (6.19), we could show that the main pumping contribution arises in these gate traces from the pumping of the odd population and not from the even one, which we also confirmed numerically. Our explanation is in line with the plateau-like character of the pair amplitude inside the Coulomb diamond, in spite of an exponential increase of the even population towards the border of the Coulomb diamonds. Another hint can be the experimental data of Fig. 6.6, which also shows plateau-like critical current inside the Coulomb diamond, assuming the correlation between $|\mathcal{F}|$ and I_c. Interestingly, we observe an exact vanishing of the main pumping contribution from p_o exactly at the resonance due to $\omega_{12} = \omega_{10}$. Insofar, we agree with the observation of a suppression of $|\mathcal{F}|$ inside the Coulomb diamond *and* exactly on the resonance as suggested in [90].

Away from the resonance lines, according to Eq. (6.16) and to the odd pumping contribution of Eq. (6.19), we see that the pair amplitude is at least suppressed by a factor of Γ/U inside the Coulomb diamond.

Outside the Coulomb diamond, we can confirm the antagonist role of the interaction U in the formation of pair amplitude, with evidence that a higher value of U leads to a

lower value of $|\mathcal{F}|$ (not shown here).
The gate traces of the pair amplitude $|\mathcal{F}|$ of panel **e** and **f** resembles the one observed from zero bias calculation in the overall shape. However, there are particular differences. First of all, we do not see a drop to zero pair amplitude at the minima near the charge degeneracy points, as in Fig. 6.2 **h**. Comparing panel **e** and **f**, it seems that a stronger background contribution to $|\mathcal{F}|$ is due to enhanced quasiparticle processes for lower values of $|\Delta_l|$. Secondly, we notice that the dips of the pair amplitude are moving in correspondence with the resonance condition of Eq. (6.23) away from the center of the Coulomb diamond. In general, a stronger deviation from the zero bias results are observed in panel **e**, where the applied bias and the superconducting gap are of comparable strength.

6.6 Summary and outlook

The investigation of the dot-pair amplitude, a measure of the proximity-induced superconducting correlations, in Josephson junctions has attracted recently a lot of interest [93–96, 117]. In general, the pair amplitude is an ideal quantity to study the effect of the coherent dynamics of Cooper pairs on an impurity, which is in our case a QD.
In our analysis, we studied a QD attached to superconducting leads using a density matrix formalism, which also captures the Cooper pair space explicitly in a particle-conserving fashion. In the leading-order of a perturbation in the coupling to the leads, we could formulate the equations of motion and the current for finite gate voltages. To achieve this, we are using the Anderson pseudospin formulation to describe the superconducting correlations. The distinction to previous work is here, besides the particle-conserving ansatz, a finite interaction as well as finite superconducting gaps of the leads. In this intermediate regime, the quasiparticle spectrum is not pushed away from the relevant energy scales of our system, with the consequence of a non-vanishing pair amplitude inside the Coulomb blockade region. This result agrees qualitatively with experimental data of a critical current 0-π transition in Josephson junctions based on a QD in CNT setup [129]. The investigation of gate- and temperature-dependent 0-π transitions constitutes another finding of our studies. Other than that, non-equilibrium results of our Josephson junction are addressed. A special focus is hereby on the discussion, where one can expect distinct features from the Cooper pair transport in the current and in the dot-pair amplitude.

In Fig. 6.10, we display a part of the overall supercurrent obtained from finite bias calculations. According to Eq. (3.38), the higher harmonics of the current, like the

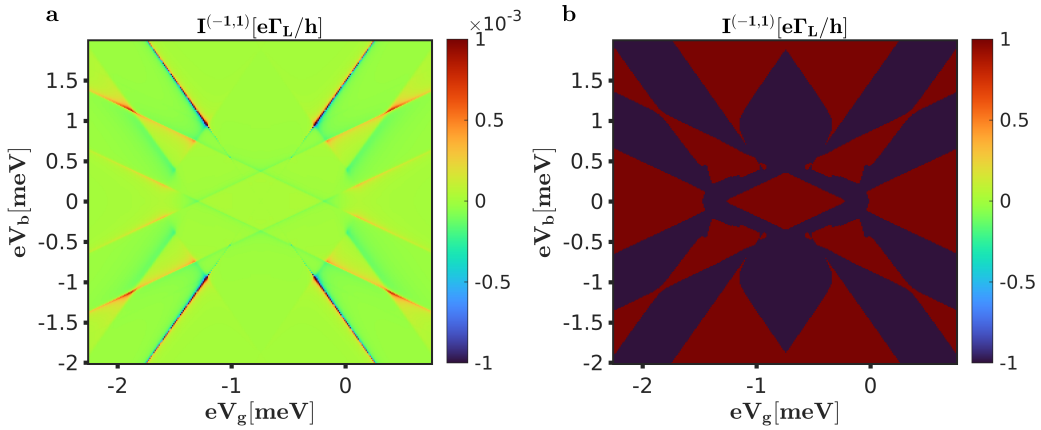

Figure 6.10: Time-dependent supercurrent for non-equilibrium calculations: In **a**, the absolute value of the current component $I^{(-1,+1)}$ is depicted, while in **b** its sign. Red regions indicate a 0-state and the blue ones a π-state. The parameters are $\phi_\mathrm{L} = -\pi/4$, $\phi_\mathrm{R} = +\pi/4$, $\gamma = 0.01\,\mathrm{meV}$, $\Gamma = 0.001\,\mathrm{meV}$, $U = 1.5\,\mathrm{meV}$, $|\Delta_l| = 0.2\,\mathrm{meV}$ and $k_\mathrm{B}T = 0.05\,\mathrm{meV}$. The central five blocks and additionally the $\hat{\rho}[(\pm 1, \mp 1)]$-blocks are used for this calculation.

depicted $I^{(-1,1)}$, are time-dependent. The frequency of $I^{(-1,1)}$ is $2\mathrm{e}V_\mathrm{b}/\hbar$. The analysis of the features in the supercurrent harmonics in non-equilibrium situations is a promising area of research [89]. It could help to explain, in a rigorous fashion, non-sinusoidal behavior of the supercurrent. Other than that, one could explore 0-π transitions in non-equilibrium situations. Together with a complete inclusion of all Γ^2-terms, one could lay the cornerstone of a consistent particle-conserving theory, which possibly helps us to understand superconducting phenomena in all its facets.

7

Final conclusion

In this thesis, we elaborated on pseudospin dynamics in hybrid nanojunctions, whereas the pseudospin was used for the description of two conceptionally different observables.

In the first occurrence, the pseudospin degree of freedom captures the orbital degree of freedom of a DQD. In this spirit, presented in Cha. 4, we brought the concept of spin resonances, shown to exist in spin valves, to the pseudospin degree of freedom. In its essence, pseudospin resonances appear due to the lifting of a valve configuration by fine-tuning the prevailing exchange fields. The effect is a bending current signal cutting through the otherwise featureless Coulomb diamonds of the DQD. This pseudospin approach has some decisive advantages in terms of its experimental realization. First and foremost, it greatly enlarges the number of possible host candidates for observing this particular interference effect since many materials, as for example CNTs, exhibit a pseudospin degree of freedom. Other than that, we could show that there is a great flexibility to achieve the necessary pseudospin valve configuration by having to change only the tunneling couplings from the QDs to the leads. In contrast, the spin polarization strength often relies on material properties and is thus hardly tunable. In this chapter, we also observed the emergence of synthetic spin-orbit with the intertwinement of spin and pseudospin in the setups due to the exchange fields at the origin of the pseudospin resonances. Hereby, the question arose if the spin and pseudospin degree are interchangeable in the utilization for spin and pseudospin resonances.

In Cha. 5, we addressed the former question by a generalization of spin and pseudospin resonances in terms of the lead polarization directions. The difference of the spin space with regard to the pseudospin space manifests itself in the setup of a spin valve with

additional parallel pseudospin polarization of the leads. There, an even greater variety of current resonances in the one-particle Coulomb diamond could be observed. At the root of the richness of the features is the interaction-induced anisotropic character of the pseudospin of the DQD in comparison to its isotropic spin space. The spin and pseudospin vectors of our system are governed by a delicate interplay of decoherence, pumping, and precession which can only be understood by also considering the dynamics of the spin-pseudospin correlators. Moreover, we could show that varying the pseudospin polarization of the leads with respect to the hard axis of the pseudospin, caused by the energetically unfavorable condition of a double occupation of one of the QDs, leads to entangled resonances. An analysis of the arising entanglement of the spin and the pseudospin in the DQD, which goes beyond a mere correlation, is hereby a central result of this chapter. Last but not least, we could conclude our investigation of spin and pseudospin resonances by identifying dephasing rather than precession as their main generating mechanism.

In the second utilization of the pseudospin degree of freedom, we use it in Cha. 6 to describe proximity-induced superconducting correlations. In our model of a QD attached to superconducting leads, we deploy a density matrix formalism which is capable of accounting explicitly in a particle-conserving fashion the Cooper pair space. We believe that this ansatz can overcome some fundamental problems non-equilibrium calculations are facing in this field. A central point of investigation is the dot-pair amplitude, captured by the Anderson pseudospin. We focus here on the leading-order of a perturbation in the coupling to the leads, while using a finite interaction and finite superconducting gaps for the leads. In this intermediate regime, we observe a non-vanishing dot-pair amplitude inside the Coulomb blockade region. Furthermore, we are able to identify the tunneling events, tied to the odd population of the QD, behind this dot-pair amplitude accumulation. Moreover, we connect the dot-pair amplitude to experimental data of 0-π transitions in Josephson junctions, which shows a good qualitative agreement with our findings. Stipulated by this comparison, we examine in detail critical current 0-π transitions, depending not only the applied gate voltage but also on the prevailing temperature. We conclude our studies with non-equilibrium results for the dot-pair amplitude and the current. In particular, we elaborate here on the expected resonances in the two quantities, which stem from the interplay of Cooper pair and quasiparticle tunneling.

Appendix

A

Sequential tunneling energy integral

The sequential tunneling contribution to the Kernel from Eq. (1.18) was given by

$$\tilde{\mathcal{K}}^{(2)} = \frac{-i}{2\pi} \sum_{\substack{nmp \\ l\alpha_1\alpha_2}} \int d\varepsilon \, \Gamma^{l,p}_{n,m} \hat{d}^{\bar{p},\alpha_2}_{n} \frac{\alpha_1\alpha_2 f_l^{(p\alpha_1)}(\varepsilon)}{i0^+ + p\varepsilon - i\hbar\mathcal{L}_{\mathrm{S}}} \hat{d}^{p,\alpha_1}_{m} \mathcal{P}. \tag{A.1}$$

The Fermi-function in this expression is obtained by the trace over the bath stemming from $\mathcal{P}$ and used the bath correlators of the Fermi-Dirac statistics

$$\mathrm{Tr}_{\mathrm{B}} \left\{ \hat{c}^{p,\alpha}_{l\boldsymbol{k}\sigma_l} \hat{c}^{p',\alpha'}_{l'\boldsymbol{k}'\sigma'_{l'}} \hat{\rho}_{\mathrm{B}} \right\} = \left\langle \hat{c}^{p,\alpha}_{l\boldsymbol{k}\sigma_l} \hat{c}^{p',\alpha'}_{l'\boldsymbol{k}'\sigma'_{l'}} \right\rangle = \delta_{ll'}\delta_{\sigma_l\sigma'_{l'}}\delta_{\mathbf{k}\mathbf{k}'}\delta_{p\bar{p}'} f_l^{(p\alpha')}\left(\varepsilon_{l\boldsymbol{k}\sigma_l}\right). \tag{A.2}$$

The superscript of the Fermi-function in Eq. (A.2) $(p\alpha')$ stems from the general expression $\mathrm{Tr}\{\hat{c}^{\dagger}_{l\mathbf{k}\sigma_l}\hat{c}_{l\mathbf{k}\sigma_l}\hat{\rho}_{\mathrm{B}}\} = \langle\hat{n}\rangle = f_l^{+}(\xi_{l\sigma_l\mathbf{k}})$ and applying the cyclic property of the trace for the different cases of left operators $\alpha = +$ and right operators $\alpha = -$.
In order to solve the energy integration, we define the Y^n-function with the integration variable x and its energy argument μ which the latter are both renormalized by $k_{\mathrm{B}}T$. Furthermore, we take the Fermi-function with a dimensionless input parameter $f^{(n)}(x) = 1/[\exp(nx)+1]$, and the Lorentzian-cutoff-function $L(\tilde{W}, x) = \tilde{W}^2/(x^2+\tilde{W}^2)$:

$$Y^n(\mu) := -\frac{i}{2\pi} \int \mathrm{d}x \frac{f^{(n)}(x) L(\tilde{W}, x)}{x - \mu + i0^+}. \tag{A.3}$$

The Lorentzian-cutoff-function originates from the applied wide-band limit with the dimensionless wide-band constant $\tilde{W} = W/(k_{\mathrm{B}}T)$ to ensure the convergence of the integration.

With the help of the residuum theorem, one obtains

$$\begin{aligned} Y^n(\mu) &= -\frac{1}{2}f^n(\mu) - \frac{in}{2\pi}\left[\mathrm{Re}\Psi^{(0)}\left(\frac{1}{2}+\frac{i\mu}{2\pi}\right) - C\right] \\ &= -\frac{1}{4} - \frac{in}{2\pi}\left[\Psi^{(0)}\left(\frac{1}{2}+\frac{i\mu}{2\pi}\right) - C\right], \end{aligned} \tag{A.4}$$

with the constant C defined as $C = \Psi^{(0)}[1/2 + \tilde{W}/(2\pi)]$ [28]. A detailed derivation of this result is given in Appx. A of [20]. One can either derive it based on a residuum-only ansatz or with the help of the Sokhotski-Plemelj theorem. The digamma-function,

$$\Psi^{(0)}(z) \coloneqq -\sum_{n=0}^{\infty}\frac{1}{n+z} + \sum_{n=1}^{\infty}\ln\left(1+\frac{1}{n}\right), \quad z \in \mathbb{C}, \tag{A.5}$$

is closely related to the Fermi-function by

$$\mathrm{Im}\Psi^{(0)}\left(\frac{1}{2}+\frac{ix}{2\pi}\right) = \frac{\pi}{p}\left[\frac{1}{2} - f^p(x)\right], \quad x \in \mathbb{R},\ p \in \{\pm 1\}. \tag{A.6}$$

Since the constant C always disappears when summing over the α-indices, we can drop C from the sequential tunneling Kernel (proof can be found in Appx. B of [20]). The final expression for the second-order Kernel $\tilde{\mathcal{K}}^{(2)}$ is obtained by inserting the energy integral function Y^n into Eq. (1.18)

$$\tilde{\mathcal{K}}^{(2)}\hat{\rho}^{\infty} = \sum_{\substack{nmp \\ l\,\alpha_1\,\alpha_2}} \alpha_1\alpha_2\,\Gamma^{l,p}_{n,m}\hat{d}^{\bar{p},\alpha_2}_n Y^{\alpha_1}\left(\frac{\Delta E_{mp\alpha_1} - p\mu_l}{k_{\mathrm{B}}T}\right)\hat{d}^{p,\alpha_1}_m\hat{\rho}^{\infty}. \tag{A.7}$$

Here we included the density matrix to highlight the fact that the energy difference $\Delta E_{mp\alpha_1}$ depends on the action of $\hat{d}^{p,\alpha_1}_m$-superoperator on the density matrix. This superoperator changes the density matrix, on which then the system Liouvillian $\mathcal{L}_{\mathrm{S}}$ is acting on to retrieve an energy difference ΔE. This projection is explicitly shown in [19].

B

Cotunneling energy integrals

The fourth-order Kernel can be formally split into the contributions $\tilde{\mathcal{K}}^{(4,D)}$,

$$\tilde{\mathcal{K}}^{(4,D)} = \frac{-i\hbar}{(4\pi)^2}\sum_{\{l\}\{p\}}\sum_{\{m\}\{n\}}\sum_{\{\alpha_i\}}\int d\varepsilon\!\!\int d\varepsilon' \alpha_1\alpha_4 \hat{d}_n^{\bar{p},\alpha_4}\frac{f_{l'}^{(p'\alpha_2)}(\varepsilon')}{i0^+ + p\varepsilon - i\hbar\mathcal{L}_{\mathrm{S}}}\hat{d}_{n'}^{\bar{p}',\alpha_3}$$
$$\frac{\Gamma^{l,p}_{n,m}\Gamma^{l',p'}_{n',m'}}{i0^+ + p\varepsilon + p'\varepsilon' - i\hbar\mathcal{L}_{\mathrm{S}}}\hat{d}_{m'}^{p',\alpha_2}\frac{f_l^{(p\alpha_1)}(\varepsilon)}{i0^+ + p\varepsilon - i\hbar\mathcal{L}_{\mathrm{S}}}\hat{d}_m^{p,\alpha_1}\mathcal{P}, \tag{B.1}$$

and $\tilde{\mathcal{K}}^{(4,X)}$,

$$\tilde{\mathcal{K}}^{(4,X)} = \frac{i\hbar}{(4\pi)^2}\sum_{\{l\}\{p\}}\sum_{\{m\}\{n\}}\sum_{\{\alpha_i\}}\int d\varepsilon\!\!\int d\varepsilon' \hat{d}_n^{\bar{p},\alpha_4}\frac{f_l^{(p\alpha_2)}(\varepsilon)}{i0^+ + p\varepsilon - i\hbar\mathcal{L}_{\mathrm{S}}}\hat{d}_{n'}^{\bar{p}',\alpha_3}$$
$$\frac{\alpha_1\alpha_4\Gamma^{l,p}_{n,m}\Gamma^{l',p'}_{n',m'}}{i0^+ + p\varepsilon + p'\varepsilon' - i\hbar\mathcal{L}_{\mathrm{S}}}\hat{d}_m^{p,\alpha_2}\frac{f_l^{(p'\alpha_1)}(\varepsilon)}{i0^+ + p'\varepsilon' - i\hbar\mathcal{L}_{\mathrm{S}}}\hat{d}_{m'}^{p',\alpha_1}\mathcal{P}. \tag{B.2}$$

There appear two qualitatively different integrals which can be expressed in terms of two types of functions, respectively the D- and X-functions. They are defined as

$$\begin{aligned} D^{nn'}(\mu,\mu',\Delta) =& \frac{-i\hbar}{4\pi^2}\int_{-\infty}^{\infty}\mathrm{d}x\int_{-\infty}^{\infty}\mathrm{d}x' \frac{f^{(n)}(x)}{x-\mu+i0^+}\frac{1}{x+x'-\Delta+i0^+}\frac{f^{(n')}(x')}{x-\mu'+i0^+} \\ =& \frac{2\pi^2 n\,(i\pi+2Cn')}{i\hbar\,(\mu-\mu')}\left[\Psi^{(0)}\left(\frac{1}{2}+\frac{i\mu}{2\pi}\right)-\Psi^{(0)}\left(\frac{1}{2}+\frac{i\mu'}{2\pi}\right)\right] \\ & -\frac{2\pi n n'}{\hbar}\sum_{k=0}^{\infty}\frac{\Psi^{(0)}\left(1+k+\frac{i\Delta}{2\pi}\right)}{\left(k+\frac{1}{2}+\frac{i\mu}{2\pi}\right)\left(k+\frac{1}{2}+\frac{i\mu'}{2\pi}\right)}, \end{aligned} \tag{B.3}$$

and

$$
\begin{aligned}
X^{nn'}(\mu,\mu',\Delta) =& \frac{i\hbar}{-4\pi^2}\int\limits_{-\infty}^{\infty}\mathrm{d}x\int\limits_{-\infty}^{\infty}\mathrm{d}x'\frac{f^{(n)}(x)}{x-\mu+i0^+}\frac{1}{x+'x'-\Delta+i0^+}\frac{f^{(n')}(x')}{x'-\mu'+i0^+}\\
=& -\frac{4\pi^2}{i\hbar}\frac{nn'}{\mu+\mu'-\Delta}\Psi^{(0)}\left(\frac{1}{2}+\frac{i\mu}{2\pi}\right)\\
&\left[\Psi^{(0)}\left(\frac{1}{2}+\frac{i\mu'}{2\pi}\right)-\Psi^{(0)}\left(\frac{1}{2}+\frac{i(\Delta-\mu)}{2\pi}\right)\right]\\
&+\frac{2\pi nn'}{\hbar}\sum_{k=0}^{\infty}\frac{\Psi^{(0)}\left(1+k+\frac{i\Delta}{2\pi}\right)}{\left(k+\frac{1}{2}+\frac{i\mu'}{2\pi}\right)\left(k+\frac{1}{2}+\frac{i(\Delta-\mu)}{2\pi}\right)}.
\end{aligned}
\tag{B.4}
$$

The D- and X-functions can be written in closed form, i.e., without an indefinite sum, for several special cases (e.g., $\Delta = 0$). In Appx. C of [20], these special cases can be found, as well as a discussion about a numerical implementation of a transport code based on these integrals. Since the expressions for the energy integrals include both the real and the imaginary part, one can calculate on the same footing the time evolution of the coherences and populations and is not dependent on an effective treatment of the fourth-order Kernel (cf. Cha. 1.3 of [26]). The final form of the fourth-order Kernel expressed with the D- and X-functions yields then

$$
\begin{aligned}
\tilde{\mathcal{K}}^{(4)}\hat{\rho}^{\infty} &= \left[\tilde{\mathcal{K}}^{(4,D)}+\tilde{\mathcal{K}}^{(4,X)}\right]\hat{\rho}^{\infty}\\
&= \sum_{\substack{\{\alpha_i\}\{l\}\\ \{n\}\{m\}\\ \{p\}}}\frac{\alpha_1\alpha_4}{k_\mathrm{B}T}\Gamma^{l,p}_{n,m}\Gamma^{l,'p'}_{n',m'}\Big[D^{\alpha_1\alpha_2}(\nu,\xi,\delta)\hat{d}^{\bar{p},\alpha_4}_{n}\hat{d}^{\bar{p}',\alpha_3}_{n'}\hat{d}^{p',\alpha_2}_{m'}\hat{d}^{p,\alpha_1}_{m}\\
&\quad + X^{\alpha_2\alpha_1}(\nu,\tau,\delta)\hat{d}^{\bar{p},\alpha_4}_{n}\hat{d}^{\bar{p}',\alpha_3}_{n'}\hat{d}^{p,\alpha_2}_{m}\hat{d}^{p',\alpha_1}_{m'}\Big]\hat{\rho}^{\infty},
\end{aligned}
\tag{B.5}
$$

with $\nu = (\Delta E_{j_3} - p\mu_l)/(k_\mathrm{B}T)$, $\xi = (\Delta E_{j_1} - p\mu_l)/(k_\mathrm{B}T)$, $\delta = (\Delta E_{j_2} - p\mu_l - p'\mu_{l'})/(k_\mathrm{B}T)$ and $\tau = (\Delta E_{j_1} - p'\mu_{l'})/(k_\mathrm{B}T)$. The subscripts $\{j_1, j_2, j_3\}$ of the energy differences ΔE indicate that these energies depend on the variables of the first (α_1, p, m), two first respective three first $\hat{d}$-superoperators.

C

Diagrammatic rules

In this chapter, we provide the diagrammatic rules for the single-timeline Liouville space. The following rules are to a large degree a repetition of the rules formulated by Michael Niklas and Andrea Donarini in their work [18, 19], with only a slight adoption to my notation and a small correction in terms of the α_i-indices.

- Draw a propagation line oriented from right to left. Fix on it $2n$ vertices, each associated with a Liouville index $\alpha = \pm$.

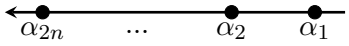

- Draw n fermionic lines, all oriented from left to right, each labelled with an index $p_i = \pm$, an overall lead index b_i comprising of its spin σ, lead l and energy ε_i, connecting the $2n$ vertices in such a way that the diagram cannot be cut in two parts without cutting a fermionic line. Example:

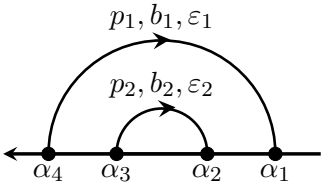

- Assign to each propagation line an energy. External lines have zero energy. The

energy is conserved at vertices.

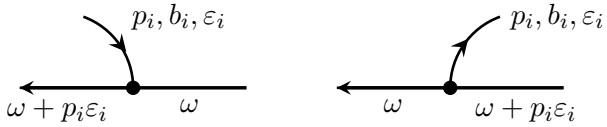

- Assign to each fermionic line the corresponding Fermi-function $f_l^{(p_i\alpha_i)}(\varepsilon_i)$, where α_i is the Liouville index of the rightmost vertex, as well as the corresponding tunneling rate matrix $\hbar/(2\pi) \times \Gamma_{n,m}^{l,p_i}$ with a prefactor. The indices of the Fermi-function and the tunneling rate matrix must be consistent with the fermionic line.

- Assign to each vertex a system operator $\hat{d}_n^{p_i,\alpha_i}$ or $\hat{d}_n^{\bar{p}_i,\alpha_i}$, respectively, for the vertex with an ingoing or outgoing fermionic line. These creation and annihilation operators of the n state must be consistent with the fermionic line $n(b_i = \sigma, l)$.

- Assign to each propagation line between vertices the propagator

$$\mathcal{G}(\omega) = \frac{1}{i0^+ + \omega - i\hbar\mathcal{L}_{\mathrm{S}}},$$

  where ω is the corresponding energy.

- Write the product of vertex superoperators and propagator, from right to left, respecting the order of the graph, while adding the Fermi-functions and tunneling rate matrices identified earlier.

- Multiply by the prefactor $(-i/\hbar)\Pi_i\alpha_i(-1)^{P\{\alpha_i\}}$, where $P\{\alpha_i\}$ is the number of equal sign vertex permutations necessary to recast the graph into a completely reduced form, which respect of the time ordering of

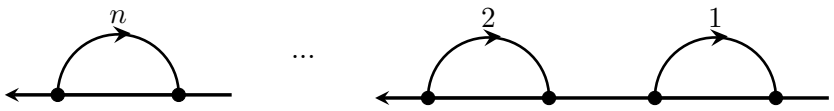

  Other than that, for each permutation, the factor $-\alpha_i\alpha_{i'}$ should be added.

- Add the summation over all α_i, p_i, l_i and σ_i indices as well as the energy integrals: $\sum_{\{\alpha_i\}}\sum_{\{p_i\}}\sum_{\{l_i\}}\sum_{\{\sigma_i\}}\int d\varepsilon_i$. The density of states are already included in the respective tunneling rate matrices.

Bibliography

[1] E. Schrödinger, *Discussion of Probability Relations between Separated Systems*, Math. Proc. Camb. Philos. Soc. **31**, 555–563 (1935).

[2] A. Einstein, B. Podolsky, and N. Rosen, *Can quantum-mechanical description of physical reality be considered complete?*, Phys. Rev. **47**, 777–780 (1935).

[3] *Press release. Nobel Prize Outreach AB 2023. Thu. 30 Mar 2023. (https://www.nobelprize.org/prizes/physics/2022/press-release/)* (The Royal Swedish Academy of Sciences, 2022).

[4] S. J. Freedman and J. F. Clauser, *Experimental test of local hidden-variable theories*, Phys. Rev. Lett. **28**, 938–941 (1972).

[5] A. Aspect, J. Dalibard, and G. Roger, *Experimental test of bell's inequalities using time-varying analyzers*, Phys. Rev. Lett. **49**, 1804–1807 (1982).

[6] A. Donarini, M. Niklas, M. Schafberger, N. Paradiso, C. Strunk, and M. Grifoni, *Coherent population trapping by dark state formation in a carbon nanotube quantum dot*, Nat. Commun. **10**, 381 (2019).

[7] T. Young, *I. The Bakerian Lecture. Experiments and calculations relative to physical optics*, Phil. Trans. R. Soc. **94**, 1–16 (1804).

[8] C. Jönsson, *Elektroneninterferenzen an mehreren künstlich hergestellten Feinspalten*, Z. Physik **161**, 454 (1961).

[9] P. G. Merli, G. F. Missiroli, and G. Pozzi, *On the statistical aspect of electron interference phenomena*, Am. J. Phys. **44**, 306 (1976).

[10] M. Arndt, O. Nairz, J. Vos-Andreae, C. Keller, G. v. der Zouw, and A. Zeilinger, *Wave-particle duality of C_{60} molecules*, Nature **74**, 4047 (1999).

[11] D. M. Cardamone, C. A. Stafford, and S. Mazumdar, *Controlling Quantum Transport through a Single Molecule*, Nano Lett. **6**, 2422–2426 (2006).

[12] S.-H. Ke, W. Yang, and H. U. Baranger, *Quantum-Interference-Controlled Molecular Electronics*, Nano Lett. **8**, 3257–3261 (2008).

[13] Z. Qian, R. Li, X. Zhao, S. Hou, and S. Sanvito, *Conceptual molecular quantum phase transistor based on first-principles quantum transport calculations*, Phys. Rev. B **78**, 113301 (2008).

[14] G. Begemann, D. Darau, A. Donarini, and M. Grifoni, *Symmetry fingerprints of a benzene single-electron transistor: Interplay between Coulomb interaction and orbital symmetry*, Phys. Rev. B **77**, 201406 (2008).

[15] D. Darau, G. Begemann, A. Donarini, and M. Grifoni, *Interference effects on the transport characteristics of a benzene single-electron transistor*, Phys. Rev. B **79**, 235404 (2009).

[16] A. Donarini, G. Begemann, and M. Grifoni, *All-Electric Spin Control in Interference Single Electron Transistors*, Nano Lett. **9**, 2897–2902 (2009).

[17] C. Rohrmeier and A. Donarini, *Pseudospin resonances reveal synthetic spin-orbit interaction*, Phys. Rev. B **103**, 205420 (2021).

[18] A. Donarini, *Lecture notes: Density matrix and its application to quantum transport*, available online at https://homepages.uni-regensburg.de/~doa17296/fisica/Teaching/ST18_DMT/ST18_DMT.html (2018).

[19] M. Niklas, *Current and noise properties of interacting nanojunctions*, (https://epub.uni-regensburg.de/37390/), PhD thesis (University of Regensburg, 2018).

[20] C. Rohrmeier, *Interference effects in the cotunnelling transport regime*, (https://epub.uni-regensburg.de/45831/), Master thesis, (University of Regensburg, 2019).

[21] S. Nakajima, *On Quantum Theory of Transport Phenomena*, Prog. Theor. Exp. Phys. **20**, 948–959 (1958).

[22] R. Zwanzig, *Ensemble Method in the Theory of Irreversibility*, J. Chem. Phys **33**, 1338–1341 (1960).

[23] H. P. Breuer and F. Petruccione, *The theory of open quantum systems* (Oxford University Press, New York, 2002).

[24] S. Koller, M. Grifoni, M. Leijnse, and M. R. Wegewijs, *Density-operator approaches to transport through interacting quantum dots: Simplifications in fourth-order perturbation theory*, Phys. Rev. B **82**, 235307 (2010).

[25] M. Leijnse, *Transport spectroscopy and control of molecular quantum dots*, (http://publications.rwth-aachen.de/record/50132/files/Leijnse_Martin.pdf), PhD thesis (RWTH Aachen University, 2010).

[26] S. Koller, *Spin phenomena and higher order effects in transport across interacting quantum-dots*, (https://epub.uni-regensburg.de/13633/), PhD thesis (University of Regensburg, 2010).

[27] A. Donarini, "Electronic transport in correlated single molecule junctions", in *Many-Body Methods for Real Materials*, Vol. 9, edited by E. Pavarini, E. Koch, and S. Zhang (Verlag des Forschungszentrum Jülich, Jülich, 2019), pp. 393–419.

[28] D. Mantelli, *Analytical and numerical study of quantum impurity systems in the intermediate and strong coupling regimes*, (https://epub.uni-regensburg.de/34135/), PhD thesis (University of Regensburg, 2016).

[29] M. Milgram, *On Some Sums of Digamma and Polygamma functions - Version (2017) and Review*, arXiv Mathematics e-prints, math/0406338 (2004).

[30] J. Koch, M. E. Raikh, and F. von Oppen, *Pair Tunneling through Single Molecules*, Phys. Rev. Lett. **96**, 056803 (2006).

[31] J. V. Holm, H. I. Jørgensen, K. Grove-Rasmussen, J. Paaske, K. Flensberg, and P. E. Lindelof, *Gate-dependent tunneling-induced level shifts observed in carbon nanotube quantum dots*, Phys. Rev. B **77**, 161406 (2008).

[32] H. Schoeller and G. Schön, *Mesoscopic quantum transport: Resonant tunneling in the presence of a strong Coulomb interaction*, Phys. Rev. B **50**, 18436–18452 (1994).

[33] J. König, H. Schoeller, and G. Schön, *Resonant Tunneling and Coulomb Oscillations*, EPL **31**, 31–36 (1995).

[34] M. Leijnse, M. R. Wegewijs, and M. H. Hettler, *Pair Tunneling Resonance in the Single-Electron Transport Regime*, Phys. Rev. Lett. **103**, 156803 (2009).

[35] P. W. Anderson, *Localized Magnetic States in Metals*, Phys. Rev. **124**, 41–53 (1961).

[36] R. Schleser, T. Ihn, E. Ruh, K. Ensslin, M. Tews, D. Pfannkuche, D. C. Driscoll, and A. C. Gossard, *Cotunneling-Mediated Transport through Excited States in the Coulomb-Blockade Regime*, Phys. Rev. Lett. **94**, 206805 (2005).

[37] M. Julliere, *Tunneling between ferromagnetic films*, Phys. Lett. A **54**, 225–226 (1975).

[38] M. N. Baibich, J. M. Broto, A. Fert, F. N. Van Dau, F. Petroff, P. Etienne, G. Creuzet, A. Friederich, and J. Chazelas, *Giant Magnetoresistance of (001)Fe/(001)Cr Magnetic Superlattices*, Phys. Rev. Lett. **61**, 2472–2475 (1988).

[39] G. Binasch, P. Grünberg, F. Saurenbach, and W. Zinn, *Enhanced magnetoresistance in layered magnetic structures with antiferromagnetic interlayer exchange*, Phys. Rev. B **39**, 4828–4830 (1989).

[40] S. Ikeda, J. Hayakawa, Y. Ashizawa, Y. M. Lee, K. Miura, H. Hasegawa, M. Tsunoda, F. Matsukura, and H. Ohno, *Tunnel magnetoresistance of 604% at 300K by suppression of Ta diffusion in CoFeB/MgO/CoFeB pseudo-spin-valves annealed at high temperature*, Appl. Phys. Lett. **93**, 082508 (2008).

[41] C. Gould, C. Rüster, T. Jungwirth, E. Girgis, G. M. Schott, R. Giraud, K. Brunner, G. Schmidt, and L. W. Molenkamp, *Tunneling Anisotropic Magnetoresistance: A Spin-Valve-Like Tunnel Magnetoresistance Using a Single Magnetic Layer*, Phys. Rev. Lett. **93**, 117203 (2004).

[42] J. Moser, A. Matos-Abiague, D. Schuh, W. Wegscheider, J. Fabian, and D. Weiss, *Tunneling Anisotropic Magnetoresistance and Spin-Orbit Coupling in* Fe/GaAs/Au *Tunnel Junctions*, Phys. Rev. Lett. **99**, 056601 (2007).

[43] H. Aurich, A. Baumgartner, F. Freitag, A. Eichler, J. Trbovic, and C. Schönenberger, *Permalloy-based carbon nanotube spin-valve*, Appl. Phys. Lett. **97**, 153116 (2010).

[44] J. R. Hauptmann, J. Paaske, and P. E. Lindelof, *Electric-field-controlled spin reversal in a quantum dot with ferromagnetic contacts*, Nat. Phys. **4**, 373–376 (2008).

[45] S. Sahoo, T. Kontos, J. Furer, C. Hoffmann, M. Gräber, A. Cottet, and C. Schönenberger, *Electric field control of spin transport*, Nat. Phys. **1**, 99–102 (2005).

[46] L. Hofstetter, A. Geresdi, M. Aagesen, J. Nygård, C. Schönenberger, and S. Csonka, *Ferromagnetic Proximity Effect in a Ferromagnet–Quantum-Dot–Superconductor Device*, Phys. Rev. Lett. **104**, 246804 (2010).

[47] A. N. Pasupathy, R. C. Bialczak, J. Martinek, J. E. Grose, L. A. K. Donev, P. L. McEuen, and D. C. Ralph, *The Kondo Effect in the Presence of Ferromagnetism*, Science **306**, 86–89 (2004).

[48] M. M. Deshmukh and D. C. Ralph, *Using Single Quantum States as Spin Filters to Study Spin Polarization in Ferromagnets*, Phys. Rev. Lett. **89**, 266803 (2002).

[49] A. Bernand-Mantel, P. Seneor, K. Bouzehouane, S. Fusil, C. Deranlot, F. Petroff, and A. Fert, *Anisotropic magneto-Coulomb effects and magnetic single-electron-transistor action in a single nanoparticle*, Nat. Phys. **5**, 920–924 (2009).

[50] K. Hamaya, M. Kitabatake, K. Shibata, M. Jung, M. Kawamura, K. Hirakawa, T. Machida, T. Taniyama, S. Ishida, and Y. Arakawa, *Electric-field control of tunneling magnetoresistance effect in a Ni/InAs/Ni quantum-dot spin valve*, Appl. Phys. Lett. **91**, 022107 (2007).

[51] A. Bordoloi, V. Zannier, L. Sorba, C. Schönenberger, and A. Baumgartner, *A double quantum dot spin valve*, Commun. Phys. **3**, 135 (2020).

[52] P. San-Jose, E. Prada, E. McCann, and H. Schomerus, *Pseudospin Valve in Bilayer Graphene: Towards Graphene-Based Pseudospintronics*, Phys. Rev. Lett. **102**, 247204 (2009).

[53] A. Rycerz, J. Tworzydło, and C. W. J. Beenakker, *Valley filter and valley valve in graphene*, Nat. Phys. **3**, 172–175 (2007).

[54] J. Li, R.-X. Zhang, Z. Yin, J. Zhang, K. Watanabe, T. Taniguchi, C. Liu, and J. Zhu, *A valley valve and electron beam splitter*, Science **362**, 1149–1152 (2018).

[55] S. Roy, K. Roychowdhury, and S. Das, *Pseudospin-valve effect on transport in junctions of three-dimensional topological insulator surfaces*, New J. Phys. **18**, 073038 (2016).

[56] M. Braun, J. König, and J. Martinek, *Theory of transport through quantum-dot spin valves in the weak-coupling regime*, Phys. Rev. B **70**, 195345 (2004).

[57] M. Margańska, D. R. Schmid, A. Dirnaichner, P. L. Stiller, C. Strunk, M. Grifoni, and A. K. Hüttel, *Shaping Electron Wave Functions in a Carbon Nanotube with a Parallel Magnetic Field*, Phys. Rev. Lett. **122**, 086802 (2019).

[58] P. Fazekas, *Lecture Notes on Electron Correlation and Magnetism* (World Scientific, 1999).

[59] J. Martinek, Y. Utsumi, H. Imamura, J. Barna ś, S. Maekawa, J. König, and G. Schön, *Kondo Effect in Quantum Dots Coupled to Ferromagnetic Leads*, Phys. Rev. Lett. **91**, 127203 (2003).

[60] J. König and J. Martinek, *Interaction-Driven Spin Precession in Quantum-Dot Spin Valves*, Phys. Rev. Lett. **90**, 166602 (2003).

[61] C. P. Poole, *Electron spin resonance: a comprehensive treatise on experimental techniques* (Courier Corporation, 1996).

[62] R. Sánchez, S. Kohler, and G. Platero, *Spin correlations in spin blockade*, New J. Phys. **10**, 115013 (2008).

[63] P. Willke, T. Bilgeri, X. Zhang, Y. Wang, C. Wolf, H. Aubin, A. Heinrich, and T. Choi, *Coherent Spin Control of Single Molecules on a Surface*, ACS Nano **15**, 17959–17965 (2021).

[64] M. Pioro-Ladrière, T. Obata, Y. Tokura, Y.-S. Shin, T. Kubo, K. Yoshida, T. Taniyama, and S. Tarucha, *Electrically driven single-electron spin resonance in a slanting Zeeman field*, Nat. Phys. **4**, 776–779 (2008).

[65] M. Hell, B. Sothmann, M. Leijnse, M. R. Wegewijs, and J. König, *Spin resonance without spin splitting*, Phys. Rev. B **91**, 195404 (2015).

[66] S. Wenderoth, J. Bätge, and R. Härtle, *Sharp peaks in the conductance of a double quantum dot and a quantum-dot spin valve at high temperatures: A hierarchical quantum master equation approach*, Phys. Rev. B **94**, 121303 (2016).

[67] P. Busz, D. Tomaszewski, and J. Martinek, *Exchange field determination in a quantum dot spin valve by the spin dynamics*, J. Magn. Magn. Mater. **546**, 168831 (2022).

[68] N. M. Gergs, S. A. Bender, R. A. Duine, and D. Schuricht, *Spin Switching via Quantum Dot Spin Valves*, Phys. Rev. Lett. **120**, 017701 (2018).

[69] S. Mundinar, A. Hucht, J. König, and S. Weiss, *Interaction-induced current asymmetries in resonant transport through interacting quantum-dot spin valves revealed by iterative summation of path integrals*, Phys. Rev. B **102**, 045404 (2020).

[70] M. Baumgärtel, M. Hell, S. Das, and M. R. Wegewijs, *Transport and Accumulation of Spin Anisotropy*, Phys. Rev. Lett. **107**, 087202 (2011).

[71] C. Rohrmeier and A. Donarini, *Precession of entangled spin and pseudospin in double quantum dots*, Phys. Rev. B **105**, 205418 (2022).

[72] W. K. Wootters, *Entanglement of Formation of an Arbitrary State of Two Qubits*, Phys. Rev. Lett. **80**, 2245–2248 (1998).

[73] S. Hill and W. K. Wootters, *Entanglement of a Pair of Quantum Bits*, Phys. Rev. Lett. **78**, 5022–5025 (1997).

[74] H. Kamerlingh Onnes, Proceedings of the Koninklijke Akademie van Wetenschappen te Amsterdam, scanned from Boston Studies in the Philosophy of Science volume 124 (page 269), 1479–1481 (1911).

[75] W. Meissner and R. Ochsenfeld, *Ein neuer Effekt bei Eintritt der Supraleitfähigkeit*, Sci. Nat. **21**, 787–788 (1933).

[76] F. London and H. London, *The electromagnetic equations of the supraconductor*, Proc. R. Soc. Lond. A **149**, 71–88 (1935).

[77] V. L. Ginzburg and L. D. Landau, "On the Theory of Superconductivity", in *On Superconductivity and Superfluidity: A Scientific Autobiography* (Springer Berlin Heidelberg, Berlin, Heidelberg, 2009), pp. 113–137.

[78] J. Bardeen, L. N. Cooper, and J. R. Schrieffer, *Theory of Superconductivity*, Phys. Rev. **108**, 1175–1204 (1957).

[79] E. Maxwell, *Isotope Effect in the Superconductivity of Mercury*, Phys. Rev. **78**, 477–477 (1950).

[80] C. A. Reynolds, B. Serin, W. H. Wright, and L. B. Nesbitt, *Superconductivity of Isotopes of Mercury*, Phys. Rev. **78**, 487–487 (1950).

[81] A. J. Leggett, *Quantum Liquids: Bose condensation and Cooper pairing in condensed-matter systems* (Oxford University Press, 2006).

[82] J. Chow, O. Dial, and J. Gambetta, *Press release. IBM Research Blog. IBM Quantum breaks the 100-qubit processor barrier. (https://research.ibm.com/blog/127-qubit-quantum-processor-eagle)* (2021).

[83] null null *et al.*, *Hartree-Fock on a superconducting qubit quantum computer*, Science **369**, 1084–1089 (2020).

[84] T. W. and, *The EcoSwing Project*, IOP Conf. Ser. Mater. Sci. Eng. **502**, 012004 (2019).

[85] *Press release. Umweltfreundliche Technologien – Preisträger 2015. (https://www.iku-innovationspreis.de/iku-info/preistraeger/2015/rwe-deutschland.php)* (IKU, 2015).

[86] *Press release. Munich wants longest superconductor cable in the world. (https://www.bayern-innovativ.de/en/page/munich-wants-longest-superconductor-cable-in-the-world)* (bayern innovativ, 2019).

[87] Y. Cao, V. Fatemi, S. Fang, K. Watanabe, T. Taniguchi, E. Kaxiras, and P. Jarillo-Herrero, *Unconventional superconductivity in magic-angle graphene superlattices*, Nature **556**, 43 (2018).

[88] B. Josephson, *Possible new effects in superconductive tunnelling*, Phys. Lett. **1**, 251–253 (1962).

[89] J. Picó Cortés, *AC dynamics of quantum dots and Josephson junctions for quantum technologies*, (http://hdl.handle.net/10486/700881), Ph.D. thesis (Universidad Autónoma de Madrid, 2021).

[90] J. Siegl, J. Picó-Cortés, and M. Grifoni, *Particle conserving approach to ac-dc driven interacting quantum dots with superconducting leads*, Phys. Rev. B **107**, 115405 (2023).

[91] L. N. Cooper, *Bound Electron Pairs in a Degenerate Fermi Gas*, Phys. Rev. **104**, 1189–1190 (1956).

[92] J. Koenig, *Quantum fluctuations in the single-electron transistor*, PhD thesis (Universität Karlsruhe, 1999).

[93] M. Governale, M. G. Pala, and J. König, *Real-time diagrammatic approach to transport through interacting quantum dots with normal and superconducting leads*, Phys. Rev. B **77**, 134513 (2008).

[94] M. Kamp and B. Sothmann, *Phase-dependent heat and charge transport through superconductor–quantum dot hybrids*, Phys. Rev. B **99**, 045428 (2019).

[95] M. Kamp and B. Sothmann, *Higgs-like pair amplitude dynamics in superconductor–quantum-dot hybrids*, Phys. Rev. B **103**, 045414 (2021).

[96] M. Heckschen and B. Sothmann, *Pair-amplitude dynamics in strongly coupled superconductor–quantum dot hybrids*, Phys. Rev. B **105**, 045420 (2022).

[97] R. C. Dynes, V. Narayanamurti, and J. P. Garno, *Direct Measurement of Quasiparticle-Lifetime Broadening in a Strong-Coupled Superconductor*, Phys. Rev. Lett. **41**, 1509–1512 (1978).

[98] A. L. Yeyati, J. C. Cuevas, A. López-Dávalos, and A. Martín-Rodero, *Resonant tunneling through a small quantum dot coupled to superconducting leads*, Phys. Rev. B **55**, R6137–R6140 (1997).

[99] P. W. Anderson, *Random-Phase Approximation in the Theory of Superconductivity*, Phys. Rev. **112**, 1900–1916 (1958).

[100] B. D. Josephson, *The discovery of tunnelling supercurrents*, Rev. Mod. Phys. **46**, 251–254 (1974).

[101] J. Tersoff and D. R. Hamann, *Theory of the scanning tunneling microscope*, Phys. Rev. B **31**, 805–813 (1985).

[102] M. T. Maurer, J. König, and H. Schoeller, *Multilevel coherences in quantum dots*, Phys. Rev. Research **2**, 033440 (2020).

[103] A. Donarini, G. Begemann, and M. Grifoni, *Interference effects in the Coulomb blockade regime: Current blocking and spin preparation in symmetric nanojunctions*, Phys. Rev. B **82**, 125451 (2010).

[104] H. A. Nilsson, O. Karlström, M. Larsson, P. Caroff, J. N. Pedersen, L. Samuelson, A. Wacker, L.-E. Wernersson, and H. Q. Xu, *Correlation-Induced Conductance Suppression at Level Degeneracy in a Quantum Dot*, Phys. Rev. Lett. **104**, 186804 (2010).

[105] J. Barański, T. Zienkiewicz, M. Barańska, and K. J. Kapcia, *Anomalous Fano Resonance in Double Quantum Dot System Coupled to Superconductor*, Sci. Rep. **10**, 2881 (2020).

[106] M. E. Torio, K. Hallberg, S. Flach, A. E. Miroshnichenko, and M. Titov, *Spin filters with Fano dots*, Eur. Phys. J. B **37**, 399–403 (2004).

[107] A. Bärnthaler, S. Rotter, F. Libisch, J. Burgdörfer, S. Gehler, U. Kuhl, and H.-J. Stöckmann, *Probing Decoherence through Fano Resonances*, Phys. Rev. Lett. **105**, 056801 (2010).

[108] Y. Joe, J. Kim, E. Hedin, R. Cosby, and A. Satanin, *Fano Resonance Through Quantum Dots in Tunable Aharonov-Bohm Rings*, J. Comput. Electron. **4**, 129–133 (2005).

[109] A. C. Johnson, C. M. Marcus, M. P. Hanson, and A. C. Gossard, *Coulomb-Modified Fano Resonance in a One-Lead Quantum Dot*, Phys. Rev. Lett. **93**, 106803 (2004).

[110] O. Karlström, J. N. Pedersen, P. Samuelsson, and A. Wacker, *Canyon of current suppression in an interacting two-level quantum dot*, Phys. Rev. B **83**, 205412 (2011).

[111] Zheng Hao, Zhang Junyi, and Berndt Richard, *A minimal double quantum dot*, Sci. Rep. **7**, 10764 (2017).

[112] K. J. G. Götz, F. J. Schupp, and A. K. Hüttel, *Carbon Nanotube Millikelvin Transport and Nanomechanics*, Phys. Status Solidi B **256**, 1800517 (2019).

[113] M. Gaass, A. K. Hüttel, K. Kang, I. Weymann, J. von Delft, and C. Strunk, *Universality of the Kondo Effect in Quantum Dots with Ferromagnetic Leads*, Phys. Rev. Lett. **107**, 176808 (2011).

[114] B. G. de Moraes, A. W. Cummings, and S. Roche, *Emergence of intraparticle entanglement and time-varying violation of Bell's inequality in Dirac matter*, Phys. Rev. B **102**, 041403 (2020).

[115] L. Magazzù, J. D. Jaramillo, P. Talkner, and P. Hänggi, *Generation and stabilization of Bell states via repeated projective measurements on a driven ancilla qubit*, Phys. Scr. **93**, 064001 (2018).

[116] M. Hell, S. Das, and M. R. Wegewijs, *Transport of spin anisotropy without spin currents*, Phys. Rev. B **88**, 115435 (2013).

[117] M. G. Pala, M. Governale, and J. König, *Nonequilibrium Josephson and Andreev current through interacting quantum dots*, New J. Phys. **9**, 278 (2007).

[118] Y. Meir and N. S. Wingreen, *Landauer formula for the current through an interacting electron region*, Phys. Rev. Lett. **68**, 2512–2515 (1992).

[119] V. V. Ryazanov, V. A. Oboznov, A. Y. Rusanov, A. V. Veretennikov, A. A. Golubov, and J. Aarts, *Coupling of Two Superconductors through a Ferromagnet: Evidence for a π Junction*, Phys. Rev. Lett. **86**, 2427–2430 (2001).

[120] J. J. A. Baselmans, A. F. Morpurgo, B. J. van Wees, and T. M. Klapwijk, *Reversing the direction of the supercurrent in a controllable Josephson junction*, Nature **397**, 43–45 (1999).

[121] J. A. van Dam, Y. V. Nazarov, E. P. A. M. Bakkers, S. De Franceschi, and L. P. Kouwenhoven, *Supercurrent reversal in quantum dots*, Nature **442**, 667–670 (2006).

[122] A. Costa, J. Fabian, and D. Kochan, *Connection between zero-energy yu-shiba-rusinov states and $0-\pi$ transitions in magnetic josephson junctions*, Phys. Rev. B **98**, 134511 (2018).

[123] T. Kontos, M. Aprili, J. Lesueur, F. Genêt, B. Stephanidis, and R. Boursier, *Josephson junction through a thin ferromagnetic layer: negative coupling*, Phys. Rev. Lett. **89**, 137007 (2002).

[124] S. Karan *et al.*, *Superconducting quantum interference at the atomic scale*, Nat. Phys. **18**, 893–898 (2022).

[125] J. Bauer, A. Oguri, and A. C. Hewson, *Spectral properties of locally correlated electrons in a bardeen–cooper–schrieffer superconductor*, J. Phys. Condens. Matter **19**, 486211 (2007).

[126] M.-S. Choi, M. Lee, K. Kang, and W. Belzig, *Kondo effect and josephson current through a quantum dot between two superconductors*, Phys. Rev. B **70**, 020502 (2004).

[127] T. Meng, S. Florens, and P. Simon, *Self-consistent description of andreev bound states in josephson quantum dot devices*, Phys. Rev. B **79**, 224521 (2009).

[128] C. Karrasch, A. Oguri, and V. Meden, *Josephson current through a single anderson impurity coupled to bcs leads*, Phys. Rev. B **77**, 024517 (2008).

[129] H. I. Jørgensen, T. Novotny, K. Grove-Rasmussen, K. Flensberg, and P. E. Lindelof, *Critical Current 0-π Transition in Designed Josephson Quantum Dot Junctions*, Nano Lett. **7**, 2441–2445 (2007).

Acronyms

BCS Bardeen–Cooper–Schrieffer.

CNT carbon nanotube.

CST coherent sequential tunneling.

DQD double quantum dot.

EPR Einstein–Podolsky–Rosen.

GME generalized master equation.

GMR giant magnetoresistance.

MRI magnetic resonance imaging.

QD quantum dot.

S-QD-S superconductor-quantum dot-superconductor.

SGPA surface Γ-point approximation.

SIAM single-impurity Anderson model.

SOI spin-orbit interaction.

STM scanning tunneling microscope.

TAMR tunneling anisotropic magnetoresistance.

TMR tunneling magnetoresistance.

Acknowledgments

I want to thank all the people who helped me during my PhD and made this time for me a particularly enriching experience, both on a scientific and a personal level.

First and foremost, my biggest gratitude belongs to Andrea. Your never-ending endurance to answer one of my many questions and your dedication to my studies deserve a big thank you. The discussions about physics with you are, for me, the part which I enjoyed the most during my PhD. It was an astonishing time with you as a supervisor!

Other than that, I want to especially thank Milena for the numerous scientific advice and guidance, in particular, with my studies of superconductivity. Moreover, I am grateful that I could be a member of your welcoming chair.

Another thank you belongs to Jordi and Julian for helping me set up my superconducting transport code. Jordi, I also owe you much for the many explanations of the theory behind it and, in general, that I could use your framework for my research.

Moritz, you know how much I liked it to be with you in the office. Without you, it would have been a different experience!

Kathleen, you can't be missing in this list. Thank you for the patience with me!

Last but not least, I want to thank all the other people who were in touch with me during my PhD, especially Luca, Bashab and Magda and the people from the Evers

chair, who joined for the lunch and coffee breaks. The discussions there will always have a special place in my heart!

This thesis was supported by the Deutsche Forschungsgemeinschaft via SFB 1277 and by the Elitenetzwerk Bayern via the doctorate program "Topologische Isolatoren".